UNIVERSITY OF BIRMINGHAM

Development of an instrument for the *in situ* Measurement of Atmospheric Ozone production rates

by

Hao Huang

A thesis submitted to the University of Birmingham

for the degree of DOCTOR OF PHILOSOPHY

School of Geography, Earth and Environmental Sciences

University of Birmingham

September 2015

Abstract

Ambient boundary layer ozone, as a secondary air pollutant and a powerful greenhouse gas, is a major threat to human health, plants and the environment. In order to develop effective air quality policy to minimise ozone pollution, it is important to gain a quantitative understanding of the chemical factors that drive tropospheric ozone production. There are a number of limitations and uncertainties in the current models and indirect methods used to estimate chemical ozone production rates. Here, an Ozone Production Rate (OPR) instrument is developed to fulfil the demand of accurately measuring ambient ozone production rates in the atmosphere. This prototype system aims to directly measure the *in situ* oxidant (O_x: O_3 + NO_2) production rate $p(O_x)$ in ambient air. This thesis describes the OPR experimental methodology, instrument properties and system characteristics. Two field deployments (London and India) are comprehensively discussed, and correction approaches are implemented to improve measurement accuracy.

The London measurement focused on a heavily polluted four day period. When the wind direction was stable (easterly), the OPR measured oxidant production rate, $p(O_x)$, showed a similar diurnal pattern to a range of related factors, including the ambient hydroxyl radical production rate $p(OH)$, the rate of change of ambient oxidant levels and, and the estimated net chemical oxidant production rate derived from indirect measurement methods. The OPR measurement results were only compared to rate of change of observed ambient oxidant levels in Delhi, India, with the results showing a similar diurnal pattern as rate of change of the ambient (*in situ*) oxidant levels. Both field measurement results, when adjusted for local solar time, exhibited a diurnal pattern in $p(O_x)$, showing sharp rise of the oxidant production rate in the morning which dropped to negative values in the afternoon. However, the

temporal pattern of the diurnal peak $p(O_x)$ levels were significantly different between the two locations. The field measurement results indicated that measured $p(O_x)$ levels could be used to assess modelled O_x production rates and changes in ambient oxidant levels under stable meteorological conditions. A refined OPR system could be a useful tool to determine the balance between advection and chemical production in controlling local ozone levels, and hence support ozone control policy.

Live long and prosper.

-----Mr. Spock

To Fei, Mum and Dad,

With love

Acknowledgements

I would like to thank a number of people and associations that have supported me through my PhD.

First and foremost, I would like to thank my supervisor Bill Bloss for all the professional guidance in these years. It was his lectures during MSc course that have given me a keen interest in atmopsheric chemistry; it was my initial motivation to decide to carry on into PhD study. I really appreciate Bill for giving me the opportunity to join such an excellent research group, many many thanks to Bill for all the knowledge, supports and encouragement.

Next I would like to thank to people who have been working in the Wolfson lab, particularly to Kate Faloon, you are the guide to give me understanding of every single detail of the instruments, I have learned so many skills from your patient demonstrating. Special thanks to Juan Najera, Suad Al Kindi and Leigh Crilley, it was a great pleasure to work with you. Thanks to Jamie Peart, Richard Johnson, Eimear Orgill and Gillian Kingston for all the lab facility support and guidance.

Thanks to GEES and NERC, for providing me the opportunity to get involved in such a stimulating research project. Thanks to people who were involved in the OPR project, including Juana Maria Delgado, David Beddows, James Lee, Nandini Kumar and Anita Dahiya.

Finally I would like to thank my wife and my family. Fei, thanks for putting my up in difficult times, you give me endless encouragements to solve the difficulties in academic field and daily life. Thanks to Mum and Dad, for all financial and spiritual support of my entire life.

Table of contents

Chapter 1. Introduction 1

1.1 Introduction to Thesis Structure 1

1.2 Structure of the Atmosphere 3

1.3 Trace gases 3

1.3.1 Nitrogen species 3

1.3.2 Volatile Organic Compounds 4

1.3.3 Radical Species 6

1.4 Tropospheric Chemistry and Ozone Formation 7

1.4.1 Photochemical Steady State 7

1.4.2 Tropospheric chemistry and OH 9

1.4.3 Ozone formation process 13

1.5 Human and Environmental Impacts of Ozone 18

1.5.1 Ozone impacts on human health 18

1.5.2 Wider environmental impacts of ozone 21

1.5.3 Role of ozone in the Earth's climate system 24

1.6 Current Tropospheric Ozone Regulations and Trends 26

1.6.1 Ozone regulations worldwide 26

1.6.2 Global ozone trend since 1950s 27

1.6.3 Ozone trends and current levels in the UK 27

1.6.4 Ozone trends in the US 32

1.7 Evaluation of Ozone Production 40

1.7.1 Models of evaluating ozone production 40

1.7.2 Global Models 41

1.7.3 Regional models 41

1.7.4 Urban models 41

1.7.5 Specialist ozone models 42

1.7.6 Models Uncertainties and Limitations 43

I. Uncertainties in ozone production chemistry. 43

II. Emissions data limitations 44

III. Climate and environmental factors 45

1.8 Existing Methods to Measure Local Chemical Ozone Production 46

1.8.1 Indirect measurement methods 46

1.8.2 NO_x photochemical steady state (PSS) 46

1.8.3 Direct measurement of Peroxy Radicals - PERCA and LIF approaches 48

I. Laser Induced Fluorescence (LIF) 48

II. Peroxy Radical Chemical Amplifier (PERCA) 49

1.9 Aim of this thesis 51

Chapter 2: Experimental Methodology and Instrument Properties 53

2.1 Direct measurement of ozone production 53

2.2 Introduction to the OPR System 55

2.2.1 Principle of the OPR approach 55

2.2.2 The OPR system's flow path 57

2.2.3 Photochemistry in the Sample and Reference Reactors 60

2.3 Individual System Components 64

2.3.1 Sampling Reactors' material 64

2.3.1.1 Quartz material 64

2.3.1.2 Ultem Material 65

2.3.2 Reactor dimensions 67

2.3.3 Air flow in the reactors 68

2.3.4 Flow straightener 71

2.3.5 Sealing disk 72

2.3.6 Reactor mounting frame 73

2.3.7 Flow rate in the reactors 74

2.3.8 MFCs 74

2.4 Photolytic NO_2 Conversion Unit 76

2.4.1 Converter Cells 77

2.4.2 Solenoid Valves 80

2.5 IGI Interface Unit and OPR core unit 83

2.5.1 OPR core unit 83

2.5.2 IGI Interface unit 84

2.6 Thermo 49i Ozone Monitor 86

2.7 OPR system configuration during the field deployments 89

2.7.1 London OPR deployment 90

2.7.2 India OPR deployment 91

2.8 Ancillary measurements 93

2.9 Summary of the Experimental methodology and instrument properties 94

Chapter 3: System Characterisation 95

3.1 Reactor Residence Time 96

3.1.1 Pulse method of residence time determination 97

3.1.2 Step method of residence time determination 100

3.2 Results of reactor residence time measurements 103

3.2.1 Open pulse method to determine residence time 104

3.2.2 Step method to determine residence time 106

3.3 Results of conversion unit residence time measurements 108

3.3.1 Step and Pulse method setup on converter cells 108

3.3.2 Summary of residence time measurement results of converter cell 110

3.4 Tests for wall losses of NO_x and O_3 in reactors 113

3.4.1 Sample / Reference reactor ozone loss test 113

3.4.2 Sample / reference reactor NO_x loss tests 117

3.5 Mass Flow Controller (MFC) calibration 121

3.6 NO_2 conversion efficiency tests 123

3.7 Calibration of the Thermo 49i Ozone Monitor 127

3.8 Limitations of the OPR system performance 128

3.8.1 The OPR measurement requirement 128

3.8.2 Actual conversion efficiency in conversion unit 128

3.8.3 PSS issue in reactor 129

3.8.4 Dark radical chemistry in reactors 129

3.9 Concluding remarks of performance tests 131

Chapter 4: London OPR deployment 134

4.1 London OPR deployment introduction 134

4.1.1 Description of OPR measurement site in London 135

4.2 Air Pollution Climatology during the ClearfLo summer IOP measurement period 141

4.2.1 Pollutant abundance and statistical distribution during the Summer IOP 148

4.2.2 Ambient NO_x and O_3 distribution during the “FIOM” pollution episode 156

4.3 Ozone Production Rate (OPR) measurement periods and data availability 162

4.3.1 Ambient Composition: Measurement Correlations 162

4.3.2 Data availability and definitions 166

4.4 Four days intensive OPR measurement period (FIOM) 169

4.4.1 Photochemical Steady State (PSS) Impacts 174

4.4.2 Traffic Emissions 175

4.4.3 Chemical Ozone Production Processes 176

4.5 Radical Production Rate: $p(OH)$ and $p(O_x)$ 185

4.5.1 Calculation of the OH yield from O^1D reaction, "f" 187

4.5.2 Contribution of OH production rate from alkene species reacting with O_3 188

4.5.3 Comparison between evaluated $p(OH)$ and measured $p(O_x)$ 189

4.5.4 Derived oxidant formation rates from HO_2 measurements 192

4.6 Advection effects on ozone mixing ratio changes during FIOM 196

4.6.1 Advection Analysis: Methodology 197

4.6.2 Advection analysis procedures 198

4.6.3 Derivation of satellite location pollutant levels 199

4.6.4 Result of advection analysis 201

4.6.4.1 NO_x and O_3 levels from advection analysis during FIOM 201

4.6.4.2 Evaluation of idealized ozone/O_x production rate 207

4.6.5 Conclusion and Limitations of the Advection Analysis 215

4.6.6 Evaluation of the Chemical Oxidant Loss Rate during FIOM 216

4.7 Uncertainties in measured $p(O_x)$ values during FIOM 219

4.8 Summary of OPR deployment in London 221

Chapter 5: System Accuracy and Correction Factors 223

5.1 Origin of Chemical Errors in ΔO_3 from the OPR system 223

5.2 A Modelling approach to parameterise the NO_2 conversion efficiency 225

5.2.1 Basis of the modelling method of conversion efficiency (CE) estimation 225

5.2.2 Calculation of $jNO_{2\ lamp}$ in converter cell 226

5.2.3 Principle of the modelling method 227

5.2.4 Conversion cell chemistry model: Calculation Procedure 228

5.2.5 Conversion Cell Chemistry Model Validation 230

5.3 ΔO_3 correction analysis 232

5.3.1 Different PSS in both reactors 232

5.3.2 Change of NO_x/O_3 values in the reference reactor 233

5.3.3 The overall artefact correction procedure 236

5.4 Limitations of the correction approach 238

5.5 Conclusion of correction approach 239

Chapter 6: OPR measurements in New Delhi, India (with improvements) 240

6.1 Background: Indian Climatology & Air Pollution 241

6.1.1 Indian Climatology 241

6.1.2 Indian Air Pollution problem 241

6.2 Introduction to the Indian OPR deployment 244

6.3 Data source and availability 247

6.4 Location information of OPR deployment site in TERI University, New Delhi ...250

6.4.1 OPR system location 250

6.4.2 Local Climatology during the measurement 250

6.5 Comparison between measured O_3 at TERI University and DPCC site....255

6.5.1 Correlation between Ozone Datasets....261

6.5.2 Mean diurnal ozone dataset comparison 261

6.6 Pollutant Characteristics at TERI during TSMT 264

6.7 Pollutant levels during TSMT....269

6.8 Comparison of measured oxidant production with changes in ambient O_x levels during TSMT 275

6.9 Comparison between OPR-measured Oxidant Production Rates $p(O_x)$ in London and New Delhi 278

6.10 Mohali OPR Deployment 284

6.10.1 Mohali Measurement Challenges. 285

6.11 Indian OPR Deployment: Concluding Remarks....286

Chapter 7: Conclusion....287

7.1 Summary of the OPR system development 287

7.2 Future work....296

References....298

List of abbreviations

AQEG Air Quality Expert Group

CPCB Central Pollution Control Board

DEFRA Department for environment, food and Rural Affairs

DPCC Delhi Pollution Control Committee

EPA US Environmental Protection Agency

FAGE Fluorescence Assay by Gas Expansion

FIOM The Four days Intensive OPR Measurement

f-NO_2 The fraction of primary NO_2 in NO_x emissions

ID/OD Inner Diameter/Outer Diameter

LIF Lacer Induced Fluorescence

MCM Master Chemical Mechanism

MFC Mass Flow Controller

NK North Kensington

OPR the Ozone Production Rate measurement system

PSS Photostationary Steady State

PERCA Peroxy Radical Chemical Amplifier

SZA Solar Zenith Angle

SLM Standard Litres per Minute

Tg Teragram

TSMT The Successful Measurement days at the TERI site

TUV Tropospheric Ultraviolet and Visible

UoB University of Birmingham

VOC Volatile organic compounds

WHO World Health Organization

Chapter 1. Introduction

The thesis describes the development, testing and deployment of a prototype system to measure *in situ* tropospheric ozone production rates. Individual chapters of this thesis introduce the background to the study, describe the principle of the ozone production rate measurement system (OPR), instrument characterisation, trial field deployments and measurement results.

1.1 Introduction to Thesis Structure

1) In Chapter 1 (Introduction), tropospheric chemistry and ground level ozone formation process are discussed, alongside a review of the harmful effects of ozone, by way of motivation for this work. Later sections cover the limitations of current methods to evaluate ozone production, and then introduce a new experimental approach to directly measure the ozone production rate.
2) In Chapter 2 (Experimental Methodology and Instrument Properties), the principle of the Ozone Production Rate (OPR) direct measurement methodology is introduced, with additional discussion of its advantages, limitations and potential applications. The properties and operating parameters of the individual system components are described in detail.
3) In Chapter 3 (System Characterisation), the performances of the various system components are comprehensively reviewed, and uncertainties, correction factors and potential limitations of the OPR system are discussed.

4) In Chapter 4 (London OPR deployment), the first OPR deployment, at North Kensington, London during summer 2012, is introduced. The OPR measurements and analysis integrating meteorological data and measurements of other ozone-chemistry-related species are presented.
5) In Chapter 5 (System Accuracy and Correction Factors), systematic correction factors applied to the OPR measurement data are discussed and their implementation presented, in order to improve OPR system accuracy.
6) In Chapter 6 (OPR measurements in New Delhi, India), the second OPR deployment, at two locations in northern India during spring 2013, is introduced. These deployments aimed to obtain proof-of-concept data of application of the OPR system in a comparatively under-studied region of high ozone formation potential. Local chemical factors that contribute to the measured ozone formation rate are discussed in the context of the measured data.
7) In Chapter 7 (Conclusion), the current state of the instrument, measurement results and achievements of the OPR development are briefly summarised. Future applications of this new measurement capability are assessed.

1.2 Structure of the Atmosphere

There are four main vertical regions of Earth's atmosphere: the thermosphere, mesosphere, stratosphere and troposphere. The troposphere is where human beings live and breathe; it is composed of the bulk gases (predominantly nitrogen, oxygen, argon and carbon dioxide), water vapour (variable fraction up to 4 % by volume in hot and humid air masses) and many types of trace gases (Mohanakumar, 2006). Approximately 90 % of the total atmospheric mass resides in the troposphere (Holloway and Wayne, 2010).

1.3 Trace gases

In addition to the major or bulk gases, there are many minor constituents or trace gases present in the troposphere. Those minor gases are important in tropospheric chemistry. The trace gaseous species related to tropospheric ozone formation are introduced in the following section.

1.3.1 Nitrogen species

In the troposphere, reactive nitrogen compounds exist primarily as oxides of nitrogen. Nitrogen oxides (NO_x= NO + NO_2) are widely present in the troposphere, which are important species in atmospheric chemistry by catalysing tropospheric ozone production (NO_x-O_3 chemistry are extensively discussed in section 1.4.3). NO_x are generated from both natural and anthropogenic sources (Zyrichidou *et al*., 2015).

Natural NO_x emissions sources include lightning, (wild) biomass burning, soil bacteria and volcanic activities (Gressent *et al*., 2014; Castellanos *et al*., 2014; Holloway and Wayne, 2010). Incomplete microbiological nitrification or denitrification in soil emits nitrous oxide

(N_2O), which is then oxidised by $O(^3P)$ to form NO in the boundary layer (Meagher and Anderson, 2000; Pidwirny, 2006). Current estimation indicates global NO_x emissions from soil source are approximately 12.9 ± 3.9 Tg N per year (Vinken *et al*., 2014). Wild biomass burning could contributes 3 to 13 Tg N emissions per year (Jaegle *et al*., 2005). While there are uncertainties in global lightning NO_x emissions, Lightning processes are estimated to emit 2 to 8 Tg N per year (Schumann and Huntrieser, 2007).

Human activities substantially contribute to tropospheric NO_x levels. High temperature (above 1300°C) combustion processes lead to over 75 % of global primary NO_x emissions to the troposphere (Holloway and Wayne, 2010). NO_x emission (as NO) from anthropogenic sources are approximately 21-28 Tg N per year (Denman *et al*., 2007) Power plants, ships and road transportation are the major anthropogenic combustion sources (Cofala *et al*., 2007). In this sense, NO_x are important primary air pollutants in the atmosphere.

1.3.2 Volatile Organic Compounds

There are many different types of volatile organic compound (VOC) present in the troposphere, in some cases at highly variable concentration. VOCs are defined as organic compounds with a boiling point less than or equal to 250 °C as measured at a standard pressure of 101.3 kPa (Eur-lex, 2004). VOCs are produced by both natural and anthropogenic sources, some of the important VOC species and their characteristics are listed in table 1.1.

Class and compound	Formula	Estimated atmospheric lifetime	Principal source types[a]	Principal sinks	Typical remote mixing ratios (ppb)
Alkanes					
Methane	CH_4	10 years	Microbial natural gas, BB	$OH^•$, Stratosphere	1.7–1.9
Ethane	C_2H_6	80 days	Natural gas, motor vehicles	$OH^•$	0.2–2
Propane	C_3H_8	17 days	LPG, motor vehicles	$OH^•$	0–1
n-Butane	C_4H_{10}	6 days	Motor vehicles	$OH^•$	0–0.5
i-Pentane	C_5H_{12}	4 days	Motor vehicles	$OH^•$	0–0.3
Alkenes					
Ethene	C_2H_4	1.7 days	Vehicle exhaust, BB, biogenic	$OH^•$, $NO_3^•$, O_3	0–0.1
Propene	C_3H_6	7 hours	Motor vehicles, BB, biogenic	$OH^•$, $NO_3^•$, O_3	0.01
Isoprene	C_5H_8	1.5 hours	Vegetation	$OH^•$, $NO_3^•$, O_3	0–1
α-Pinene	$C_{10}H_{16}$	3 hours	Vegetation	$OH^•$, $NO_3^•$, O_3	0–1
Alkynes					
Ethyne	C_2H_2	24 days	Vehicle exhaust, BB	$OH^•$	0–1
Aromatics					
Benzene	C_6H_6	12 days	Motor vehicles, solvents	$OH^•$	0–0.5
Toluene	C_7H_8	2.5 days	Motor vehicles, solvents	$OH^•$	0–0.5
m-Xylene	C_8H_{10}	0.6 days	Motor vehicles, solvents	$OH^•$	0–0.1
Aldehydes					
Formaldehyde	HCHO	4 hours	HC oxidation, vehicle exhaust, BB	$OH^•$, $NO_3^•$, $h\nu$	0.1–0.5
Acetaldehyde	CH_3CHO	11 hours	Vehicle exhaust, HC oxidation, biogenic	$OH^•$, $h\nu$	0.1–0.2
Ketones					
Acetone	$CH_3C(O)CH_3$	16 days	HC oxidation, biogenic	$OH^•$, $h\nu$	0.3–1
Acids					
Formic acid	HCOOH	~1 week	HC oxidation, BB, biogenic	Scavenging	0–5
Acetic acid	CH_3COOH	~1 week	HC oxidation, BB, biogenic	Scavenging	0–2
Peroxides					
Methyl hydroperoxide	CH_3OOH	2 days	HC oxidation	Scavenging, $OH^•$, $h\nu$	0–1
Alcohols					
Methanol	CH_3OH	16 days	Biogenic, HC oxidation	$OH^•$	0.4–2.0
Sulfur gas					
Dimethyl sulfide	CH_3SCH_3	3 days	Oceans	$OH^•$, $NO_3^•$	0–200 ppt

[a]HC, hydrocarbon; LPG, liquid petroleum gas; BB, biomass burning.

Table 1.1. Some important VOC species found in the troposphere (Blake and Blake, 2002).

Table 1.1 provides an overview of some important VOCs present in the troposphere, with an indication of their main sources and sinks. Methane, as a hydrocarbon, is the most abundant VOC in the troposphere overall (Theloke and Friedrich, 2011). Methane is a key species in hydroxyl radical (OH) reactions in the free troposphere; it is also an important species in other radical chain reactions. Emitted VOCs are primary air pollutants, but their chemical processing leads to the formation of secondary VOC compounds in the atmosphere (Kim *et al*., 2011).

1.3.3 Radical Species

Atmospheric free radicals (species with unpaired electrons) are key intermediates in chemical processing leading to the removal of emitted compounds and the formation of secondary species, including pollutants such as ozone. The hydroxyl radical (OH) is the central gaseous species in tropospheric chemistry, particularly during the daytime. OH radicals are highly reactive; their reactions initiate the majority of VOC degradation processes, although O_3, NO_3, halogens and photolysis also contribute to the degradation of some VOC species (Bloss, 2009).

Unlike the stratosphere, ozone only exists in low mixing ratios (relatively speaking) in the troposphere (*e.g.* tens to low hundreds of parts per billion, compared to parts per million in the stratospheric ozone layer) (Wargan *et al*., 2010). As a secondary pollutant, ozone is formed through the oxidation of VOCs in the presence of NO_x under sunlight in the troposphere. However, stratosphere-troposphere exchange could contribute to up to 8.5 % of total tropospheric ozone burden (Collins *et al*., 2000; Hsu and Prather, 2009). The tropospheric chemical ozone formation process is described in detail in section 1.4.3.

1.4 Tropospheric Chemistry and Ozone Formation

1.4.1 Photochemical Steady State

Ozone is a secondary air pollutant, formed through the oxidation of VOCs in the presence of NO_x. Under sunlight, there is a null cycle between NO_x and ozone which, in the absence of other atmospheric chemical reactions, establishes the NO_x-O_3 photochemical steady state (PSS).

$$NO_2 + h\nu\ (\lambda \leq 420\ nm) \rightarrow NO + O \qquad (j_{1.1}) \qquad (1.1)$$

$$O + O_2 + M \rightarrow O_3 + M \qquad (1.2)$$

$$NO + O_3 \rightarrow NO_2 + O_2 \qquad (k_{1.1}) \qquad (1.3)$$

$$[NO] / [NO_2] = j_{1.1} / k_{1.1} [O_3] \qquad (1.4)$$

NO_2 is photolyzed by UV light (under 420 nm) in solar radiation (Trebs *et al*., 2009). During the daytime, in the absence of other processes, this null cycle controls the relative abundance of NO, NO_2 and O_3, but this null cycle alone does not lead to net ozone production. Neglecting other photochemical processes, the abundance of NO_x and O_3 is highly dependent on the solar radiation and local emissions. The timescale of this null cycle may be assessed as $1/ j_{1.1}$. In a typical urban environment (*e.g.* North Kensington urban background site in London), emissions modify the photolysis-driven NO_x-O_3 interactions: in the early morning (before 6:00), ambient NO_2 level is relatively high, NO and O_3 levels are low. When rush hour begins (ca. 7:00), NO_x level is elevated immediately due to vehicle emissions, while O_3 levels decrease due to NO titration effect. After the rush hour (ca. 9:00), NO_x levels drop down rapidly, O_3 levels start a positive trend due to NO_2 photolysis by the rising solar

radiation (neglecting other processes, full ozone chemistry is discussed in section 1.4.3). The O_3 level peaks at middle of the day. As the sunlight begins to fade in the afternoon, O_3 levels fall with a negative trend until the end of the day. During the afternoon rush hour (ca. 17:00-20:00), NO_x reach its second diurnal peak due to elevated vehicle emission. This typical urban NO_x-O_3 diurnal cycle is illustrated in Figure 1.1.

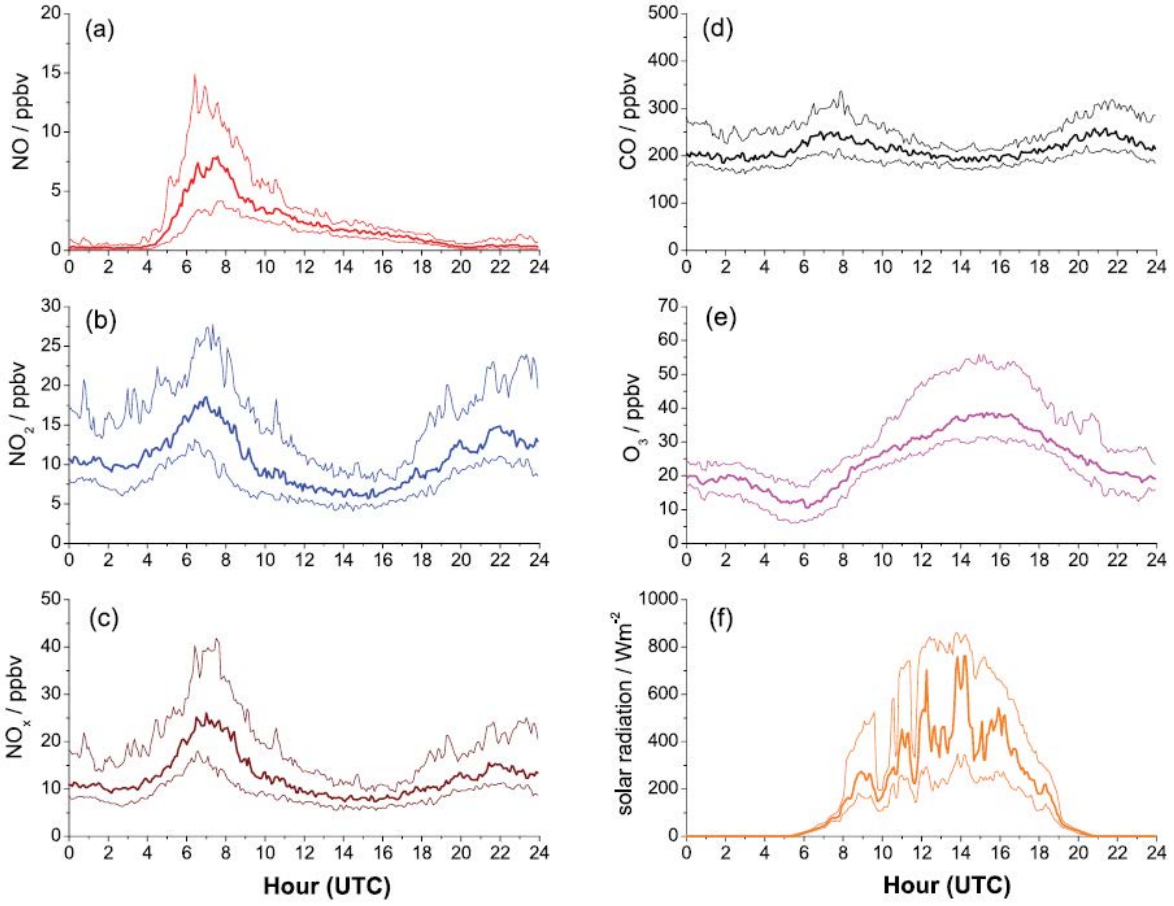

Figure 1.1. The 5 minute-averaged diurnal cycle for (a) NO, (b) NO_2, (c) NO_x, (d) CO, (e) O_3, and (f) solar radiation at the NK site during the summer IOP. Thick lines correspond to the median and the thin lines are the corresponding quartiles (Bohnenstengel *et al*., 2015).

1.4.2 Tropospheric chemistry and OH

Reactions driven by OH radicals modify the NO_x-O_3 PSS leading to net ozone production. OH is the key species for tropospheric chemistry in the daytime, its central role is emphasised in Figure 1.2 which also illustrates some important tropospheric chemical reactions.

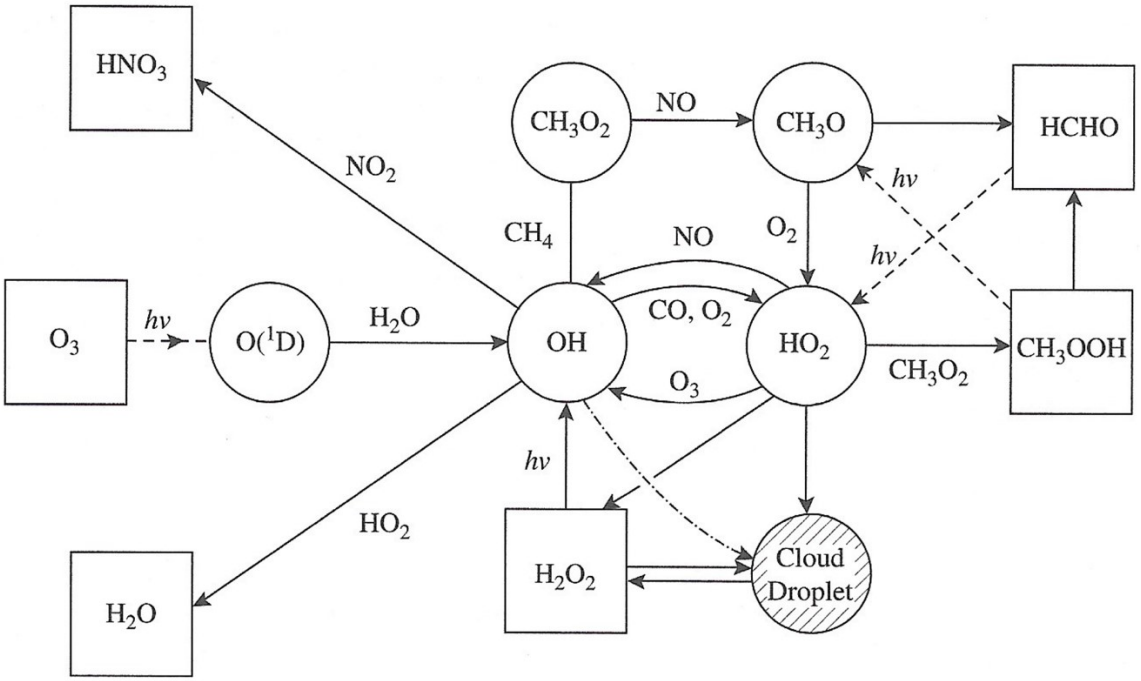

Figure 1.2. An overview of gaseous chemistry in the troposphere. This figure shows the principal reactions related to OH and HO_2 radicals, which are key drivers of tropospheric oxidation (Holloway and Wayne, 2010).

The dominant primary OH source in the free troposphere is from the photolysis of ozone. OH is formed from ozone photolysis by UV light (at wavelengths less than approximately 310 nm) through the (subsequent) reaction of $O(^1D)$ atoms with water vapour (Bauer *et al.*, 2000). The OH formation reactions are then:

$$O_3 + h\nu\ (\lambda < 310\ nm) \rightarrow O(^1D) + O_2 \quad (1.5)$$

$$O(^1D) + H_2O \rightarrow OH + OH \quad (1.6)$$

H_2O is a trace component (0.1 – 4 %) in the troposphere, only a small fraction (typically ca. 10 %) of all $O(^1D)$ atoms react with H_2O to form OH; The majority of $O(^1D)$ atoms (typically ca. 90 %) are converted to ground state $O(^3P)$ by collision with N_2 and O_2 (Matsumi and Kawasaki, 2003; Holloway and Wayne, 2010;), and go on to regenerate O_3:

$$O(^1D) + M \rightarrow O(^3P) + M \qquad M=N_2, O_2 \qquad (1.7)$$

$$O(^3P) + O_2 + M \rightarrow O_3 + M \qquad (1.8)$$

In the free troposphere, the main precursor to form OH is ozone (HONO is another important source of OH in urban regions (Kim *et al*., 2014)); ozone levels therefore largely determine the oxidative capacity of the troposphere. OH initiates the oxidation process of many trace gases, including the most abundant species carbon monoxide (CO) and methane (CH_4). In the free troposphere, ideally ca. 70 % of all OH reacts with CO; ideally about 30 % of total OH reacts with CH_4 (although in most boundary layer locations reactions with many other species dominate removal of OH) (Holloway and Wayne, 2010).

$$OH + CH_4 \rightarrow CH_3 + H_2O \qquad (1.9)$$

$$OH + CO \rightarrow H + CO_2 \qquad (1.10)$$

Reaction (1.9) and (1.10) produce the active species H and CH_3, which under tropospheric conditions overwhelmingly react with the abundant gas O_2 to form peroxy radicals (HO_2, and one example of organic peroxy radicals, CH_3O_2).

$$H + O_2 + M \rightarrow HO_2 + M \qquad (1.11)$$

$$CH_3 + O_2 + M \rightarrow CH_3O_2 + M \qquad (1.12)$$

The fate of the peroxy radicals is highly dependent on local NO_x levels in the troposphere. Urban areas tend to exhibit high levels of NO_x. Consequently, NO is abundant and forms the primary reaction partner for peroxy radicals:

$$HO_2 + NO \rightarrow OH + NO_2 \quad (1.13)$$

$$CH_3O_2 + NO \rightarrow CH_3O + NO_2 \quad (1.14)$$

HO_2 reacts with NO to regenerate OH; organic peroxy radicals (RO_2) react with NO to form an alkoxy radical (RO). Specifically, reaction (1.14) describes CH_3O_2 (one example of the RO_2 family) reacting with NO to form CH_3O (i.e. RO). Alkoxy radicals, RO, usually react with O_2 in the troposphere, producing a carbonyl species (in the case of CH_3O, formaldehyde HCHO) and HO_2

$$CH_3O + O_2 \rightarrow HCHO + HO_2 \quad (1.15)$$

HCHO can be photolyzed with UV light (at wavelengths lower than 330 nm) to form H and HCO in the troposphere (Topaloglou *et al*., 2011; Carbajo *et al*., 2011). Both go on to regenerate HO_2.

$$HCHO + h\nu\ (\lambda<330\ nm) \rightarrow H + HCO \quad (1.16)$$

$$H + O_2 + M \rightarrow HO_2 \quad (1.17)$$

$$HCO + O_2 \rightarrow CO + HO_2 \quad (1.18)$$

The peroxy radical regeneration and cycling processes are key reactions to convert NO into NO_2 (alongside NO reacting with ozone). The oxidation of VOCs, forming peroxy radicals driving the conversion of NO to NO_2, leads to net ozone production in the troposphere.

If peroxy radicals are present in areas with very low NO concentrations, they react with each other:

$HO_2 + HO_2 \rightarrow H_2O_2 + O_2$ (1.20)

$CH_3O_2 + HO_2 \rightarrow CH_3OOH + O_2$ (1.21)

The products of both reactions (H_2O_2 and CH_3OOH) are relatively stable and water soluble and often dissolved in water droplets and rain as their sinks. Reactions (1.20) and (1.21) remove peroxy radicals from the troposphere under very clean (low-NO_x conditions) (Holloway and Wayne, 2010).

In addition to VOCs, other gaseous species make a significant contribution to OH removal processes in polluted areas. For example, reaction with NO_2 is an important OH sink in urban polluted areas, this reaction is presented in (1.22) (Fried *et al*., 1997).

$NO_2 + OH + M \rightarrow HNO_3 + M$ (1.22)

1.4.3 Ozone formation process

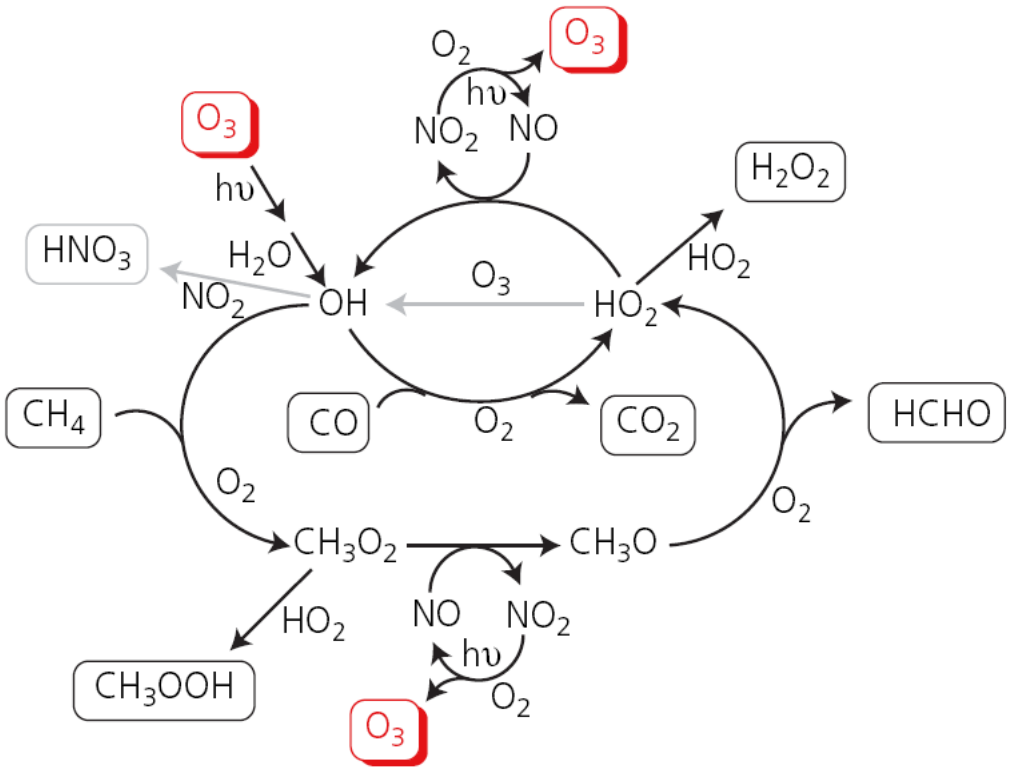

Figure 1.3. Summary of ozone formation chemical process in the free troposphere (The Royal Society, 2008).

OH oxidation reactions, discussed in section 1.4.2, lead to the formation of peroxy radicals, which react with NO to form NO_2 in polluted areas. As ozone is produced from photolysis of NO_2 in the troposphere, OH oxidation reactions lead to net ozone production. The ozone production cycle in a polluted area (one with some abundance of NO_x) may therefore be summarised as follows, for the two simplest cases (CO and CH4 oxidation):

$$OH + CO \rightarrow H + CO_2 \quad (1.23)$$

$$H + O_2 + M \rightarrow HO_2 + M \quad (1.24)$$

$$HO_2 + NO \rightarrow OH + NO_2 \quad (1.25)$$

$NO_2 + h\nu\ (\lambda \leq 420\ nm) \rightarrow O + NO$ (1.26)

$O + O_2 + M \rightarrow O_3 + M$ (1.27)

Alternatively, for the OH oxidation of CH_4, the ozone production cycle is presented as,

$OH + CH_4 \rightarrow CH_3 + H_2O$ (1.28)

$CH_3 + O_2 + M \rightarrow CH_3O_2 + M$ (1.29)

$CH_3O_2 + NO \rightarrow CH_3O + NO_2$ (1.30)

$NO_2 + h\nu\ (\lambda \leq 420\ nm) \rightarrow O + NO$ (1.31)

$O + O_2 + M \rightarrow O_3 + M$ (1.32)

Reactions (1.23) to (1.32) describes the net ozone production cycle in the troposphere. However, the ozone production rate is highly dependent on the absolute and relative reactant levels (NO_x and VOCs). Three main regimes of ozone formation may be identified, related primarily to the abundance of NO_x, summarised qualitatively in Figure 1.4:

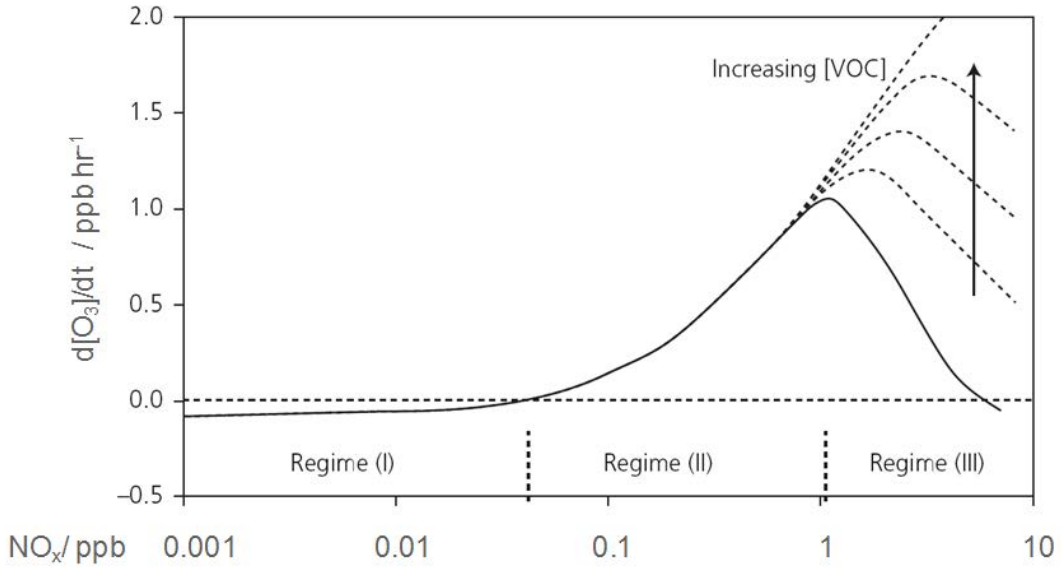

Figure 1.4. Idealised dependence of chemical ozone production rate upon NO_x and VOC levels (The Royal Society, 2008).

In regime I, NO_x levels are extremely low (below approximately 0.05 ppb), and the main fates of peroxy radicals are self- and cross-reactions, and reaction of HO_2 with O_3. In the absence of significant NO-to-NO_2 conversion, overall ozone destruction results, through $HO_2 + O_3$, and through photolysis followed by $O(^1D) + H_2O$.

In regime II, when NO_x levels are higher, peroxy radicals undergo reaction with NO, leading to NO_2 formation, photolysis and ozone production. The compensation point is reached (a few tens of ppt), where the net ozone production rate is zero overall (Krupa and Manning, 1988; Cox, 1999). As NO_x levels further increase, ozone destruction processes becomes less important, as the ozone production cycle begins to dominate. Net ozone production begins in this regime; the ozone production rate increases as the NO_x level increases through more rapid RO_2 + NO reactions (Cox, 1999).

In regime III, when NO_x level increases above a few ppb, other OH sink reactions begin to become significant, in particular reaction with NO_2 ($OH + NO_2 + M \rightarrow HNO_3 + M$). As reaction with NO_2 dominates over reaction with VOCs, at higher NO_x levels with OH abundance, and hence the rate of RO_2 formation, falls, and ozone production rates decrease, unless VOC levels increase to counter the competition for reaction with OH and form peroxy radicals to initiate NO to NO_2 conversion.

The NO_x-dependence of the ozone production rate identifies the NO_x-limited regime (regime I and II in Figure 1.4, where ozone production rates increase with increases in NO_x) and the VOC-limited (or ozone saturated) regime (regime III in Figure 1.4), where the ozone production rate falls with increasing NO_x, but increases with higher VOC levels. The "VOC-limited" terminology is misleading as increases in VOC levels increase the ozone production rate in regimes I and II also (although less significantly than in regime III), it is better termed

the "NO_x saturated" regime. In a typical urban environment with abundant NO_x, regime III often applies, while for areas a few hundred kilometres downwind of the urban environment are often seen as a NO_x limited environment (regimes I and II).

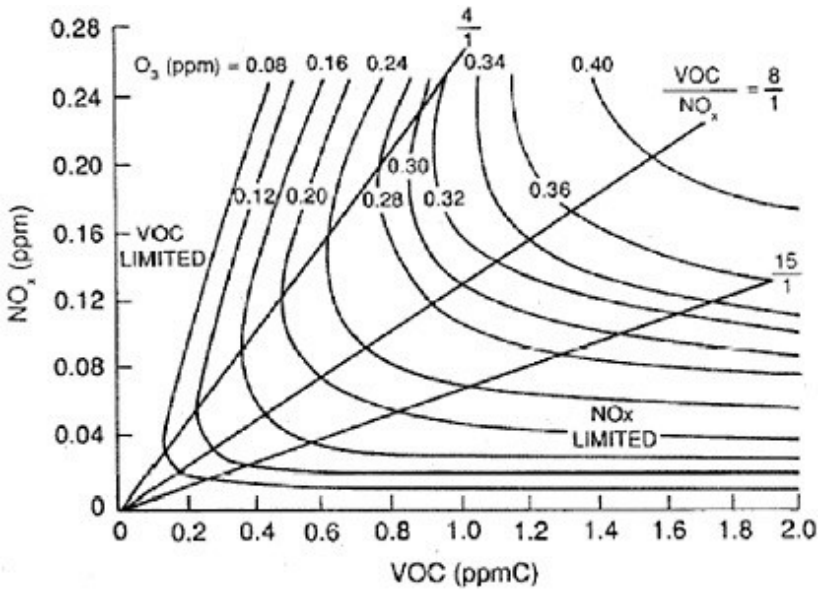

Figure 1.5: An ozone isopleth graph, which is used to determine the NO_x and VOC dependence of the ozone production rate under a given environmental scenario (given chemical conditions) (NCR, 2008).

The ozone isopleth graph (Figure 1.5) provides an alternative graphical representation of the two ozone production regimes' relationships. The isopleth describes the ideal ozone levels at variable levels of VOC and NO_x. The distribution ratio between VOC and NO_x is essential in determining ozone levels. Two main NO_x to VOC ratios (1:4 and 1:15) in the isopleth describe the two groups of delimited ozone production regimes, as discussed in Figure 1.4, the NO_x-limited and VOC-limited regimes.

The VOC-limited NO_x-saturated area on the left presents a typical urban environment, where NO_x is abundant as a consequence of anthropogenic (traffic) emissions, leading to a low ratio of VOC to NO_x. The right area of the graph describes the NO_x limited environment, which more often corresponds to rural areas, where NO_x emissions from anthropogenic

sources are low, but VOC levels (from anthropogenic and potentially biogenic sources) may be significant (the lifetime of NO_x, 12 - 24 hours, is shorter than that of many (but not all) VOCs, so NO_x is removed from an air mass downwind of a city more rapidly that VOCs, and the ozone regime tends to evolve from VOC-limited to NO_x-limited). The 1:4 and 1:15 NO_x to VOC ratios showing in Figure 1.5, are often considered to delimit the ozone production regimes (NCR, 2008).

1.5 Human and Environmental Impacts of Ozone

1.5.1 Ozone impacts on human health

Ozone is a powerful oxidant, causing direct and indirect oxidative damage to cells by damaging cell function or reducing antioxidant defence mechanisms (Mudway and Kelly, 2000). For example, ascorbate is a protective antioxidant found in lung lining fluid (LLF) (Kelly, 2003). Ozone reacts with and removes ascorbate, and consequently, ozone begins to react with other inner substrates to form harmful secondary products, leading to cell inflammation. As a result, the damaged lung tissue leads to reduced lung function at the blood/air interface (The Royal Society, 2008).

Ozone also acts as a strong irritant to mucosa. Exposure of mucosa to ozone leads to respiratory system problems, such as coughing and inflammation of the airways. Short-term exposure to high level of ozone reduces lung function and causes breathe difficulty (EPA, 2013). Evidence has shown short-term exposure to high levels of ozone significantly increases the risk of dying for all ages. Overall non-accidental death rates were increased (0.2 % - 0.6 %) with each 5 ppb increase in ground level ozone (Gryparis *et al*., 2004). Long-term exposure to ozone is associated with increased lung susceptibility to infections and aggravation of lung diseases such as asthma, emphysema and chronic bronchitis (EPA, 2013).

Certain groups of people are more vulnerable to high levels of ground level ozone. People who are active outdoors have higher exposure time to ozone, and a greater ventilation rate. Children and teenagers, who often spend more time outdoors, may have their developing lungs damaged permanently. Evidence suggests long-term ozone exposure reduces lung

function growth and results reduced lung function in adulthood (WHO, 2003). Another group of vulnerable people are those who have pre-existing lung diseases, and are particularly sensitive to exposure to high levels of ozone. For instance, asthmatics could have serious symptoms when they are exposed to high ozone environments (EPA, 2013).

A recent pollution event allowed some of these effects to be evaluated for the UK. During the first two weeks of August in 2003, a major heatwave hit most European areas including the UK. The peak in ambient temperature recorded was 38.5 °C in the UK. The UK National Statistics office reported 2045 more deaths, compared to the average for the same period over the years 1998 - 2002, during the heatwave period (4 to 13 August 2003) (Stedman, 2004). At the same time, ozone levels at Lullington heath site (A rural background site in Sussex, south-east England, 115 km from continental Europe-France) were substantially higher than August levels in previous years. This rural background site was selected to represent the regional background ozone level during the heatwave period.

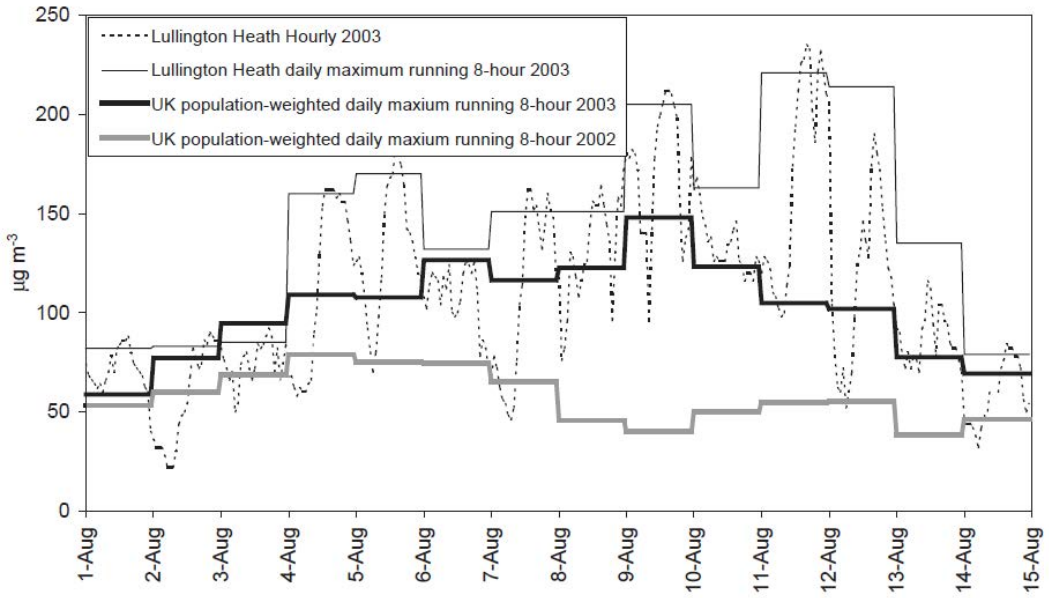

Figure 1.6. Ozone trends of UK population-weighted daily maximum running 8-hour ozone concentration in year 2002 and 2003. In contrast with Lullington Health site hourly measured and its daily maximum running 8-hour ozone concentration in year 2003, from 1 August to 15 August. Lullington Heath site data were measured in a national nature reserve (Stedman, 2004).

The increased ambient ozone level, together with other pollutants (notably particulate matter, PM) and high temperatures during the first two weeks of August, led to increased mortality rates during this period (Stedman, 2004). The heatwave and pollution episode extended over Western Europe, where effects were if anything more pronounced; *e.g.* The mortality rate increased in 9 French cities, by factors ranging from 10.6 % to 174.7 % (Filleul *et al.*, 2003).

There is substantial evidence from medical, cohort and epidemiological studies that both the acute and the chronic effects of ozone upon the respiratory system shortens human life and causes increased mortality. The combination of high ozone, high temperatures and the presence of elevated levels of other air pollutants - a combination which may recur more frequently under future climate conditions - therefore has a significant public health impact (The Royal Society, 2008).

1.5.2 Wider environmental impacts of ozone

Ground level ozone also has negative impacts upon animals, plants and the wider environment. Ozone directly damages plants, by entering the stomata of leaves during respiration associated with the photosynthesis process. Once ozone enters a leaf, two mechanisms cause damage to the plant. When ozone levels are moderate to low, entry of ozone to the leaves triggers the plant's defence mechanism and gene expression (the process by which information from a gene is used in the synthesis of a functional gene product), causing an extra energy requirement to regenerate antioxidants by synthesis. The plant leaves' growth rate and consequently carbon capture are reduced by the reduced overall energy supply. When levels of ozone are high, ozone obstructs the plant's repair and detoxification capacity (The Royal Society, 2008). The direct damage (reduction of carbon capture and plant's self-repairing mechanism) causes plants to be potentially unhealthy and more vulnerable to other plant diseases, which in turn can lead to unhealthy symptoms including necrosis, tissue collapse and chlorosis (lack of chlorophyll in plants' leaves). Ozone tends to have greatest effect on nearly mature leaves, due to the need of carbon capture at this stage, they are most vulnerable to ozone damage. Both older and younger leaves are more resistant to ozone exposure. In high level ozone environments, plant's leaves tend to have health problems, such as bronzing, stippling and flecking (Edward, 2004). Crop fields are particularly sensitive to continuous exposure to high levels of ozone, resulting reduced crop growth. Wheat, soybean, rice and maize are the key crops worldwide (Lobell *et al*., 2011). In order to provide protection of crops, the AOT40 metric has been widely adopted: AOT40 is the hourly mean ozone level accumulated over a threshold ozone concentration of 40 ppb during daylight hours in the growing season. Current the UK air quality strategy and EU targets for AOT40 are 9000 ppb hours (to be calculated from one hour (May to July)), to be

archived by 2010 (averaged over 5 years) (Royal Society, 2008). This metric may be used to assess the ozone damage to crops during their growing stages, and threshold levels for AOT40 may be established for the protection of vegetation (Mills *et al*., 2007).

A modelling study was performed to evaluate the global wheat, soybean and maize reductions due to exposure to ozone (Avnery *et al*., 2011). Two metrics were used to evaluate crop loss by ozone exposure: seasonal daylight exposure time (8:00 to 20:00) and accumulated ozone exposure hours over a threshold of 40 ppb (AOT40). The MOZART-2 model for ozone and related chemical tracers was used to evaluate crop reductions. The two metrics were set at variable values during the experiment. Depending on different settings of the two metrics, the global wheat, soybean and maize productions were reduced from 2.2 % to 15 % in weight of million tons. The estimated crop reductions are equal to approximately 79 to 121 million tons of crops, worth 11 to 18 billion USD in the year 2000 (Avnery *et al*., 2011). Another model assessment of crop loss arising from ozone exposure estimated there are currently 7 % - 12 % wheat loss, 6 % - 16 % soybean loss, 3 % - 4 % rice loss and 3 % - 5 % maize loss due to ozone exposure globally (Van Dingenen *et al*., 2009). This evaluation suggests estimated overall crop reductions worth 14 to 26 billion USD (Result from second model assessment, due to the additional estimation of rice loss).

Both model studies were based upon differing metrics. By comparing the two essential metrics (seasonal exposure time and AOT40) that reduce crop production, AOT40 is thought to be less important than seasonal exposure time in terms of ozone exposure impacts (Van Dingenen *et al*., 2009). Van Dingenen *et al*. further concluded that if current air quality legislation were successfully implemented globally by the year 2030, global maize and soybean production loss rates would remain similar to their current levels, but rice and wheat

would suffer additional 1 % to 6 % reductions in global production. These results are sobering in the context of the food demand for a growing global population.

In contrast to Europe and North America, air quality legislations are not fully implemented in developing countries, India and China are two examples (Gurjar *et al*., 2008; Wang and Hao, 2012). Many developing countries are agricultural producing countries, and so increasing ozone burdens are going to cause further crop losses at present and in the future.

1.5.3 Role of ozone in the Earth's climate system

While climate can modify ozone production and destruction, ozone itself is an important contributor to climate change (Doherty *et al.*, 2013). Ozone is a powerful greenhouse gas in the atmosphere, with an average radiative forcing of 0.35 W m^{-2} (range from 0.25 to 0.65 W m^{-2}) (Barker *et al.*, 2007), was and is considered the third most important greenhouse gas after CO_2 and CH_4 (discounting water vapour). As ozone has a relatively short lifetime (weeks), the warming effects from ozone have a strong regional variability (Holloway and Wayne, 2010).

Tropospheric ozone increase has made a significant contribution to the global radiative forcing of climate since the pre-industrial era (IPCC, 2013); estimated increases in ozone since that period are shown in the Figure 1.7:

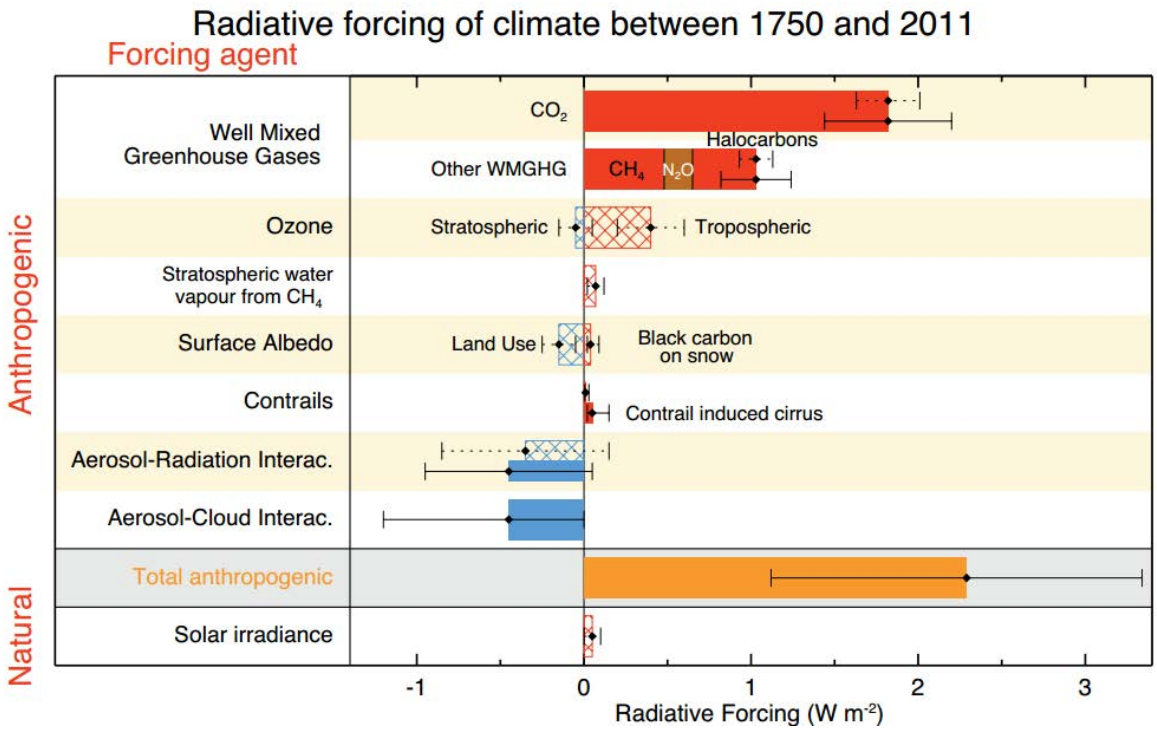

Figure 1.7. Radiative forcing of climate between 1750 and 2011 (Myhre *et al.*, 2013).

In addition to the direct radiative forcing of tropospheric ozone, its impact on reducing vegetation growth leads to an additional strong indirect effect to increase the radiative forcing of ozone by up to 0.4 W m^{-2} (Sitch *et al*., 2007). Such indirect radiative forcing effects (from ozone) could contribute more to global warming than the direct radiative effects (of ozone) (Stevenson *et al*., 2013).

Ozone is the one of the main source of hydroxyl radicals, which are one key determinants of tropospheric oxidation capacity (Bloss *et al*., 2005; Ren *et al*., 2006). As discussed in section 1.4.3, CH_4, NO_x, CO and non-methane VOCs (NMVOCs) are important ozone precursors. The increase in abundance of these species since the pre-industrial era has significantly increased the tropospheric ozone level, with methane responsible for most of the ozone change (Chang *et al*., 2009; Stevenson *et al*., 2013). Apart from being an important greenhouse gas, the increase in tropospheric ozone level (and hence in hydroxyl radicals) also increases the oxidizing capacity of the atmosphere. As the hydroxyl radical is the crucial factor in controlling methane levels, the increase of ozone level has reduced the CH_4 lifetime and abundance in the atmosphere - a negative climate feedback effect (Prinn, 2003).

Currently, agreements regarding tropospheric ozone control are not included in international treaties (such as the Kyoto Protocol) - there is no global framework in place for the direct management of ozone. Stronger legislation (than exits within current policy) is required to reduce ozone precursor emissions, and so to mitigate the impacts of ozone on both air quality and climate change (Doherty *et al*., 2013).

1.6 Current Tropospheric Ozone Regulations and Trends

1.6.1 Ozone regulations worldwide

The European Union has developed air quality legislation to regulate levels of a number of air pollutants. In the latest European Union air quality directive 2008/50/EC, the target for ozone was set at 120 $\mu g/m^3$ - approximately 60 ppb (parts per billion, by volume, depending upon temperature and pressure) as maximum daily 8-hour mean, not to be exceeded more than 25 times each year (from data averaged over 3 years) (AQEG, 2009).

In the United State of America (US), the National Ambient Air Quality Standards (NAAQS) stated a target value for ozone of 75 ppb (by volume), as the annual fourth-highest maximum daily 8-hour mean (from data averaged over 3 years). However, the proposed regulation discussed by the "Obama" Ozone Clean Air Act aims to lower the ozone threshold to the 65 to 70 ppb range to lower the potential public health risk (Davenport, 2014). The US ozone limit is slightly higher than the EU air quality standard (EPA, 2013).

The World Health Organization (WHO) set a guideline value for ozone levels not to exceed a daily 8-hour mean of 100 $\mu g/m^3$ (approximately 50 ppb) in the year 2005. WHO describes this threshold as providing adequate protection to public health, but note that some negative health impacts (by ozone exposure) may potentially happen under this threshold. The WHO reported an estimated 1-2 % increase in daily mortality rate at this guideline limit ozone level (WHO, 2005).

1.6.2 Global ozone trend since 1950s

Global ozone levels have shown a positive trend since the 1950s to 2010, by up to 30 ppb in 60 years in some regions (Parrish *et al*., 2012). Figure 1.8 describes this positive trend over various measurement sites worldwide:

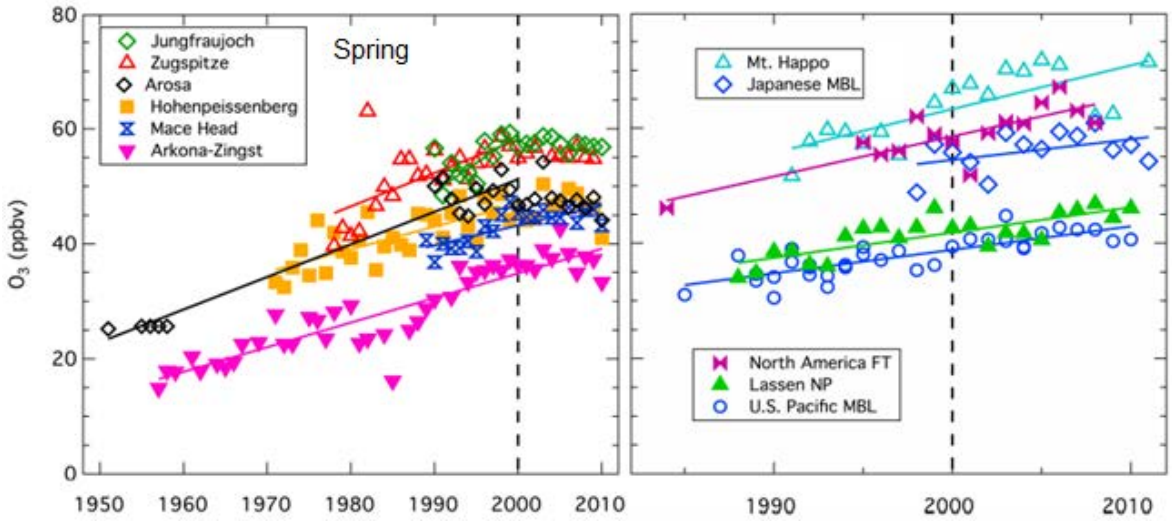

Figure 1.8. Comparison of spring time trends in ozone concentrations measured at various sites on Earth: all measurement sites in Europe (left panels), Western North America and Japan (right panels). The coloured lines describe the linear regression to measured data (Parrish *et al*., 2012).

Strong evidence also indicates that the northern hemispheric background ozone levels raised by up to 10 µg m^{-3} per decade from 1975 to 2005 (Raes and Hjorth, 2006).

1.6.3 Ozone trends and current levels in the UK

Measured data from a range of UK background monitoring sites (13 rural and 5 urban sites) indicated that annual mean surface ozone levels in the UK have been steadily increasing from 1990 to 2006, by up to 0.94 ppb per year in rural regions and 1.98 ppb in urban sites per year. (Vingarzan, 2004; Jenkin *et al*., 2008). This positive ozone level trend continues to present days (Munir *et al*., 2013).

In the urban areas, measured data from UK urban monitoring sites report an increase in annual mean ozone levels over the last decade. The reduction of urban NO_x emissions contributes to this trend, as the "urban decrement" phenomenon is reduced by lowered NO emissions. Background ozone levels have been rising but peak ozone events falling (AQEG, 2009). Peak ozone episodes have been associated with particular meteorological conditions, in particular abnormally hot years (heatwave events in UK), such as 1995, 2003 and 2006 (Rooney *et al*., 1998; Lee *et al*., 2006; Rebetez *et al*., 2009). Change in ambient temperature are found to exert a positive relationship to surface ozone level (Doherty *et al*., 2013).

The 2003 August heatwave event was a particular example: the ozone levels during August were much higher than comparable periods in other years with the elevated temperature (highest temperature at 38.5°C) (Figure 1.9). Ozone levels during this period was also higher than other months in 2003 (Figure 1.10) (Vieno *et al*., 2010). The elevated ozone concentration was due to the weather conditions favouring the accumulation of emitted VOCs and NO_x, and fine weather intensifying the photochemical reactions leading to ozone formation (AQEG, 2009).

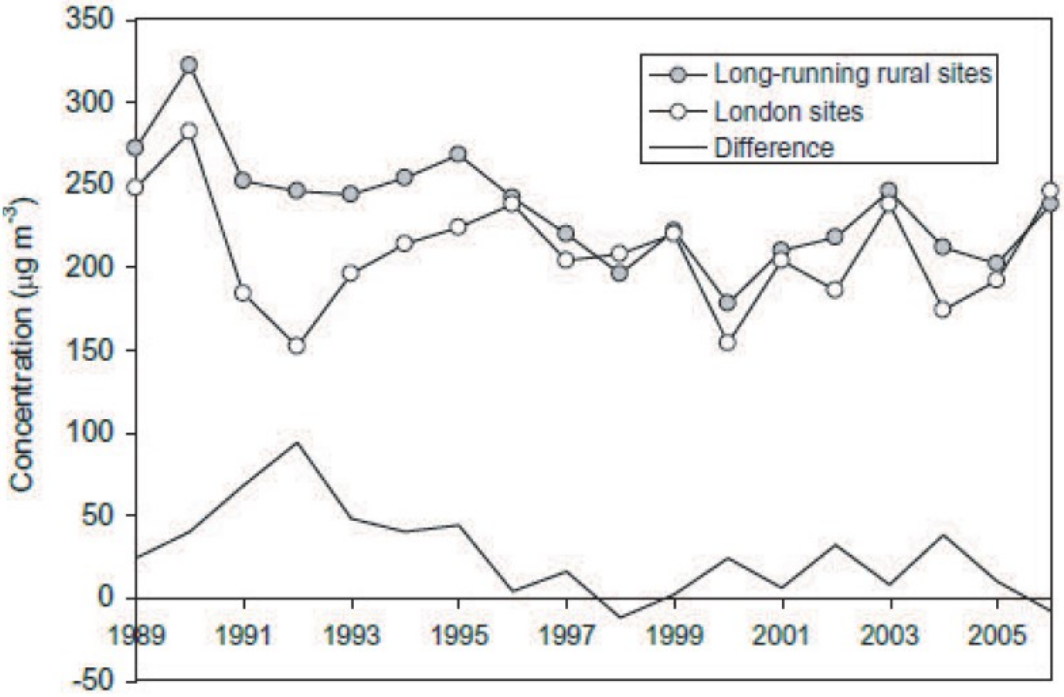

Figure 1.9. Maximum hourly mean ozone concentration (Peak ozone concentration) in each year at London urban sites and other UK areas' rural sites from 1989 to 2006 (AQEG, 2009).

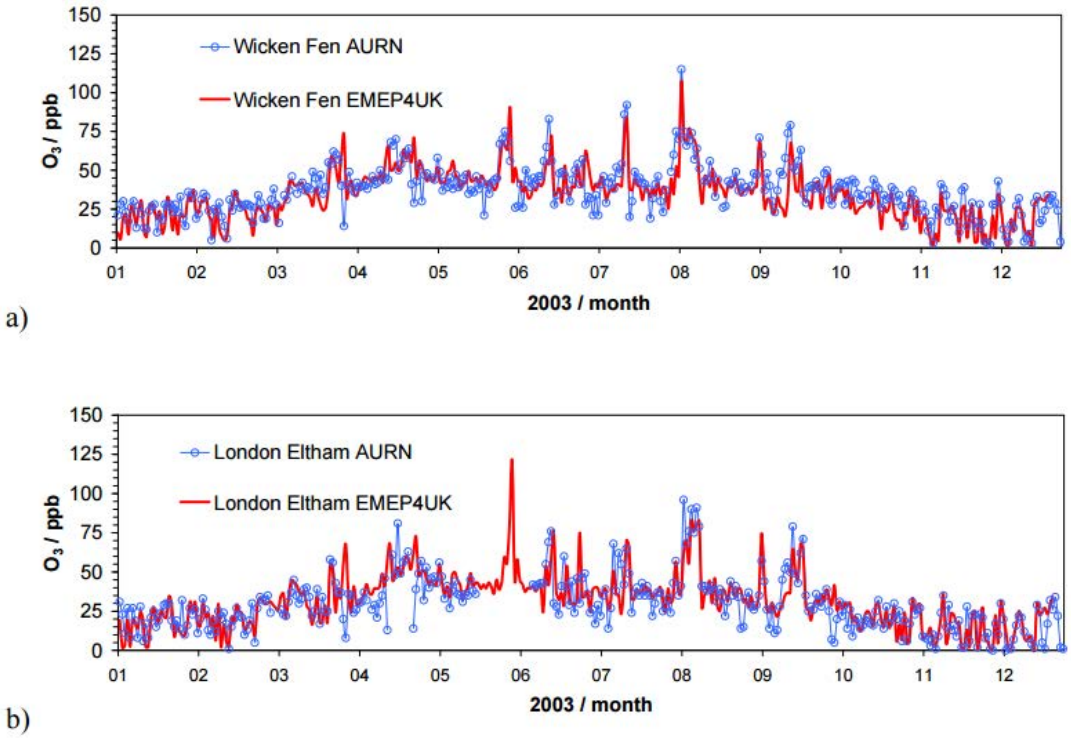

Figure 1.10. Measured (blue) and modelled (red) mid-afternoon (14:00-15:00) hourly mean surface ozone (in ppb unit) for each day of 2003 at (a) Wicken Fen (rural background site) and (b) London Eltham (suburban background site)

In urban regions of UK, ozone levels are variable. Observed data indicates that annual mean ozone concentration in urban areas are lower than in the surrounding rural areas. The UK urban background sites indicate a larger annual mean ozone level increase than at roadside sites from 1999 to 2009 (AQEG, 2009).

Annual mean ozone levels in UK rural areas have also been increasing from 1990 to 2008 (AQEG, 2009), this positive trend continues to present days (Kulkarni *et al*., 2015). However, the rural ozone level increase was not as fast as the increase in ozone levels in urban areas. Reported annual mean ozone levels in rural areas are highly dependent on monitoring site location. Transboundary movement of ozone precursors, hemispheric background ozone concentrations and variable annual regional photochemical generation of ozone are three factors that alter annual mean ozone concentrations in UK rural areas. From 2000 to 2008, rural areas in the south east show greater annual mean ozone concentrations than those in north-eastern rural areas by up to 3 ppb (AQEG, 2009). The reason for this behaviour is the transport of ozone precursors from central Europe to the south east area of England. Variable annual hemispheric background ozone levels also contribute to variable annual mean ozone levels. The increasing northern hemispheric background ozone level (up to 2% per year from 1970 to 2006) greatly influences the UK annual mean ozone trend (Jenkin *et al*., 2008).

The UK daily peak ozone concentrations (maximum of 1-hour ozone concentration) displays a trend of decreasing levels in both urban and rural sites, due to the on-going NO_x and VOC emissions reductions over the past 20 years (AQEG, 2009; Munir *et al*., 2013). However, due to meteorological factors, the daily peak ozone concentration is variable between different years (Jenkin *et al*., 2008; Munir *et al*., 2013).

UK annual mean ozone concentrations in urban areas are expected to rise over the next 20 years and approach their surrounding rural areas' ozone concentration (AQEG, 2009), if NO_x emissions from vehicles continue to fall (a supposition which recent data calls into question). The reduced NO_x scavenging effect is the main factor in this prediction; vehicle emission controls are expected to reduce NO_x concentrations in urban areas, leading to less ozone reduction.

Another important factor is the fraction of primary NO_2 (f-NO_2) in NO_x emissions. Recent studies suggested the measured f-NO_2 ranges from 8 % to 40 % (depending on vehicle and fuel types), so the widely applied f-NO_2 of 5 % used in emission inventories is a significant underestimation. (AQEG, 2007) The exhaust treatment for diesel vehicles significantly contributes to the increasing f-NO_2. The diesel exhaust treatment system, catalytic diesel particulate filter (CDPF), first introduced to London in the early 2000s, is now widely applied to London buses. CDPF aims to oxidize CO and hydrocarbons to CO_2 in the exhaust. It has certain contributions to particulate matter controls, but during the oxidation process, the CDPF actively converts NO to NO_2. Vehicles with CDPF installed have a higher f-NO_2, increasing diesel vehicles' NO_x emissions. (Greater London Authority, 2008) The increasing primary NO_2 in total NO_x emissions leads to increasing ozone levels, following NO_2 photolysis.

HONO, as an important ozone precursor, has been increasing as a fraction of total vehicle NO_x emission (f-HONO), accompanied with the increasing primary NO_2 emission (AQEG, 2007). It is commonly agreed that HONO is mainly formed heterogeneously on surfaces in the presence of water and NO_2 (Lammel and Perner, 1988; Harrison *et al*., 1996).

HONO is photolyzed under solar radiation to produce OH as follows (Gratien *et al*., 2009):

$$HONO + h\nu\ (300\ nm < \lambda < 405\ nm) \rightarrow NO + OH \quad (1.33)$$

HONO is an important source of OH throughout the daytime, especially in urban areas, where the increasing fractional HONO emission may significantly change the oxidizing capacity of the local atmosphere (Tang *et al*., 2015). A small fraction of HONO within NO_x emissions (1-2 %) leads to a substantial increase in oxidant levels, particularly during pollution episodes (reaching a maximum of ca. 11 ppb) (Jenkin *et al*., 2008). Increasing HONO emission also contributes to ozone formation in urban areas.

Rural ozone levels are predicted to increase over the next 20 years. The increasing northern hemispheric background ozone level makes a significant contribution to increasing rural ozone concentrations. In addition, global climate changes will influence regional ozone concentrations in the UK (*e.g.* transboundary winds transporting ozone precursor species across North West Europe to the UK) (Vingarzan, 2004). These factors will potentially affect both UK rural and urban ozone concentrations in the near future (AQEG, 2009).

1.6.4 Ozone trends in the US

The EPA has stated that US national annul mean ozone levels have been decreasing from 1980 to 2010 (EPA, 2013). However, the annual ozone level trend is highly variable between different regions in the US. Recent research suggested that annual mean ozone level was on a negative trend in eastern US area from 1990 to 2010, but in western regions of US, annual mean ozone level was increasing by an average of 0.34 ppb per year during these two decades (Parrish *et al*., 2009; Cooper *et al*., 2012). Result of such differences are shown in the following figures:

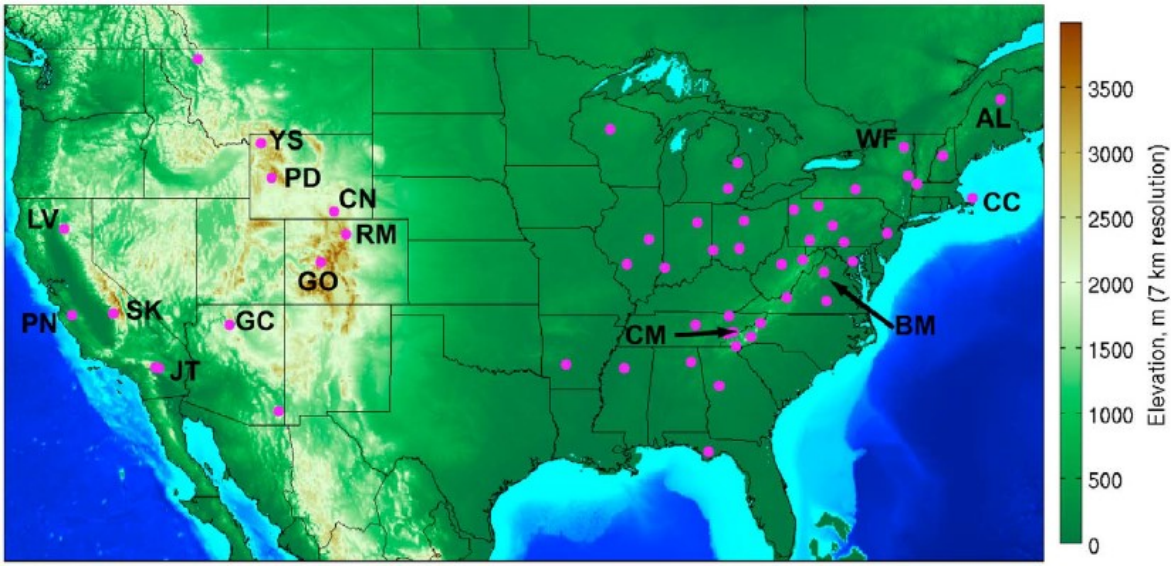

Figure 1.11. 53 rural sites to coverage of western and eastern US regions, abbreviations stand for different monitoring site names (Cooper *et al*., 2012).

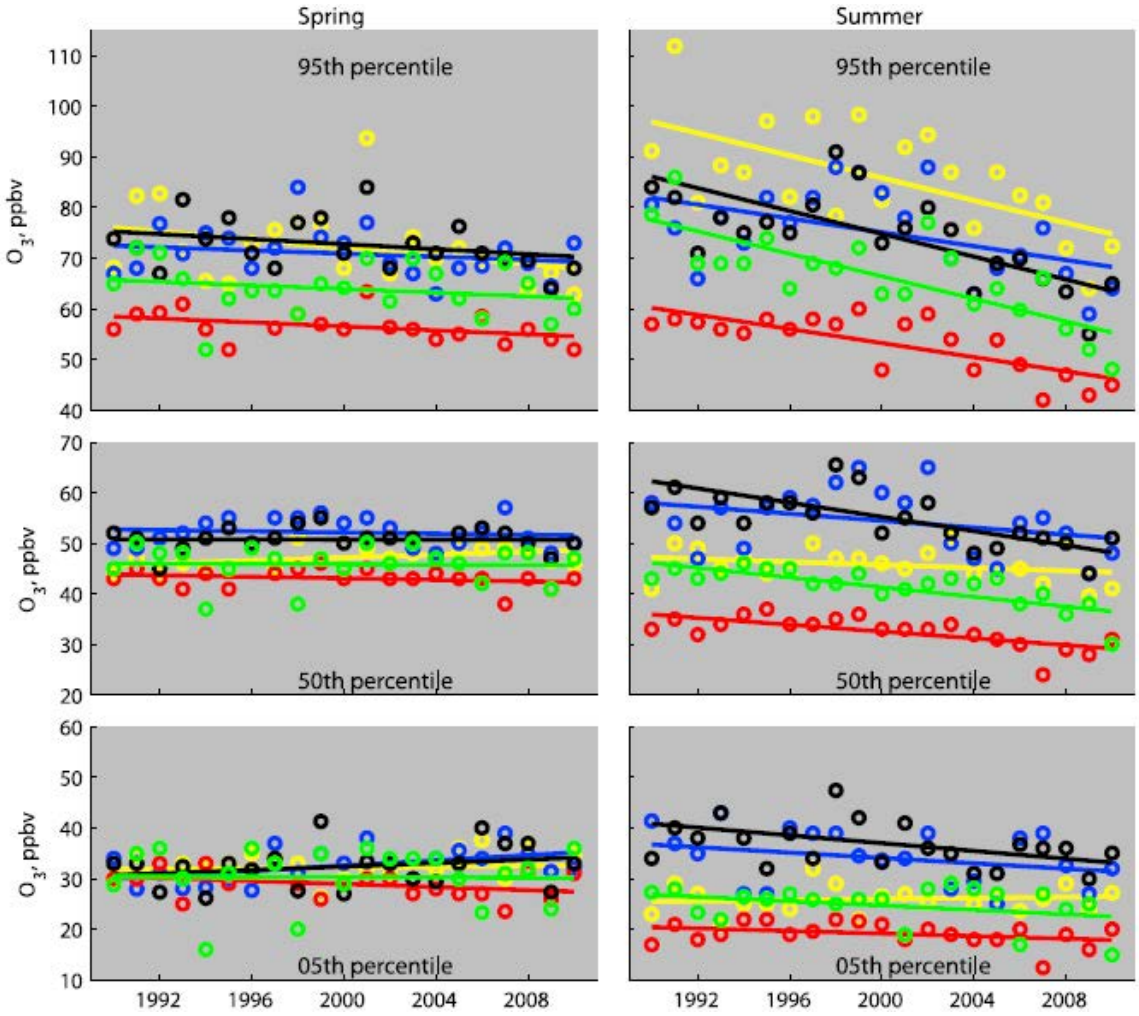

Figure 1.12. 1990-2010 Ozone trends at 6 high elevation western US sites: Cape Cod (CC - yellow), Cove Mountain (CM - blue), Ashland (AL – red), Big Meadows (BM – black) and Whiteface Mountain WF – green). Shown are the 95th (top), 50th (middle) and 5th (bottom) ozone percentiles for spring and summer seasons (Cooper *et al*., 2012).

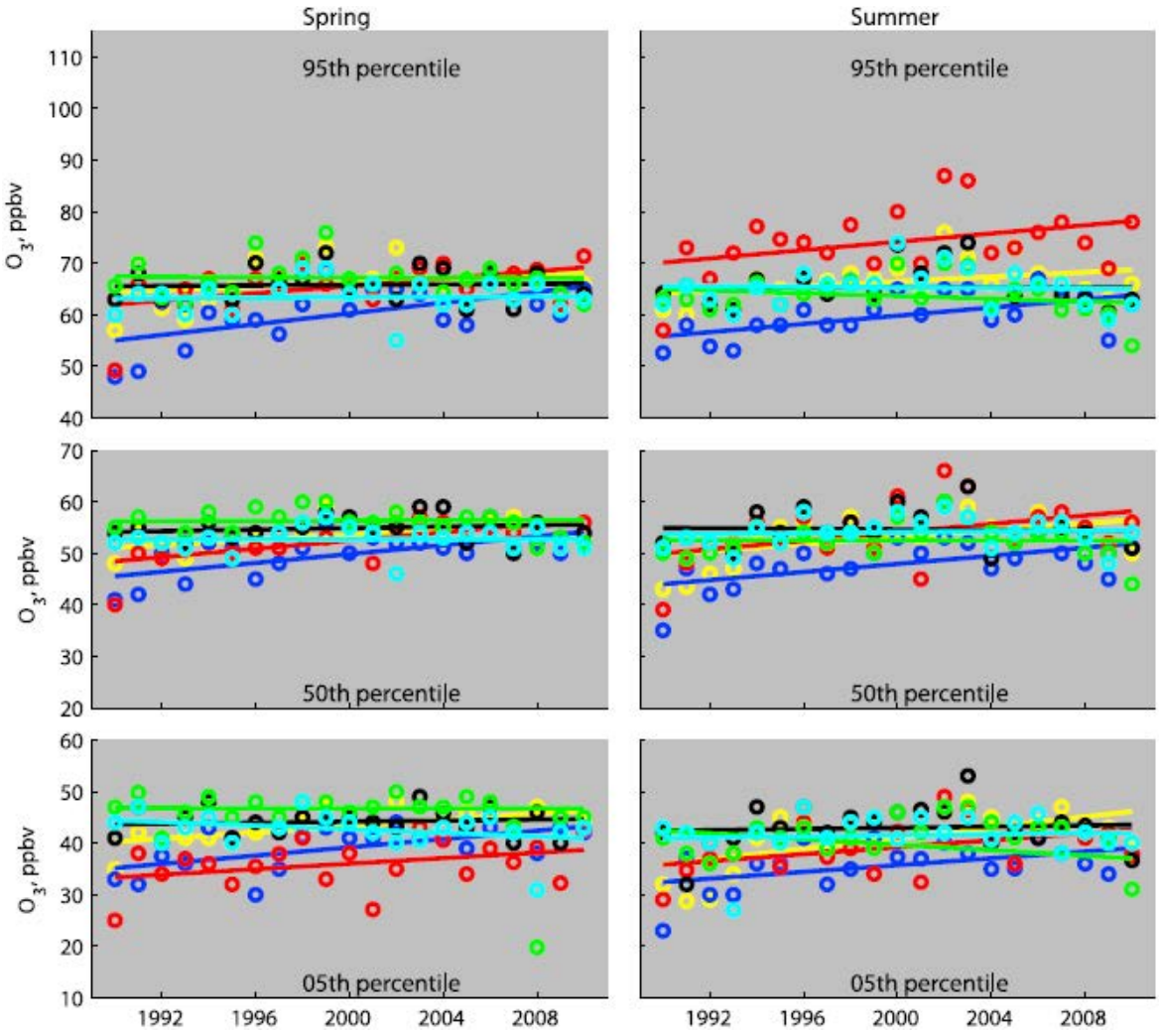

Figure 1.13. 1990-2010 Ozone trends at 6 high elevation western US sites: Grand Canyon (GC - yellow), Yellowstone (YS - blue), Rocky Mountain (RM – red), Centennial (CN – black), Gothic (GO – green) and Pinedale (PD – cyan). Shown are the 95th (top), 50th (middle) and 5th (bottom) ozone percentiles for spring and summer seasons (Cooper *et al*., 2012).

Two research projects also showed evidences of the positive ozone trend in western US and negative ozone trend in eastern US during the similar time period (Figure 1.14, from 1984 to 2004; Figure 1.15, from 1980 to 2007) (Jaffe and Ray, 2007; Lefohn *et al*., 2008).

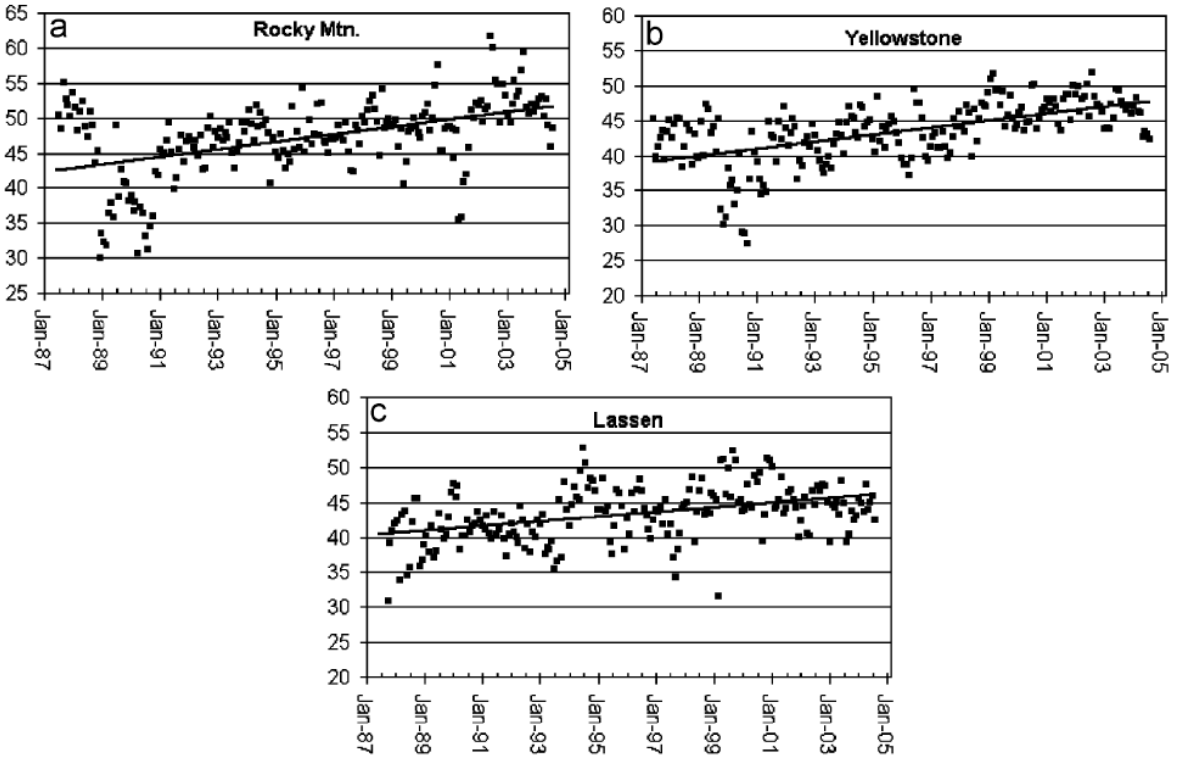

Figure 1.14. Deseasonalized daytime monthly mean ozone levels for rural sites in western US (from 1984 to 2004): (a) Rocky Mountain National Park, (b) Yellowstone National Park, (c) Lassen Volcanic National Park (Jaffe and Ray, 2007).

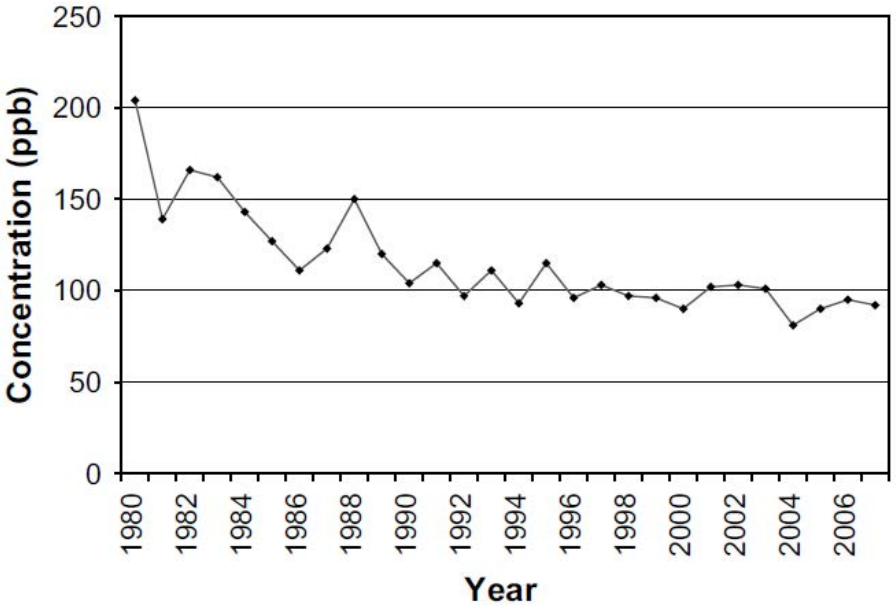

Figure 1.15. Annual fourth highest daily 8-hour-mean maximum ozone concentration (as an indicator of annual ozone level in EPA ozone standard) by year (1980-2007) at Fairfield county, Connecticut monitoring site (an eastern US site 110 km north from New York city) in the US (Lefohn *et al*., 2008).

As a secondary air pollutant, the ozone level is dependent primarily on the domestic ozone precursor emissions in the US. The main ozone precursors are NO_x, non-methane VOCs (NMHCs), CH_4 and CO (see section 1.4.3 for comprehensive ozone formation process). Anthropogenic emission sources are dominant for NO_x and CO, while CH_4 arises from both natural and anthropogenic sources, and many VOCs are primarily biogenic in origin. The overall ozone precursor emissions have been declining in the US from 1990 to 2010 (Parrish *et al.*, 2012), in particular anthropogenic emissions of CO and NO_x, which have declined nationwide in the US between 2000 and 2011 (Figure 1.16) (Kumar *et al.*, 2013).

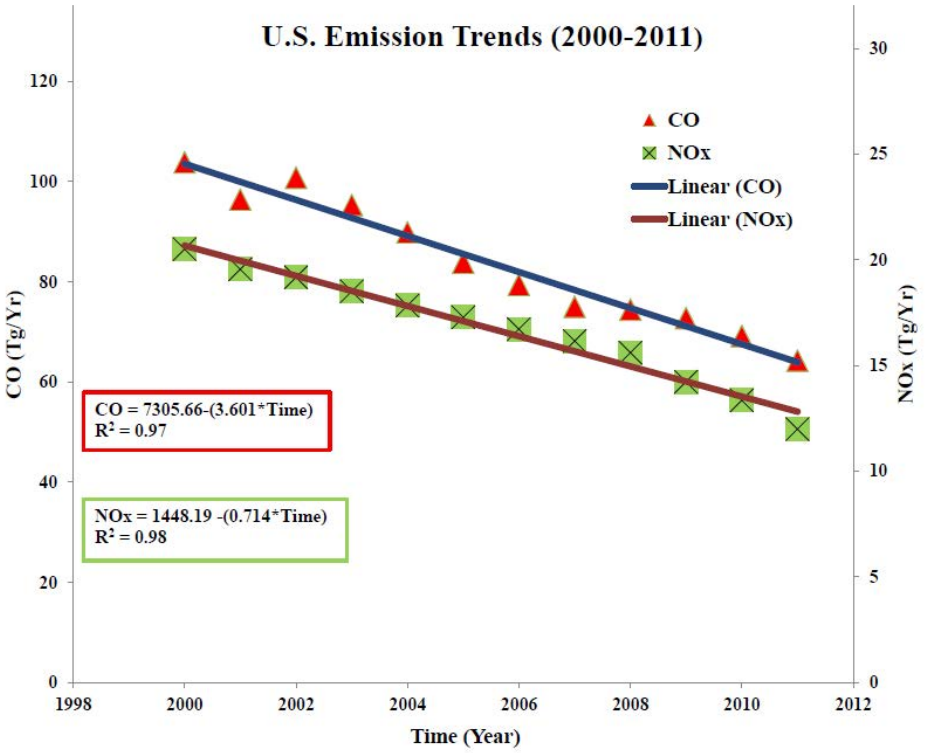

Figure 1.16. US anthropogenic emissions (unit in Tg per year) of CO and NO_x from 2000 to 2011 (Kumar *et al.*, 2013).

The annual mean ozone levels in the US are thought to be falling due to continuously declining domestic ozone precursor emissions. Both national annual ozone and eastern regions ozone level have been declining. However, as Figure 1.13 and Figure 1.14 show,

ozone levels in the western US, especially coastal regions, show a positive trend which is not congruent to the reduced precursor emissions. A possible reason to cause such increased ozone levels is the foreign emissions of ozone precursors transported from East Asia to the western US (Reidmiller *et al*., 2009).

Current ozone control strategies focus on controlling the principal ozone precursors emissions shown in Figure 1.17:

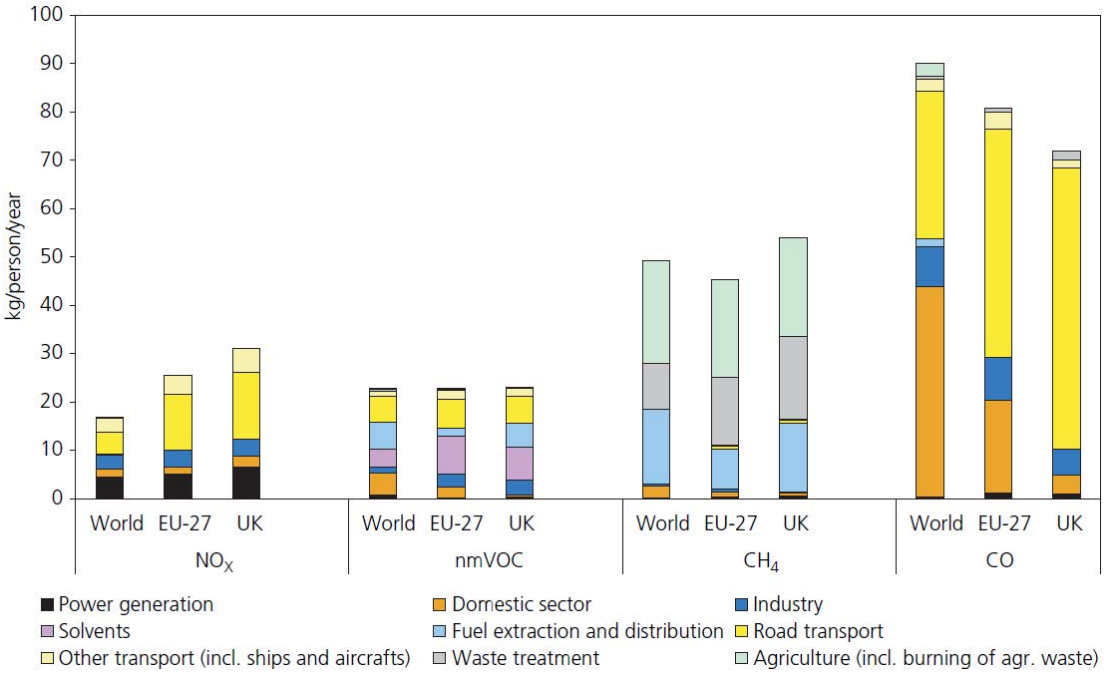

Figure 1.17. Per-capita emissions of the O_3 precursors (NO_x, CH_4, CO, non-methane VOC) from man-made sources in the year 2000 (The Royal Society, 2008).

Control policy for NO_x and VOCs emissions have been implemented in Europe since the late 1980s (Vestreng *et al*., 2009; AQEG, 2009). Control strategies have been partly successful in reducing most European and UK regions' peak ozone concentrations, annual mean ozone level were variable in different regions (AQEG, 2009). Reducing VOCs have been reported to almost always lead to ozone reductions (Xie *et al*., 2011). Consequently, anthropogenic VOCs emission source control is an effective method to reduce ozone

concentration. NO_x emissions control effects are area-dependent and more complicated to generalise: NO_x emission control are effective to reduce ozone concentration in general, but the effect of reduction in NO_x is also dependent on local NO_x : VOC ratios and meteorological factors (transportation of ozone precursors from surrounding regions).

International cooperation is essential in ozone reduction, as the lifetime of ozone, and its precursors, is such that air quality is a cross-boundary issue. Current control strategies are predominantly based on model predictions – despite a variable numbers of uncertainties existing in such models. These uncertainties are discussed in the following section 1.7.

1.7 Evaluation of Ozone Production

Ambient ozone arises from the combination of transport processes and local chemical ozone production. Although it is relatively easy to measure the ambient ozone levels using commercial ozone monitors, it is important to understand the factors driving ozone production (whether from local chemical production or transported from other regions), and in particular to have a quantitative understanding of the ozone production rate, and its likely response to specific emissions controls, in order to accurately predict future ozone levels (and hence their health, ecosystem and climate impacts), and to develop efficient air pollution control policy (i.e. to identify those emissions controls with the greatest impact upon ozone, and other pollutants)**.**

1.7.1 Models of evaluating ozone production

Models are commonly used worldwide as tools to evaluate tropospheric ozone production and abundance. One main advantage of modelling is its modest cost, in contrast to expensive *in situ* pollutant measurements (to evaluate ozone production rate from the historical pollutant data). Modelling is also the only approach capable of predicting future ozone production at regional and global scales. Most ozone models are built upon chemical, meteorological and emissions factors, with application ranges which are highly variable, from Global-level to city-scale (Williams *et al*., 2011). In general, there are three groups of ozone models: the global model, the regional model and the urban model.

1.7.2 Global Models

Global ozone models have been developed to simulate atmospheric chemical transport and transformation on a global scale. They may be used in stratospheric or tropospheric chemistry evaluation or both. Global models allow the full advection and mixing of long-lived pollutants to be considered, which may be appropriate to ozone lifetimes of weeks in the troposphere, but suffer from high computational cost and low spatial resolution with grid squares typically hundreds of km wide (Donner *et al*., 2011).

1.7.3 Regional models

In contrast with global models, regional models evaluate much smaller areas; from a maximum of few thousands of kilometres to a few hundreds of kilometres in extent. As a much higher resolution model type, regional models tend to have more detailed local emission inventory data, more extensive tropospheric chemical schemes and more local transport / meteorology data. The contribution from location-specific factors are often included in those models. The majority of national air quality predictions are derived from regional models, sometimes run or nested within global simulations (Emery *et al*., 2012).

1.7.4 Urban models

Urban models target air pollution on a city scale; their outcomes are highly dependent on projected local ozone precursor emissions. Dispersion models are often integrated with urban models. Operating over a small spatial domain, such models can afford a high degree of chemical complexity, using detailed chemical mechanisms. The MCM (Master Chemical Mechanism) is an example of highly detailed chemical mechanism that simulate the gas-phase chemical process of VOC oxidation based on published laboratory and theoretical data

(Derwent *et al*., 2010). VOCs are important ozone precursor species, such that accurate ozone formation predictions require comprehensive VOC treatment in models. Currently, the degradation of methane and 142 non-methane VOCs is represented in the MCM (Jenkin et al., 2003; Saunders et al., 2003). The advantage of using the MCM is the relatively large number of VOCs included, however, this is still a small fraction of the total VOC species present in the atmosphere. In addition, VOC chemistry is not fully understood in some situations. In the past, the MCM model has been widely tested against more than 300 simulation chamber experiments (Derwent *et al*., 2010). The MCM has been used as a primary reference tool to assist the development of other reduced mechanisms. It is often run in a box model framework.

1.7.5 Specialist ozone models

The photochemical trajectory model (PTM) has been extensively used to simulate regional ozone formation during short term ozone episodes. This model includes several very detailed chemical schemes, running along trajectories within a European area. As a scenario chemistry model, the PTM is used to quantify individual VOC (and their sources') contributions to transboundary ozone formation and ozone transport across North West Europe (Williams *et al*., 2011). As a specialist model, PTM uses are limited in both spatial and temporal coverage. A recent example of the PTM application is during the UK summer Pollution in the Urban Midlands Atmosphere (PUMA) campaign: Modelled local ozone levels were found to agree relatively well (correlation is approximately 90 %) with measurements at a suburban site in Birmingham (Walker *et al*., 2009).

1.7.6 Models Uncertainties and Limitations.

Air pollution models have been widely used in air quality strategy formulation and control policy making; the modest cost is an important factor. However, many limitations and uncertainties are inherent in atmospheric chemical modelling, which may affect evaluations of modelled ozone levels. These are briefly summarised below, in three main categories:

I. Uncertainties in ozone production chemistry.

There are a range of uncertainties in the internal mechanisms which drive atmospheric chemistry models. Firstly, the chemical mechanisms are necessarily incomplete (incomplete simulation of actual VOCs in the troposphere, discussed in section 1.7.6) and fail to replicate HO_x levels (a key test of chemical mechanism performance) observed over rainforests (*e.g.* Leliveld *et al*., 2008) or in polluted urban environments (Hofzumahaus *et al*., 2009). The commonly used MCM mechanism is an example of an extensive (yet incomplete) chemical mechanism showing substantial disagreements to other models (although methane and 142 non-methane VOCs are represented) (Figure 1.18). The impacts of halogen-catalysed chemistry on ozone level is another area which is not included in most models. Recent studies indicated the lack of photochemical reactions of iodine oxides in models could lead to overprediction of ozone levels by up to 15 % (Sarwar *et al*., 2015).

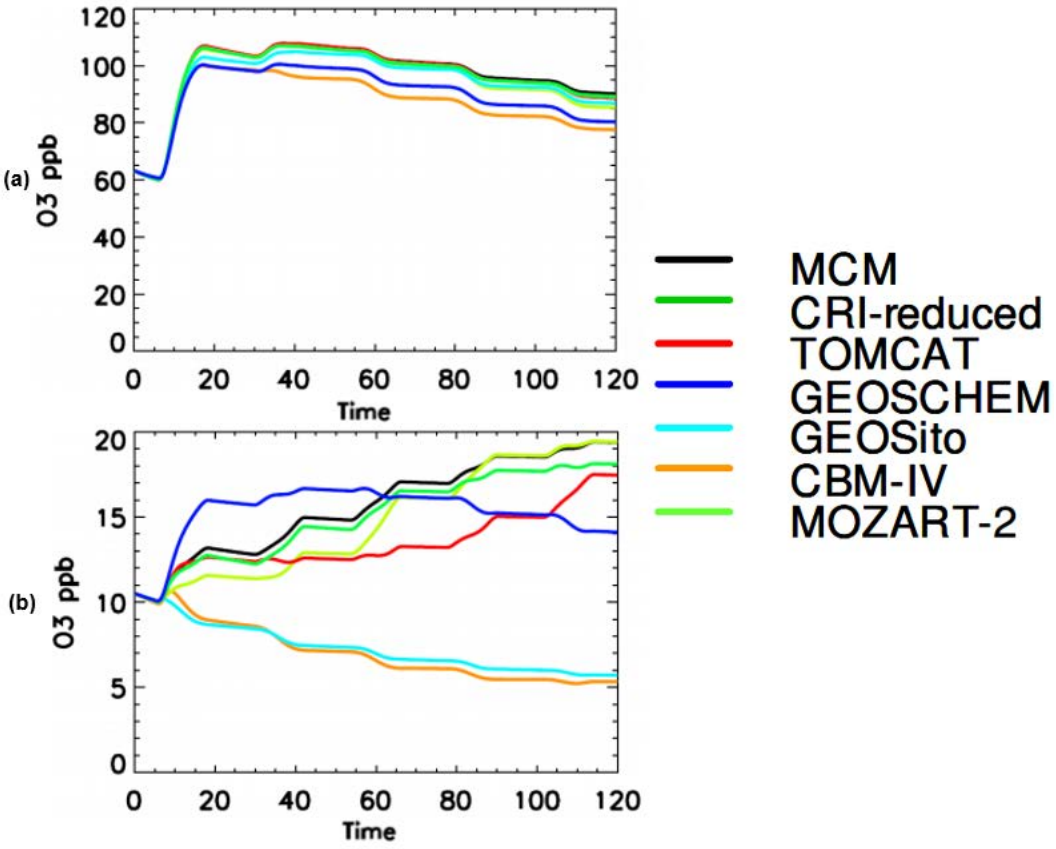

Figure 1.18. Based upon identical initial conditions - (a) Industrial area, (b) Biogenic source emissions dominated area, and identical inventory data, the predicted ozone levels simulated by the MCM, CRI-reduced, TOMCAT, GEOSCHEM, GEOSito, CBM-IV and MOZART-2 models over 120 hours (Emmerson and Evans, 2009).

II. Emissions data limitations

Emissions measurements are necessarily incomplete, missing the extensive pool of ozone precursor species (Lewis *et al.*, 2000). Measurement errors of emissions have been recorded in many cases. For example, o-VOCs (Langford *et al.*, 2009) and NO_x/primary NO_2 (Carslaw *et al.*, 2011) measurements have been shown to be inaccurate. Field measurements of total OH reactivity show a substantial "missing" component to VOC loading – and hence ozone formation (*e.g.* Di Carlo *et al.*, 2004). Emissions from Asia remain as a major uncertainty at present. Air pollutant control policy and legislation in developing Asian countries are not as

well-established as in the US and European countries; consequently, Asian emission data s are going to remain uncertain in models in the future.

III. Climate and environmental factors

Both meteorological and ecological processes that influence ozone production, deposition and dispersion are not fully taken into many models. For example, stratosphere-troposphere exchange processes, atmospheric blocking and natural lightning effects are present in most global climate-chemistry models (Bowdalo *et al*., 2016), but comprehensive understanding of their roles to ozone formation are lacking. Climate factors such as soil water balance and water cycles need to be better represented in climate models to improve predictions of heatwave and high pollution episode-driven spatial and temporal distribution of ozone into the future. These climate factors particularly affect ozone concentrations at regional scales (Young *et al*., 2013).

1.8 Existing Methods to Measure Local Chemical Ozone Production

Alongside modelling approaches, there are several indirect methods which have been employed to determine the local, *in situ* chemical ozone production rate.

1.8.1 Indirect measurement methods

The chemical ozone production rate can be evaluated using measured data of NO_x, O_3 and RO_x species, alongside knowledge of photochemical parameters. There are two methods for the indirect measurement of chemical ozone production: the NO_x photochemical steady state method and peroxy radical (HO_2 and RO_2) method (using either Laser Induced Fluorescence (LIF) (Heard *et al*., 2013) or Peroxy Radical Chemical Amplifier (PERCA) measurements (Green *et al*., 2006).

1.8.2 NO_x photochemical steady state (PSS)

As discussed in section 1.4.1, the NO_x-O_3 PSS is defined by:

$$NO_2 + h\nu\ (\lambda \leq 420\ nm) \rightarrow NO + O \qquad j_{1.34} \qquad (1.34)$$

$$O + O_2 + M \rightarrow O_3 + M \qquad (1.35)$$

$$NO + O_3 \rightarrow NO_2 + O_2 \qquad k_{1.36} \qquad (1.36)$$

If the PSS reactions are the only reactions occurring, then

$$d[NO]/dt = -k_{1.36}[NO][O_3] + j_{1.34}[NO_2] = 0 \qquad (1.37)$$

Subsequently,

$NO_2 / NO = k_{1.36} [O_3] / j_{1.34}$ (1.38)

$k_{1.36} = 1.8 \times 10^{-14}$ cm^3 molecule^{-1} s^{-1} (at 298K) (Sander *et al*., 2011)

This is the Leighton ratio, where $k_{1.36}$ is the NO + O_3 reaction rate constant and $j_{1.34}$ the photolysis frequency for NO_2.

However, in the free troposphere, peroxy radicals are involved in ozone production reactions (section 1.4.2):

$NO + HO_2 \rightarrow NO_2 + OH$ $k_{1.39}$ (1.39)

$NO + RO_2 \rightarrow NO_2 + RO$ $k_{1.40}$ (1.40)

where $k_{1.39}$ and $k_{1.40}$ are the reaction rate constant of peroxy radicals with NO. With consideration of PSS reactions, the NO-NO_2 conversion could be described (under PSS condition):

$$d[NO]/dt = -k_{1.36}[NO][O_3] + j_{1.34}[NO_2] - k_{1.39}[NO][HO_2] - k_{1.40}[NO][RO_2] = 0 \quad (1.41)$$

Then,

$$j_{1.34}[NO_2] - k_{1.36}[NO][O_3] = k_{1.39}[NO][HO_2] + k_{1.40}[NO][RO_2] \quad (1.42)$$

If the PSS reactions are the only processes occurring, then the right hand side part of equation (1.42) is absent, and $j_{1.34}[NO_2] - k_{1.36}[NO][O_3] = 0$, as in the PSS. However, peroxy radicals are involved in ozone production reactions in the free troposphere, and give rise to an imbalance between the terms $j_{1.34}[NO_2]$ and $k_{1.36}[NO][O_3]$. The ozone production rate is given by the non-ozone-reaction rate of conversion of NO to NO_2, which is equal to $k_{1.39}[NO][HO_2] + k_{1.40}[NO][RO_2]$ (from E (1.41)). The evaluated ozone production rate $p(O_3)$

(by PSS method) equals to $j_{1.34}[NO_2] - k_{1.36}[NO][O_3]$. If NO, NO_2, O_3, $j_{1.34}$ and $k_{1.36}$ are known, the ozone production rate can therefore be estimated / calculated.

1.8.3 Direct measurement of Peroxy Radicals - PERCA and LIF approaches

In the right part of equation (1.42), the conversion rate of NO to NO_2 equals the NO_2 photolysis rate at equilibrium, which is the ozone production rate. If HO_2, RO_2 and NO levels are measured, the ozone production rate is then evaluated as:

$$d[NO]/dt = k_{1.39}[NO][HO_2] + k_{1.40}[NO][RO_2] \quad (1.43)$$

$$p(O_3) = k_{1.39}[NO][HO_2] + k_{1.40}[NO][RO_2] \quad (1.44)$$

This method is based upon measurement of peroxy radical concentrations, in contrast to estimation of the conversion rate of NO to NO_2 in the first method. There are many different organic peroxy radicals (RO_2) in reality. Consequently, there is no single value of $k_{1.40}$ which applies – $k_{1.40}$ differs for every different RO_2 species, and also varies with temperature and pressure.

Currently, there are two methods that measure HO_2 and RO_2 levels, LIF and PERCA.

I. Laser Induced Fluorescence (LIF)

The Fluorescence Assay by Gas Expansion (FAGE) approach measures OH radicals by LIF, allowing the OH radical measurement to be utilised to measure HO_2 and RO_2 level by adding NO in the FAGE. This measurement process is described in following reactions (1.43) to (1.46)

$$NO + HO_2 \rightarrow NO_2 + OH \quad (1.45)$$

$RO_2 + NO \rightarrow RO + NO_2$ (1.46)

$RO + O_2 \rightarrow HO_2 + R'CHO$ (1.47)

$HO_2 + NO \rightarrow OH + O_2$ (1.48)

Controlled NO level in the FAGE enables the (separate) measurement of HO_2 or RO_2, alongside OH, by LIF, a new development recently presented by Heard *et al*., 2013.

II. Peroxy Radical Chemical Amplifier (PERCA)

The PERCA is an indirect measurement of HO_2 and RO_2; this instrument converts HO_2 to NO_2 molecules by the following reactions (1.46) - (1.48):

$HO_2 + NO \rightarrow OH + NO_2$ (1.49)

$OH + CO \rightarrow CO_2 + H$ (1.50)

$H + O_2 + M \rightarrow HO_2 + M$ (1.51)

Each time an HO_2 molecule enters the PERCA, an NO_2 molecule is produced, then HO_2 is regenerated by reaction with existing CO in the instrument. This process is a repeating cycle. PERCA measures HO_2 as NO_2 molecules with some well-established NO_2 measurement approach. The RO_2 radical measurement is similar in the PERCA (Green *et al*., 2006).

Both LIF and PERCA measure the total levels of RO_2, the lack of speciation in RO_2 species leads an uncertain $k_{1.39}$ value (a single estimated mean value for a range of different RO_2 species is often applied). The actual $k_{1.39}$ is variable for individual RO_2 species, consequently the use of a mean value creates uncertainty when evaluating the rate of the NO + RO_2 reaction.

PERCA and LIF measurements were deployed during the first OPR field measurement, at North Kensington, London during summer 2012. Results from both methods are discussed further in Chapter 4 (London OPR deployment).

1.9 Aim of this thesis

The unknown and complex range of peroxy radicals present in the atmosphere is the main uncertainty in both the LIF and PERCA indirect ozone production rate measurement methods, alongside the PSS indirect measurement method which neglects peroxy radical reactions while evaluating ozone production rate, and suffers from uncertainties introduced by the limited precision in evaluation of equation 1.42. In addition, the PERCA and LIF approaches are highly technically and chemically complex, and both are expensive systems.

The aim of this work is to develop a relatively simple, direct measurement method to accurately measure *in situ* ozone production rates in ambient air, to improve upon the accuracy and the precision achievable with indirect measurement methods and with numerical models. This new approach is referred to the "ozone production rate measurement system (OPR)". Both atmospheric climate and chemistry models would benefit from this new system's potential improvement of the precision and accuracy in ozone production rate evaluation. The OPR direct measurement method will also enable an effective and accurate way to quantify the importance of local chemical ozone production (compared with, for example, transport) by comparing OPR measurement to rate of change in ambient ozone levels.

The thesis therefore aims to assess the broad hypothesis that local chemical processes make a significant contribution to changes in ozone levels experienced at specific measurement locations (compared with, for example, advection, mixing or deposition) - and to quantify the extent to which this is the case.

The principle of OPR's direct measurement approach is extensively discussed in the following Chapter 2: Experimental Methodology and Instrument Properties.

Chapter 2: Experimental Methodology and Instrument Properties

This chapter describes the Ozone Production Rate (OPR) measurement system: the measurement principle, approach and detailed components. Each OPR system component is introduced separately in the following sections, which describe their materials, functionality and operating principle. Finally, the configuration of the OPR system during the field campaigns in London and India (described fully in Chapters 4 and 6) is outlined. Detailed system performance, instrument characterisation and calibration is covered in the following Chapter (3: System characterisation).

2.1 Direct measurement of ozone production

As discussed in Chapter 1, current methods for assessing chemical ozone production rates suffer from identified uncertainties, motivating the development of alternative approaches to investigate chemical ozone formation: the ozone production rate (OPR) measurement system. This approach directly measures the local (*in situ*) chemical ozone production rate, avoiding limitations of model approaches, and alternative, indirect, measurement methods. It is derived from a concept pioneered by Cazorla & Brune (2010).

The ozone production rate in the atmospheric boundary layer is the combination of three processes: advection, deposition and chemical ozone production (and destruction).

$$\partial [O_3]/\partial t = \underbrace{pO_3 - lO_3}_{\text{Chemistry}} - \underbrace{(v/H)[O_3]}_{\text{Deposition}} + \underbrace{u_i\, \partial[O3]/\partial x_i}_{\text{Advection}}$$

pO_3 = chemical ozone production

lO_3 = chemical ozone loss

v = deposition velocity

H = mixed layer height

u_i = ozone velocity in three directions

$\partial[O_3]/\partial x_i$ = ozone gradient in three directions (corresponding to u_i)

The OPR system aims to determine the chemical production and loss term in equation 1.1, ($pO_3 + lO_3$), which is referred as $p(O_3)$ in later Chapters (extensively used as $p(O_x)$, see section 2.2.1). In the free troposphere, when $p(O_3)$ is measured by the OPR system, with additional measurement of the *in situ* ozone level, the sum of deposition and advection effects can be determined. When surface ozone deposition velocity v and the mixed layer height H are known, the deposition effect can be estimated. Subsequently, the advection effect of ozone can then be determined.

2.2 Introduction to the OPR System

2.2.1 Principle of the OPR approach

The key components of the OPR system are a pair of quartz glass sampling reactors, through which ambient air is drawn. The two sampling reactors are identical in their dimensions, designs and materials. One of the two reactors is uncoated, allowing solar radiation (UV) to penetrate through the walls, simulating the photochemical ambient air conditions within the reactor - referred as the "Sample Reactor". Within the Sample Reactor, the aim is for radical chemistry to continue at an identical rate to that in the sampled ambient air. The other reactor is completely enclosed in a UV blocking jacket (section 2.3.1) to eliminate short-wavelength radiation. This eliminates (most) radical sources, and hence ozone-forming radical cycling, in this reactor, which is referred to as the "Reference Reactor". The main concept of the OPR system approach is then to compare the difference in ozone abundance between the two reactors, to evaluate the change (increase) in ozone in the sample reactor, relative to the reference reactor, and hence determine the ozone formation rate. In this ideal scenario, the measured difference in ozone between the reactors directly represents the net ozone production from radical chemistry in the sample reactor, and as the mean residence time of ambient air in each reactor may be measured, the net ozone production rate may be obtained, presented as:

$p(O_3) = \Delta O_3 / t_{mean\ res}$

ΔO_3: The differential O_3 abundance between two reactors.

$t_{mean\ res}$: Mean residence time of ambient air in the reactor

In practice a number of additional factors need to be considered in assessing the validity of the principle outlined above. These include ozone/NO_x loss on the reactor wall (inner surface), dark radical sources, NO_2 to O_3 conversion efficiency and NO_x-O_3 partitioning effects.

An important feature of the OPR approach arises from the NO_x-O_3 photochemical steady state behaviour: When ambient NO_x and O_3 enter both reactors, the NO + O_3 and NO_2 photolysis reactions are in balance (with minor contributions from other processes, such as the peroxy radical reactions leading to ozone formation). In the sample reactor, solar radiation mimics that in ambient air, and the NO_x-O_3 photochemical steady state (PSS) is maintained. In the reference reactor, solar UV radiation is eliminated, and NO_2 photolysis is consequently reduced; therefore, there is some net reaction of NO with O_3 to form NO_2. Consequently, the PSS in the reference reactor is different from the PSS in the sample reactor, leading to a difference in ozone exiting the reactors (in the absence of any ozone formation chemistry). This issue is comprehensively discussed in chapter 5.

To address this issue, the system is operated to measured differences in oxidant O_x (equal to the sum of O_3 + NO_2) exiting the two reactors, and hence the measurement determines the rate of production of O_x. This is in fact a more useful quantity, as NO_2 and O_3 are rapidly interchanged through reaction with emitted NO, and moreover it renders the measurement robust to variations in NO levels from local emissions (*e.g.* traffic emission), which typically vary on a seconds-minutes timescale compared with the measurement averaging period of hours and upwards. To achieve this change, a conversion unit (section 2.4) is introduced to photolytically convert NO_2, in the flow from each reactor, into O_3 (+ NO); the difference in

ozone between the flow from each reactor is measured after this conversion unit, and therefore represents the net production of O_x.

The concept of net oxidant production rate is more properly rewritten as, the net oxidant production rate:

$p(O_x) = \Delta O_x / t_{mean\ res}$

ΔO_x: The differential O_x abundance between two reactors.

$t_{mean\ res}$: Mean residence time of ambient air in the reactor.

2.2.2 The OPR system's flow path

As introduced in section 2.2.1, the detailed OPR system schematic is then shown in the following Figure 2.1,

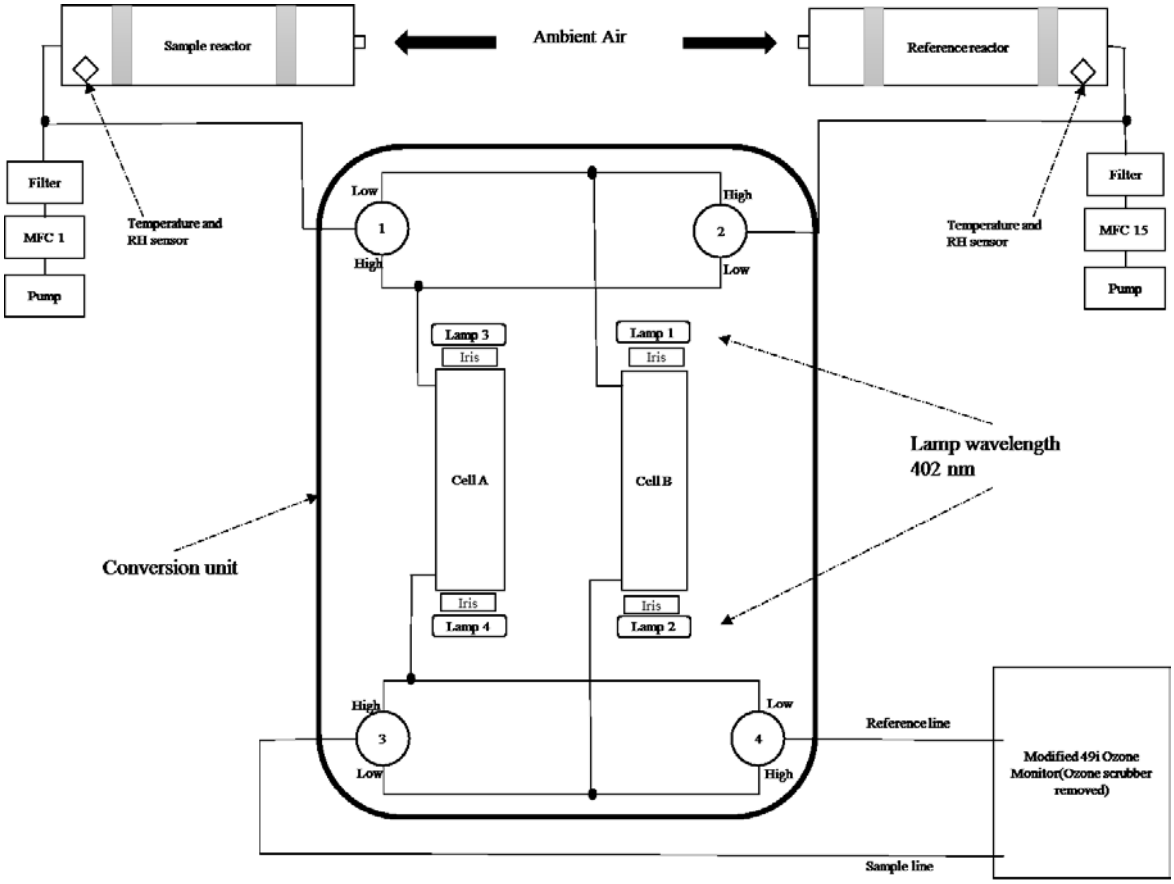

Figure 2.1. OPR system gas flow schematic.

Figure 2.2. OPR core unit (OPR system components without the dual sampling reactors) during ClearfLo London summer IOP (located in white circle area).

Figure 2.1 describes the OPR system components, which includes the dual sampling reactors, the NO_2 conversion unit (comprising a pair of converter cells) and a modified Thermo 49i UV-absorption ozone monitor. Parametric details of the individual system components are introduced in following section 2.3, 2.4, 2.5 and 2.6.

Ambient air is continuously draw into the two reactors at a constant flow rate (photochemistry details in both reactors are in section 2.2.3), then enters the NO_2 conversion

unit via 6 mm diameter PTFE tubes. The main function of the NO_2 conversion unit is to convert NO_2 to O_3 with high efficiency (although less than 100 %, as discussed in section 3.6 & the "correction" Chapter 5), allowing the differential O_x abundance between the two reactors to be determined. A pair of converter cells are built into the conversion stage with two UV LED (λ = 402 nm, see Section 4.3.1 for details) lamps at each end. In the converter cells, NO_2 in both the sample and reference flows is converted into O_3. In the conversion unit, the flow is periodically switched such that air from the sample and reference reactors passes through each conversion cell alternately, to average out any difference in conversion efficiency between the two converter cells. After the air flow exits the NO_2 conversion unit, a modified thermo 49i UV-absorption ozone monitor is connected to both the sample flow and reference flow. The ozone monitor measures the differential O_3 level between two flows. The operating principle of the modified ozone monitor is discussed in section 2.6. The differential O_3 abundance between the two flows, measured by the ozone monitor, is referred as ΔO_x: the difference in O_x abundance between two reactors.

2.2.3 Photochemistry in the Sample and Reference Reactors

The dominant primary daytime hydroxyl radical (OH) source in the free troposphere is the photolysis of O_3. Similarly in the sample reactor, OH is formed following the photolysis of O_3 by UV radiation at wavelengths below approximately 310 nm, and the subsequent reaction of $O(^1D)$ with water vapour as shown below:

$$O_3 + h\nu \rightarrow O(^1D) + O_2 \quad (2.1)$$

$$O(^1D) + H_2O \rightarrow OH + OH \quad (2.2)$$

HONO photolysis is another significant photolytic source of OH radicals (Kim *et al.*, 2014):

$$HONO + h\nu\ (300\ nm < \lambda < 405\ nm) \rightarrow OH + NO \quad (2.3)$$

The O_3 and HONO photolysis processes continues to react in the sample reactor. OH production initiates oxidation processes in the sample reactor, such as OH reactions with common VOC species (*e.g.* CO and CH_4). The oxidation processes subsequently form peroxy radicals (RO_2) following reaction with O_2 in ambient environment. These process are present as:

$$OH + CH_4 \rightarrow CH_3 + H_2O \quad (2.4)$$

$$OH + CO \rightarrow H + CO_2 \quad (2.5)$$

The oxidation reactions produce H and CH_3, both of which react with O_2 to form peroxy radicals (RO_2)

$$CH_3 + O_2 + M \rightarrow CH_3O_2 + M \quad (2.6)$$

$$H + O_2 + M \rightarrow HO_2 + M \quad (2.7)$$

In urban/suburban environments, peroxy radicals tend to react with the abundant NO to form NO_2,

$$HO_2 + NO \rightarrow OH + NO_2 \quad (2.8)$$

$$CH_3O_2 + NO \rightarrow CH_3O + NO_2 \quad (2.9)$$

The NO_2 produced from peroxy radical chemistry is then photolyzed to NO + O, and the O atoms react with O_2 to form O_3. The HO_2 reacts with NO to regenerate OH, CH_3O_2 reacts with NO to produce CH_3O – an alkoxy radical (RO). CH_3O subsequently reacts with atmospheric O_2 to produce HO_2 and formaldehyde (HCHO),

$$CH_3O + O_2 \rightarrow HCHO + HO_2 \quad (2.10)$$

This regenerates HO_2, contributing to NO_2 formation. HCHO can be photolyzed with wavelength lower than 338 nm to form H and HCO under sunlight during daytime. Both H and HCO are precursors to generate HO_2, again to potentially contribute to NO_2 formation.

$$HCHO + h\nu\ (\lambda < 330\ nm) \rightarrow H + HCO, \quad (2.11)$$

$$H + O_2 + M \rightarrow HO_2 \quad (2.12)$$

$$HCO + O_2 \rightarrow CO + HO_2 \quad (2.13)$$

These peroxy radical regeneration and cycling processes are core reactions for NO_2 formation during daytime in ambient air, and also within the sample reactor. The incoming UV radiation penetrates through the sample reactor's quartz glass with minimal attenuation to initiate OH production, NO_2 photolysis and hence net O_3 production.

$$NO_2 + h\nu \rightarrow NO + O \quad (2.14)$$

$$O + O_2 + M \rightarrow O_3 + M \quad (2.15)$$

The NO_x-O_3 photochemical steady state (PSS) is established continuously, but differently, in both reactors. During the daytime, in absence of other tropospheric chemical reactions, there is a null cycle between NO_x and O_3.

$$NO_2 + h\nu \xrightarrow{j_{2.16}} NO + O \quad (2.16)$$

$$O + O_2 + M \rightarrow O_3 + M \quad (2.17)$$

$$NO + O_3 \xrightarrow{k_{2.18}} NO_2 + O_2 \quad (2.18)$$

$$[NO] / [NO_2] = j_{2.16} / k_{2.18}\ [O_3] \quad (2.19)$$

This null cycle regulates the background O_3 and NO_x levels, but does not lead to net O_3 production.

In contrast, the reference reactor is surrounded by a jacket which blocks the incoming UV radiation under ca. 400 nm. As a result, the primary OH formation processes (short wavelength O_3 photolysis, and photolysis of HONO and HCHO) are effectively eliminated in the reference reactor.

Pre-existing HO_2 and RO_2 radicals will continue to react in the reference reactor, but in the absence of photolytic initiation, the termination reactions will rapidly lead to their removal. Dark radical sources (*e.g.* alkene ozonolysis; reactions of NO_3 radicals) will not be affected by the UV filtering, and will proceed unattenuated in both reactors, leading to OH formation and NO to NO_2 conversion. However, in the reference reactor, the resulting NO_2 photolysis rate ($j_{NO2\ reference}$) is substantially slowed ($j_{NO2\ reference} = 0.14\ j_{NO2\ sample}$, see Section 5.3.1). Overall, the impact of the dark source of OH radicals upon ozone production is still largely (> 85 %) captured by the system.

2.3 Individual System Components

2.3.1 Sampling Reactors' material

The OPR system includes a pair of sampling reactors as the core intake component. Both reactors are built identically from quartz glass tubes (SiO_2). However, the reference reactor is enclosed with an additional jacket, made of Ultem (Polyetherimide, $C_{37}H_{24}O_6N_2$).

2.3.1.1 Quartz material

Quartz, also known as fused quartz or fused silica, is a special type of glass. The composition of quartz is silicon dioxide (SiO_2) in non-crystalline form. Unlike other glass products with added ingredients, the fused quartz is the purest form of SiO_2. The silicon oxygen chemical bond gives quartz glass high temperature stability and chemical inertness. Its softening temperature is 1600°C. The fused quartz glass has more than 90 % transmission rate from 175 nm to 2200 nm (Figure 2.3), this covers the complete visible spectrum with extension to solar ultraviolet and infrared light.

In the OPR system, most sunlight penetrates the quartz sample reactor with less than 10% loss (RMI, 2015) to initiate photolysis and radical chemistry in the sample reactor. The reference reactor has the same properties, with exception of UV radiation being substantially attenuated under approximately 400 nm wavelength by the addition of an Ultem jacket (see Section 2.3.1.2).

The converter cells are cylindrical tubes, also made from quartz, each end of the converter cell has a thin (0.3 cm thickness) fused silica window to allow the LED lamp's UV radiation (390 - 395 nm) to be transmitted and initiate NO_2 photolysis with a high conversion efficiency.

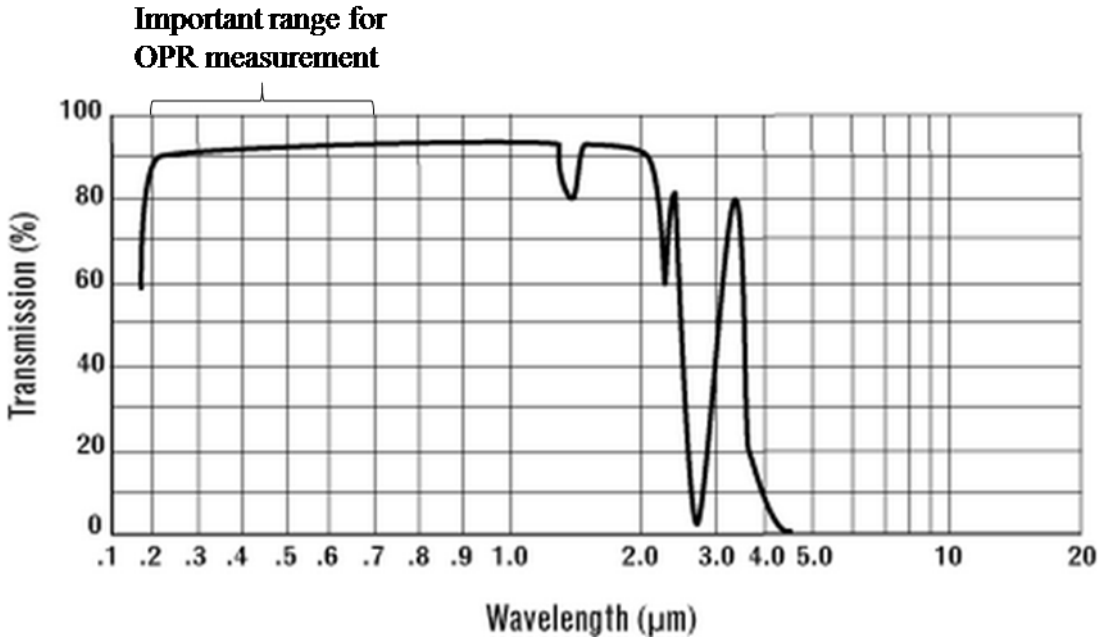

Figure 2.3. Quartz glass light transmission as a function of wavelength (μm) (RMI, 2015).

2.3.1.2 Ultem Material

The reference reactor is completely wrapped with an Ultem jacket to attenuate the incoming UV, it has a light brown appearance derived from the Ultem film.

Ultem is the brand name for Polyetherimide (PEI), its molecular formula is $(C_{37}H_{24}O_6N_2)_n$. It is an amber colour, high melting point (204 to 232 °C) polymer. This material is mouldable and durable at ambient temperatures.

The Ultem jacket surrounding the reference reactor comprises a single layer of 0.5 mm thickness, which was found through laboratory tests to satisfactorily reduce the UV radiation (see Figure 2.4).

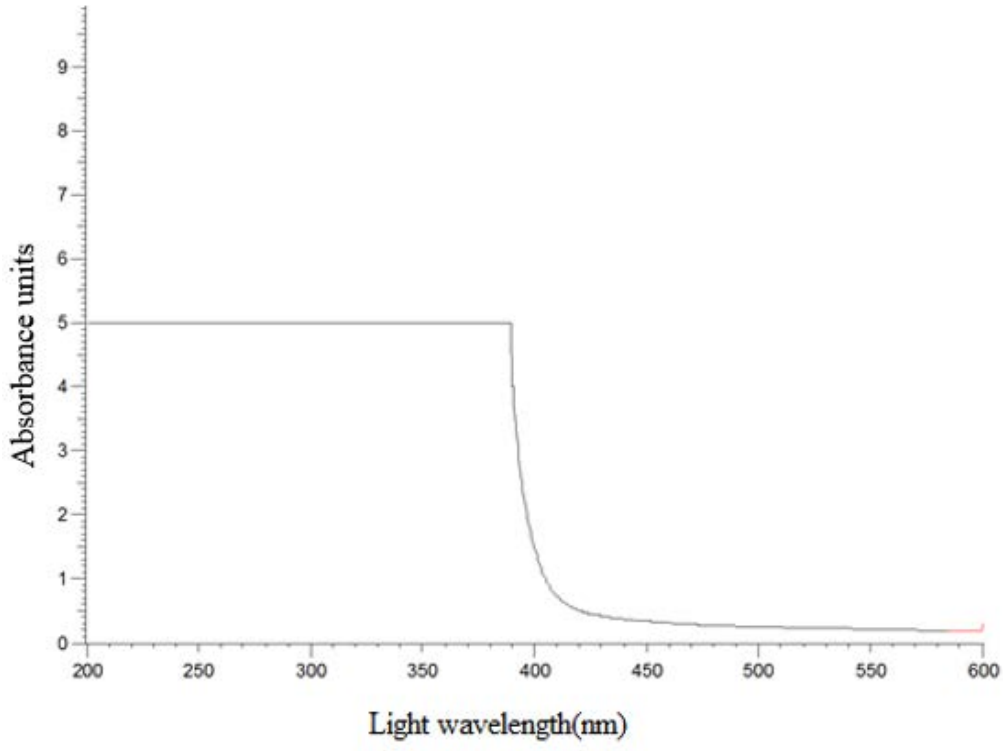

Figure 2.4. Absorption of a single layer of Ultem film as a function of wavelength (200 – 600 nm), data were taken from a Camspec M550 UV-visible absorption spectrometer.

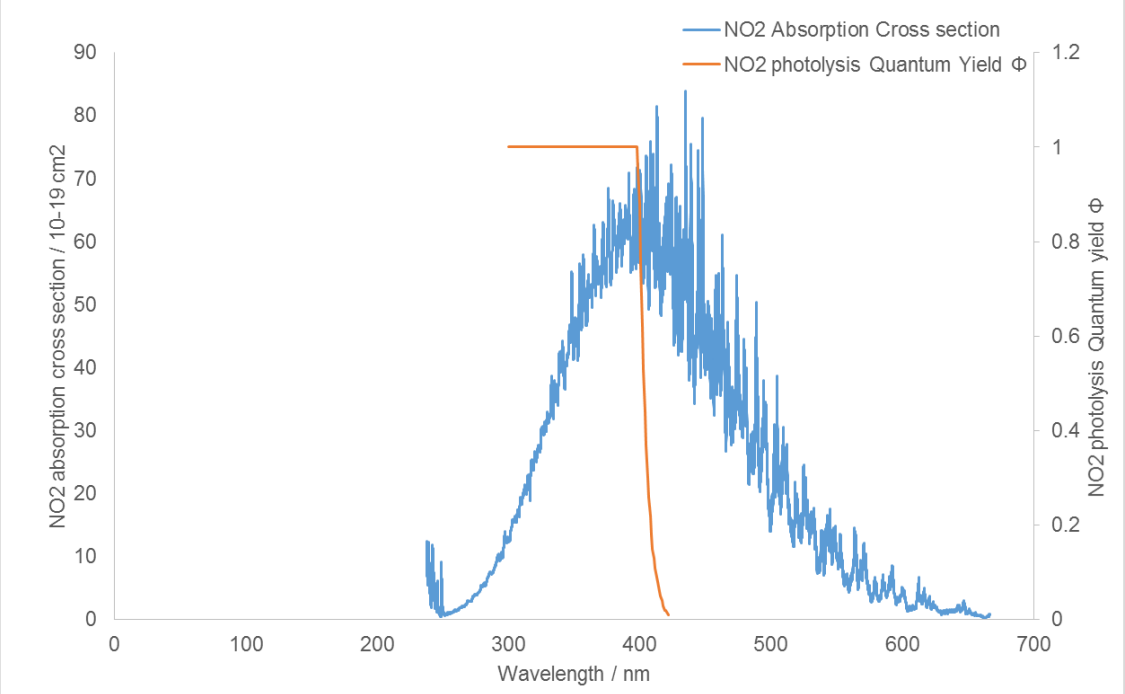

Figure 2.5. Primary axis (left) is the NO_2 absorption cross section as a function of wavelength at 298K; Secondary axis (right) is the NO_2 photolysis quantum yield (Φ_{NO2}) as a function of wavelength at 298 K (Sander *et al.*, 2011).

According to the Beer-Lambert law, light transmission is expressed in terms of an absorbance shown below,

$A_\lambda = - \log_{10} (I/I_0)$

A_λ is the light absorbance at certain wavelength.

(Assuming light transparency is 100%)

I is the intensity of light passed through the sample.

I_0 is the intensity of incident light before passing through the sample.

Figure 2.3 indicates the Ultem material has high light absorbance in excess of 5 between 200 nm and 400 nm wavelength range, then falling rapidly to 0.5 above 420 nm wavelength. Transmission of UV light within this wavelength range is therefore less than 0.001. Figure 2.4 describes the rapid increase of NO_2 photolysis quantum yield (Φ_{NO2}) from wavelength 422 nm (0.01), and reaching a maximum value below 398 nm (1). This Figure also indicates the NO_2 absorption cross section, which maximises at approximately 413 nm wavelength. Therefore, the Ultem material eliminates most NO_2 photolysis reactions by allowing minimal transmission of UV light under 400 nm wavelength. Consequently, the Ultem jacket eliminates most photolytic radical chemistry in the reference reactor.

2.3.2 Reactor dimensions

The quartz glass sampling reactors comprise 70 cm length tubes with an OD of 18 cm and an ID of 17.6 cm (the tube wall thickness is 0.2 cm), each reactor has a volume of approximately 17 litres. Before use, each tube's surface was cleaned then rinsed with distilled water and slowly dried at room temperature.

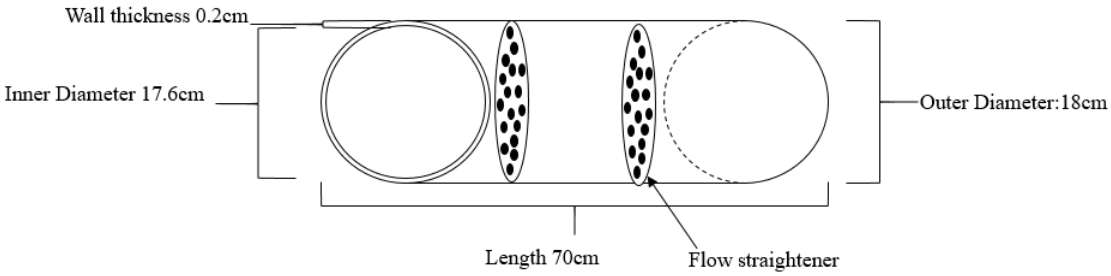

Figure 2.6. Sample reactor's shape and dimensions – 17 litres (with flow straightener built in, details in section 2.3.4).

2.3.3 Air flow in the reactors

The two sampling reactors are effectively closed conduits, their cross sections are circular. This type of conduit is formally termed as a "pipe". There are three types of flow movements in a closed conduit, termed laminar, transitional and turbulent flows.

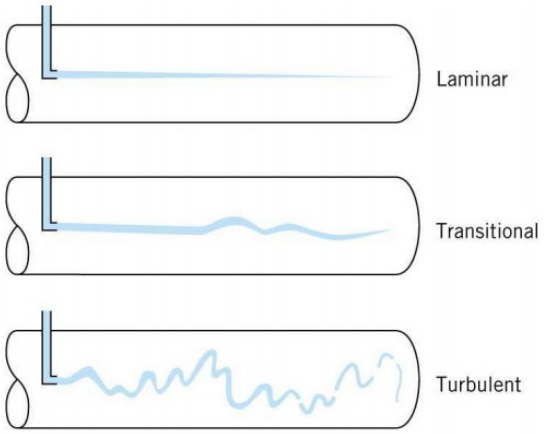

Figure 2.7. Air flow types in a closed conduit (Visavale, 2015).

The laminar flow occurs when fluid moves slowly with parallel flow lines. When the fluid moves faster, and the flow-line fluctuates randomly in many directions with time, the flow is termed as turbulent. If the fluid is moving at an intermediate velocity, there are irregularities in the flow-lines, but the flow is overall well defined, it is termed as transitional flow (Wilcox, 1998).

Flow type in a pipe can be characterised by the pipe dimensions and flow properties by the dimensionless Reynolds number,

$$N_r = \frac{VD\rho}{\eta} = \frac{VD}{\nu}$$

N_r - Reynolds number

V - Velocity of flow (m/s)

D – Diameter of pipe (m)

ρ – Density of fluid (kg/m^3)

η – Dynamic viscosity (kg/m.s)

ν – Kinematic viscosity (m^2/s)

When the Reynolds number is less than 2000, the flow is in the laminar regime. When Reynolds number is more than 4000, the flow is in the turbulent regime. Reynolds numbers between 2000 and 4000 are considered to be transitional flow. In the OPR reactors,

$$N_r = \frac{VD}{\nu} = \frac{0.00137611\text{m/s} * 0.18\text{m}}{1.460\text{x}10-5\ \text{m2/s}} = (0.00137611\ \text{m/s} \times 0.18\ \text{m})/\ 1.460\text{x}10^{-5}\ \text{m}^2/\text{s} = 1.70$$

The calculated Reynolds number indicates that flow in sample reactors are very strongly in the laminar flow regime. However, flow visualisation experiments (with added smoke tracer, repeated 5 times, see Figure 2.8) on flow patterns inside the reactors were performed, which suggested that the flow in each reactor was turbulent - reflecting the fact that the calculated flow type applies after passage along an infinitely long pipe, and laminarity takes some time be established - the turbulence reflecting the gas admittance through a central aperture in the sealing disks (Figure 2.9). For this reason, the flow straighteners were introduced; after

installation of the flow straightener to each reactor, the turbulent flow was clearly visually changed to an essentially laminar pattern with many fewer vortices. This improvement was further validated by the stable residence time measurements (pulse series) obtained during calibration tests (see further discussion in section 3.3).

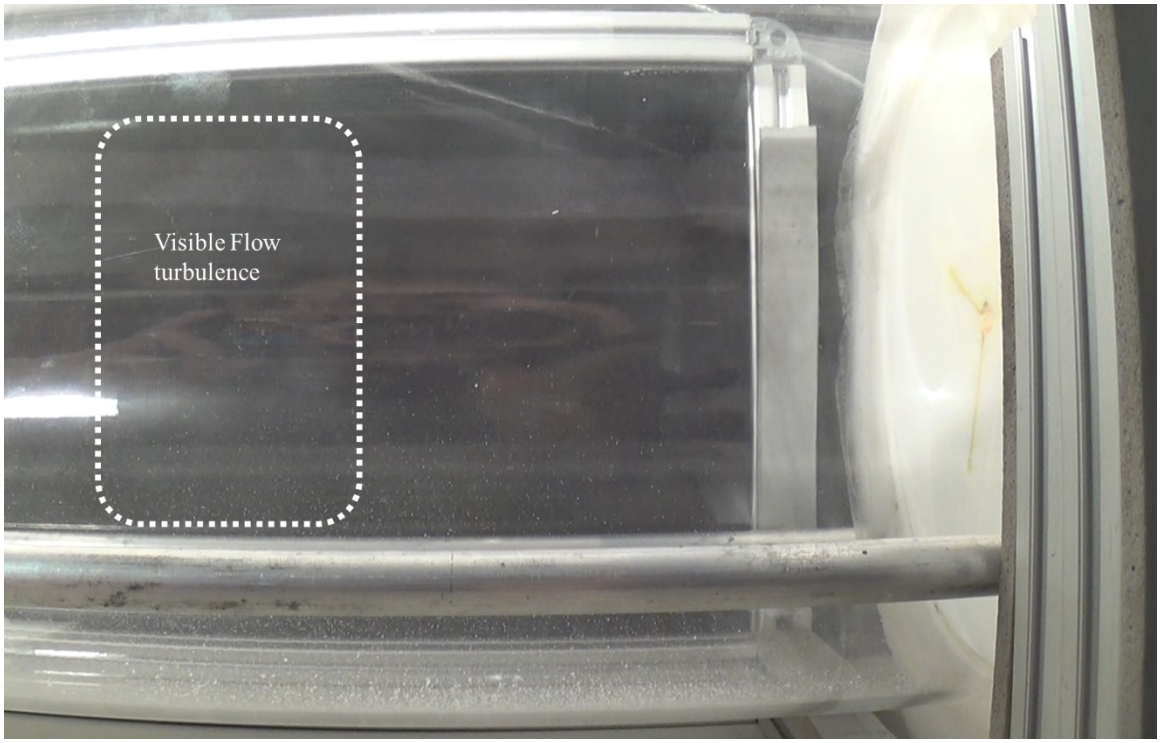

Figure 2.8. Flow visualisation experiment with added smoke tracer, the circle area shows visible flow turbulence.

2.3.4 Flow straightener

Two flow straighteners are placed inside each reactor at equal distance of 9 cm from the end of reactor.

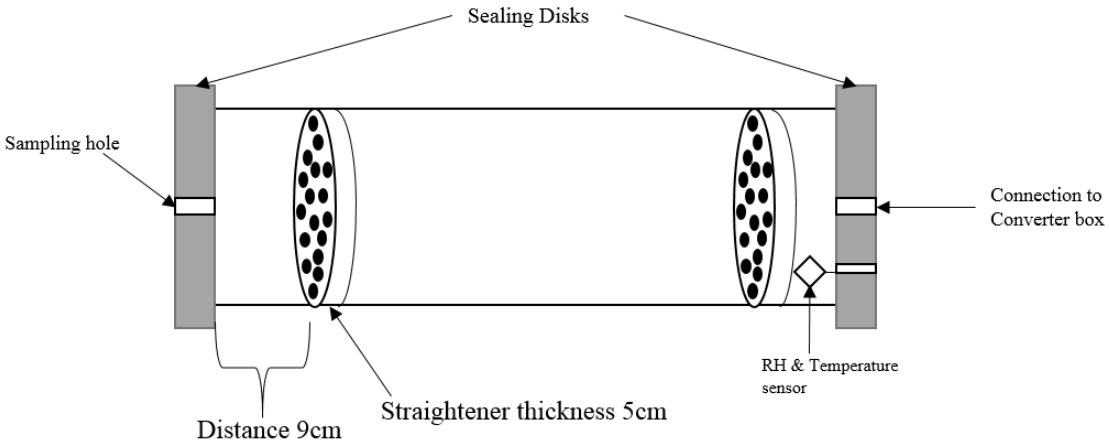

Figure 2.9. Flow straightener arrangement within quartz reactor.

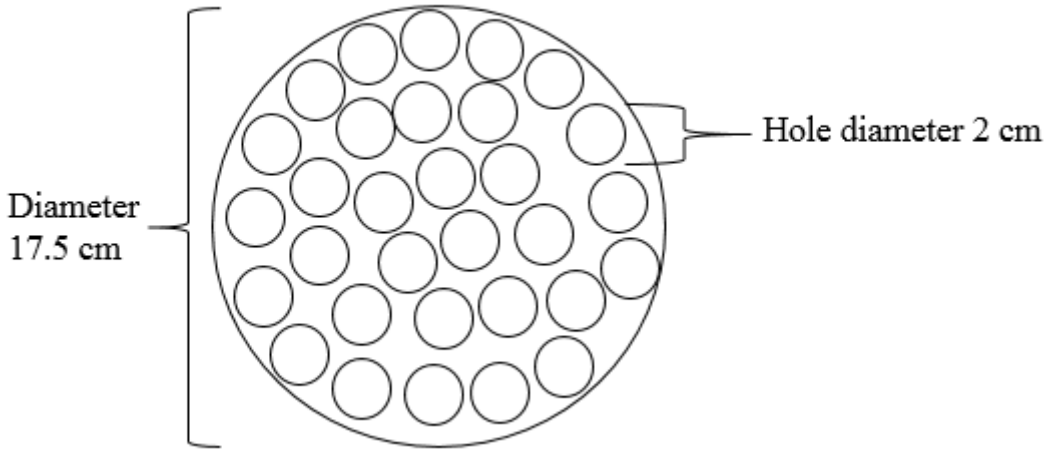

Figure 2.10. Flow straightener structure in detail (For demonstration only, holes are regularly distributed in actual disk).

Both straighteners are identical; they are made from PTFE material. PTFE is preferred for its chemical resistance properties, and in particular is inert with respect to reaction with O_3. The straightener comprises a disk with 37 holes bored through as closely placed as possible.

This disk has an overall thickness of 5 cm and a diameter of 17.5 cm. After subtracting the area of the holes, the straightener has a surface area of 124 cm^2. This porous (on a large scale) structure allows air to pass through easily, whilst being guided into a substantially laminar flow pattern in the sampling reactors.

2.3.5 Sealing disk

Each reactor's end was sealed with two identical PTFE disks to build a closed volume.

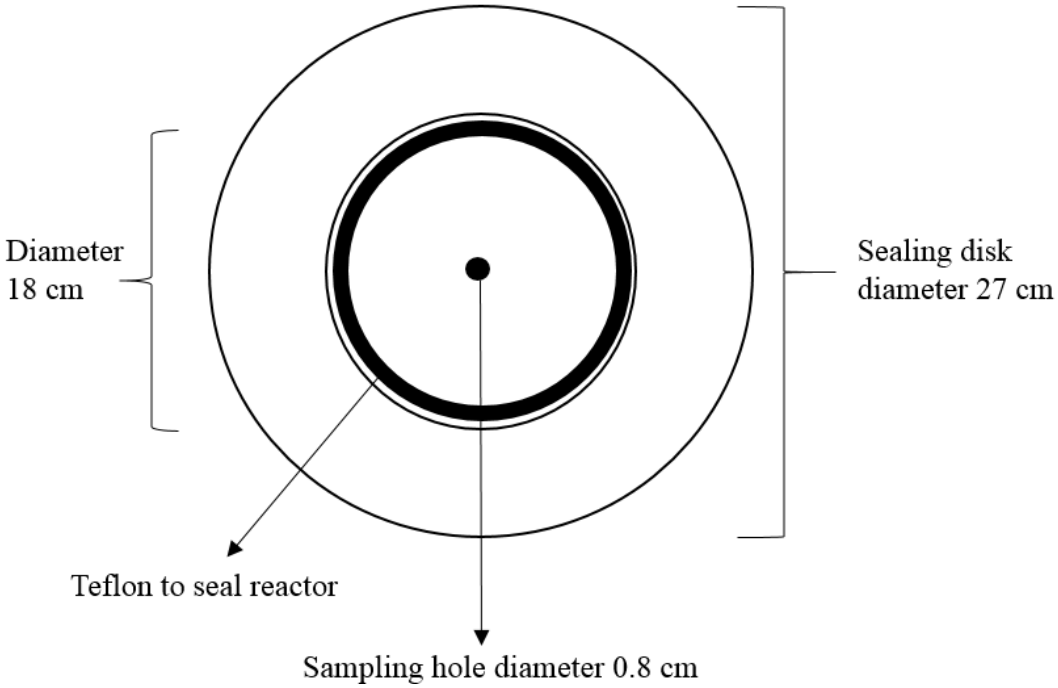

Figure 2.11. Sealing disk's structure and dimensions.

In the middle of both sealing disks, a 0.8 cm diameter inlet was formed to accommodate an appropriate Swagelok fitting for 6 mm inlet line tubing. Ambient air was drawn through the sampling hole in the centre of the sealing disk. The air flow reached the opposite end of the reactor, and then flowed into the conversion unit through 6 mm OD PTFE tubing.

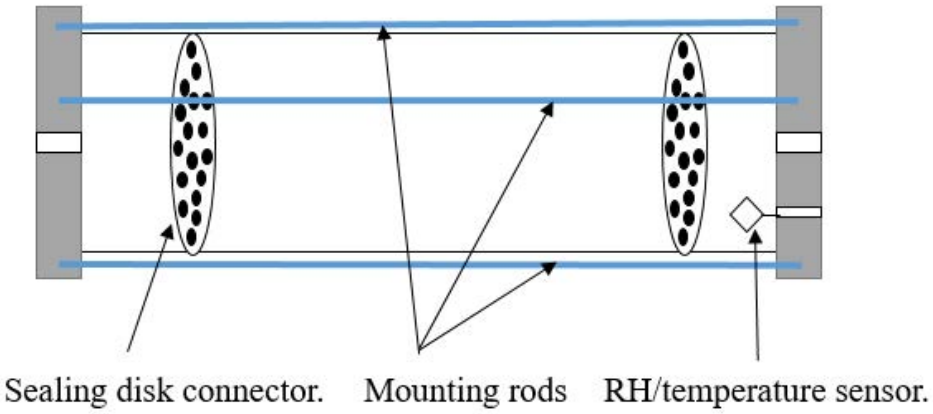

Figure 2.12. Sealing disks and their mounting rods.

Each pair of sealing disks were held in place on the reactor with three stainless steel rods under compression to enhance sealing stability and durability. Both ends of rods are screwed tightly into premade screw sockets on the sealing disk.

An additional aperture on the outlet side sealing disk was made to allow relative humidity (RH) and temperature sensor probes to be introduced, and perform continuous measurement in the ambient air inside each reactor. The probes were positioned inside the reactor, beside the outlet side sealing disk to avoid adding air turbulence to the ambient air flow at the sampling side.

2.3.6 Reactor mounting frame

The dual sampling reactors were mounted on an aluminium frame, of dimensions 64 cm × 24 cm × 55 cm, a cuboid shaped frame which can be securely placed on flat surface (*e.g.* roof of the sampling stations; see Chapters 4 and 6) using straps, and (through cushioning) securely holding and providing some protection for the fragile sampling reactors.

2.3.7 Flow rate in the reactors

Ambient air was continuously drawn through the reactors, regulated by a combination of regulated suction forces from the ozone monitor, and additional air withdrawal controlled by mass flow controllers (MFCs) ahead of external pumps. Each MFC was set to 1.4 standard litres per minute (SLM) flow rate, while the ozone monitor has a 1.4 SLM total intake, which adds 0.7 SLM flow intake to each of the sample and reference reactor flows. Therefore, the ambient air flows into each reactor at a total rate of 2.1 SLM. The ideal plug flow indicates an estimated reactor residence time of 486 seconds (using reactor volume divided by flow rate: 17 L / 2.1 SLM), but actual residence time is extensively discussed in section 3.1 and 3.2.

2.3.8 MFCs

A Mass Flow Controller (MFC) is a device used to measure and regulate gas and fluid flows. It is often used when accurate measurement and control of a mass flow of gas is required independent of pressure changes and temperature changes, in a given flow range.

The MFCs in the OPR system are Brooks model 5850S, and operated using the pressure difference between the ambient air and the (external) pumps. During field deployments, model 5850S MFCs were connected to the sample and reference reactor outlets as shown below,

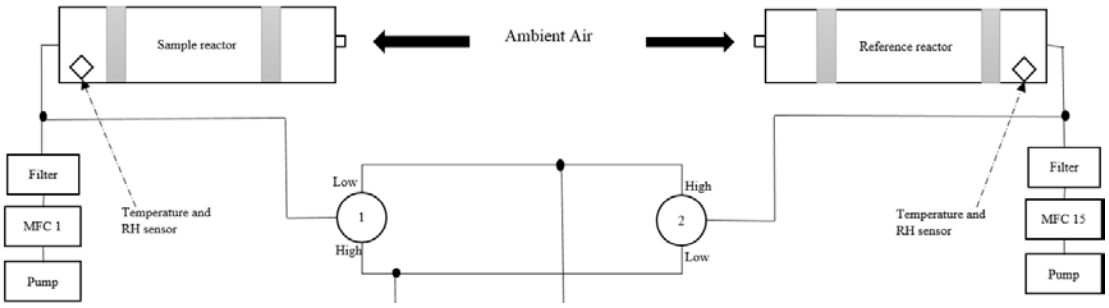

Figure 2.13. MFC flow control schematic.

Each reactor employs one MFC to regulate the air flow rate, alongside the ozone monitor withdrawal through the conversion unit. The MFCs were connected to the IGI interface unit allowing operator control via computer.

2.4 Photolytic NO_2 Conversion Unit

The conversion unit comprises a large aluminium housing (to shield the harmful UV radiation from LED converter lamps), with a pair of extraction fans installed on the cover lid to draw hot air from inside, powered through with a 12 V DC power supply. The conversion unit also has four openings which accommodate the UV lamps (which have built-in cooling fans, to blow air into the conversion unit housing).

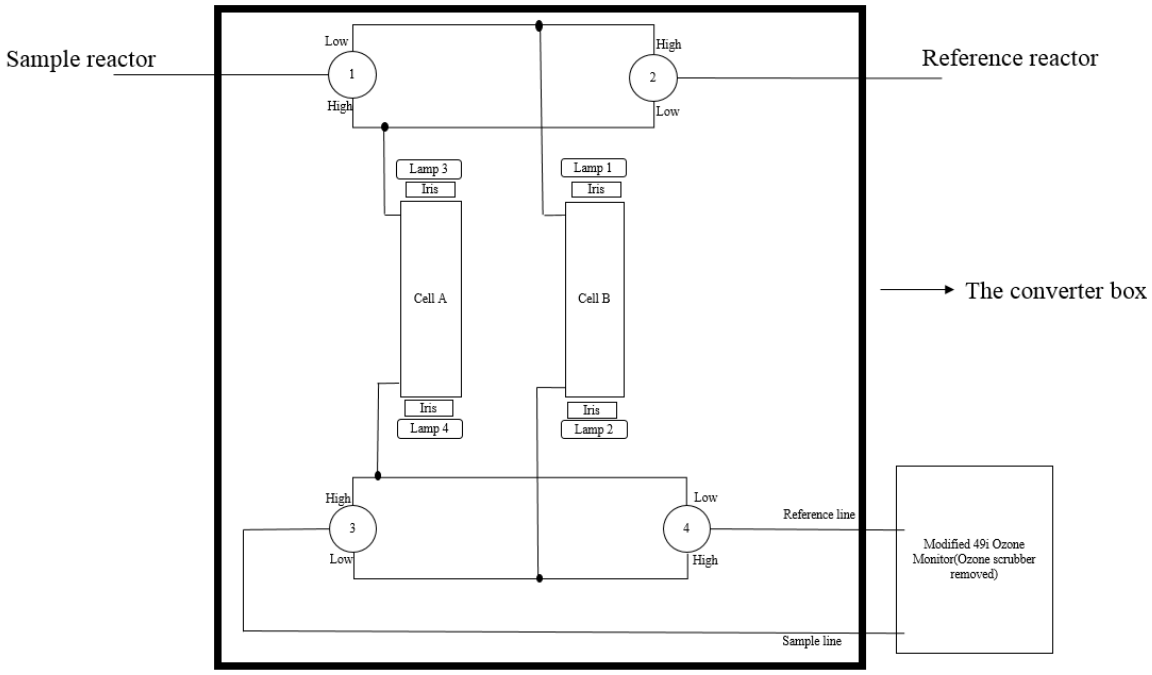

Figure 2.14. Conversion unit schematic - heavy line indicates components located within the conversion unit housing.

2.4.1 Converter Cells

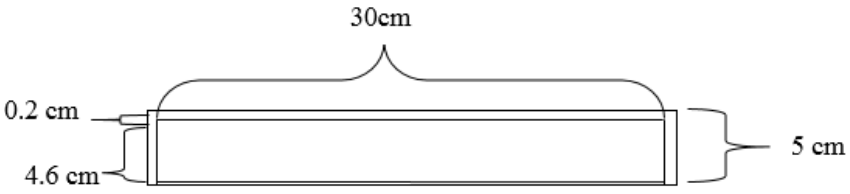

Figure 2.15. Converter cell dimensions.

In the conversion unit, a pair of identical converter cells are mounted on the bottom of the housing surface. As shown in Figure 2.15, each converter cell comprises a quartz tube with 4.6 cm inner diameter, 5 cm OD and 30 cm in length. The converter cells are made of quartz to minimise ozone loss and maximise UV radiation transmission, each cell is sealed with a quartz window which is attached by Torrseal adhesive. Both converter cells were wrapped externally with tin foil to increase the UV radiation intensity internally through reflection.

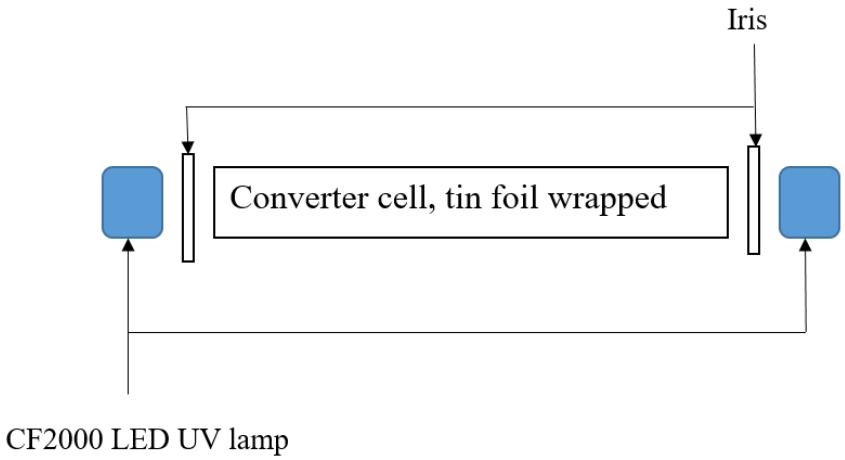

Figure 2.16. Quartz converter cell, iris and a pair of CF2000 LED UV lamps.

Two LED UV lamps (Clearstone technology, CF2000 Rev 3.0) are mounted securely at each end of the converter cells. As discussed in section 2.3.1, NO_2 photolysis is initialized by UV radiation (starting from wavelength 422 nm (Φ_{NO2} = 0.01) to 398 nm and below (Φ_{NO2} = 1) (Figure 2.5). The lamp output was measured using an Ocean Optics USB4000 fibre

spectrometer, located approximately 2 cm in front of each LED UV lamp to measure the emission spectrum.

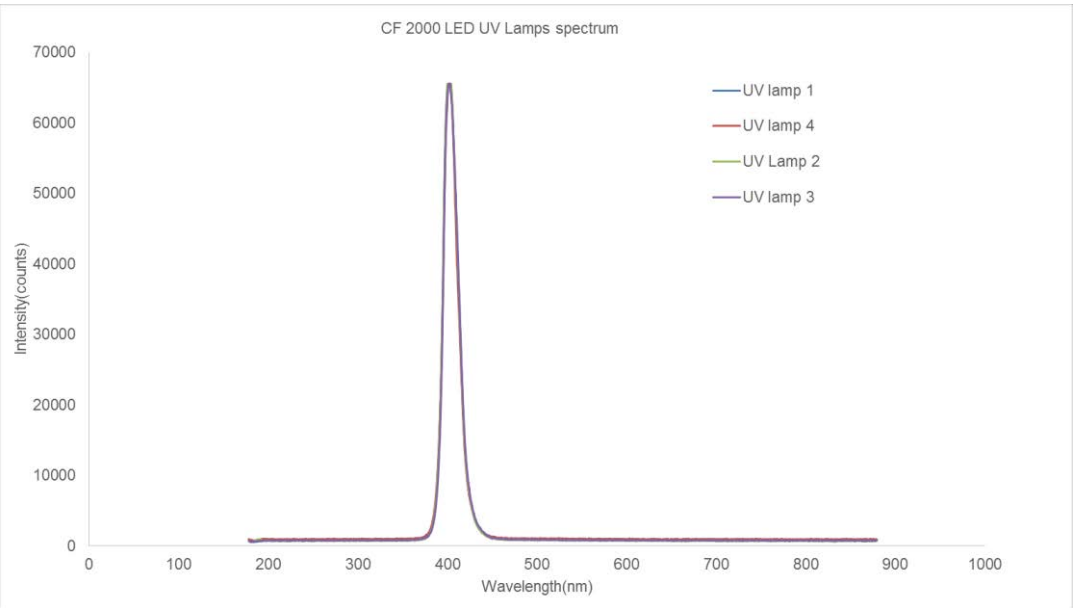

Figure 2.17. Spectrum of CF 2000 UV lamps 1, 2, 3 and 4, measured light intensity as a function of wavelength.

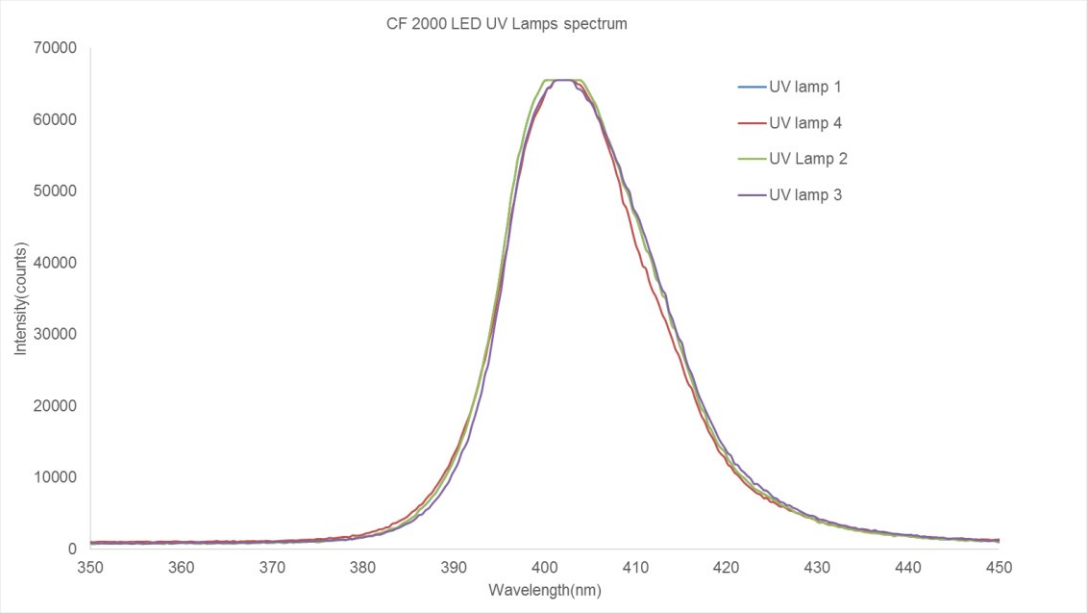

Figure 2.18. Spectrum of CF 2000 UV lamps 1, 2, 3 and 4 from 350 to 450 nm wavelength, measured light intensity as a function of wavelength.

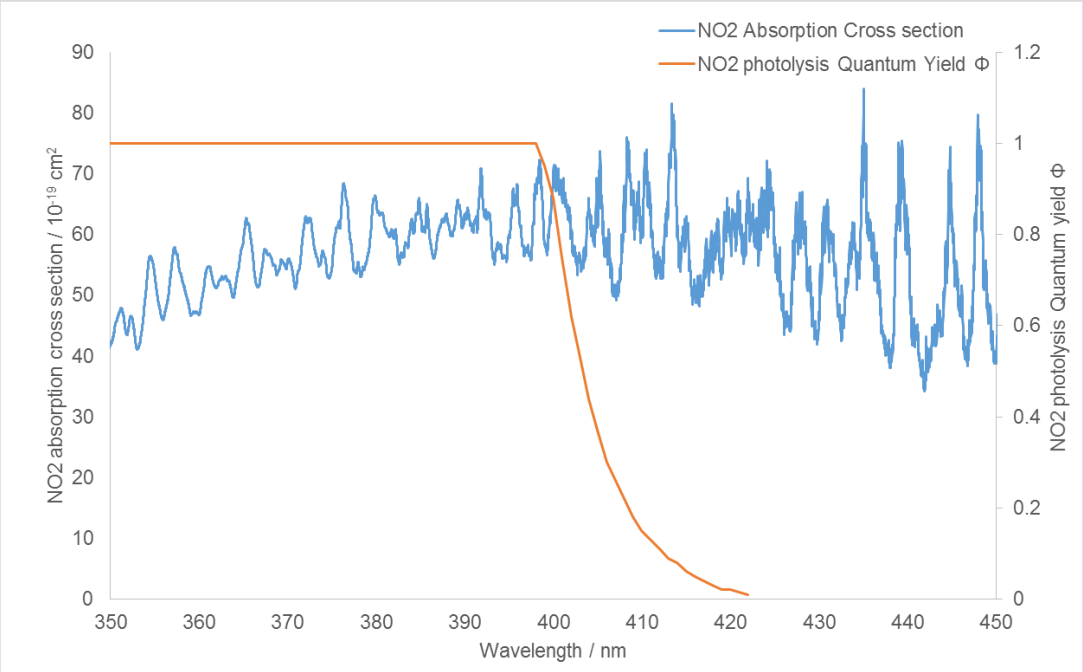

Figure 2.19. Primary axis (left) is the NO_2 absorption cross section as a function of wavelength at 298K; Secondary axis (right) is the NO_2 photolysis quantum yield (Φ_{NO2}) as a function of wavelength at 298K. Wavelength is between 350 nm and 450 nm (Sander *et al.*, 2011).

All four lamps' peak output of light intensity are at approximately 402 nm wavelength, as they are described in Figure 2.18. In contrast with Figure 2.19, the peak output of light intensity (402 nm) corresponds to an NO_2 photolysis quantum yield of 0.62 (at 298K) and an NO_2 absorption cross section at 57 10^{-19} cm^2. This result indicates the lamps have a good (but not ideal) overlap with the NO_2 cross section and photolysis quantum yield, and so can be expected to deliver a reasonable NO_2 photolysis rate. The NO_2 photolysis frequency obtained and corresponding NO_2 to O_3 conversion efficiency in the converter cell are discussed further in section 3.6.

An iris was installed between each UV lamp and converter cell end window (Figure 2.16), located 0.3 cm from the UV lamp and 1.5 cm from converter cell window. The iris' (maximum) aperture ID was 5 cm. They were used to regulate the amount of incoming UV radiation to converter cells, allowing the UV radiation intensity in each cell to be adjusted,

potentially balancing the slight differences in lamp output intensity. However, in practice each iris was used at maximum aperture during the two field deployments, for maximum UV irradiation of the converter cells.

2.4.2 Solenoid Valves

Four three-way solenoid valves were built into the base of the conversion unit to regulate the switching between sample and reference flows through each photolysis cell (Figure 2.20 and 2.21). The valve switching system in each conversion unit was connected through 6 mm outside diameter PTFE tubing. The valve switching system periodically switches valve settings, typically every 5 or 10 minutes, to average out any variation in conversion efficiency between two converter cells.

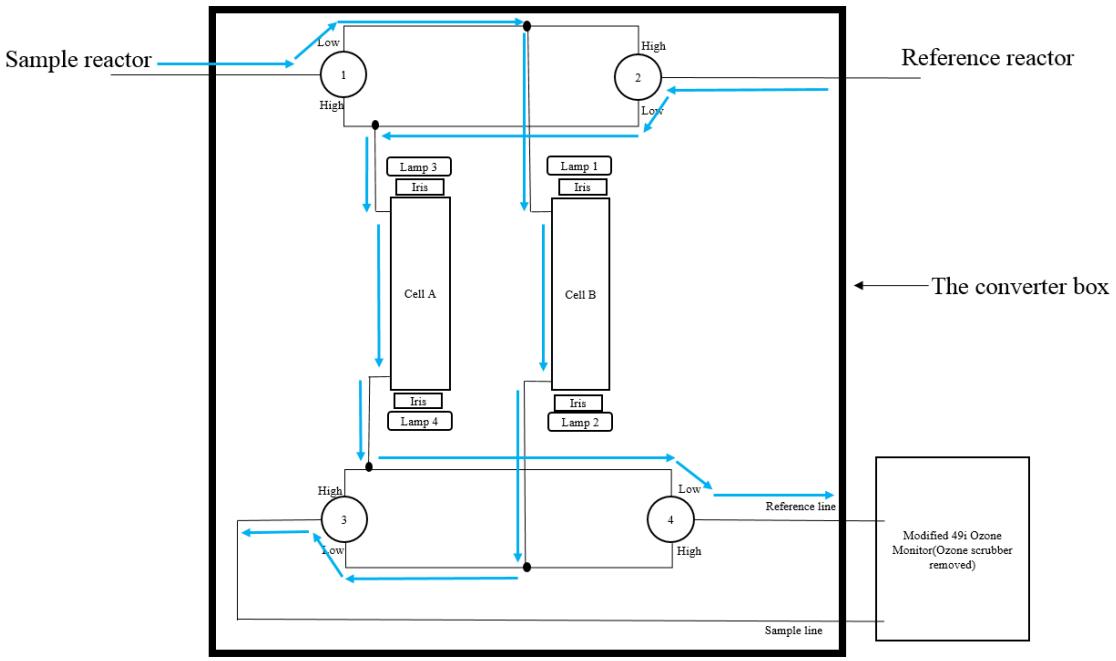

Figure 2.20. Solenoid valves showing flow pathways with all valves set to “low”: Corresponding to the sample reactor connected to conversion cell B, and the reference reactor connected to conversion cell A.

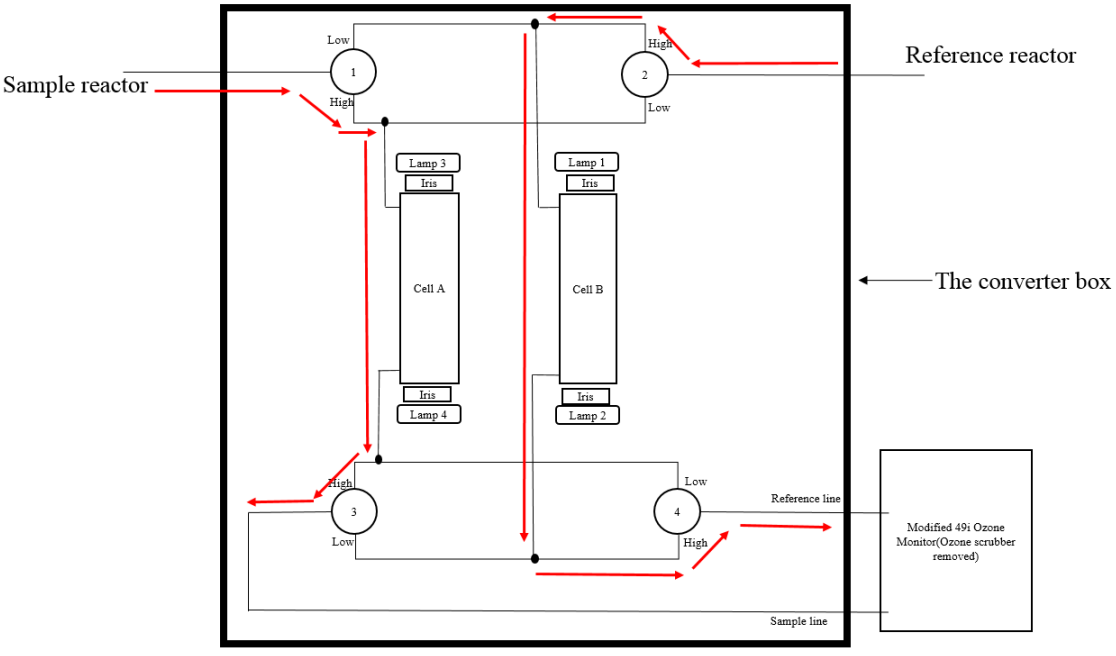

Figure 2.21. Solenoid valves showing flow pathways with all valves set to “high”: Corresponding to the sample reactor connected to conversion cell A, and the reference reactor connected to conversion cell B.

As Figure 2.20 illustrates, Valve 1 is connected to sample reactor, Valve 2 is connected to reference reactor, Valve 3 is connected to sample gas stream line of 49i ozone monitor, and Valve 4 is connected to reference gas stream line of 49i ozone monitor (after ozone monitor modification, see section 2.6). Connections were made with 6 mm OD PTFE tubing and unions to minimise ozone loss. The solenoid valves have two settings, either high or low, and the valves were connected such that all valves need to be set at the same setting during OPR operation. In Figure 2.21, when all valves were set to "high", the sample reactor flow entered converter cell A, and then entered the sample gas stream line of the ozone monitor, while the reference reactor flow entered converter cell B, and then entered the reference gas line of the ozone monitor. When all valves are set to low (as Figure 2.20 shows), the situation is reversed. Air from the sample reactor flows into converter cell B before entering the sample gas stream line of the ozone monitor, while flow from the reference reactor flows into converter cell A, and then to the reference gas stream line of the ozone monitor.

2.5 IGI Interface Unit and OPR core unit

2.5.1 OPR core unit

During the London and Indian field deployments, the core OPR system components were installed on a multi-layered aluminium frame, sized 60cm x 90cm x 105cm. It is the "core unit" of the OPR system, its structure is described in the following Figure 2.22:

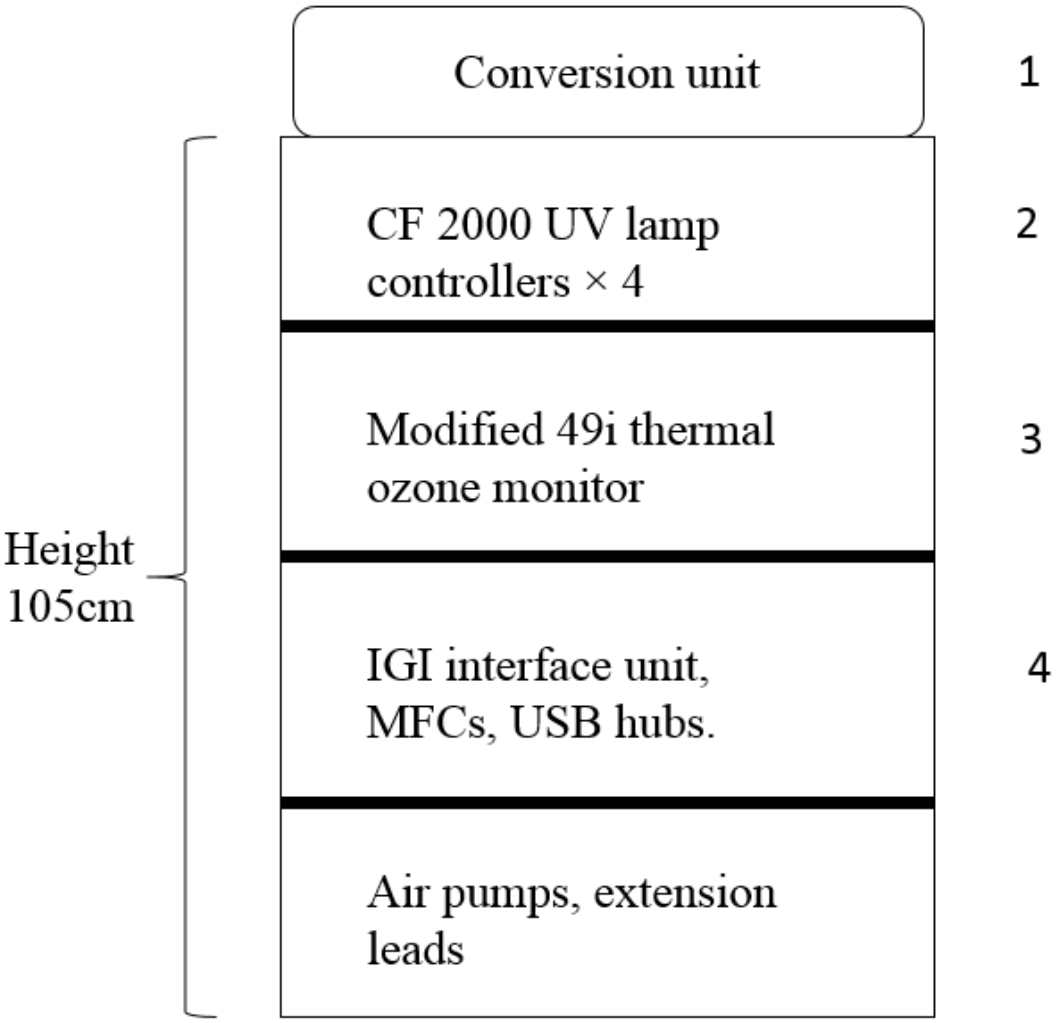

Figure 2.22. OPR core unit (built in an aluminium frame) and its components.

The aluminium frame consists of four layers, the conversion unit was placed on top of the first layer (1) (for ease of access and maximum cooling), which was on top of the main frame.

The PTFE tubes from the two sampling reactors, located in the ambient air, were connected into the conversion unit. The four CF 2000 UV lamp controllers were placed on the second layer (2) of the frame. The modified 49i thermo ozone monitor was placed in the third layer (3); it is connected to the IGI interface unit with data cables. In the fourth layer (4), the MFCs, USB hubs and IGI interface unit were located, while the final layer housed power cabling, and the two reactor air pumps. The core unit was always deployed indoors during the field deployments described in this thesis; only the dual sampling reactors were placed outdoors under sunlight for ambient air sampling.

2.5.2 IGI Interface unit

The IGI interface unit is the essential component of the OPR system, providing the interface between the Thermo 49i ozone monitor, solenoid valves, mass flow controllers and temperature / RH probes, and the control computer (laptop) via USB 2.0 connection, allowing the laptop to fully control the OPR system operation and log data.

The IGI programme has two main functions - flow control and data acquisition of the OPR system. First of all is the MFC and valve control, IGI programme allows user to manually adjust and control MFCs flow rates, with additional on-screen display of the flow rates setting and measured flow rates. Valve switching is also included in the controlling option. The automated sequences of MFC and valve switching settings are programmable via the software functions, to run the OPR system continuously through (*e.g.* 10 minutes periodical flow switching between the NO_2 converter cells). The second essential function is displaying and recording data from the system - ozone monitor and RH/temperature sensing probes. In both cases, these are displayed in real time, and logged to file alongside all system

parameters. Data are logged every 4 to 6 seconds during OPR deployment period in ASCII file format for subsequent analysis.

2.6 Thermo 49i Ozone Monitor

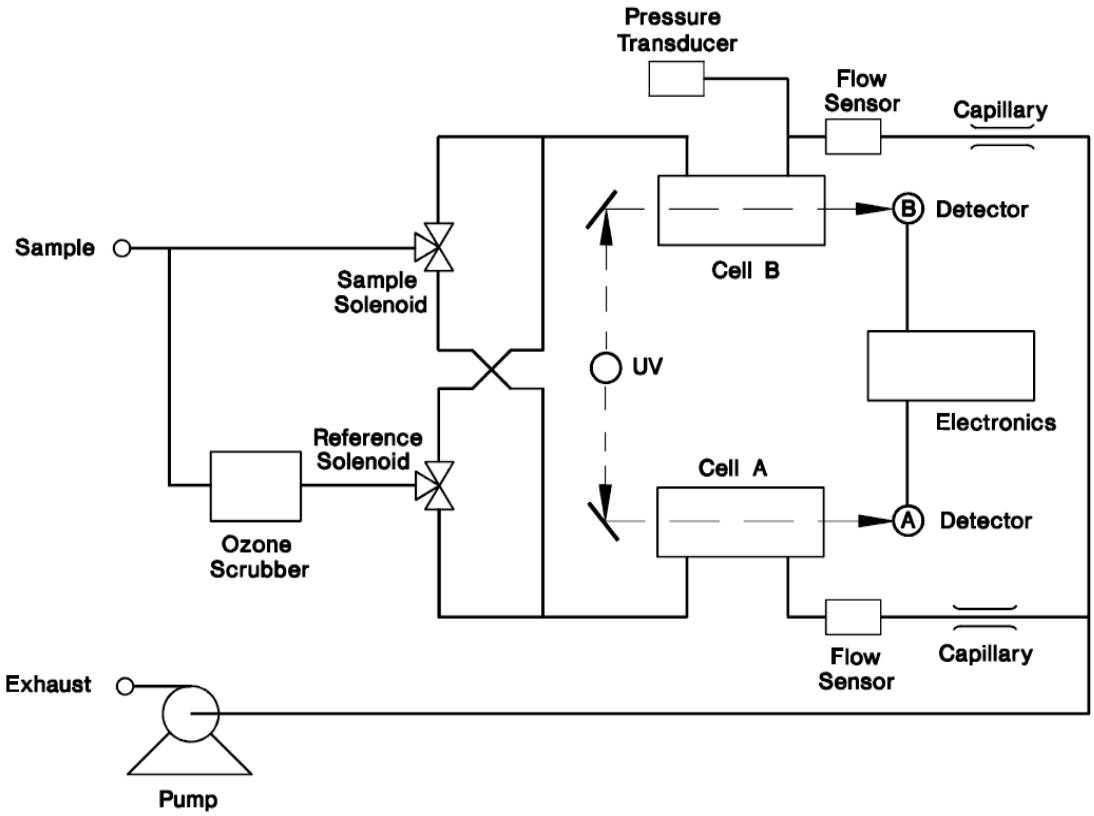

Figure 2.23. Model 49i flow schematic. (Thermo Electron Corporation, 2004)

The 49i ozone monitor is based on the principle that ozone molecules absorb UV light at a wavelength of 254nm. The degree to which UV light is absorbed is directly related to the ozone concentration as described by the Beer-Lambert Law:

$I/I_0=e^{-KLC}$

Where:

K = molecular absorption coefficient, 308 cm^{-1} (at 0 °C and 1 atmosphere pressure)

L = length of cell, 38cm

C = ozone concentration

I = UV light intensity of sample with ozone (sample gas)

I_0 = UV light intensity of sample without ozone (reference gas)

The sample air is drawn into the 49i monitor SAMPLE bulkhead and is split into two gas streams, as shown in Figure 2.23. In the standard manufacture monitor configuration, one gas stream flows through an ozone scrubber to become the reference gas (I_0), the reference gas then flows to the reference solenoid valve. The sample gas (I) flows directly to the sample solenoid valve. The solenoid valves alternate the reference and sample gas streams between cells A and B every 10 seconds. When cell A contains reference, cell B contains sample gas and vice versa.

The UV light intensities of each cell are measured by detectors A and B. When the solenoid valves switch the reference and sample gas streams to opposite cells, the light intensities are disregarded for several seconds to allow the cells to be flushed. The model 49i calculates the ozone level for each cell and outputs the average level to both the front panel display and the analogue outputs.

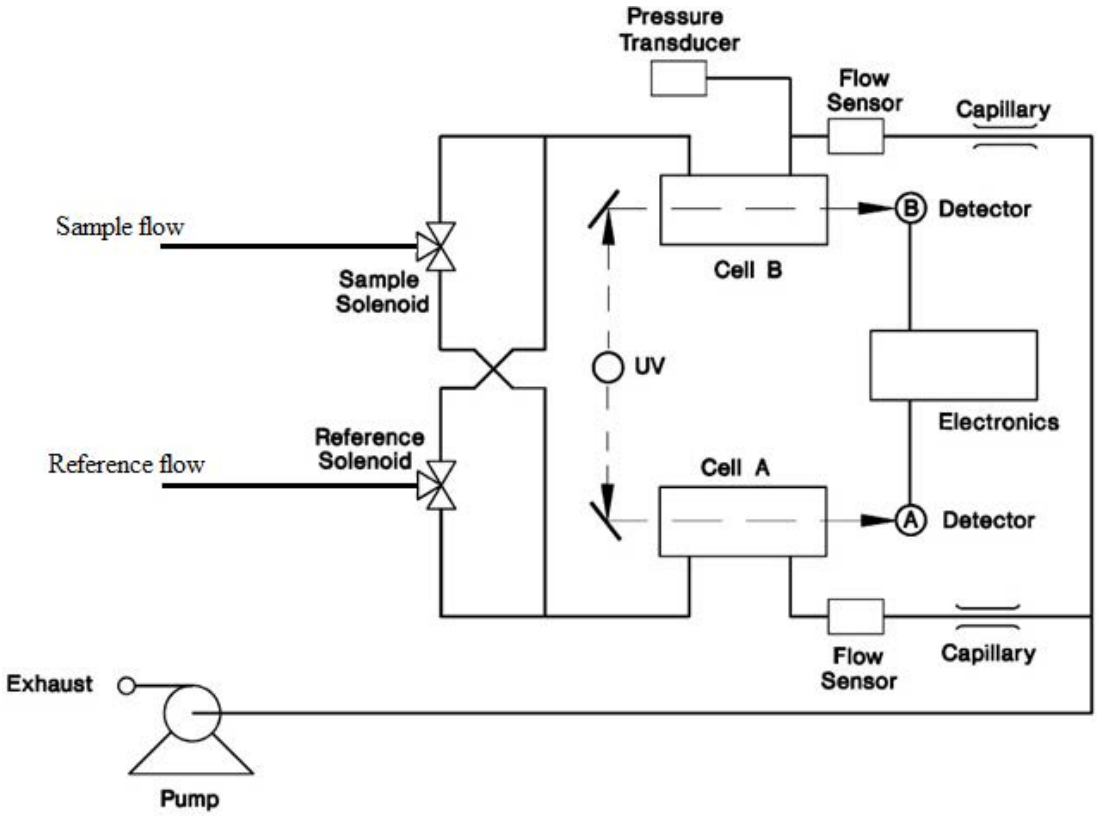

Figure 2.24. Modified Model 49i flow schematic in OPR system, Ozone scrubber removed.

During the OPR deployment, the SAMPLE bulkhead and the ozone scrubber were removed. The single sampling inlet of 49i ozone monitor was replaced with two lines, the sample gas stream line and reference gas stream line. The sample gas stream tube was connected to the sample reactor flow via 6 mm OD PTFE tubing and connections. The reference gas stream had identical setup to the sample gas stream but was connected to the reference reactor flow. The ozone scrubber at the reference gas stream tube was removed to allow flow from the reference reactor to enter the 49i monitor as a reference gas. As a result, instead of measuring the absolute ambient ozone level, the modified 49i ozone monitor measures the difference in ozone level between the two flows (gas streams), which is referred as "ΔO_x".

2.7 OPR system configuration during the field deployments

Two field deployments were performed during the development of the OPR system described in this thesis. The first field deployment was accomplished in London (July to August), as part of the ClearfLo (Clean Air for London) 2012 summer IOP (Intensive Observation Period) – see Chapter 4. The primary objective of the London deployment was to test the practicability and stability of the OPR system. Many gaseous species of potential relevance to ozone chemistry were measured during the summer IOP by other UK HEIs; these data were used to interpret the OPR measurements as discussed in Chapter 4. ClearfLo provided a good opportunity to test the practicability of the OPR approach, by comparisons between indirect oxidant production rate measurement and direct oxidant production rate measurement based on ozone chemistry-related gaseous species data.

The second OPR field deployment was performed in India (April to May 2013) - see Chapter 6. The main objective of this deployment was to obtain proof-of-concept data for the application of the OPR approach to assess the contribution of local emissions processing to overall ozone formation in an under-explored air pollution climatology. The Indian weather characteristics and pollution were significantly different from those encountered in the UK, was and provided an important opportunity to test the OPR system's performance under different and challenging environmental conditions. The Indian deployment covered two measurement sites: Delhi and Mohali. Full details of the Indian deployment are given in Chapter 6.

2.7.1 London OPR deployment

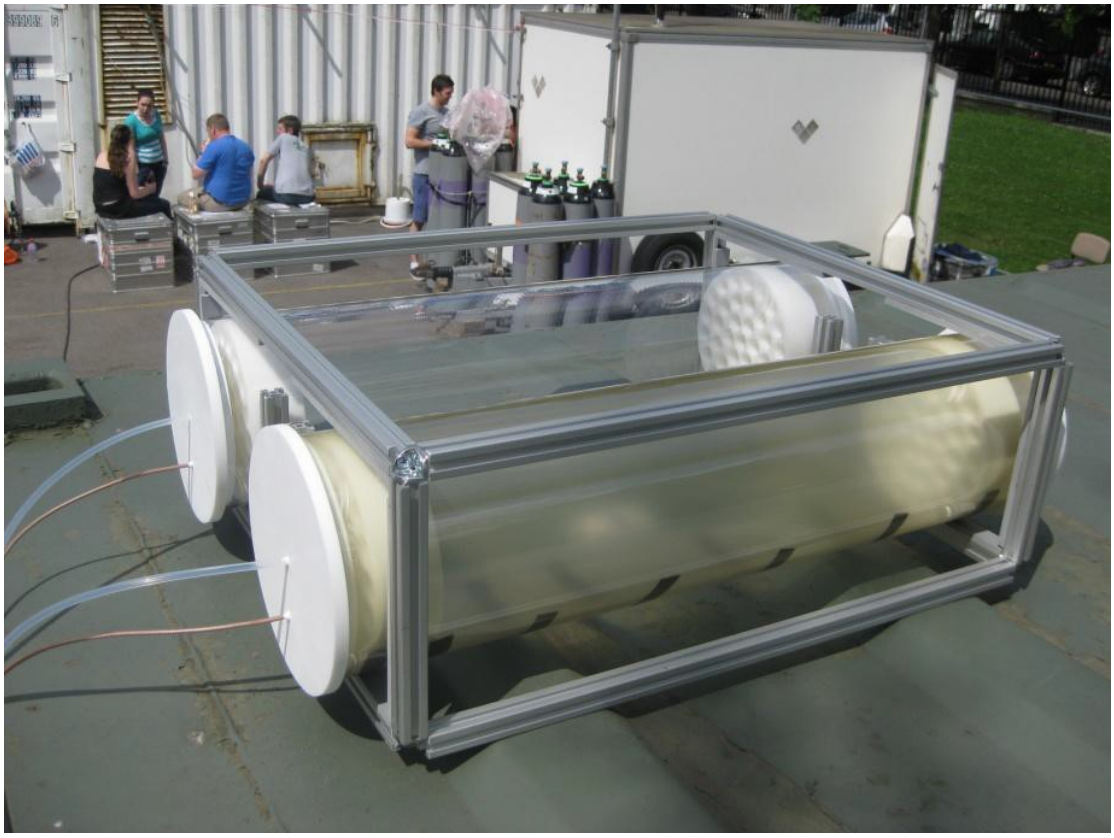

Figure 2.25. The dual reactors and mounting frame on top of the container roof, North Kensington sampling site, London 2012.

From 25 July 2012 to 19 August 2012, the OPR system was deployed at the North Kensington monitoring site, as a component of the ClearfLo summer IOP in London. The OPR core unit was installed inside of the "Birmingham" portacabin; the dual sampling reactors (Figure 2.25) were positioned on top of the cabin, with PTFE tubes connected to the core unit. (Figure 2.2)

Ambient NO_x, O_3, outdoor RH & temperature, reactor's internal RH & temperature, light intensity, and OPR data were measured by as part of the OPR deployment during the London project, alongside very many further atmospheric components measured by other groups.

Automatic valve switching (to balance conversion efficiency in two converter cells) was set to every 5 minutes in the conversion unit, giving a 10-minute overall instrument duty cycle.

Full details of the London campaign, data measurement and results are given in Chapter 4: London OPR deployment in 2012.

2.7.2 India OPR deployment

Figure 2.26. OPR deployment at TERI University measuring site, Delhi, April 2013.

Figure 2.27. OPR deployment at Mohali measuring site, Mohali, May 2013.

From 26th April 2013 to 06th April 2013, the OPR system was deployed at TERI University, south of Delhi, India. The OPR sampling reactor was located on top of a 5-story administration building. (Figure 2.26)

From 07th May 2013 to 16th May 2013, the OPR system was deployed at Mohali, near Chandigarh in the north of India. In this case the OPR sampling reactors were located on top of the 3 story central analytical facility building (Figure 2.27).

2.8 Ancillary measurements

A small HOBO monitor (model number is U-12-011) was normally placed beside the dual reactors to record the ambient RH, temperature and light intensity as an ambient environment sensor. It continuously records the data every 60 seconds. Data is periodically downloaded via a USB disk during the two field deployments of the OPR system. The principal use for the HOBO monitor was to record any shading (due to trees, frame, sampling towers and other sheltering objectives) of the OPR reactors, at the precise measurement site - photochemical data analysis was conducted using higher quality irradiance measurements *e.g.* spectral radiometers, as described in chapter 4.

2.9 Summary of the Experimental methodology and instrument properties

This chapter has introduced the principle of the OPR measurement, and described the core components of the OPR system, including sampling reactors, NO_2 to O_3 conversion unit and modified 49i ozone monitor. The following chapter (3: System Characterisation) describes each component's performance and characterisation, which determines the overall OPR system performance.

Chapter 3: System Characterisation

This chapter describes each major component of the OPR system, and presents the results of characterisation experiments performed to assess the instrument performance, and in order to gain an insight into the potential uncertainties and correction factors applicable to the measured ozone production rate $p(O_x)$. Six principal characterisation tests were performed to measure key factors which influence the ultimate oxidant production rate derived. These tests included:

-Reactor gas residence time determination.

-Conversion unit gas residence time determination.

-Tests for wall losses of NO_x and O_3 in reactors.

-Mass Flow Controller (MFC) calibration tests.

-NO_2 conversion efficiency measurement in conversion unit.

-Calibration of the Thermo 49i ozone monitor.

The final part of this chapter integrates the outcomes of these tests to summarise the performance and limitations of the OPR system as deployed in the field measurements presented in the following chapters.

3.1 Reactor Residence Time

As discussed in section 2.2.1, derivation of the ozone production rate $p(O_x)$ using the OPR system requires knowledge of the mean sample / reference reactor residence time; accurate measurement of the reactor residence time is critical to the determination of the chemical oxidant production rate, $p(O_x)$.

$p(O_x) = \Delta O_x / t_{\text{mean res reactor}}$

ΔO_x: The measured differential oxidant abundance between two reactors.

$t_{\text{mean res reactor}}$: Mean residence time of ambient air in each reactor (sample / reference reactor).

The simplest approach to estimate the residence time in a vessel is to compare the total volume to the total gas volumetric flow rate. For the OPR system, these values are 17021 cm^3 and 2100 cm^3/min, corresponding to a "plug flow" residence time of 486 seconds. However, in reality, the residence time of an air parcel in a "pipe" (the OPR sampling reactor is effectively a closed conduit) does not have a single value. The sampled air has a range or distribution of residence times, depending on the flow route taken through the reactor by individual air parcels, and hence the overall flow conditions.

In a closed pipe-like environment (*e.g.* the sampling reactors), residence time distributions may be measured by introducing a non-reactive tracer into the system at the inlet. The tracer flow through the reactor changes the tracer concentration and the response is found by measuring the concentration of the tracer at the outlet. The tracer needs to be stable and unreactive to the environment. Although a minor proportion of introduced ozone reacts with the wall (inner surface) of the reactors (discussed in Section 3.4), for reasons of convenience, ozone was used as a suitable tracer to determine the mean residence time of the reactors.

Estimating the residence time distribution requires measurement of the time elapsed since the ozone input started (or changed) and the output ozone level after exiting reactor. Overall, there are two ways to test a fluid residence time distribution through a closed conduit vessel: the Pulse method and the Step (or decaying) method.

3.1.1 Pulse method of residence time determination

The principle of the pulse method is based on introducing a pulse of a tracer species into the sample vessel, and then monitoring the concentration of the tracer at the vessel outlet. During the pulse residence time test of the OPR reactors, ozone was released for 40 seconds (as a square-wave pulse) into the reactor, with a Thermo 49i ozone monitor (set up in its standard, absolute-measurement configuration) measuring the ozone level at the reactor outlet. In a discrete pulse approach, the pulse duration must be much shorter than the reactor residence time.

The typical tracer concentrations expected during the pulse method are shown in the following figures, for a simulated and idealised residence time distribution (in practise, the actual residence time of each reactor is much longer, see Section 3.2.2):

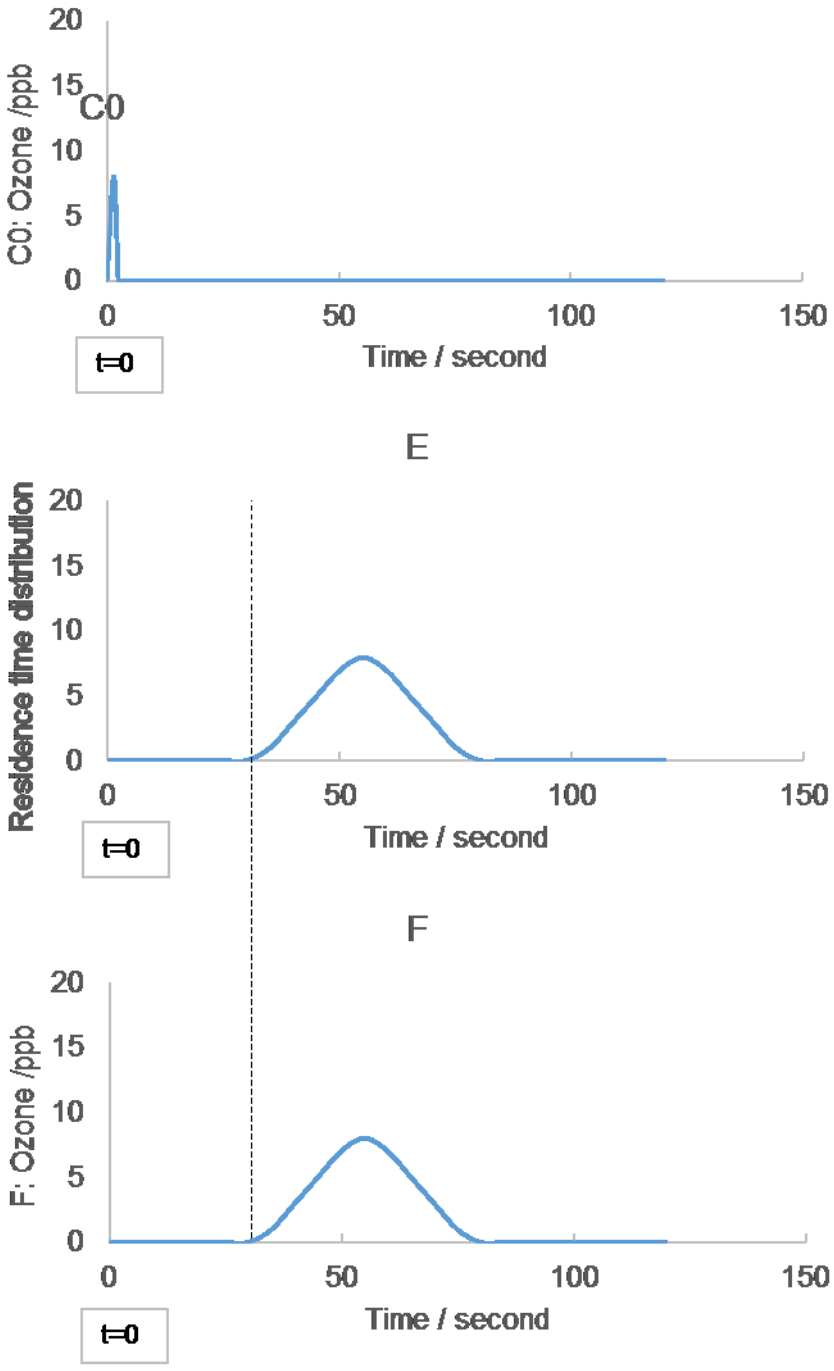

Figure 3.1: a) The simulated time variation of ozone level at cell inlet (as a conserved tracer), using the "pulse" approach; b) Idealised residence time distribution in cell, distribution function referred to as "E"; c) Simulated time variation of ozone level measured at the cell outlet, referred as "F". This figure is for demonstration only, it does not include actual data from tests.

If the pulse is infinitely short, Figures 3.1b and 3.1c will be the same: as the ozone pulse flows through reactor, output concentrations reflect the residence time distribution, given by the mean of both curves E (Figure 3.1b) and F (Figure 3.1c). In practice, the pulse is as short as possible, but is finite.

The residence time distribution as a function of time t is termed as E(t) in Figure 3.1b. Similarly, the outlet ozone concentration F as a function of time is termed as F(t). The residence time distribution E(t) of the cell is unknown, but F(t) is determined by ozone monitor.

To derive the mean residence time from the measured outlet concentrations as a function of time (*i.e.* from F(t)) the values of F must be normalised, and are then equal to the (normalised) values for E(t). Normalisation is achieved by dividing the value of E(t) and F(t) by the area under each curve E and F, given by the integral of E(t) and F(t), with respect to time. The mean residence time determination from the Pulse method is then presented as:

$$t_{\text{mean res pulse}} = \frac{\int E(t) \times t}{\int E(t)} = \frac{\int F(t) \times t}{\int F(t)} \tag{3.1}$$

In practice, the integration is performed at the time resolution of the ozone measurements (*e.g.* 5 seconds for sample reactor), and the mean residence time is determined via:

$$t_{\text{mean res pulse}} = \frac{\Sigma E(t) \times t}{\Sigma E(t)} = \frac{\Sigma F(t) \times t}{\Sigma F(t)} \tag{3.2}$$

3.1.2 Step method of residence time determination

The principle of the step method is based on introducing a continuous stable level of a tracer into the reaction vessel, and then stopping the input of the tracer, and tracking the concentration of the tracer at the vessel outlet until the tracer level reaches zero. Typically the input is shut off (rather than rising from zero to some level) as stopping a flow can be much more cleanly achieved than starting one. During the step approach to measuring the residence time test of reactor, ozone was introduced to the reactor for 20 – 30 minutes until a stable level was reached, then the ozone input was switched off (the Hg lamp forming O_3 was turned off), with the air flow remaining at the same flow rate through the reactor. An ozone monitor was used to measure the ozone level at the reactor outlet.

The typical / idealised tracer concentrations during the step method are shown below:

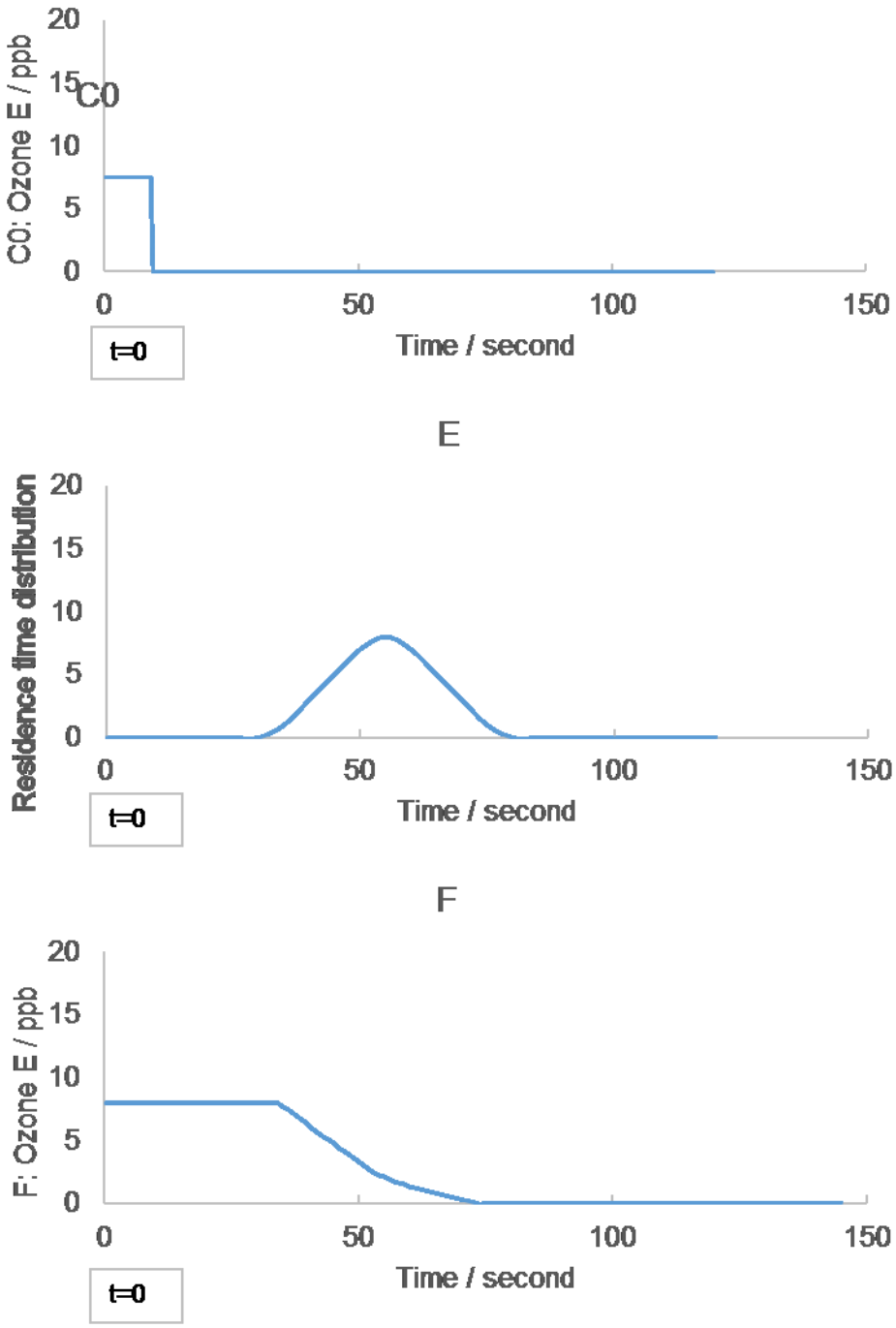

Figure 3.2: a) Time variation of ozone level at cell inlet (as a conserved tracer), using the "step" approach; b) Idealised residence time distribution in cell, distribution function referred to as "E"; c) Simulated time variation of ozone level measured at the cell outlet, ozone curve referred as "F". This figure is for demonstration only, it does not include actual data from tests.

When the ozone input is stopped, the tracer air parcels experience a range of residence times in the reactor, as shown in Figure 3.2b. E(t) is unknown, but the ozone levels at the outlet are measured as F(t). In the step method, E(t) is normalized by initial ozone concentration at time 0, which is termed as C_0. It is presented as,

$$E(t) = \frac{C(t+dt) - C(t+dt)}{C0} = \frac{Ct2 - Ct1}{C0} \quad (3.3)$$

dt is the time step between each measurement point.

t_1 and t_2 represent the first and second measured time points, or more generally, any two consecutive time points.

From the pulse method test, $t_{mean\ res}$ is derived as $\frac{\Sigma\ E(t) \times t}{\Sigma\ E(t)}$, when equation (3.2) is substituted in equation (3.3), the result is presented as,

$$t_{mean\ res\ step} = \frac{\sum t \times \frac{Ct2 - Ct1}{C0}}{\sum \frac{Ct2 - Ct1}{C0}} = \frac{\sum (\frac{t2+t1}{2}) \times (Ct2 - Ct1)}{\sum Ct2 - Ct1} \quad (3.4)$$

Rearranging equation (3.4), the mean residence time via the step method is then given by:

$$t_{mean\ res\ step} = \frac{\sum (\frac{t2+t1}{2}) \times (Ct2 - Ct1)}{\sum Ct2 - Ct1} \quad (3.5)$$

3.2 Results of reactor residence time measurements

Two slightly different variations of the pulse method were implemented to test the reactor residence time distribution, referred as the "*open pulse method*" and the "*closed pulse method*". For the open pulse method, the reactor inlet was not physically connected to the ozone tracer flow - the reactor inlet was left open (as in normal ambient measurements), with ozone in the surrounding ambient air being drawn into the reactor by the pumps (within the O_3 monitor, and bypass pump). For the closed pulse method, a closed system was used, ozone flowing into the reactors through a sealed manifold, with flow regulated by MFC, and no interface with the ambient air. The closed pulse method was more convenient and easier to set up experimentally, but concern remained that the flow conditions (through an inlet line) did not mimic the ambient sampling configuration, which could affect the residence time. A schematic of the open pulse method is shown in Figure 3.3, the closed pulse method was very similar but with the O_3 generator connected to an air cylinder, regulated by an MFC, and then directly connected to the reactor.

3.2.1 Open pulse method to determine residence time

The open pulse method was used to test the reactor residence time. This method most closely simulates the manner in which actual ambient air is sampled into the reactors during OPR field deployments. The residence time measurement schematic is shown in Figure 3.3.

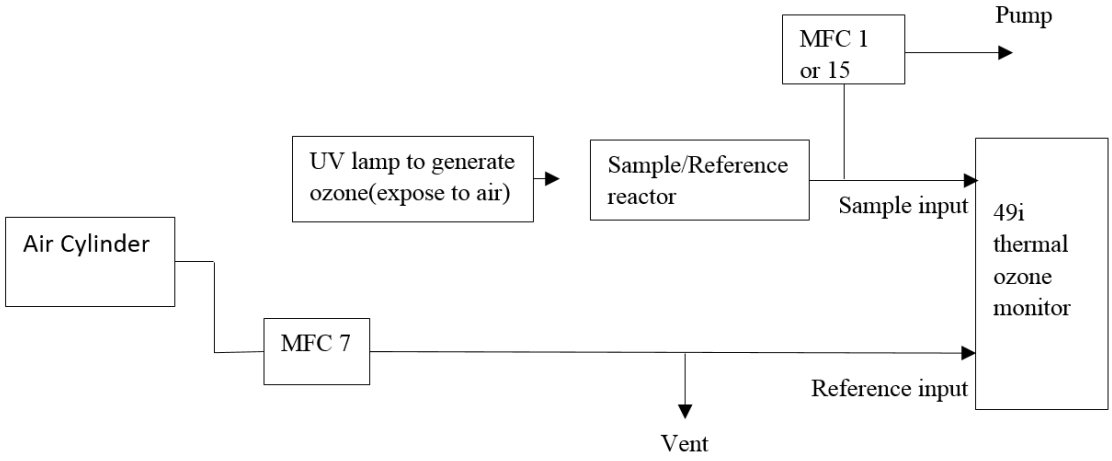

Figure 3.3. Reactor residence time test schematic with open pulse method.

The MFCs were set to draw air at same flow rate (2.1 SLM) as the total flow in OPR field deployments. Figure 3.4 shows typical outlet ozone mixing ratio - time traces from successive pulse experiments:

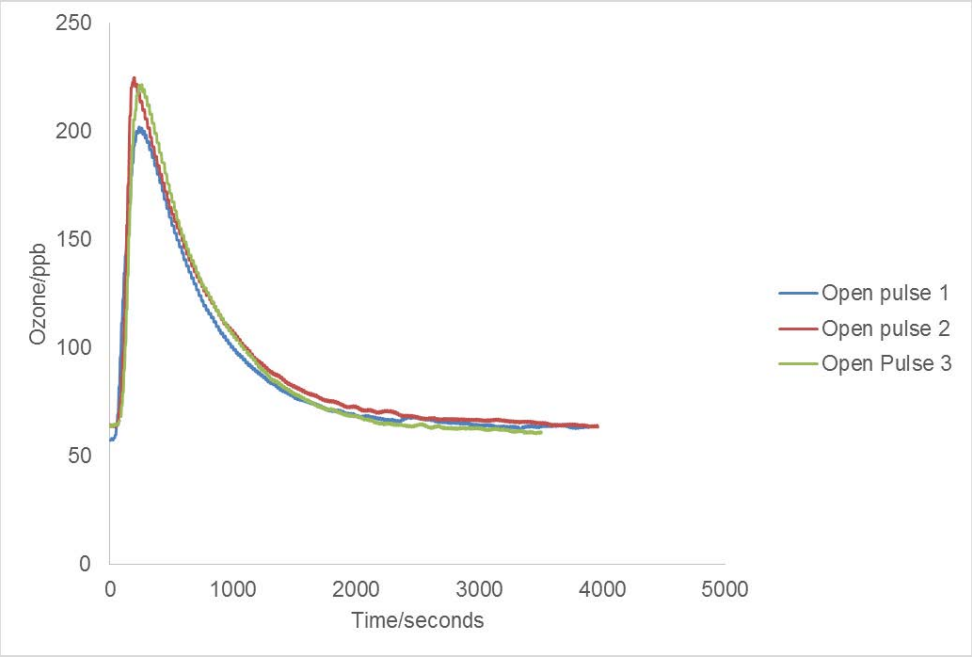

Figure 3.4. Time variation of ozone levels at outlet of reactor, for residence time tests using the pulse method.

Two identical sets of 3 pulses residence time tests were performed (total of 6 tests) with the open pulse method setting; 5 identical residence time tests were performed with the closed pulse method setting.

Open pulse method results indicated the mean residence time "$t_{mean\ res\ reactor}$" of reactor is 710 ± 133 (± 1 S.D.) seconds; the median reactor residence time determined was 701 ± 133 (± 1 S.D.) seconds.

Closed pulse method results indicated the mean residence time "$t_{mean\ res\ reactor}$" of reactor is 484 ± 63 (± 1 S.D.) seconds; the median reactor residence time determined was 484 ± 63 (± 1 S.D.) seconds.

3.2.2 Step method to determine residence time

In comparison, typical outlet ozone mixing ratio - time traces from successive step experiments are shown in following figure:

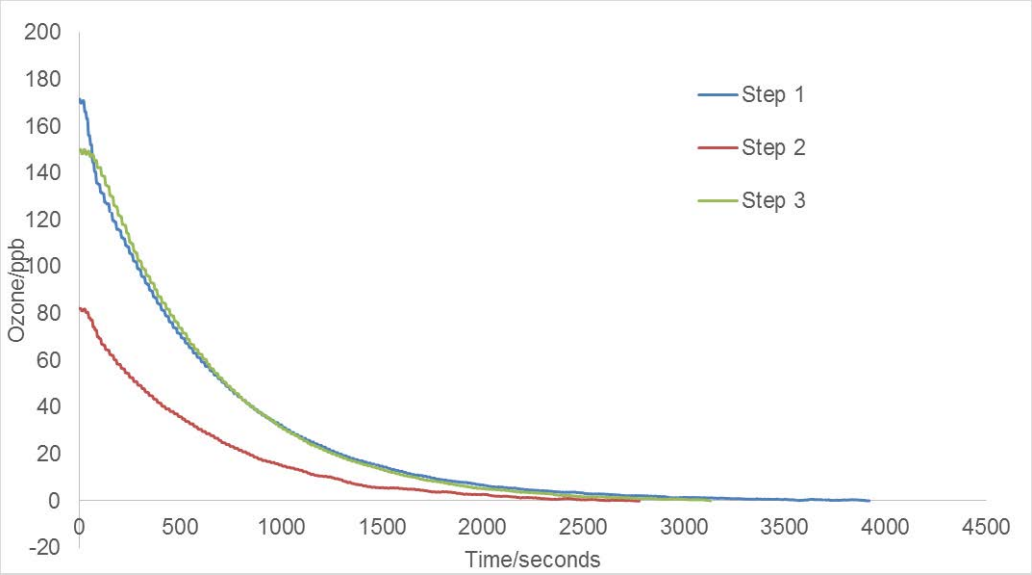

Figure 3.5. Time variation of ozone levels at outlet of reactor, for residence time tests using the step method.

Two identical sets of 3 pulses residence time tests were performed (total of 6 tests) with the step method setting. The step method experiment results indicated the mean residence time "$t_{mean\ res\ reactor}$" was 603 ± 33 (± 1 S.D.) seconds; the median reactor residence time determined was 593 ± 33 (± 1 S.D.) seconds.

The calculated residence time for plug flow indicates an estimated residence time of 486 seconds (using reactor volume divided by flow rate: 17 L / 2.1 SLM), but the flow within the reactor is complex and partially turbulent, rather than reflecting a simple plug of gas. The Reynolds number of reactor was 1.7 - suggested a highly laminar flow regime, but laminar flow takes some time (and distance) to establish in a conduit vessel (see Section 2.3.3), hence a mean residence time somewhat longer than the plug flow value is not unexpected.

The residence time determined by the step and closed pulse methods are shorter than that obtained with the open pulse method. Both step and closed pulse methods use an enclosed system with flows into the reactor regulated by MFC; in comparison, the open pulse method better replicates the field measurement conditions of an open inlet of free ambient air suction flow, with the sample flow drawn into the instrument by pumping from the reactor exit. For this reason, the results from the open pulse method were, *a priori*, preferred as most accurately representing the actual instrument deployment configuration, with differences between the methods ascribed to differing turbulence within the reactors as a consequence of the forced input flow.

To conclude, a total number of 17 residence time tests were performed to determine the mean residence time of reactor: 6 tests by open pulse method, 6 tests by step method and 5 tests by close pulse method.

The mean residence time "$t_{mean\ res\ reactor}$" of both reactors are 710 ± 133 (± 1 S.D.) seconds.

3.3 Results of conversion unit residence time measurements

The flow residence time in the NO_2 photolytic converter cells (built in the conversion unit) does not directly impact upon the oxidant production rate determination (unlike the reactor residence time), but is an important parameter both to understand the system behaviour, and in support of model simulations of the conversion efficiency variation with ambient NO_x and O_3 levels (section 5.2). Accordingly, residence time measurement experiments were performed for the converter cells.

3.3.1 Step and Pulse method setup on converter cells

The residence time tests for the converter cells were similar to the residence time tests for the sample and reference reactors. However, unlike the reactors with an open sampling inlet, the converter cells are built in a closed system in the conversion unit with a sealed inlet line; therefore, the closed pulse and closed step methods were used to evaluate the mean air residence time in converter cells, as these replicated the actual flow set-up. A schematic of residence time tests in converter cells are shown as:

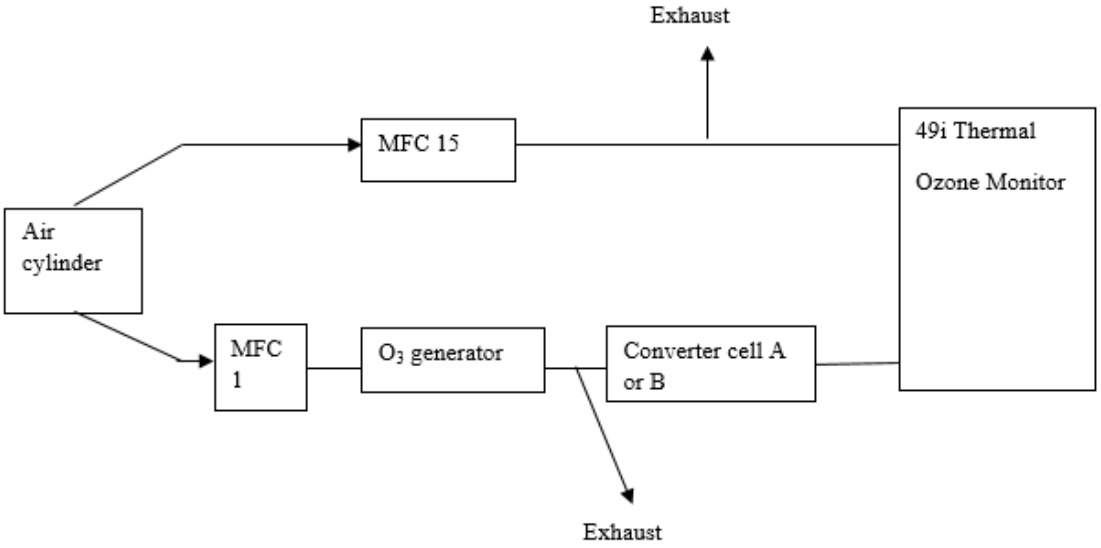

Figure 3.6. Schematic of step/pulse residence time tests in the converter cells.

This test used an ozone generator to generate ozone as a tracer. The ozone generator consisted of a UV mercury lamp located beside a short quartz tube, allowing UV radiation to photolyze synthetic air flowing (from cylinder) through the tube and generate a stable amount of ozone. Two exhausts were connected in the system to vent excess flow and allow converter cell residence time to be determined by the ozone monitor pumping rate, as in the real OPR measurement configuration (ozone monitor in differential ozone measurement configuration).

3.3.2 Summary of residence time measurement results of converter cell

Five sets of Pulse / Step method residence time test were performed to determine mean residence time of the converter cell. All tests were performed with identical system setting, apart from variation of the ozone input levels (which does not interfere with residence time). The ozone levels measured during tests are shown in following Figure 3.7a&b:

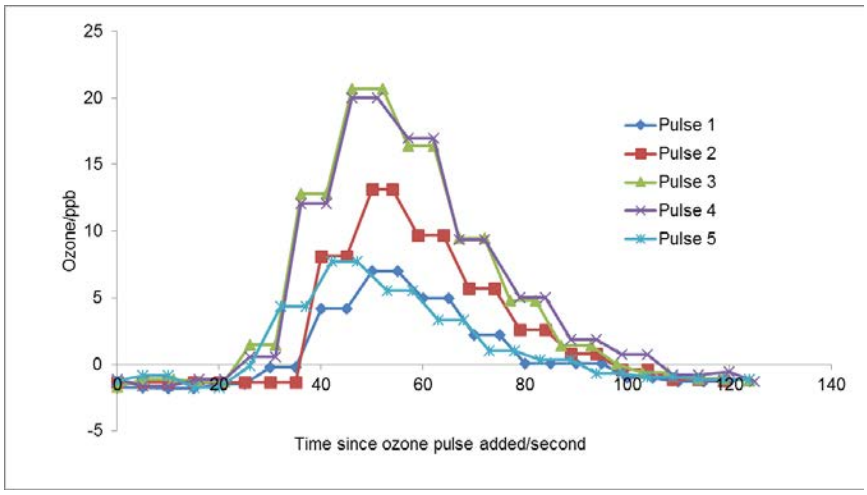

Figure 3.7a. Time variation of ozone levels at outlet of reactor, for residence time tests using the pulse method.

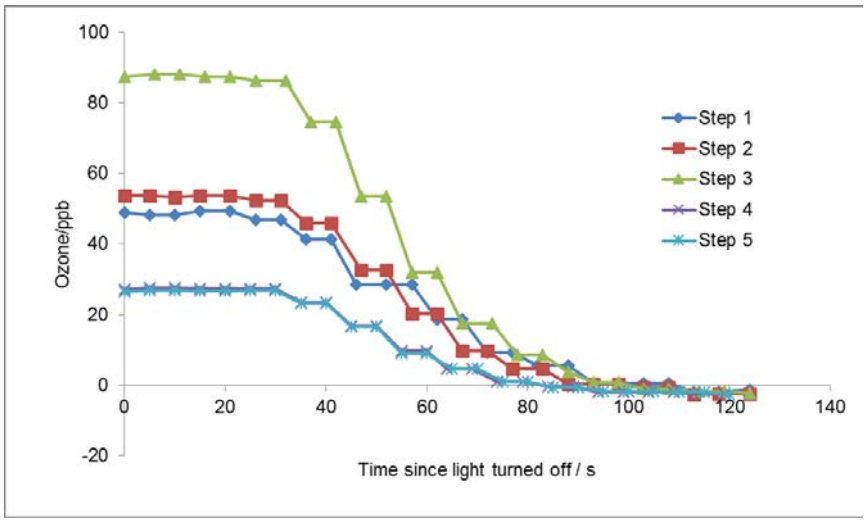

Figure 3.7b. Time variation of ozone levels at outlet of reactor, for residence time tests using the step method.

Both figure showed results for experiments on cell A, which was used to represent both identical converter cells A and B. The mean residence time of converter cells are shown in the following table:

Converter Cell A & B	Pulse method	Step method
Mean residence time $t_{mean\ res\ converter}$ (seconds)	55 ± 3 (± 1 S.D.)	52 ± 1 (± 1 S.D.)
Median residence time $t_{mean\ res\ converter}$ (seconds)	56 ± 3 (± 1 S.D.)	51 ± 1 (± 1 S.D.)

Table 3.1. The mean residence time results of converter cell A & B (derived from 5 sets of test by each method).

The calculated residence time for plug flow is then presented as:

$t_{calculated\ res}$ = $Volume_{converter\ cell}$ / flow rate

Where $Volume_{converter\ cell}$ = 0.498L

Flowrate is 0.7 SLM

Therefore, $t_{calculated\ res}$ = 0.5 L / 0.7 SLM = 0.71 minutes = 43 seconds.

Both the closed pulse and closed step residence time results for the converter cell agree well (55 ± 3 (± 1 S.D.) seconds vs 52 ± 1 (± 1 S.D.) seconds), giving confidence in their accuracy. The plug flow residence time estimation is close to the mean residence time, suggested the mean residence time derived from both pulse and step methods are reasonable.

Such similarity in residence time determination of the converter cell may be contrasted with the residence time determination of reactors, where the plug flow residence time (486 seconds) was substantially lower than the actual residence time of 710 seconds, reflecting the much larger distribution of flow pathways through the large closed conduit reactors.

To conclude, the mean residence time from pulse method was used to represent both converter cell: 55 ± 3 (± 1 S.D.) seconds.

3.4 Tests for wall losses of NO_x and O_3 in reactors

A key uncertainty in the OPR system is the impacts of the walls upon the sampled air chemical composition - arising from losses of sampled NO_x and O_3, and other reactive intermediates, and potential production of HO_x precursors such as HCHO and HONO. A series of experiments were performed to assess the loss of introduced NO_x and O_3 to the reactor walls, as a function of relative humidity (RH) and illumination, factors which have previously been identified as affecting wall losses in comparable systems (Cazorla and Brune, 2010).

3.4.1 Sample / Reference reactor ozone loss test

The sample reactors and converter cells are made of quartz with PTFE connecting components and end pieces. As discussed in the methodology chapter, quartz is a chemically inactive material, the silicon-oxygen chemical bond gives quartz glass high temperature stability and chemical inertness. PTFE also displays high chemical inertness. However, O_3 removal (up to 27.8% of input concentration) on inner surface of quartz glass tube have been reported previously (Itoh *et al.*, 2011). As such losses would directly cause an artefact to impact upon the measured $p(O_x)$ values. Furthermore, if there was an imbalance of O_3 removal between two reactors, this artefact is aggregated.

Wall loss tests were performed to determine this artefact. Moreover, during ambient measurements, the reactor surfaces may change, as a consequence of deposition of particles and low-volatility gases, which potentially react with O_3.

Ozone wall loss tests were performed to quantitatively measure any wall loss effects under sunlit and dark environments in both reactors. Three sets of identical experiments were

performed for each system configuration with same environmental conditions (in continuous days with similar solar radiation level); each set of the ozone wall loss experiment took approximately 3 hours to stabilize the reading in order to complete the test. The RH of the airflow was set to certain values in these tests (discussed below). A flow schematic for the ozone wall loss tests is shown below:

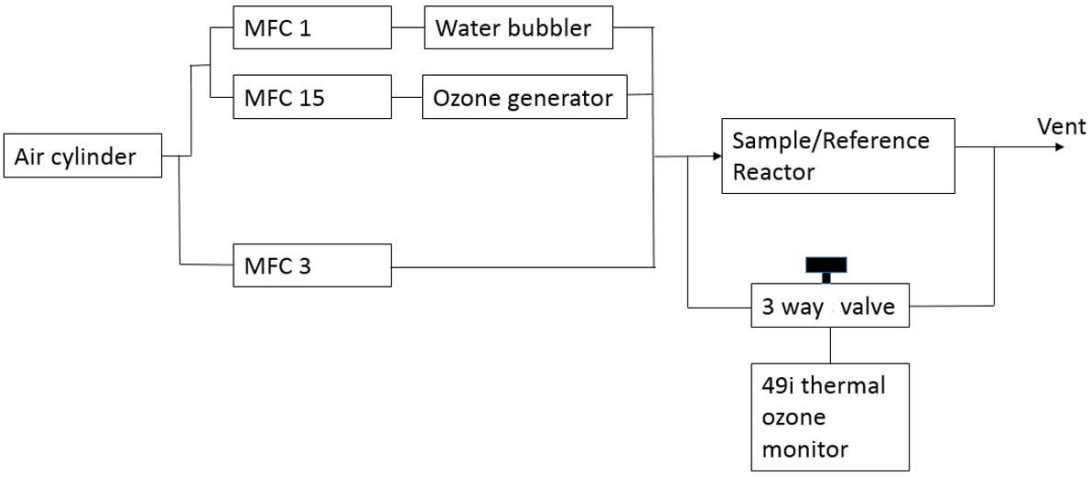

Figure 3.8. Flow schematic of ozone wall loss test. A water bubbler was used to humidify synthetic air. The ozone generator (introduced in section 3.3.1) produced an adjustable and stable amount of ozone. MFCs were used to regulate flow rate, and the valve used to switch the ozone monitor between measuring the input and output flow before / after the reactors, with the monitor configured in absolute (not differential) ozone measurement mode.

During the ozone wall loss tests, the sample / reference reactors were positioned in the ambient environment, with exposure to natural solar radiation during the day (filtered by the Ultem layer in the case of the reference reactor). As Figure 3.8 shows, the reactor is built with a three-way valve system. The left end (inlet) of the reactor is connected to synthetic air and three-way valve; the synthetic air flow is controlled by series of MFCs shown in Figure 3.8 with humidity control unit-the water bubbler, which allows synthetic air to entrain water vapour (to increase RH in air flow, as a humidifier). A RH sensor in the reactor reports the actual *in situ* RH of the synthetic air flow. The exit of the reactor was connected to an exhaust vent and three-way valve. This valve controls the synthetic air flow to the ozone

monitor. The ozone generator was able to generate an adjustable and stable mixing ratio of ozone in the synthetic air flow. By altering the valve, the input ozone level of the synthetic air before and after passing through the reactor was measured by the ozone monitor.

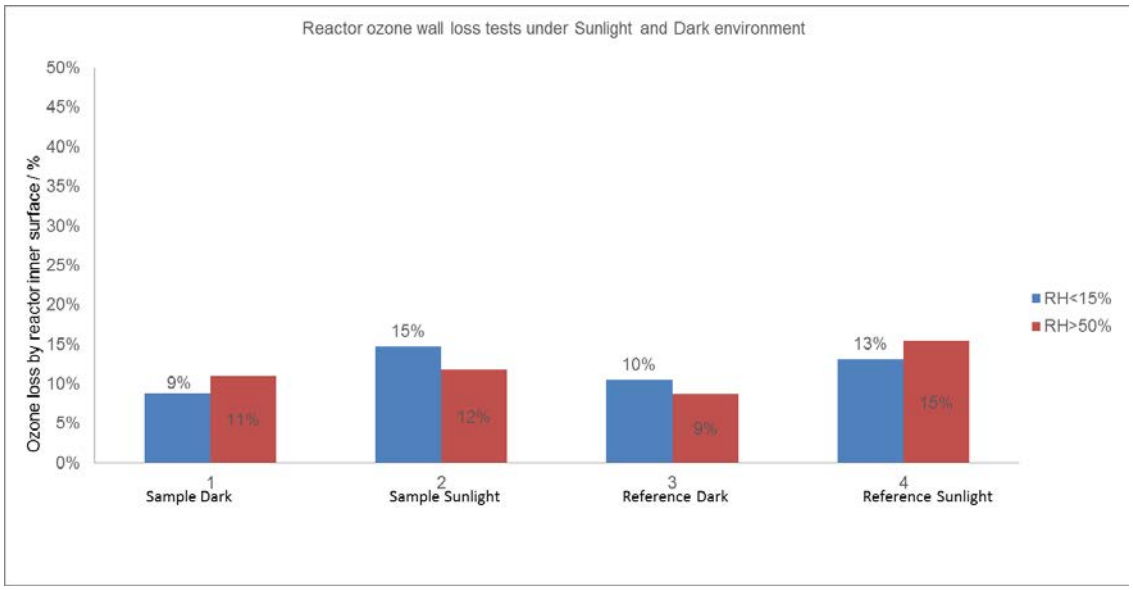

Figure 3.9. Measured ozone losses in the sample / reference reactors, as a function of ambient illumination level and flow RH (blue = low RH (dry air flow, no humidifier was implemented), <15 %; red = high RH, > 50 %; in practice, high RH is ca. 70-80%). Numbers on the figure indicate the ozone loss percentage measured.

In Figure 3.9, the blue bars describe ozone losses (in %) in the reactors under dry (<15 % RH) conditions, the minimum measurable with the available sensors); the red bars describe ozone loss for the reactors under higher RH conditions (> 50 % RH - in practice the RH was ca. 70-80 %). 3 sets of the identical wall loss test were performed for each test group. Test groups 1 and 2 show the sample reactor ozone loss under dark and sunlit conditions; test groups 3 and 4 shows the reference reactor ozone loss under dark / sunlit conditions. For these tests the introduced ozone mixing ratio varied between 100 and 140 ppb: this range of ozone is beyond the ambient ozone level usually encountered (at least in the UK), but gave a good (*i.e.* large) signal to measure; experiments at lower ozone levels showed the same, proportional, ozone loss.

The ozone loss due to wall effects was ca. 10 % under both dark and sunlit conditions in the reactors, with no significant variation with either illumination level or RH. As exposure to ambient air might alter the wall behaviour (through passivation effects, and possible deposition of low volatility gases and particles to the reactor walls), the ozone loss tests were repeated (after an interval of 10 months) with very similar results obtained (Figure 3.10). However, in this case only one set of data were obtained, such that statistical equivalence could not be confirmed.

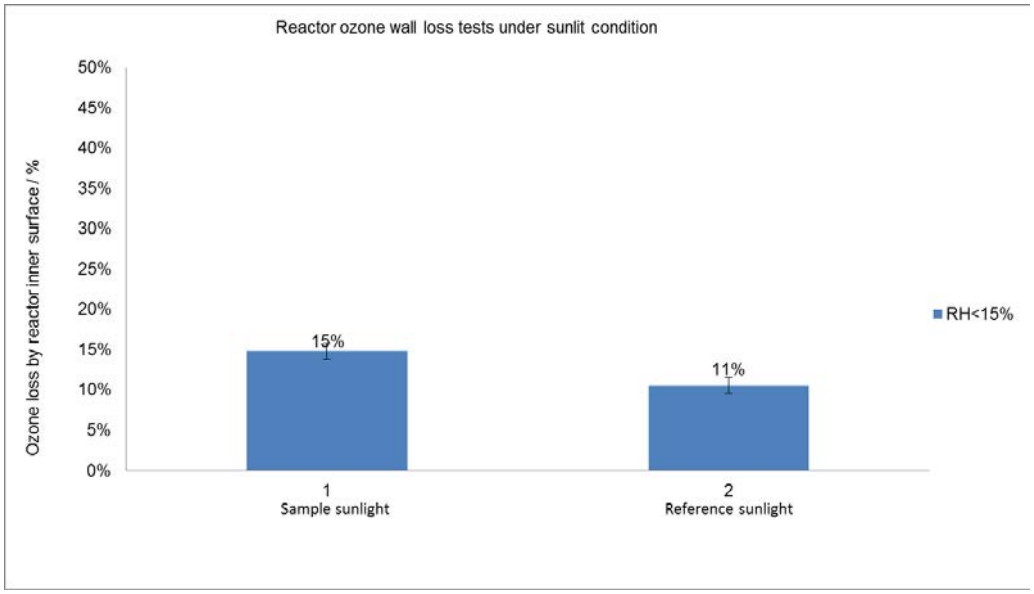

Figure 3.10. Repeat of ozone wall loss tests performed in October 2013, ca. 10 months after the previous measurements. Bars indicate the measured ozone loss due to wall effects, for sample and reference reactor (low RH, <15 %). Numbers on the figure indicates the ozone loss percentage measured.

3.4.2 Sample / reference reactor NO_x loss tests

Possible NO_x losses through the reactors are another important factor that could influence the OPR system measurements (both by changing the chemistry, and through the contribution of NO_2 to the measured O_x). Previous study reported that NO_2 loss became significant in their MOPS system when RH levels were above 50%. At 70% RH, the NO_2 wall loss rate could reach as much as 50%, which was three times higher than the loss at RH values below 50 % (Cazorla & Brune, 2010). However, Cazorla & Brune's MOPS system used Teflon film (Fluorinated ethylene propylene (FEP), 0.05mm thickness) reactors, which have different material characteristics (surface reactivity) to the OPR system's quartz reactors.

In order to characterise any NO_x wall loss effect, a range of NO_x loss tests were performed in a closed system with synthetic air, in a manner analogous to the ozone loss tests. A flow schematic of the NO_x wall loss tests is shown below:

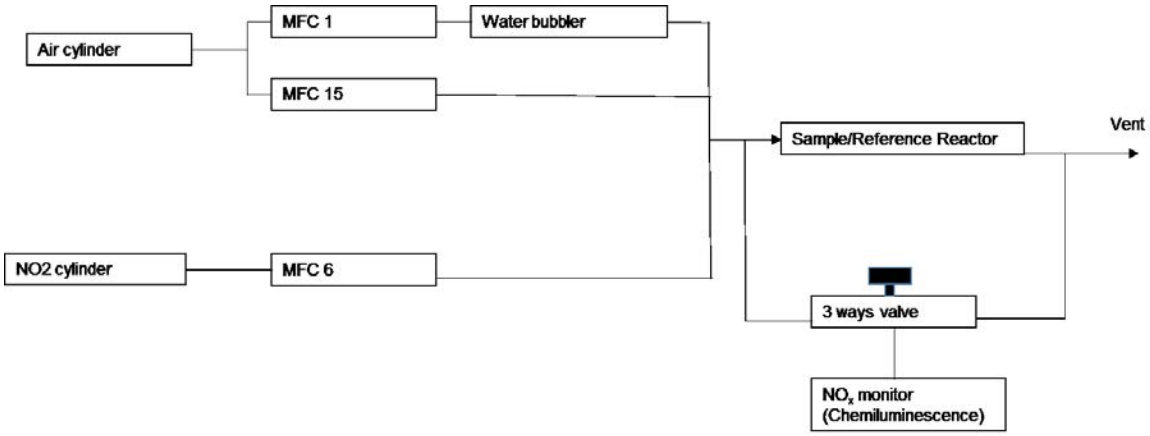

Figure 3.11: Schematic of NO_x wall loss tests. NO_2 cylinder concentration is 900 ± 50 ppb.

The experiment method was similar to that employed for the previous ozone wall loss tests, but with the thermo 42i chemiluminescence NO_x monitor connected to the 3 ways valve

instead of 49i ozone monitor; typical NO_x wall lost test results are shown in Figures 3.12 and Figure 3.13:

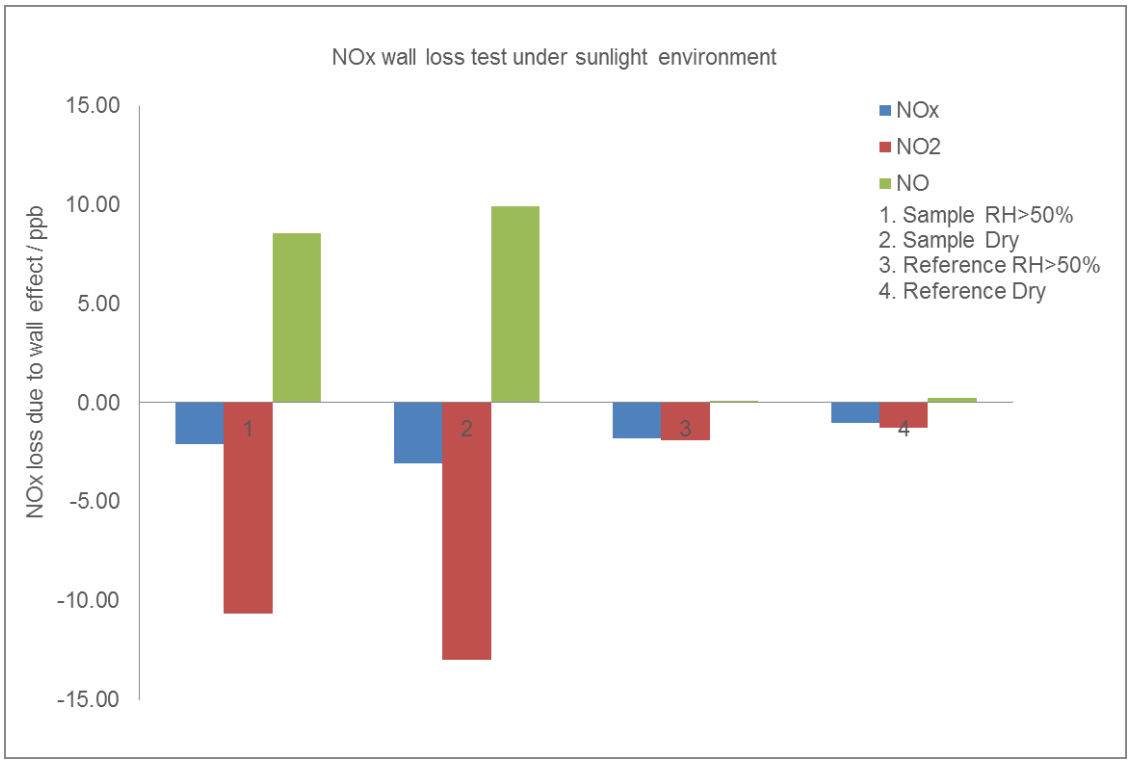

Figures 3.12. Measured NO_x loss values (in unit of ppb) due to reactor wall effects, as a function of flow RH under sunlit conditions. Different reactor and RH combinations are mentioned in the figure legend. The synthetic NO_2 addition was manually set to 65 ppb during this experiment.

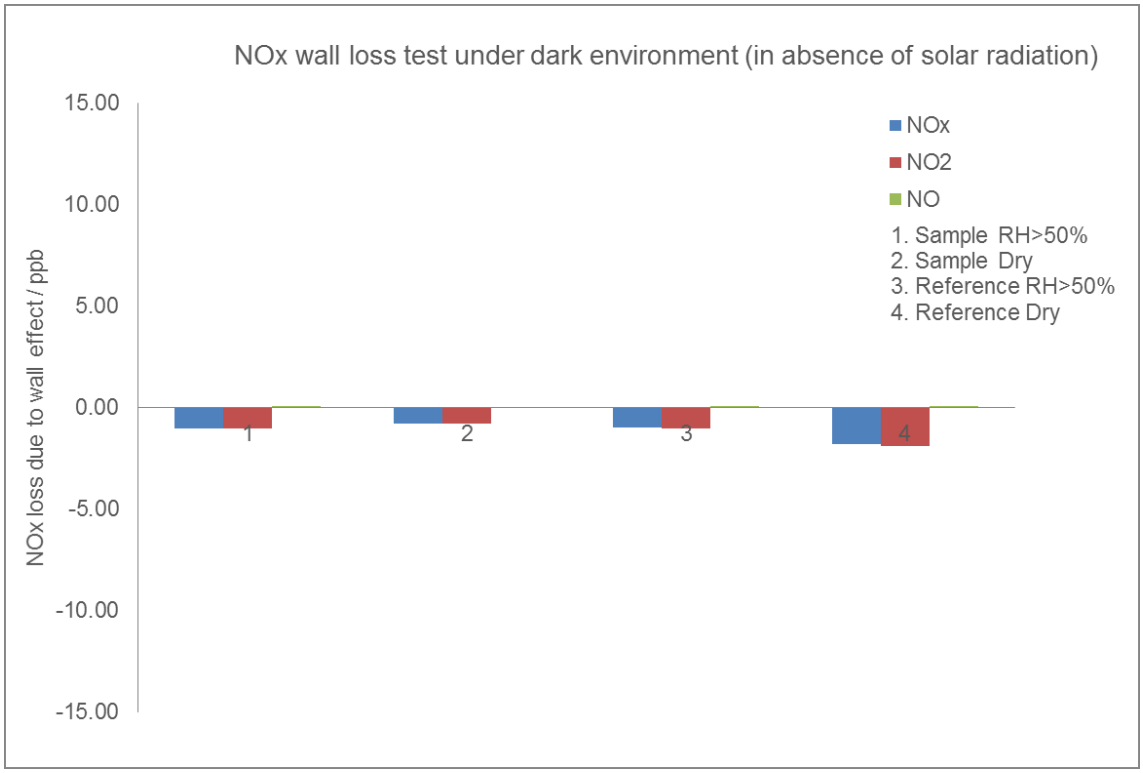

Figure 3.13. Measured NO_x loss values (in unit of ppb) due to reactor wall effects, as a function of flow RH under dark conditions (in absence of solar radiation). Different reactor and RH combinations are mentioned in the figure legend. The synthetic NO_2 addition was manually set to 65 ppb during this experiment.

Due to the limited time of solar radiation and frequent rainfall when tests were performed, only two identical tests were performed for each test group in Figure 3.12 and 3.13 (one less test than ozone wall loss test for each group). During the NO_x wall loss effect tests, the synthetic NO_2 addition was manually set to an overall level (post-dilution) of 65 ppb. According to the cylinder specification, the NO level was expected to be zero, but the NO_x monitor measured an NO input ranging from 0.3 to 0.8 ppb - probably a consequence of cylinder degradation and/or NO_2 decomposition on the regulator surfaces. This reading was neglected. Consequently, the total NO_x input for each test effectively equalled the NO_2 input, with very low NO addition.

Figure 3.13 indicates relatively low levels of NO and NO_2 loss caused by the reactor wall, with no significant variation observed between different RH values under dark environmental conditions. The addition of solar radiation significantly increases the surface loss effect for NO_2 in the sample reactor as shown in Figure 3.12, but is primarily due to NO_2 photolysis under solar radiation, reflected in the increase in NO and modest loss of NO_x overall. This was confirmed by the results from the reference reactor (with Ultem jacket to attenuate solar radiation, as presented in section 2.3.1.2), which showed much smaller changes in NO_2 and NO, and an overall NO_x loss of ca. 1 ppb (± 0.4 ppb S.D. from lowest detectable limit of 42i chemiluminescence NO_x monitor), which equal to 1.5 % of NO_2 input (65 ppb). Although the solar radiation caused the differences between test groups, more repetition of the tests for each group would allow statistical comparison between test group 1 and 2 to test group 3 and 4 to improve the accuracy of the tests.

Derived from ozone loss values presented in Figure 3.12 and 3.13, the overall NO_x loss due to wall effects under sunlight environment is 1.8% ± 0.7% (± 0.4 ppb S.D. from lowest detectable limit of 42i chemiluminescence NO_x monitor), the overall NO_x loss due to wall effects in dark environment is 3.08% ± 1.29% (± 0.4 ppb S.D. from lowest detectable limit of 42i chemiluminescence NO_x monitor) of NO_x monitor. The NO_x loss due to wall effects are much smaller than O_3 loss (ca. 10%). Compared to ambient ozone levels, NO_x levels are usually smaller, consequently, the overall NO_x loss due to wall effects in reactors are minor. The NO_x wall loss effect was then neglected in the analyses presented in chapters 4, 5 and 6.

3.5 Mass Flow Controller (MFC) calibration

The MFCs were regularly (two to four times per year) maintained and calibrated during the OPR development. When performing a calibration test, the selected MFC inlet was connected to an air cylinder, its outlet was directly connected to a reference (Defender 2000 model) flow meter. By reading the MFC *in situ* flow rate from IGI programme, and comparing it to the display screen of the Defender flow meter, a regression analysis between the two instruments could be generated. The following Figures show the (typically excellent) correlations between flow rates for a given MFC and the calibrating flow meter:

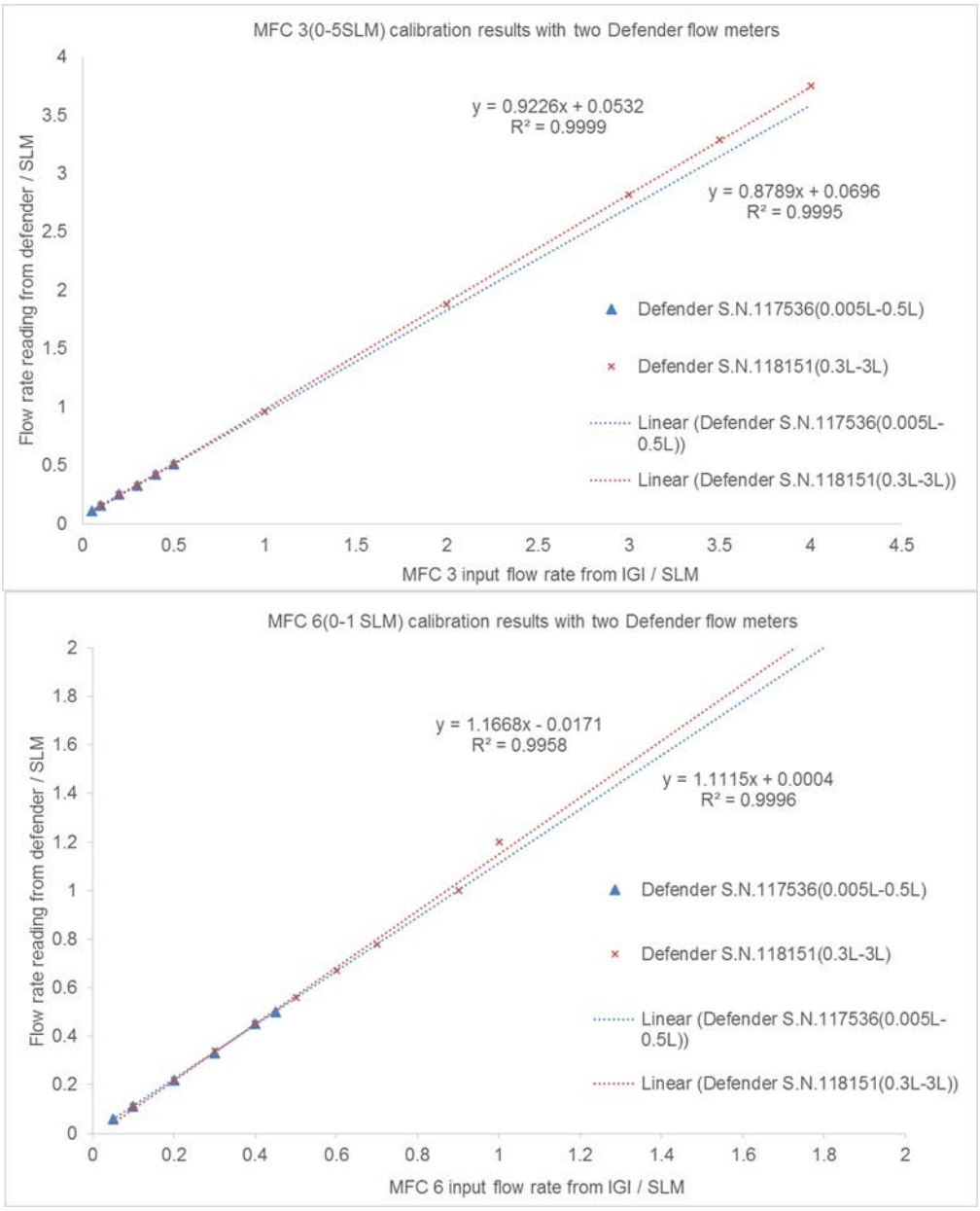

Figure 3.14. Examples of MFC (label number 3 & 6 in the OPR system) calibration results, showing precise and accurate MFC readings. The regression parameters (gradient, intercept) were used to correct the MFC settings for analysis.

3.6 NO_2 conversion efficiency tests

As discussed in the chapter 2 section 2.4, the conversion unit photolyses NO_2 to produce O_3 (and NO) in converter cells A and B. A high conversion efficiency is required for the overall measurement approach of determining the rate of change of total oxidant, O_x. A range of the "differential" conversion efficiency tests were performed to test the conversion efficiency of both cells. The flow schematic of the "differential" conversion efficiency tests is presented below; this reproduces the OPR flow settings during the field measurements.

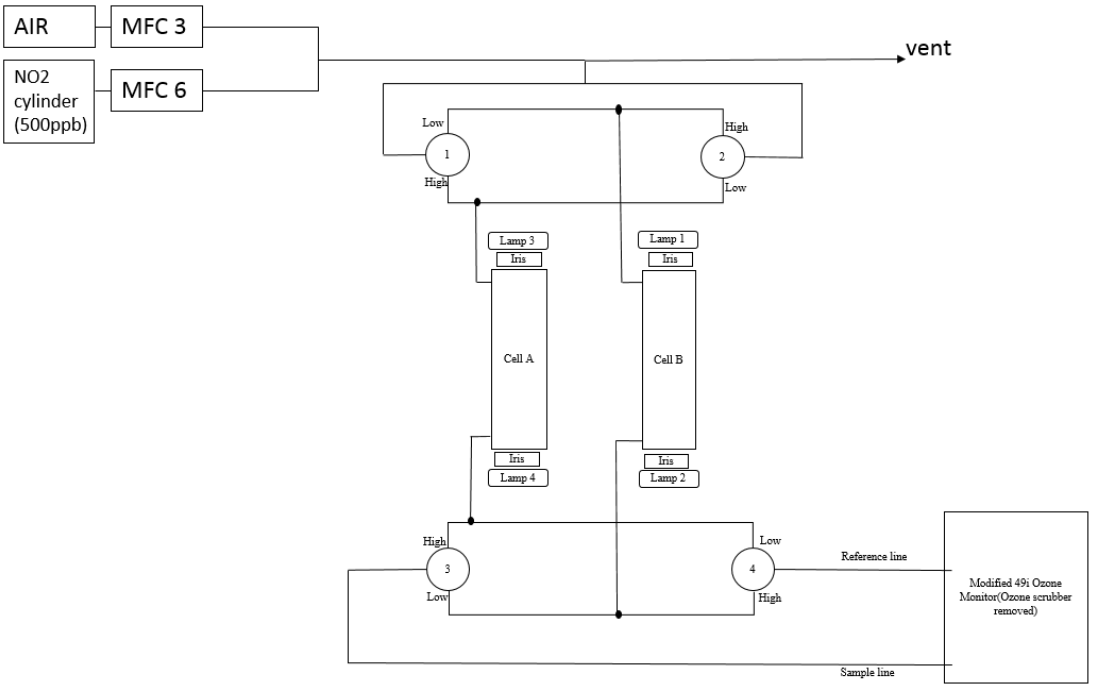

Figure 3.15. Differential conversion efficiency test schematic.

The basic principle of the differential conversion efficiency test is to compare the differential value of O_3 between reference and sample lines entering the O_3 monitor (shown on Figure 3.15) as a function of switching the four UV photolysis lamps on/off. The 49i Thermo ozone monitor was configured in its "differential" mode to perform the conversion efficiency tests; hence this test was termed the "differential conversion efficiency test"; it could also be

readily repeated in the field without changing the ozone monitor configuration, which was not desirable to adjust too many times to avoid damaging the connections.

The experiments were carried out by controlled NO_2 addition, regulated by MFCs, with either UV lamps 1 and 2, or 3 and 4, alternately on and off. The difference in the resulting ozone levels between two flows were then assessed using the ozone monitor, to determine the converted ozone level from the NO_2 addition.

The main advantage of such a differential method is the accuracy, as this method reproduces the flow setting of the OPR system in field measurements, the flow rate in both sample and reference lines are same as the OPR system during deployment. An alternative approach (of directly measuring absolute ozone levels, or measuring the loss of NO_2) would not be possible under the field deployment arrangement, as the total flow into the O_3 and NO_2 monitors (in absolute measurement configuration) would be 1.4 and 1.0 SLM respectively, significantly in excess of the 0.7 SLM flow through the conversion cells during normal operation condition. In contrast, direct measurements *are* possible for the sample / reference reactors, whose total flow easily exceeds that of the monitors.

The valve and lamp settings used for the differential conversion efficiency tests were as follows (see Figure 2.21 for flow pattern):

	Converter cell A CE test	Converter cell B CE test
Lamp 1&2	Off	On
Lamp 3&4	On	Off
Valve setting	all high	all high

Experiments were performed as a function of NO_2 mixing ratio in synthetic air, over a range from approximately 10 - 120 ppb, in a pseudo-random order. 4 sets of identical experiments were performed for conversion efficiency tests on each cell, with temperature maintained at ca. 20 °C and RH at 55%.

The results of both cells' conversion efficiency tests are presented in following Figure,

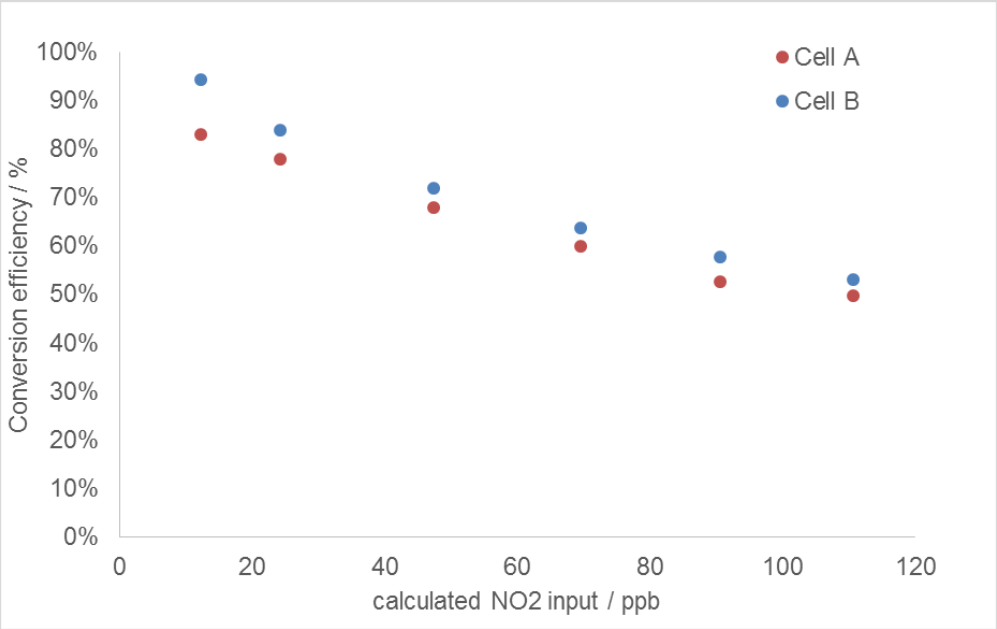

Figure 3.16. Conversion efficiency test result of converter cell A and B.

The converter cell "differential" conversion efficiency measurements show the NO_2-O_3 conversion efficiency varies as a function of NO_2 mixing ratio, over the range from 12 ppb to 110 ppb. Figure 3.16 shows a descending trend as NO_2 input level increases. When the synthetic NO_2 level is 12 ppb, both cells reach their highest conversion efficiency measured: For cell A this is 83 %, while for cell B a value of 94 % is obtained. When the synthetic NO_2 level is 110 ppb, conversion efficiency in cell A falls to 50%, and to 53% in cell B.

Both measurements showed falling conversion efficiency with increasing NO_2 level. This is as expected from considerations of the NO_x - O_3 PSS; as NO_2 is converted to O_3 and NO, the NO + O_3 → NO_2 back reaction continues to occur in the converter cell. At higher levels of NO_2, higher O_3 and NO will be present, and the rate of the back reaction will increase, aggravating this phenomenon. Chapter 5 outlines a model-based approach to characterise, and correct for, this effect.

Figure 3.16 also indicated that the overall NO_2 to O_3 conversion efficiency in cell B is always slightly higher than cell A, probably a consequence of differences in the intensity and alignment of the UV photolysis lamps. In actual field deployments, the slightly different conversion efficiency between the two cells was balanced (averaged out) by periodic valve switching (to alternate between each converter cell) and corresponding data averaging during ambient measurements.

3.7 Calibration of the Thermo 49i Ozone Monitor

As the ozone monitor is the essential analytical component of OPR system, its accuracy is crucial to the OPR results overall. The performance of the OPR ozone monitor was assessed by comparison with the NCAS (National Centre for Atmospheric Science) standard ozone generator, an NPL-accredited secondary calibration standard, once during the ClearfLo summer IOP 2012 in London. The resulting comparison in measurements for various artificially introduced ozone levels is shown in Figure 3.17:

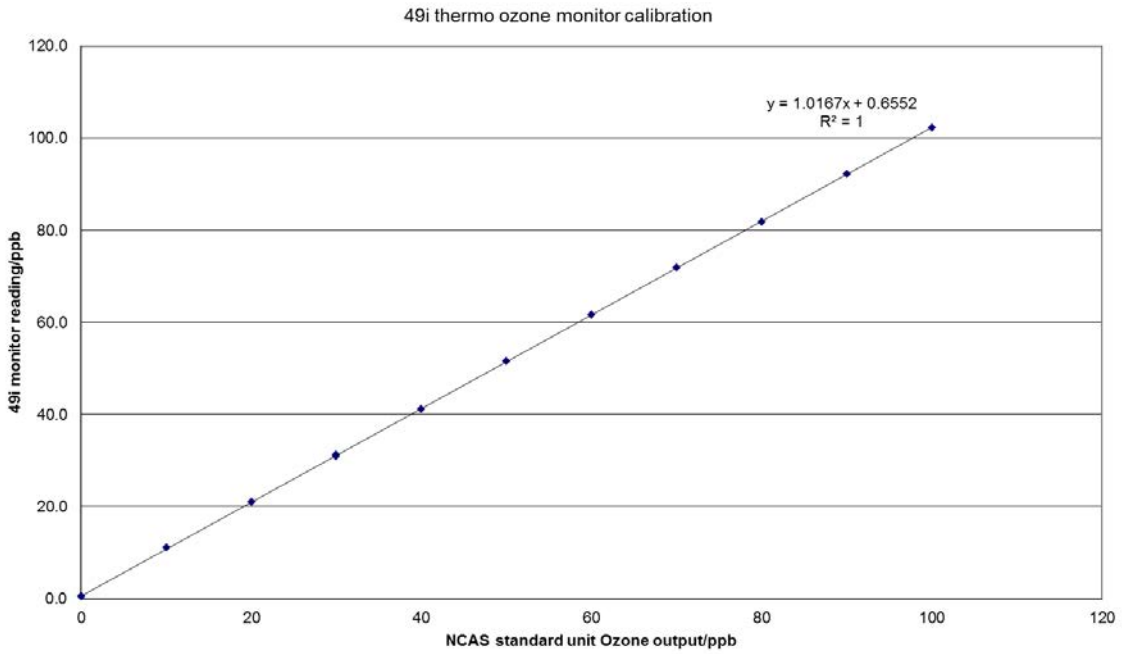

Figure 3.17. 49i thermo ozone monitor (used by OPR system) calibration result.

The results indicated that the OPR ozone monitor was performing well within manufacturer specification, with an accuracy of better than 2%, and no correction was applied to the measured data.

3.8 Limitations of the OPR system performance

After the characterisation experiments of key components in the OPR system, certain limitations of the system performance are considered in the following sections:

3.8.1 The OPR measurement requirement

The major limitation of the OPR system performance is the requirement for solar radiation. As discussed in Section 2.2, the OPR approach is based upon measuring the difference in oxidant levels between sample and reference reactor, which differ in turn due to the differing solar radiation level. Consequently, when there is no light (*i.e.* at night), both sample and reference reactors are effectively identical, and the OPR system is not able to measure any signal. Ozone production does not occur in the absence of sunlight (required for NO2 photolysis), so this restriction is not fundamental, but it has the further consequence that "dark" reactions will proceed equally in both reactors, and will be missed from the measured ozone production rate (see below).

3.8.2 Actual conversion efficiency in conversion unit

NO_2-O_3 conversion efficiency tests from section 3.6 were based upon synthetic NO_2 addition only (minor NO addition from NO_2 cylinder was neglected). The results indicated the importance of the back reaction of NO with O_3, but the tests as described in this chapter did not take account of this effect. A correction procedure to account for these effects is introduced in Chapter 5, as in the actual field measurement environment, NO and O_3 are abundant and immediately variable in ambient air, and so the actual NO_2 conversion efficiency is dependent on ambient NO_x and O_3 levels.

3.8.3 PSS issue in reactor

As stated in 2.2.3, the photostationary steady state (PSS) established in the sample and reference reactors are different, causing the flow exiting from reference reactor to have a reduced O_3 level and elevated NO_2 level relative to the sample reactor. The subsequent incomplete and differing NO_2 conversion (see Section 3.6 and 3.8.2) leads to a non-zero differential measured O_3 level (and hence inferred O_x) between the sample and reference flows. As a result, there is always an artefact reading from the differential measured O_x levels (measured as O_3) between two flows. This artefact is comprehensively discussed in chapter 5, and a correction approach introduced.

3.8.4 Dark radical chemistry in reactors

Although ozone formation does not occur at night, night time or "dark" reactions may occur during the day, producing radicals (*e.g.* OH) and contributing to ozone formation. As these reactions would not differ between the sample and reference reactors (no solar radiation dependence), their contribution to ozone formation would be missed by the OPR approach. Alkene ozonolysis and the reactions of NO_3 radicals are the two main dark HO_x radical sources which would fall into this category. Peroxy radicals react with NO_3 to generate OH radicals and NO_2, presented in following reactions:

$$NO_2 + O_3 \rightarrow NO_3 + O_2 \quad (3.6)$$

$$HO_2 + NO_3 \rightarrow OH + NO + O_2 \quad (3.7)$$

$$RO_2 + NO_3 \rightarrow RO + NO_2 + O_2 \quad (3.8)$$

Reaction (3.8) leads to oxidant production (NO_2 as part of O_x) in absence of solar radiation. The OH radicals from reaction (3.7) potentially react with VOCs and CO to regenerate

peroxy radical, to react with NO to form NO_2. However, NO_3 levels are expected to be negligible during daytime, as NO_3 is rapidly photolyzed, even in the reference reactor (by long-wavelength daylight).

Alkene species also contribute to oxidant production in the dark environment, by reaction with ozone. An example (ethene) ozonolysis reaction is:

$$C_2H_4 + O_3 \rightarrow 2CH_2O + O \quad (3.9)$$

$$O + O_2 + M \rightarrow O_3 + M \quad (3.10)$$

$$CH_2O + O_2 \rightarrow HCO + HO_2 \quad (3.11)$$

$$HCO + O_2 \rightarrow HO_2 + CO \quad (3.12)$$

Reactions (3.6) to (3.12) constitute a dark HO_x source in both reactors.

During the OPR field measurements, solar radiation was reduced in the reference reactor (see Section 2.3.1), causing both reduced OH formation (through *e.g.* ozone and HCHO photolysis), but also reduced NO_2 photolysis - as noted in section 5.3.1, j_{NO2} in the reference reactor is only a factor of 0.14 of j_{NO2} in the sample reactor. Consequently, although dark sources of OH may proceed in both reactors, net ozone production from these is much reduced in the reference reactor, and the OPR is still sensitive to this chemistry – but will underestimate its impact, by approximately 15 % (the remaining NO_2 photolysis rate). As alkene-ozone reactions are a minor source of HO_x radicals during daytime overall, impacts of dark radical sources are not expected to substantially bias the OPR measurements.

3.9 Concluding remarks of performance tests

This chapter has described the performance of the key OPR system components, and characterised the principal measurement effects arising from their implementation, which impact on the measured $p(O_x)$ data. A brief summary of the OPR systematic performance evaluation is shown in the following table:

	Results	Notes
Pulse vs Step method to determine mean residence time in closed conduits	Open Pulse method was the most suitable method.	Both methods used in analysis sections.
Reactor mean residence time	710 ± 133 seconds	Derived from open pulse method.
Conversion unit (Converter cell A&B) mean residence time	55 ± 3 seconds	Derived from pulse method.
Ozone reactor inner wall loss test	ca. 10% O_3 loss	No significant variation with illumination level or RH, contributed to overall uncertainty of OPR measurement.
NO_x reactor inner wall loss test	1.8% ± 0.7% in sunlit environment, 3.08% ± 1.29% in dark environment	Much smaller loss rate than O_3, neglected in data analysis in chapter 4,5 & 6.
MFC calibration	Regression analysis showed good correlation. $R^2 = 0.99$	Example of MFC 3 & 6.
49i Ozone monitor calibration	Very good correlation. $R^2 = 1$	Performed during ClearfLo summer IOP.
NO_2 to Ozone conversion efficiency test	From 94% to 50%, depends on NO_2 input level.	Conversion efficiency falls linearly with increasing NO_2 level, caused by PSS. An alternative method to determine actual conversion efficiency is introduced in chapter 5.
Three main limitations of the OPR system performance	Solar radiation requirement; actual (*in situ*) conversion efficiency; PSS issue in reactor.	Both conversion efficiency and PSS issue comprehensively discussed in chapter 5; Correction factor to this artefact is introduced in chapter 5.
Dark radical chemistry	Will be underestimated by ca. 15%	Alkene-ozone reactions are minor source of HO_x radicals during the daytime, this impact is negligible.

Potential uncertainties in the OPR measurements are further are discussed in the following chapters, in the context of field measurements (chapter 4) and system accuracy and correction factors (chapter 5).

Chapter 4: London OPR deployment

This chapter, and chapter 6, present results from two trial campaigns of the prototype OPR system. The first chapter outlines the first measurement campaign, which was carried out in London from 21st July to 23rd August 2012, while the second focuses upon a further campaign which was carried out in New Delhi and Mohali (India) from 23rd April to 16th May 2013. In each case, a detailed description of each campaign is given, followed by presentation of the data obtained, analysis and discussion.

4.1 London OPR deployment introduction

The ClearfLo (Clean Air for London) programme was a large collaborative research project involving ten academic institutions in the UK, funded by the UK Natural Environment Research Council (NERC). The aim of ClearfLo was to provide integrated measurements of gaseous and particulate species and meteorology of London's urban atmosphere at street level and elevated sites, complemented by models to analyse the processes responsible for poor air quality in London. Two intensive observation periods (IOPs) were performed, during winter 2012 (From 6 January to 11 February) and summer 2012 (From 21 July to 23 August). The summer IOP period was performed during the Olympic Games. More intensive measurements performed during the IOP periods provided a detailed assessment of air pollutants, complementing long-term observations throughout the project. The ozone production rate (OPR) measurement system was involved as part of the two ClearfLo intensive measurement periods; during the first (winter) IOP as a first trial deployment, and then as a more refined measurement during the second (summer) IOP.

4.1.1 Description of OPR measurement site in London

The ClearfLo project aimed to measure air pollutants both at the surface and elevated locations in London and surrounding areas. Most measurements were made 3-5 metres above the ground level. In central London, Marylebone Road, North Kensington, Westminster City Council and the BT tower sites were the main measurement sites for long term and IOP measurements. The Marylebone Road (MR) site is a kerbside site located 1 metre from the 6 lane A501; the road is very busy and frequently congested (DEFRA, 2014). The North Kensington (NK) site is an urban background site located in the grounds of Sion Manning School. The site is 5 metres from St. Charles Square, a quiet residential road. The two elevated sites were the BT tower site and Westminster City Council building site. The BT tower measurement site was near Marylebone Road, at height of 190 metres above the surface, while the Westminster City Council building was on Marylebone Road with instruments sampling at a height of 30 metres above the surface. There were also three rural monitoring sites surrounding the city of London: the Harwell, Detling and Chilbolton sites. The Harwell site is located beside an agricultural field to west of London, 83 km from central London. The Detling site is located in an agricultural field to the southeast of London, 55 km from central London, and the Chilbolton site is located to the southwest, 90 km from central London. Measurement site locations are shown in Figure 4.1.

The intensive measurements relevant to this thesis were performed during the IOPs in the playground of Sion Manning School, which was 10 metres from the established North Kensington AURN (Automatic Urban and Rural Network) air quality site. The playground was an open area; most instrument inlets were located at or slightly above roof level on top

of shipping containers, 2-5 metres above the ground. The OPR system was deployed in a similar manner.

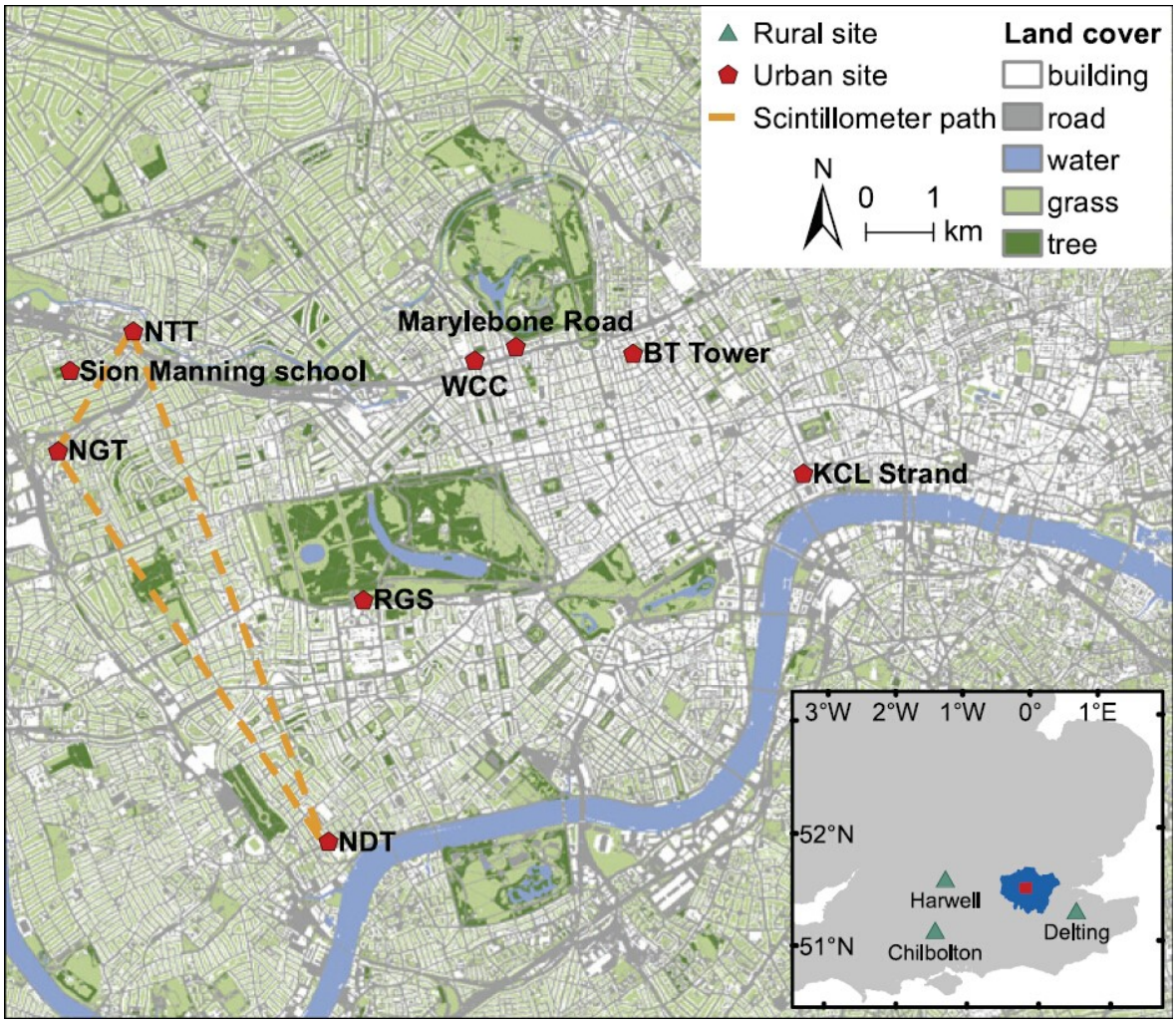

Figure 4.1. ClearfLo summer IOP measurement were undertaken in London (Blue shaded area) and at three rural sites (green triangles). The urban observations were conducted at several locations in central London (red in inset and main map) north of the River Thames (blue, main map). For reference, Hyde Park is the green area directly north of the Royal Geographical Society (RGS; with the Institute of British Geographers) site. The North Kensington site is shown as Sion Manning school on the map, it is 6 km northwest from central London (Bohnenstengel *et al*., 2015).

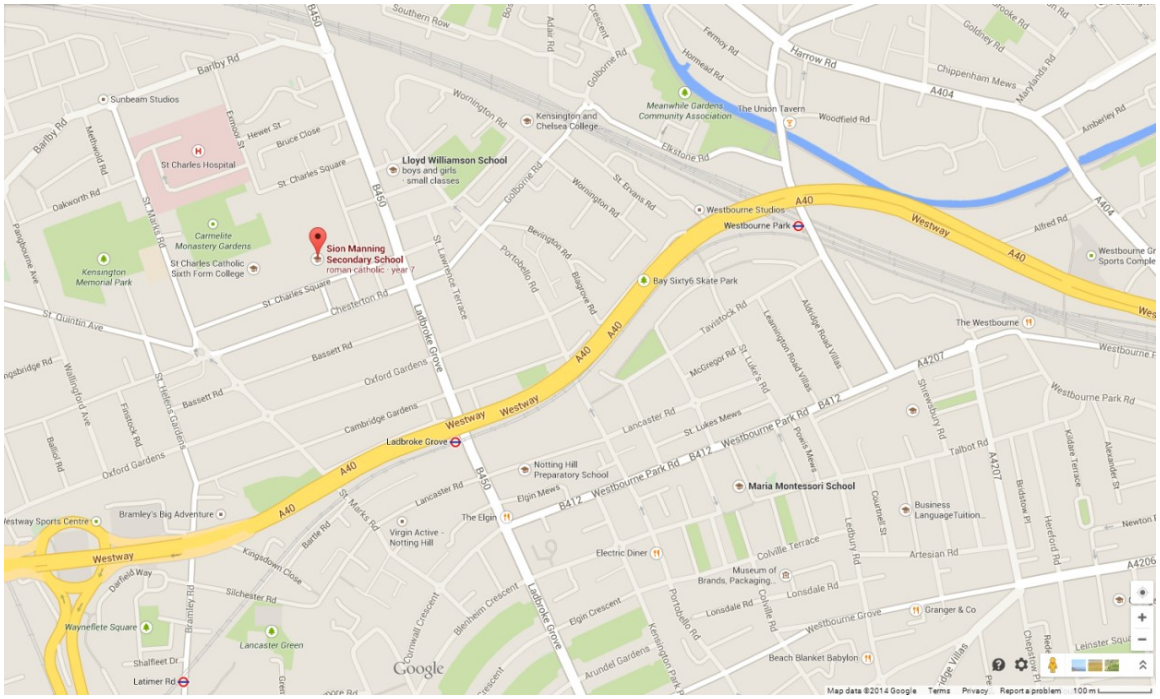

Figure 4.2. The North Kensington measurement site location (Sion Manning School) and its surrounding area, London 2012 (Google, 2014).

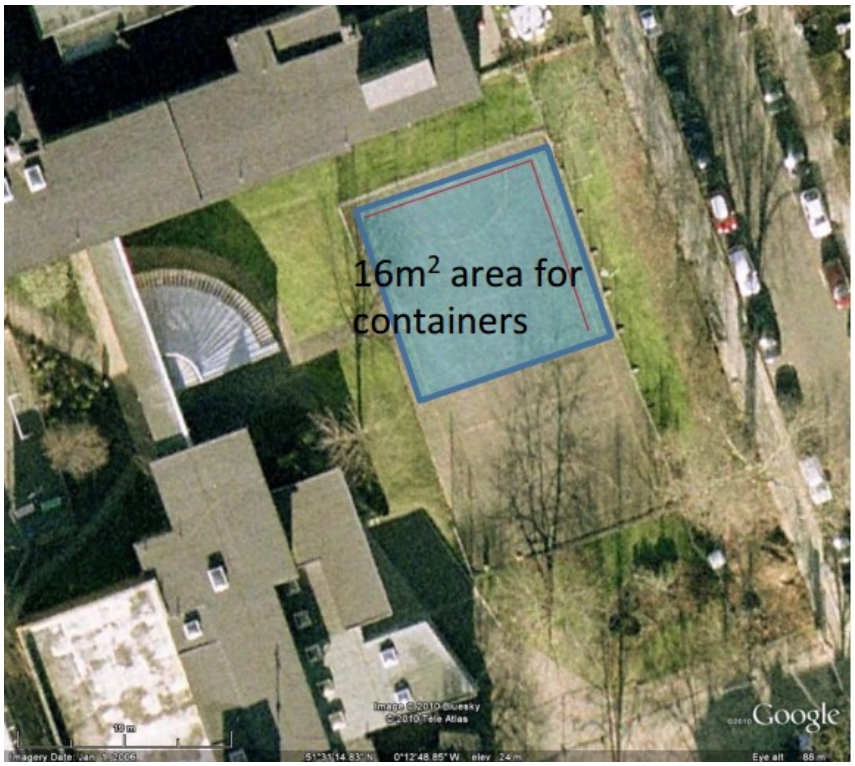

Figure 4.3. Satellite image of the Sion Manning School playground used for IOP instrument deployments, North Kensington.

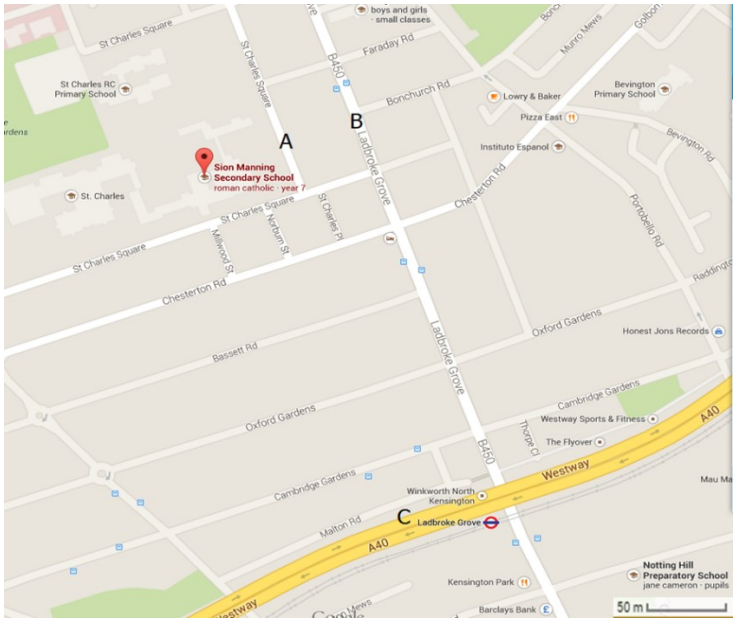

Figure 4.4. Local roads near the NK site and Sion Manning School. A: St Charles Square; B: B450 Ladbroke Grove; C: A40 Westway (Google, 2014).

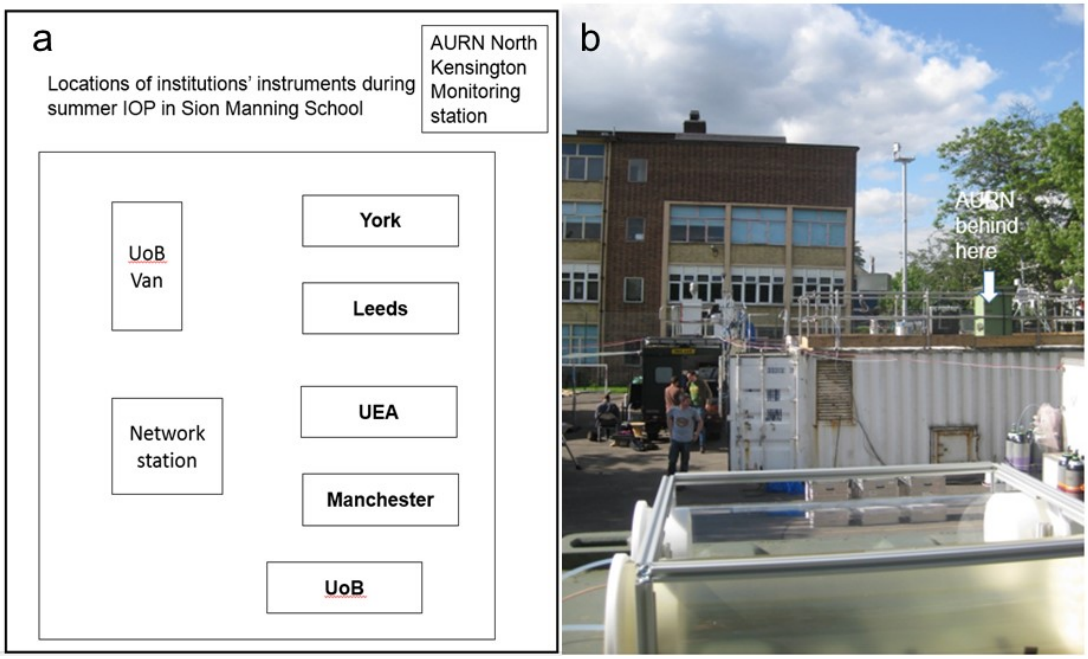

Figure 4.5. (a) Detailed locations of the various University instrumented containers at the NK site during the summer IOP; (b) Photograph of the measurement site with OPR sampling reactors in the foreground, view from the South towards the North.

Figure 4.2 describes the location of Sion Manning School and its immediate surrounding area. As Figure 4.5a shows, the instruments deployed during the summer IOP were positioned on the school's playground. There were five shipping containers / portacabins on

the playground from different Universities (Fig 4.5a). The OPR was deployed in / above a portacabin at the southern end of the playground, with the system's sampling reactors positioned on top of the cabin, with the controlling components, conversion cells, O_3 monitor etc. located inside the cabin, alongside the CEH Chemical Ionisation Mass Spectrometer. The University of Birmingham (UoB) portacabin was located about 3 metres from the adjacent container (Manchester), and approximately 40 metres from the North Kensington long term (AURN) monitoring station in the north-east corner of the playground.

As Figure 4.3 shows, the Sion Manning School playground is an open area with a few trees (less than 5-10 metres height) around the east and south sides. The School is surrounded by residential buildings, located at distances of 50-200 metres from the playground. There are several roads in this urban background area; the nearest road is shown in Figure 4.4 as St Charles Square (A), a residential area road with very minor traffic flow within 40 metres from the NK site. Point B in Figure 4.4 is the B450 Ladbroke Grove, this is a road with small business and retail stores, where traffic was observed to be free-flowing throughout the day; it is connected to the Ladbroke Grove London Underground station. The NK site is 140 metres from this road. Point C indicates the A40 Westway, a major / busy road with 6 lanes of traffic into/out of central London, located to the south of the site: the linear distance between the A40 and the NK site is 410 metres.

During the summer IOP, many gaseous components and particulate species were measured continuously by the consortium. A list of the pollutant measurements of relevance to chemical ozone production, and which are considered in more detail in the following sections, is given in Table 4.1. A full list of instruments deployed / measurements made can be found in Bohnenstengel *et al.*, 2015.

Summer IOP data				
Species measured	Location	Instrument	Institution	Comment
O_3	North Kensington	TEI 49i O_3	York, Birmingham	Two sets of data, data discussed in thesis
NO	North Kensington	AL5002 CO/TEI 42i NO_x	York	Data discussed in thesis
NO_2	North Kensington	AQD NO_x/TEI 42i NO_x	York, Birmingham	Two methods of measurement: Photolytic and thermal
HONO	North Kensington	York LOPAP	York	Data discussed in thesis
HO_2	North Kensington	FAGE	Leeds	Data discussed in thesis
RO_2	North Kensington	FAGE	Leeds	Data not yet finalised
HO_2+RO_2	North Kensington	PERCA	Leicester	No data obtained
OH	North Kensington	FAGE	Leeds	Data discussed in thesis
$d[O_3]/dt = \Delta O_3$	North Kensington	OPR	Birmingham	Data discussed in thesis

Table 4.1. Gaseous species of potential relevance to ozone chemistry measured during the ClearfLo 2012 summer IOP at the North Kensington site in London. The target species, measurement approach and corresponding institutions are briefly shown in the table.

4.2 Air Pollution Climatology during the ClearfLo summer IOP measurement period

As discussed in chapter 1, ambient NO and NO_2 levels are directly related to ozone abundance and to ozone formation ozone chemistry. A complete time series of the measured NO, NO_2 and O_3 mixing ratios at the NK site (data from the AURN monitoring site) is shown in Figure 4.6 below,

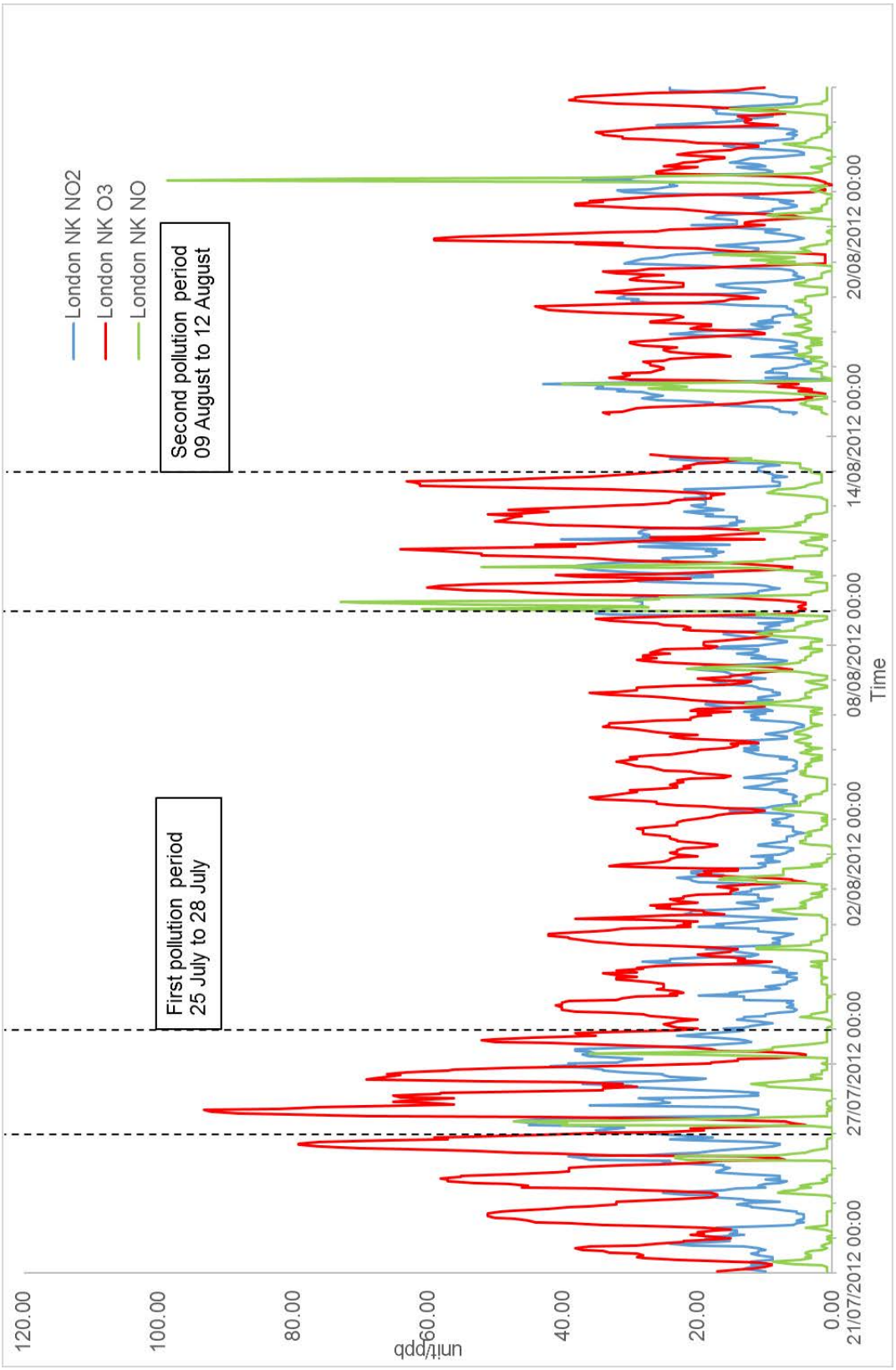

Figure 4.6. Time series of ambient NO, NO_2 and O_3 as measured at the NK site (AURN data) during the ClearfLo summer IOP.

During the summer IOP at the NK site, the hourly average O_3 mixing ratio was 27 ppb (with a standard deviation of 16 ppb). The maximum O_3 mixing ratio observed was 107 ppb, and the minimum O_3 mixing ratio was 2 ppb. Most of the measured O_3 mixing ratios were distributed around the 20-40 ppb range (frequency distributions presented below). Two more heavily polluted periods are apparent from inspection of Figure 4.4. The first of these ran from approximately 25 to 28 July, around the time of the Olympic Games opening ceremony. NO_x and O_3 levels were elevated during this period, with the maximum ambient O_3 level of 107 ppb reached on 25 July 2012. The second pollution period extended from 9 to 12 August; O_3 levels reached around 75 ppb. The second pollution period, referred to hereafter as the "Four days Intensive OPR Measurement (FIOM)" period, is discussed in detail in section 4.2.2. The NK site as an urban background monitoring station was broadly representative of regional urban conditions during the summer IOP periods, the averaged diurnal pattern of some measured pollutant species (NO_x, O_3 and CO) during this period are presented in the follow Figure,

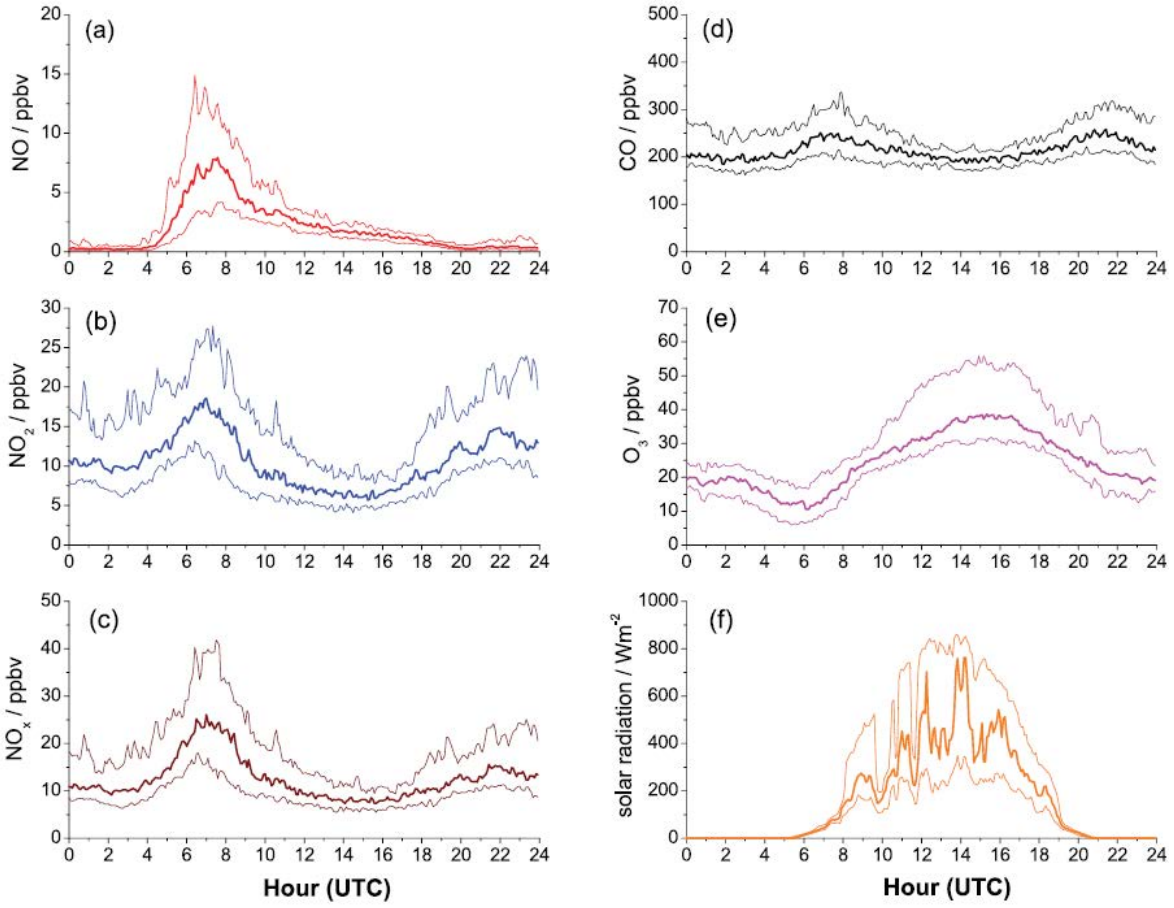

Figure 4.7. The 5 minute-averaged diurnal cycle for (a) NO, (b) NO_2, (c) NO_x, (d) CO, (e) O_3, and (f) solar radiation at NK site during the summer IOP. Thick lines correspond to the median and the thin lines are the corresponding quartiles (Bohnenstengel *et al.*, 2015).

Figure 4.14 (c) displays the typical urban NO_x diurnal pattern with double peaks appearing during the "rush hours" in early morning and mid-late afternoon,

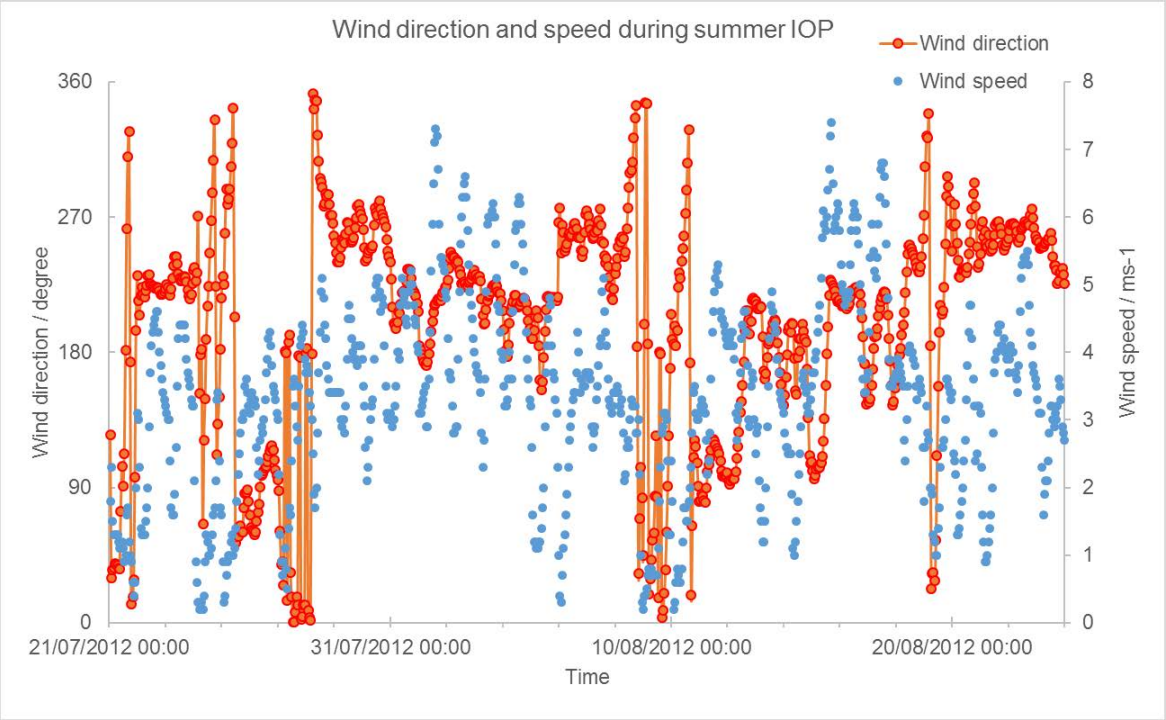

Figure 4.8. Wind direction and speed at NK site during Summer IOP (21st July to 23rd Aug 2012). Data from AURN NK site.

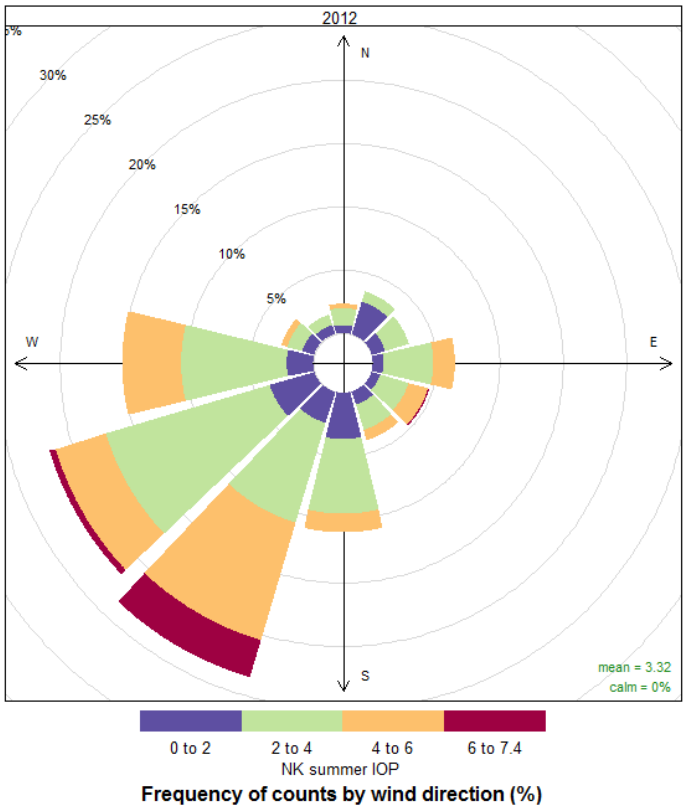

Figure 4.9. Wind rose during summer IOP (21st July to 23rd Aug 2012) at NK site. Data from AURN NK site.

During the summer IOP, majority of hourly wind directions were south-westerly, with a large range of variations from $1ms^{-1}$ to $7ms^{-1}$. Consequently, the air mass over NK site are expected to have a complex range of origins, showing in the following air mass figure using NAME model,

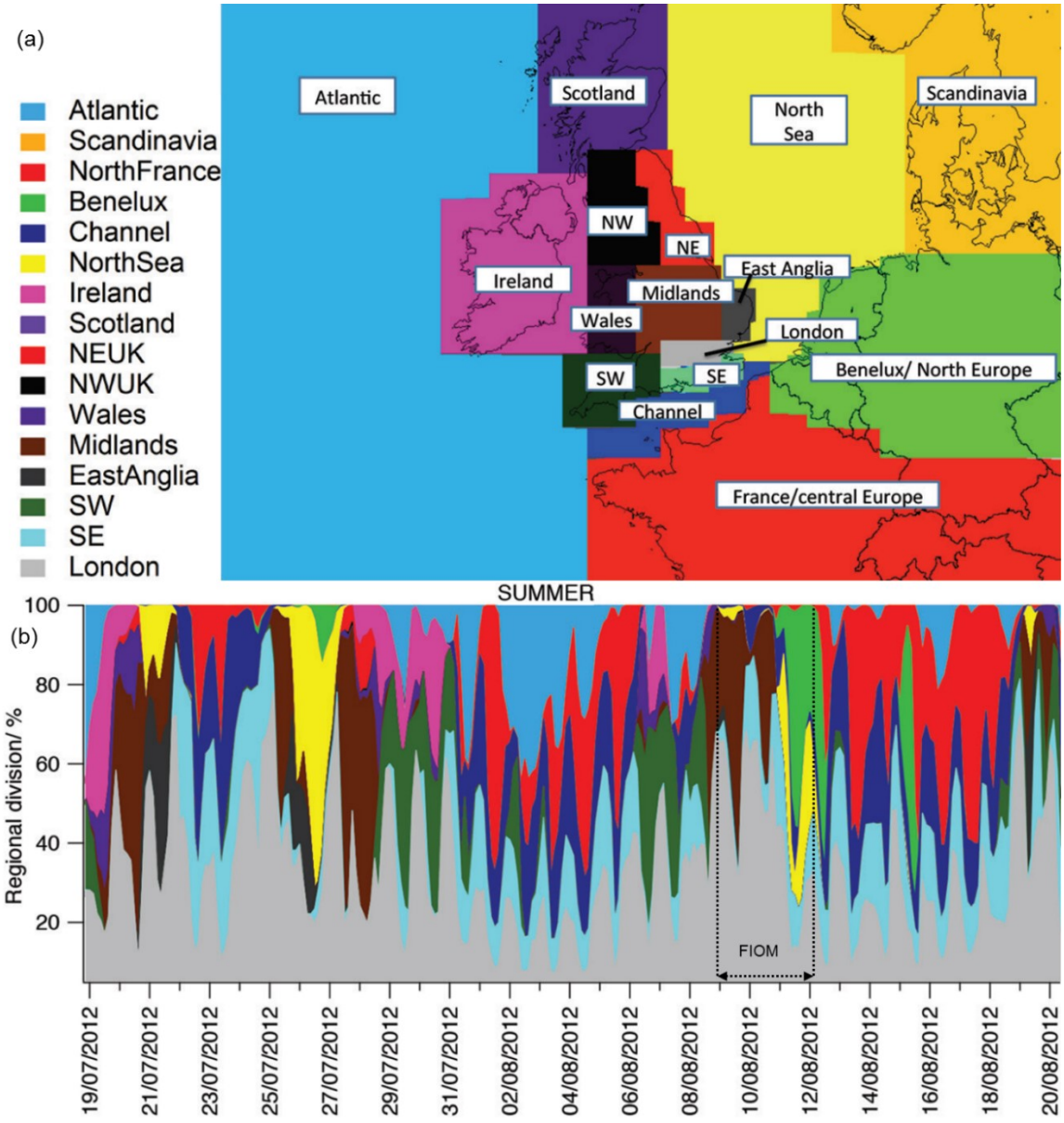

Figure 4.10. (a) Regions for the origin of air masses, and percentage time spent over each region by air masses arriving in London, computed using the NAME model, during (b) the CleafLo summer IOP (Bohnenstengel *et al*., 2015).

During the FIOM period, the sampled air mass origin was largely from London (Grey) and SE (Light blue) areas; Midlands (Brown), Benelux/North Europe (Green), North Sea (Yellow) areas contributed to the rest of the air mass origins. There was little contribution from Channel (Dark Blue), Scotland (Purple) and France (Red) areas to the air mass origin. Only air masses of Atlantic origin were essentially absent during the FIOM period. As Figure 4.23b shows, on a day-to-day basis air masses were from various areas with varying proportions during the ClearfLo summer IOP. However, the majority of air masses during the ClearfLo summer IOP originated in the London area. The FIOM period had similar characteristics as the whole summer IOP in terms of air mass origin; therefore, in addition to the sunny weather conditions, the FIOM period was felt to represent a typical summertime urban pollution episode. The London campaign data analysis in later sections of this chapter focuses on the FIOM period, especially on the 11th and 12th August 2012 (the second two day period of the FIOM period).

4.2.1 Pollutant abundance and statistical distribution during the Summer IOP

A number of rural sites were involved in the ClearfLo project. One of them was the Harwell AURN long term monitoring site in Oxfordshire. It is located in an open agricultural field on the Harwell Science campus, with a minor road 140 metres to the south of the monitoring station. The Harwell site is 83 km from central London; this monitoring station is taken to represent upwind regional rural conditions in the following discussion. A comparison between the time series of O_3, NO and NO_2 between the NK and Harwell sites was taken, to give an overview of contrasts in pollutant levels between the urban and rural areas.

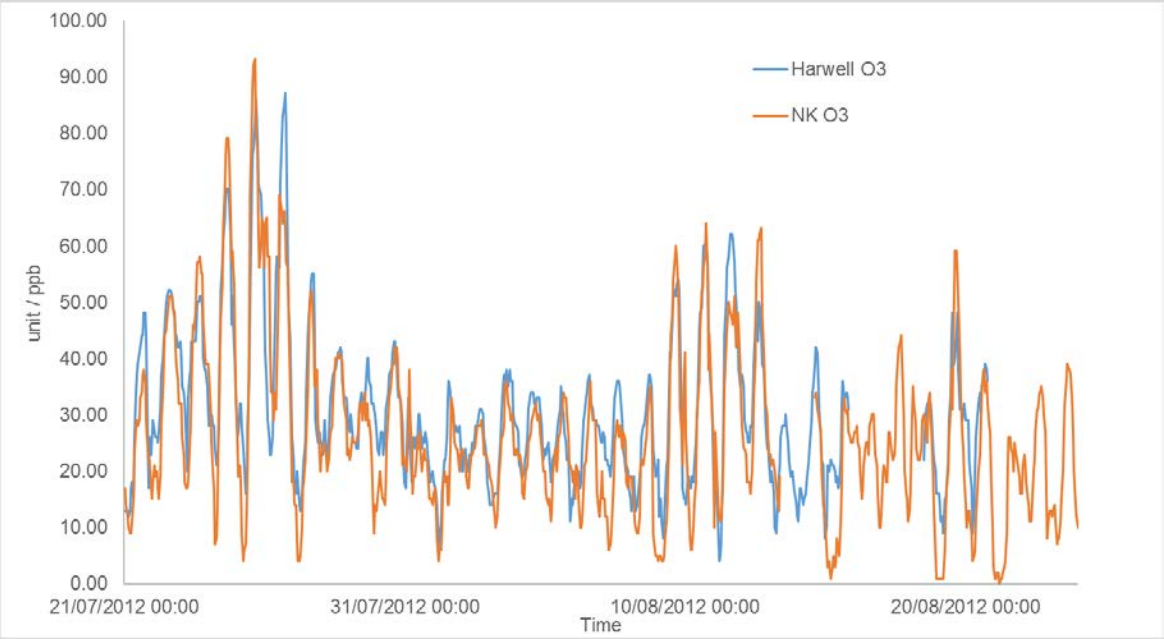

Figure 4.11. Time series of ambient O_3 as measured at the NK and Harwell site (AURN data) during the ClearfLo summer IOP.

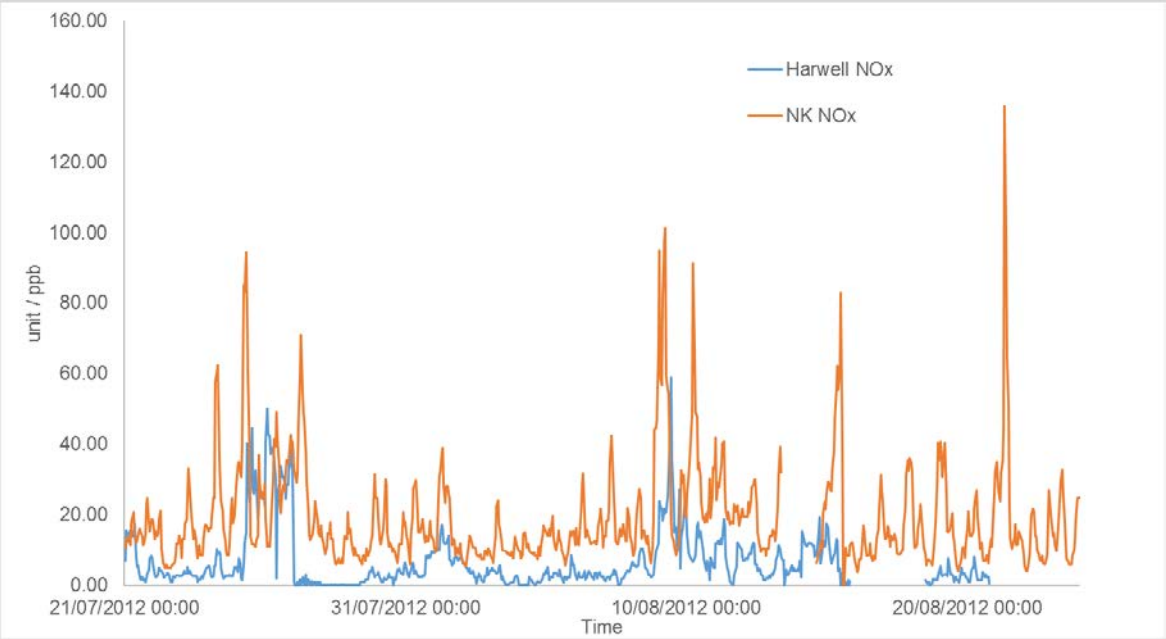

Figure 4.12. Time series of ambient NO_x as measured at the NK and Harwell site (AURN data) during the ClearfLo summer IOP.

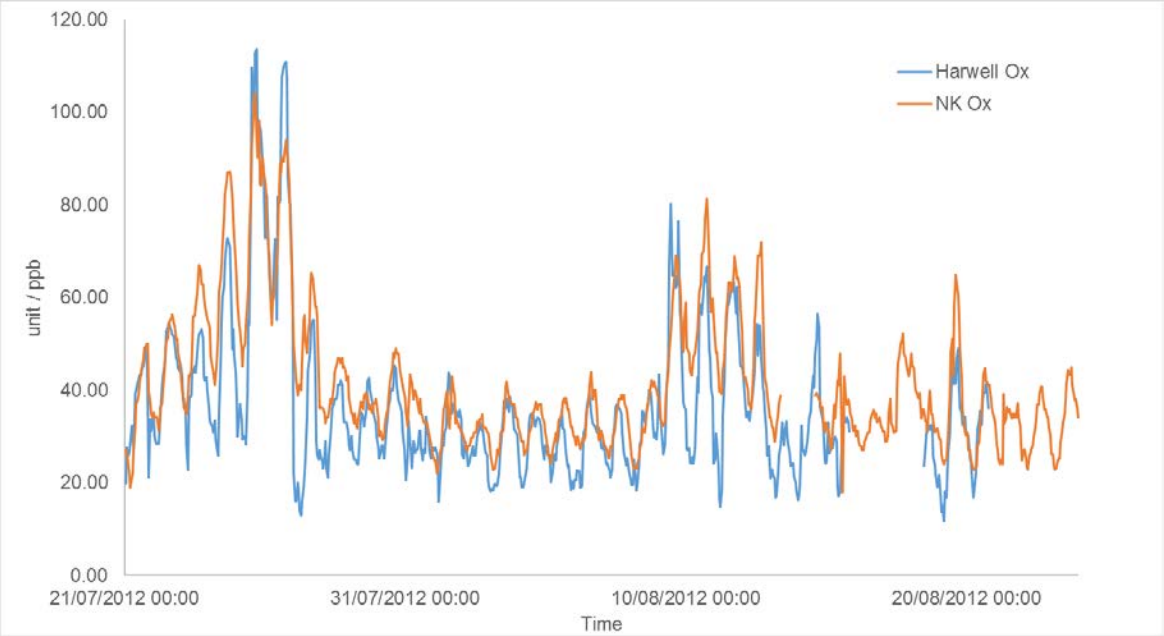

Figure 4.13. Time series of ambient O_x as measured at the NK and Harwell site (AURN data) during the ClearfLo summer IOP.

It was clear that overall NO_x levels at NK were much higher than at Harwell, primarily due to the local traffic emission in central London. O_x levels at the NK site were also 5 to 10 ppb higher than those at Harwell, but the O_3 levels were similar at both locations. A possible

reason to cause such similarity could be the NO-to-NO_2 titration process, it is so-called "urban decrement effect" – the reaction between NO, emitted (primarily) from traffic in an urban area, with O_3 to cause reduced NO and O_3 and elevated NO_2. To further investigate this possibility, a comparison of the frequency distributions of O_3, NO and NO_2 between the NK and Harwell sites was undertaken, to distinguish the contrasting characteristics between urban and rural O_3 and NO_x levels during the summer IOP, and provide a first estimate of the London (urban) increment in pollution levels. The results obtained are shown in the following Figures 4.14 to 4.17:

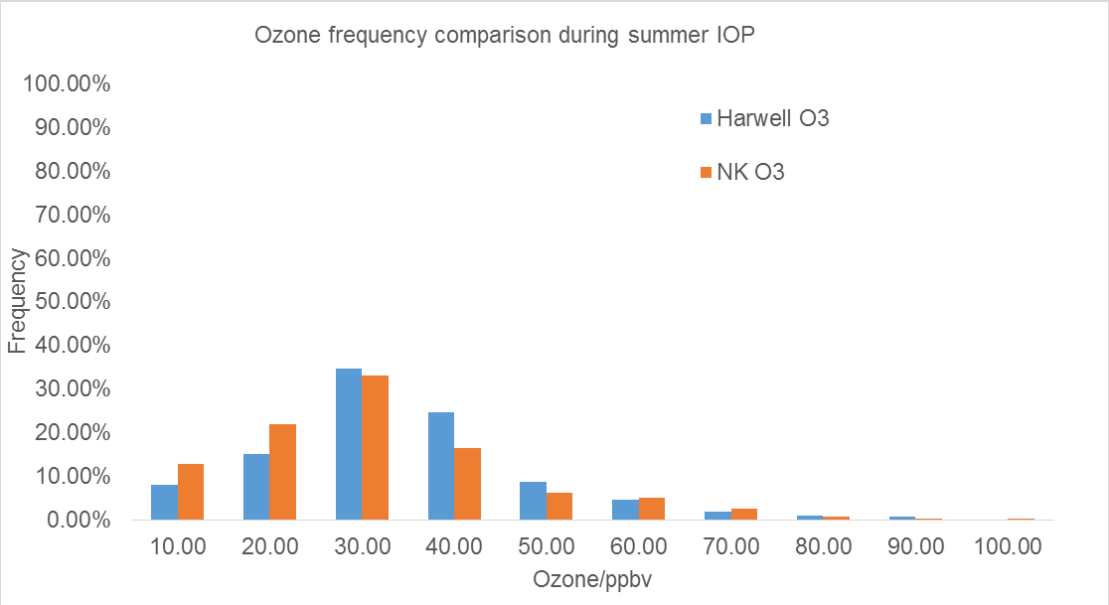

Figure 4.14. Frequency distribution of hourly O_3 mixing ratio measured at the Harwell (blue) and NK (orange) sites during the ClearfLo summer IOP – AURN data.

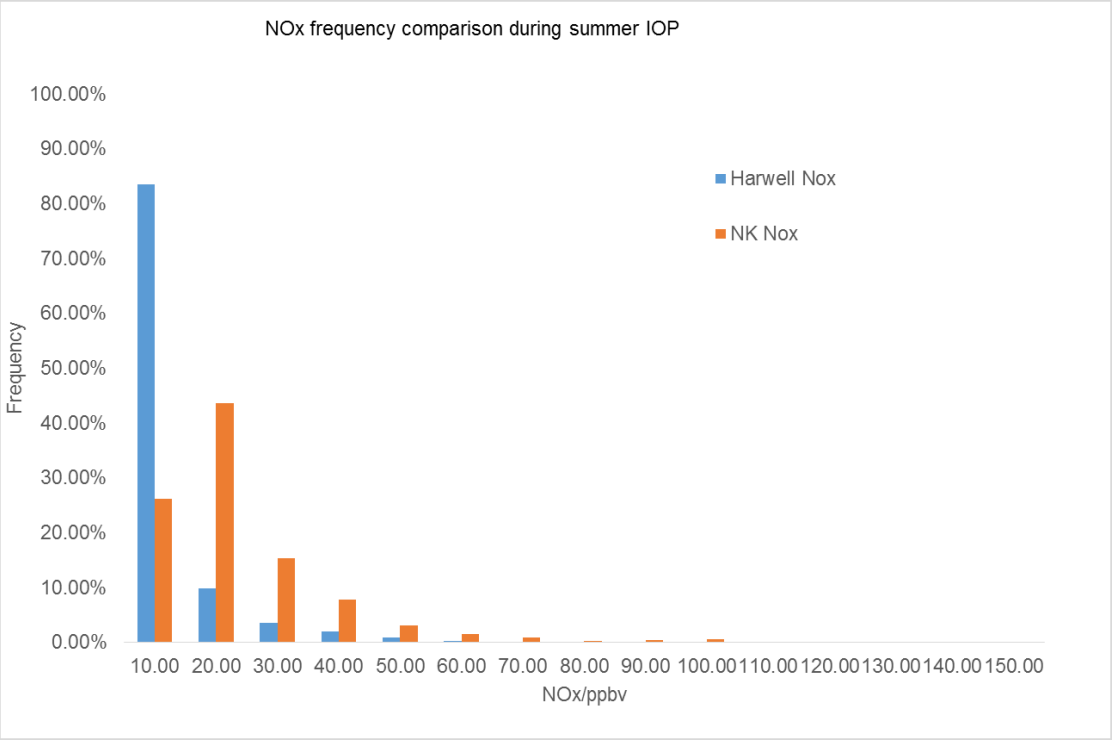

Figure 4.15. Frequency distribution of hourly NO_x mixing ratios measured at the Harwell (blue) and NK (orange) sites during the ClearfLo summer IOP – AURN data.

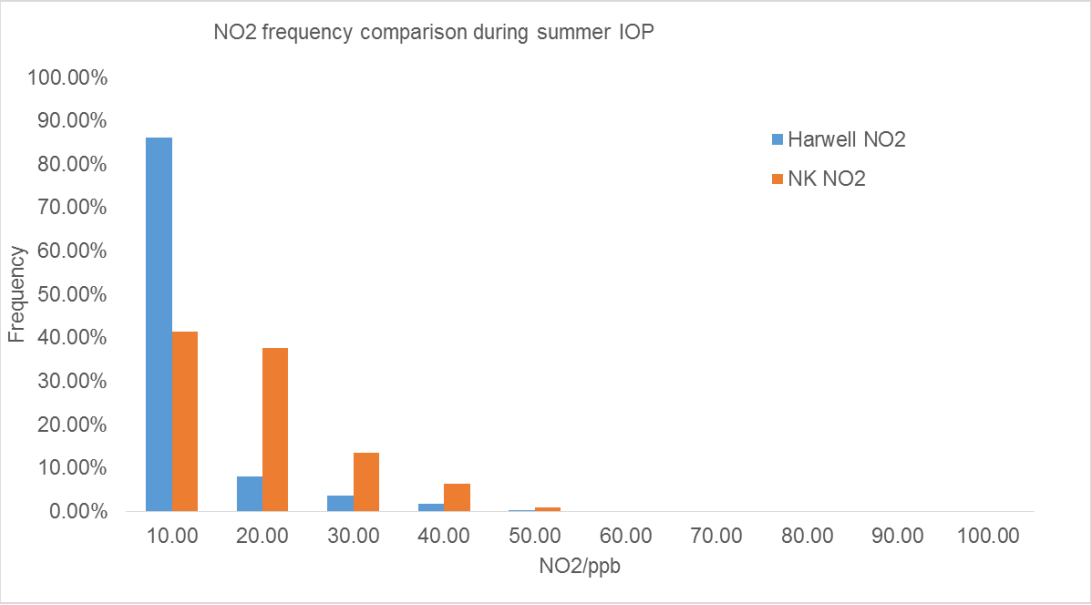

Figure 4.16. Frequency distribution of hourly NO_2 mixing ratio measured at the Harwell (blue) and NK (orange) sites during the ClearfLo summer IOP – AURN data.

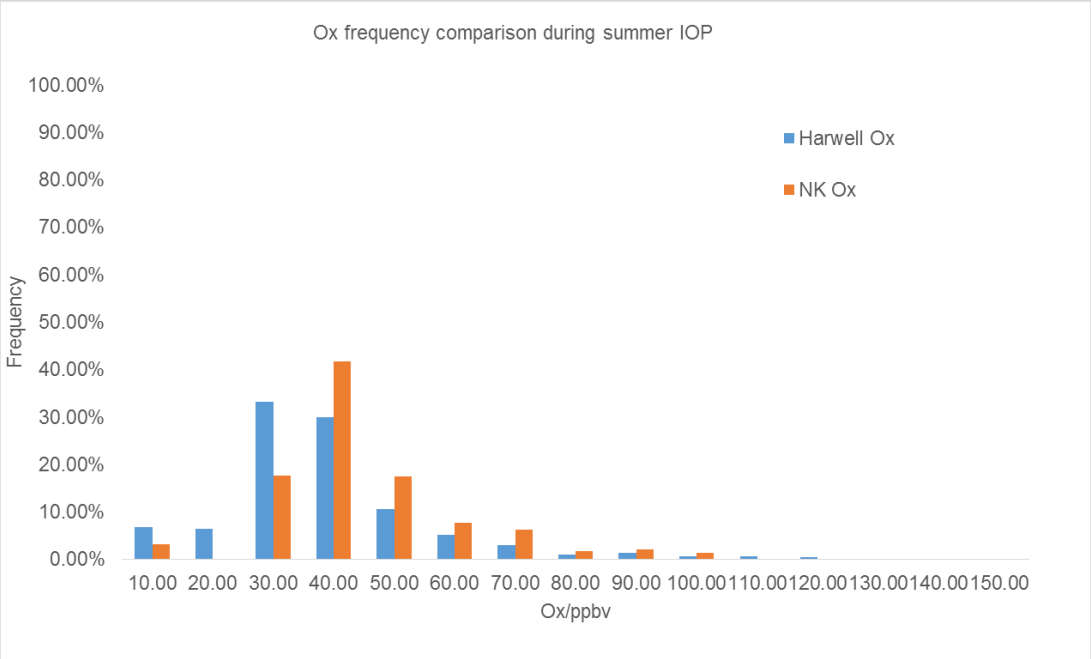

Figure 4.17. Frequency distribution of hourly O_x mixing ratio measured at the Harwell (blue) and NK (orange) sites during the ClearfLo summer IOP – AURN data.

Figure 4.14 presents the hourly O_3 mixing ratio frequency distributions between the contrasting NK and Harwell locations during the ClearfLo summer IOP. The data indicate that more than 50 % of the hourly O_3 mixing ratios were distributed between 20 and 40 ppb for both the urban (NK) and rural (Harwell) sites. The NK site had a slightly higher frequency of occurrence of hourly O_3 mixing ratios under 20 ppb; the Harwell site had a higher frequency of occurrence of hourly O_3 mixing ratios between 20 ppb and 50 ppb range. Both sites had similar O_3 frequency distributions (approximately 10%) in the 50 to 70 ppb range, with the NK site showing a slightly higher frequency of occurrence of this range. It was uncommon to see O_3 above 70 ppb at either site, with only 4% of all observed O_3 values above this limit.

Figure 4.15 shows pronounced differences in NO_x mixing ratios between rural (Harwell) and urban (NK) areas (as was expected). In general, the Harwell site had much lower levels of NO_x than NK. The Harwell site is a rural monitoring site, local traffic emissions are minor

in the surrounding area; NO_x mixing ratios at Harwell were predominantly distributed in the 0 to 10 ppb range (83 % of all values). In addition, the hourly mixing ratio at Harwell was below 20 ppb over 90 % of the time. In contrast, as an urban background site in central London, only 26 % of the hourly NO_x mixing ratios measured at the NK site were distributed between 0 and 10 ppb range. Most of NO_x mixing ratio values for NK were distributed in the 10 to 20 ppb range (43 % of all values). 23 % of hourly NO_x mixing ratios were between 20 and 40 ppb. In summary, at Harwell, hourly NO_x mixing ratios were below 10 ppb 83 % of the time, which represented typical rural conditions with modest NO_x emissions from anthropogenic sources. At NK, approximately 60 % of hourly NO_x mixing ratios were between 10 and 30 ppb, with 30 % above 30 ppb. As an urban background monitoring station, many more anthropogenic NO_x sources were to be expected than for Harwell. While the NK site is located in a residential area, it is more than 400 metres from the nearest major highway, the 6-lane A40. Traffic NO_x emissions were expected to be relatively low in the immediate vicinity of the NK site.

The overall NO_2 level at the Harwell site was lower than at the NK site during the summer IOP (Figure 4.16), displaying similar behaviour to the NO_x frequency distribution shown in Figure 4.15. Measured hourly NO_2 mixing ratios at Harwell were below 10 ppb over 86 % of the time during the summer IOP. In contrast, NO_2 hourly mixing ratios measured at the NK site were only below 10 ppb for less than half (41 %) of the time during the summer IOP. NO_2 mixing ratios at the NK site were between 10 and 30 ppb 51 % of the time, but were rarely observed to exceed 40 ppb: At the NK site, both the NO_x frequency distribution (Figure 4.15) and the NO_2 frequency distribution (Figure 4.16) showed very limited occurrence of NO_x/NO_2 levels in excess of 30 ppb (approximately 10 %). The frequency of occurrence of NO_x mixing ratios between 10 and 30 ppb was 60 %; it was close to the

frequency of occurrence of NO_2 (51%) at this range (reflecting the predominance of NO_2 within NO_x). NO_x mixing ratios at the NK site were under 10 ppb for 26 % of the total summer IOP period; NK NO_2 mixing ratios were under 10 ppb for 40 % of the total summer IOP time. Those two comparisons demonstrate the majority of NO mixing ratios to be below 30 ppb, and of NO mixing ratios making a minor contribution to the total NO_x level. The NO emission was not the dominant factor to contribute to NO_x levels that were higher than 40 ppb during the summer IOP. The urban decrement effect could potentially contribute to the low NO level at NK site. To examine this factor further, the frequency distribution of O_x ($=NO_2 + O_3$) was examined.

The O_x frequency distribution (Figure 4.17) shows similarities to a combination of the NO_2 and O_3 frequency distributions (previous Figures). At the Harwell site, O_x mixing ratios were under 20 ppb for 12 % of the total summer IOP period; while at the NK site, O_x levels were only below 20 ppb for 3 % of the time. 33% of hourly O_x mixing ratios at Harwell were distributed between 20 and 30 ppb, while for the NK site only 17% of the total hourly mixing ratios lay in this range. For the 30 to 50 ppb range, O_x levels represented 60 % of observations at NK and 40 % of observations at Harwell. At both sites, fewer than 10% of the hourly mixing ratios of O_x were above 50 ppb. The O_x frequency distribution (Figure 4.17) shows that the NK site had a higher frequency of occurrence of high levels of O_x than Harwell – indicative of direct emissions of NO_2 (rather than just of NO, which would not affect O_x), and/or net oxidant production (through either chemical processes or advection and/or entrainment).

The pollutant frequency distributions shown above (Figures 4.14-4.17) indicate that the Harwell site represented a typical rural environment with low levels of NO_x while the NK

site represented a typical urban environment with higher levels of NO_x. The similarity in O_3 levels between the two sites was possibly caused by the urban decrement effect, offsetting chemical ozone formation. However, during the polluted periods within the summer IOP (*i.e.* the FIOM period), levels of NO_x and O_3 were substantially elevated, leading to a markedly different pollutant frequency distribution.

4.2.2 Ambient NO_x and O_3 distribution during the "FIOM" pollution episode

A further pollutant frequency distribution analysis was performed for the FIOM period, similar to those described above for the overall summer IOP. This analysis was based on the four-day period of continuously measured data from the NK monitoring station during the FIOM period, 9-12 August 2012 inclusive. (Figure 4.18, 4.19, 4.20 and 4.21) Data from "FIOM" period was also included in the analysis for the whole summer IOP presented above, from Figures 4.14, 4.15, 4.16 and 4.17.

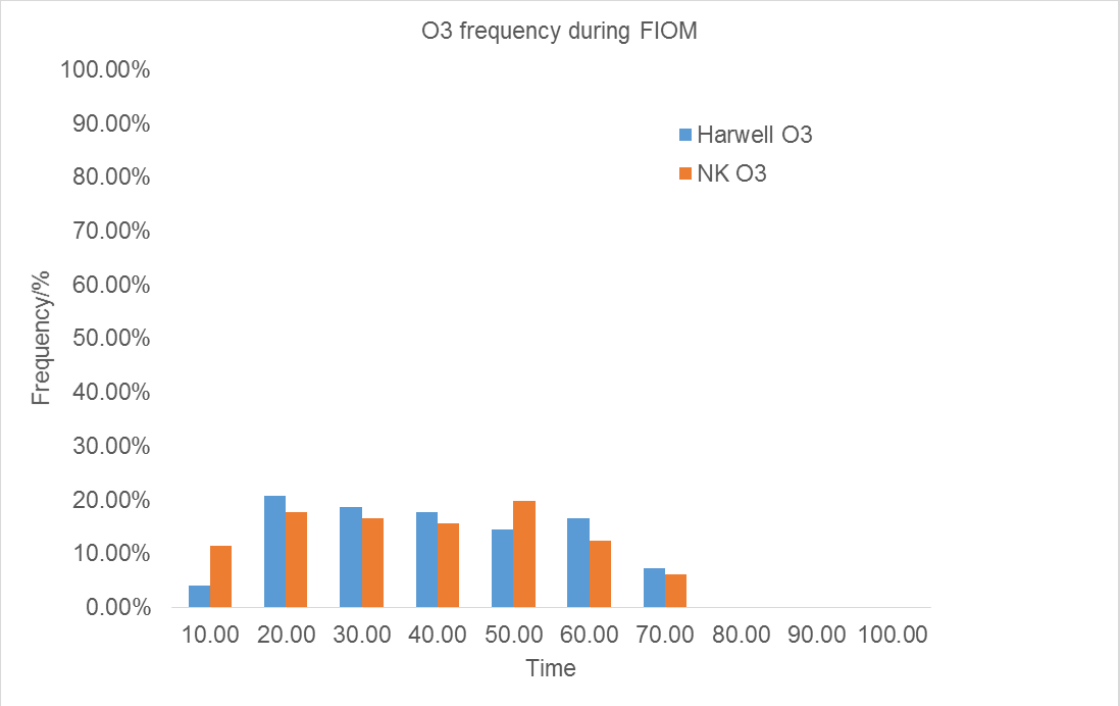

Figure 4.18. Frequency distribution of hourly O_3 mixing ratio measured at the Harwell (blue) and NK (orange) sites during the ClearfLo summer IOP – AURN data.

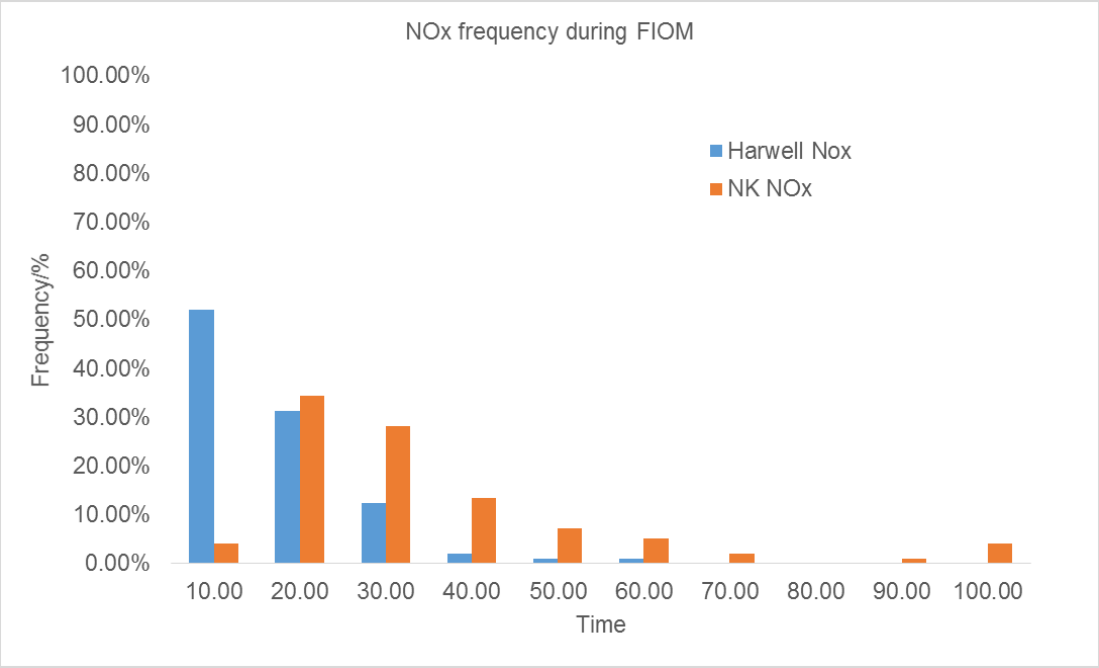

Figure 4.19. Frequency distribution of hourly NO_x mixing ratios measured at the Harwell (blue) and NK (orange) sites during FIOM – AURN data.

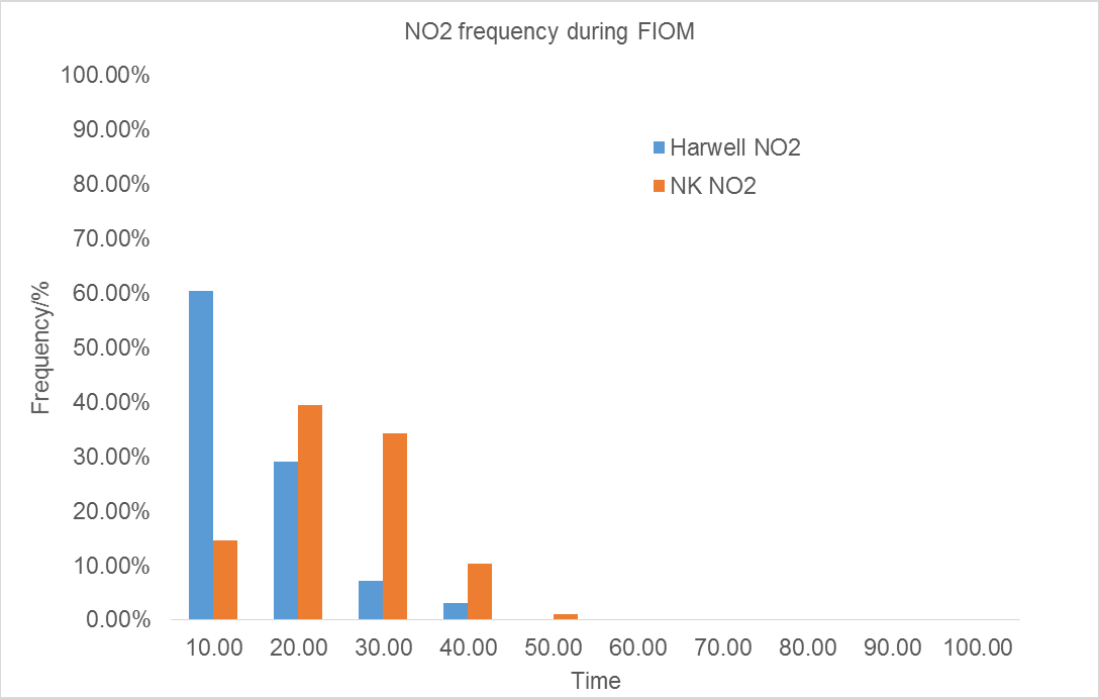

Figure 4.20. Frequency distribution of hourly NO_2 mixing ratios measured at the Harwell (blue) and NK (orange) sites during FIOM – AURN data.

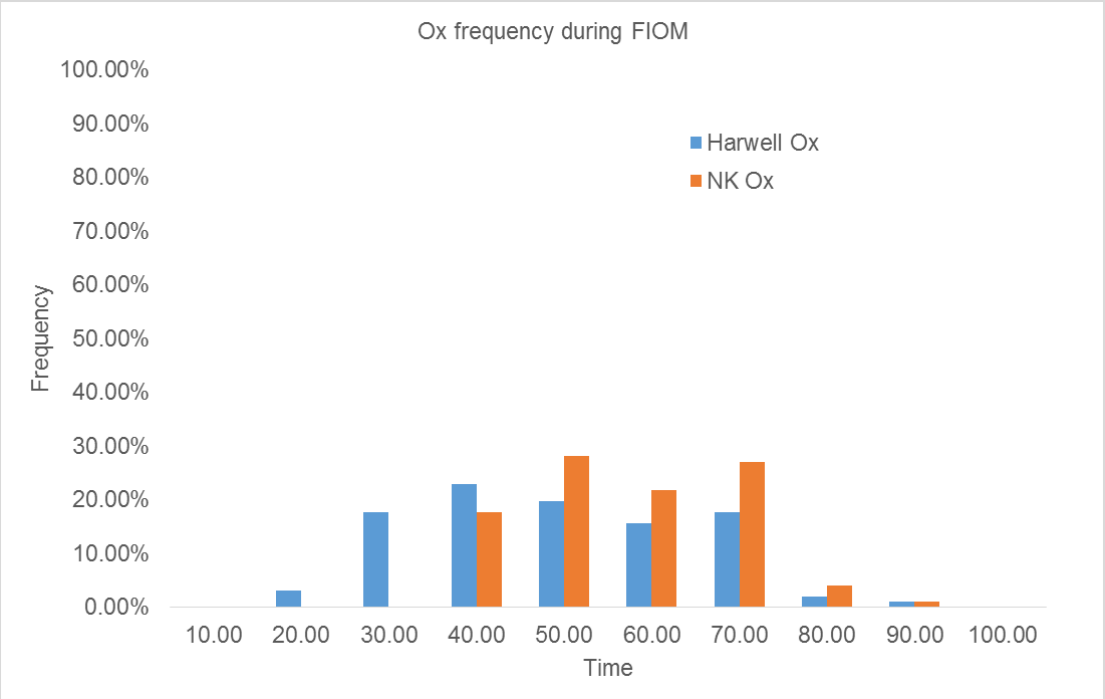

Figure 4.21. Frequency distribution of hourly O_x mixing ratios measured at the Harwell (blue) and NK (orange) sites during FIOM – AURN data.

Figure 4.18 shows the differential hourly O_3 mixing ratio frequency distribution for two locations (NK and Harwell) during the second pollution period (FIOM). The FIOM data indicated that approximately 50 % of the hourly O_3 mixing ratios were distributed between 10 and 40 ppb for both urban (NK) and rural (Harwell) sites during the FIOM period; The Harwell site showed slightly higher frequency of occurrence of hourly O_3 over NK site in this range. The NK site had a slightly higher frequency of occurrence of hourly O_3 mixing ratios between 40 and 60 ppb than Harwell site (35% compared with 32% during the FIOM period). Measured hourly O_3 mixing ratios above 60 ppb and less than 10 ppb were uncommon during the FIOM period, both NK and Harwell sites showed less than 10 % of O_3 frequency of occurrence in those ranges. In general, the differences between two sites' O_3 mixing ratios frequency distributions were minor, data indicated similar frequency of occurrence of O_3 in all ranges at two sites. However, the overall O_3 level during the FIOM were much higher than the O_3 levels during the whole summer IOP. Figure 4.18 (FIOM)

showed much higher frequency of occurrence of O_3 above 50 ppb than Figure 4.14 (Summer IOP) at both measurement sites. The overall O_3 levels were elevated during FIOM (Figure 4.6), but potentially on a regional basis.

The majority of hourly NO_x mixing ratios at the NK site were distributed between 10 and 30 ppb during FIOM (62%); only 4% of hourly NO_x mixing ratios were between 0 and 10 ppb. Hourly NO_x levels above 50 ppb were uncommon at NK site. In contrast, 52% of hourly NO_x mixing ratios were distributed between 0 and 10 ppb at Harwell site. The majority (83% of total values) of hourly NO_x mixing ratios at Harwell site were less than 20 ppb during FIOM. The Figure 4.19 pronounced higher frequency of occurrence of hourly NO_x (during FIOM period) above 20 ppb than the summer IOP at NK site, the Harwell site remained with low level of NO_x.

Figure 4.20 shows the frequency distribution of the hourly NO_2 mixing ratio during the FIOM period, displaying similar behaviour to the summer IOP NO_2 frequency distribution shown in Figure 4.16. Hourly NO_2 mixing ratios at the Harwell site was below 10 ppb over 86 % of the time during the summer IOP; only 60 % of the NO_2 mixing ratios were distributed below 10 ppb during the FIOM. At the NK site, the majority (79%) of NO_2 mixing ratios were distributed between 0 and 20 ppb during the summer IOP; in contrast, the majority (73 %) of NK NO_2 mixing ratios were distributed between 10 and 30 ppb during the FIOM period. Figure 4.20 shows evidence of elevated overall NO_2 levels in the urban area during the FIOM period.

Figure 4.14 presents a much higher overall O_x level at NK site than Harwell site, 77 % of the NK hourly O_x mixing ratios were distributed between 40 and 70 ppb, while only 53 % of Harwell hourly O_x mixing ratios were distributed in this range. Over 40 % of the Harwell

hourly O_x mixing ratios were distributed between 10 and 40 ppb, only 17 % of the NK hourly O_x mixing ratios were distributed in this range. During the FIOM, the NK site had a much higher frequency of occurrence of hourly O_x mixing ratios above 50 ppb than the summer IOP. The minimum NK hourly O_x mixing ratio was 30 ppb during the FIOM period, in contrast, 20 % of the summer IOP's hourly O_x mixing ratio were below 30 ppb. The Harwell site displayed similar behaviour of hourly O_x mixing ratio as the NK site. The majority (76 %) of Harwell hourly O_x mixing ratios were distributed between 30 and 70 ppb during the FIOM period; the majority (63 %) of Harwell hourly O_x mixing ratios were distributed between 20 and 40 ppb during the summer IOP. Those data indicated that the overall O_x levels were elevated at both sites during the FIOM.

The FIOM frequency distribution analysis displayed different behaviour in hourly NO_x and O_3 mixing ratios over a short (four day) pollution period than for the overall summer IOP. The FIOM frequency distribution showed elevated NO_x and O_3 levels at both NK and Harwell sites. The two sites both had elevated overall O_3 levels; the NK site had slightly lower overall O_3 levels than Harwell site. The elevated NO_x level reflected an increased urban decrement causing lower overall O_3 at the NK site. This analysis confirmed occurrence of the urban decrement effect during the OPR measurement period.

To conclude, the NO_x and O_3 pollutants frequency distributions analysis did not consider any meteorological factors or effects from other related pollutants through photochemical reactions. However, the analysis highlights the potential contributions of local NO_2 emissions, and of ozone formation chemistry, to O_x levels at the NK site, and the impact of the "urban decrement" effect from abundant NO emissions upon both O_3 and NO_2 levels. The analysis shows the potential for direct ozone / oxidant production rate measurements –

i.e. measures of $p(O_x)$ as derived from the OPR system – to further probe these factors. This is the focus of the following sections.

4.3 Ozone Production Rate (OPR) measurement periods and data availability

The OPR ambient measurement system was deployed at the North Kensington site from 7 January to 28 January 2012 as part of the ClearfLo winter IOP, followed by measurements from 25 July to 19 August 2012 as part of the ClearfLo summer IOP. The OPR system was only operated on days with clear skies and good weather conditions (no rain / mist / fog). During the winter measurements, the OPR system suffered a number of technical difficulties and teething problems; moreover, the weather was cloudy and rainy during many measurement days – and in any case photochemical ozone formation would be expected to be minimal. The winter measurement period was considered as a trial to test the basic deployment and stability of OPR system, with the data obtained during that period deemed to be unsuitable for use; these are not discussed further. Summer measurements were successfully performed during most days with clear sky and sunny weather during the ClearfLo summer IOP: The successful measurement days were (parts of) 25, 26, 27, 30 of July, and 2, 3, 6, 9-12, 14 and 17-19 of August 2012. There were however many minor data gaps during the successful measurement days' OPR data, caused by calibrations / tests and episodically by an intermittent software (communication) bug.

4.3.1 Ambient Composition: Measurement Correlations

From 26 July-19 August (throughout the summer IOP), the University of Birmingham's ozone and NO_x monitors were operated to measure ambient O_3 and NO_x mixing ratios, in parallel with the AURN instruments. In both cases, instrument inlets were located adjacent to the Birmingham portacabin, 40 metres south of the AURN North Kensington monitoring

site. Data from the two instruments agreed well - see Figures 4.22, 4.23 and 4.24 (time series of O_3, NO and NO_2 of both measurements) and Figure 4.25, 4.26, 4.27 and 4.28 (correlation plots of both measurements).

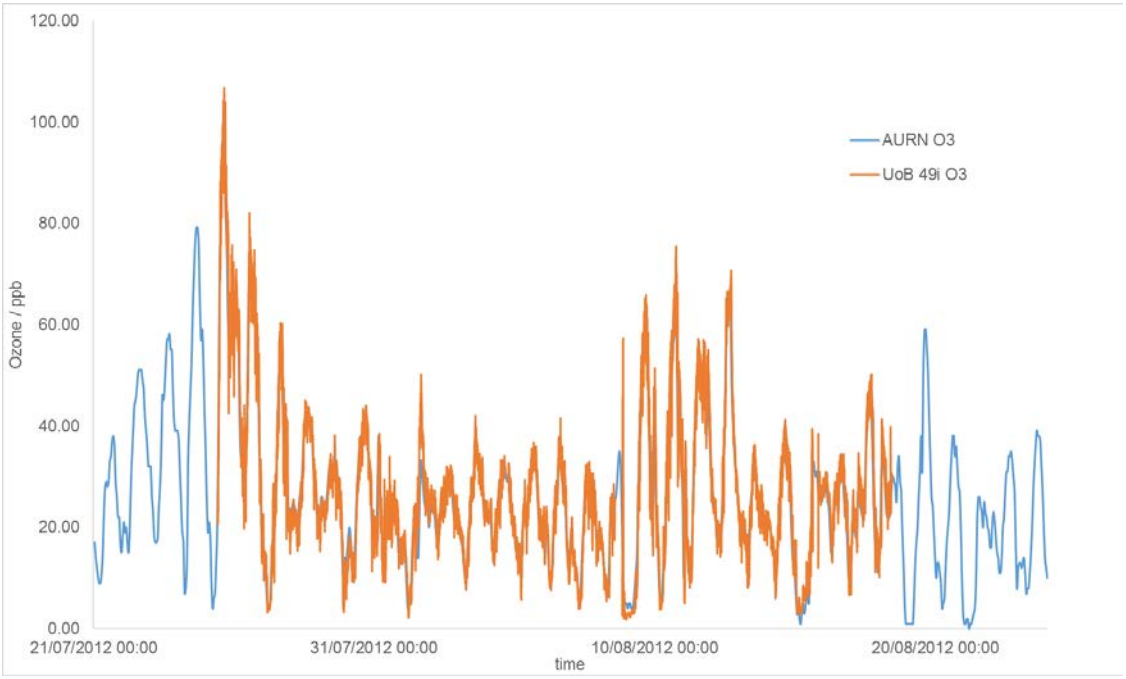

Figure 4.22. Comparison between ambient O_3 measured using the UoB's Thermo 49i monitor (sampling from the Birmingham portacabin) and data from the NK AURN site.

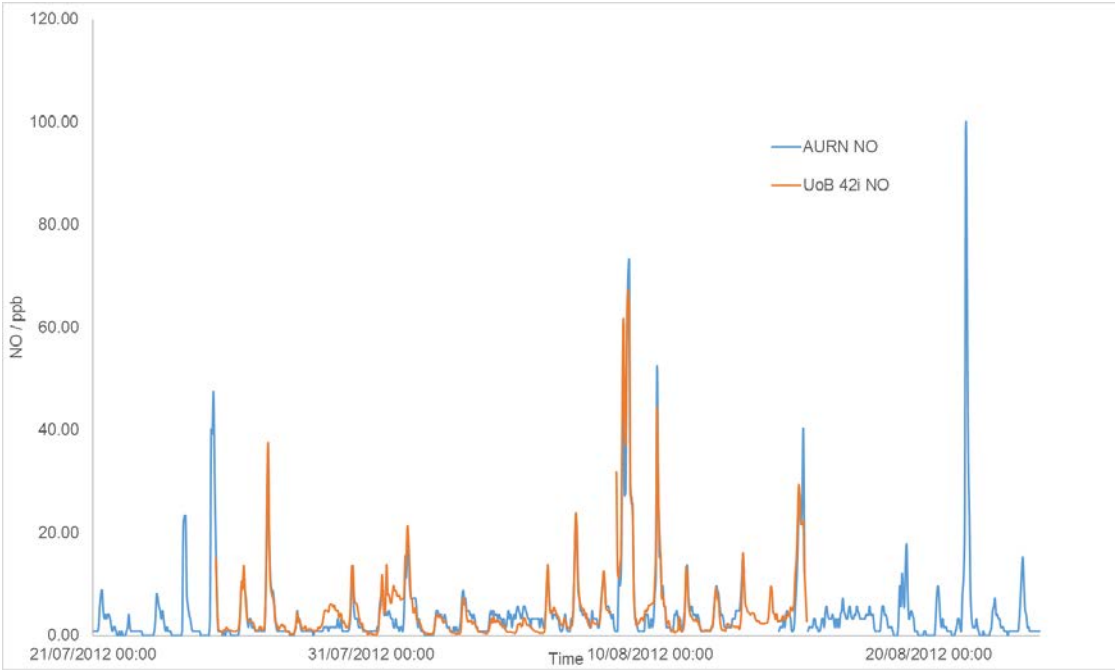

Figure 4.23. Comparison between ambient NO measured using the UoB's Thermo 42i monitor (sampling from the Birmingham portacabin) and data from the NK AURN site.

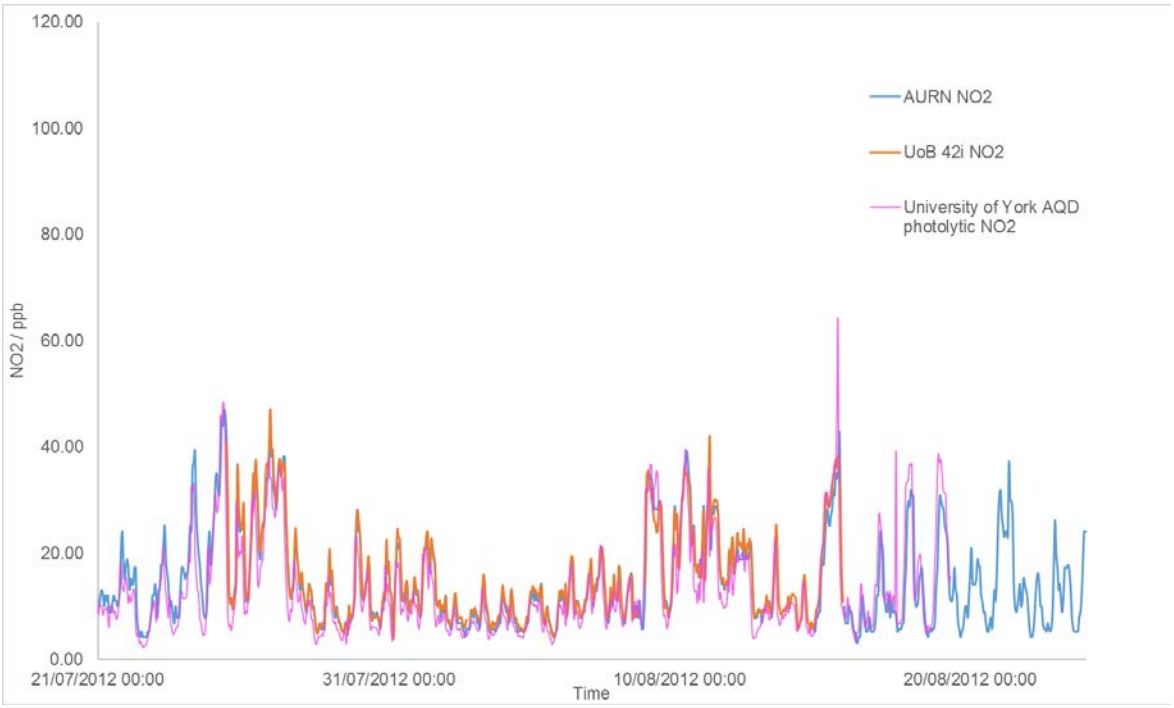

Figure 4.24. Comparison between ambient NO_2 measured using UoB's Thermo 42i monitor (Sampling from the Birmingham portacabin), data from the NK AURN site and data from University of York's AQD NO_x monitor.

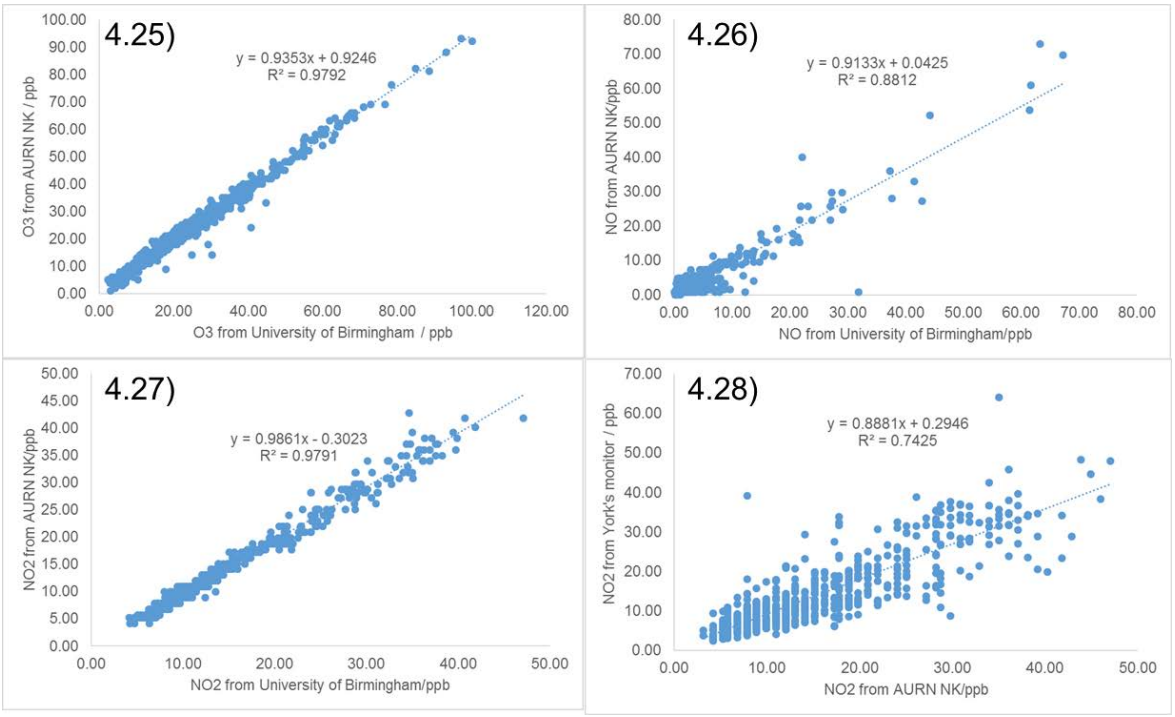

Figure 4.25. Regression analysis between the UoB and AURN O_3 data at NK site; Figure 4.26. Regression analysis between the UoB and AURN NO data at NK site; Figure 4.27. Regression analysis between the UoB and AURN NO_2 data at NK site; Figure 4.28. Regression analysis between the AURN and University of York NO_2 data (photolytic NO_2 monitor) at the NK site.

The Birmingham (and NK AURN) Thermo 42i NO_x monitors in fact measure all ambient NO_y species as NO_2; they operate via a thermal decomposition approach (heated Mo catalyst) which is not selective in reducing NO_2 to NO, and rather will also convert other NO_y species such as HONO and N_2O_5 into NO, leading (in principle) to slightly overestimated ambient NO_2 levels. The University of York's photolytic based AQD NO_2 monitor does not retrieve NO_y species as NO_2 in its internal reading, and so should give a more specific / accurate measurement of ambient NO_2. The correlation plot (Figure 4.28) between York and AURN NK suggested measured ambient NO_2 levels from York were lower than those obtained by the AURN instrument, consistent with the assumption of overestimated ambient NO_2 level.

However, the differences between the two data sets were relatively small. For consistency in treatment of NO_x measurements (and convenience), the AURN data were used in the following analyses of this chapter.

4.3.2 Data availability and definitions

In addition to ambient NO_x and O_3 data, a range of other photochemical parameters were measured during ClearfLo summer IOP and are utilised in the following analyses. These measurements (summarised in Table 4.2) included HONO (measured by the University of York/Wuppertal using the LOPAP approach), OH (measured by University of Leeds using the Fluorescence Assay by Gas Expansion-FAGE technique) and HO_2 (measured by University of Leeds using the FAGE technique). Meteorological parameters were also measured during the summer IOP. Those parameters include temperature, RH and wind speed/direction. The radiation parameters (photolysis frequencies) $j(O^1D)$ and j(HONO), were measured by the University of Leicester Spectral Radiometer. A full list of data and their sources is presented in table 4.2,

Data discussed	Sources
O_3	AURN sites and UoB Thermo 49i monitor
NO	AURN sites and UoB Thermo 42i monitor
NO_2	AURN sites and UoB Thermo 42i monitor
HONO	LOPAP approach by University of York
HO_2	University of Leeds
RO_2	Not available at the time of writing
OH	University of Leeds
ΔO_3	OPR system, University of Birmingham
jO^1D	PERCA University of Leicester
jHONO	PERCA University of Leicester
VOC (total reactivity)	University of Leeds
Meteorological data (temperature, wind speed/direction)	AURN sites

Table 4.2. A list of data discussed in chapter 4 and 6, data sources included.

In the following discussion, a specific terminology for the different "data products" discussed is used, defined as follows:

Specific word	Definition
ΔO_3	The measured raw signal value by OPR system. Unit is ppb.
dO_x/dt	dO_x is the change of actual measured O_x value by AURN NK site, dt is the change of unit time on hourly basis, the dO_x/dt represent the rate of change of measured O_x in unit time. Unit is ppb $hour^{-1}$.
dNO_x/dt	dNO_x is the change of actual measured NO_x value by AURN NK site; dt is the change of unit time on hourly basis, the dNO_x/dt represent the rate of change of ambient NO_x in unit time. Unit in ppb $hour^{-1}$.
$p(O_x)$	The measured Ox production rate from OPR system, it was derived by the measured ΔO_3 divided by residence time. Unit in ppb $hour^{-1}$.
p(OH)	The incomplete production rate of OH, derived from calculation. It is the combination of HONO photolysis, ozone photolysis and Alkene species reaction with ozone. Unit in molec cm^{-3} s^{-1} or ppb $hour^{-1}$.
$p_c(O_x)$	(Estimated) Calculated chemical oxidant production rate from HO_2 measurement
$l(O_x)$	Estimated chemical oxidant loss rate
$p_e(O_x)$	Estimated net chemical oxidant production rate: $p_e(Ox) = p_c(O_x) + l(O_x)$

Table 4.3. Definitions used in subsections of chapter 4.

As previously described in Figure 4.6, there were two heavy pollution periods during the summer IOP. The OPR system (and many other ClearfLo instruments) were undergoing calibration and trial measurements during first pollution period, as the summer IOP was only scheduled to start on 25 July 2012; consequently, the measured data were too incomplete for useful analysis. The second pollution period (the FIOM period) ran from 9-12 August (Thursday to Sunday). The OPR and most other instruments / species measurements were fully operational during second pollution period. The FIOM period was characterised by sunny days with clear sky conditions.

4.4 Four days intensive OPR measurement period (FIOM)

The FIOM period was particularly important for the OPR system evaluation, as it was the first time that the OPR system had continuously measured daily diurnal data, alongside measurements of related gas-phase photochemical oxidation pollutants from other institutions' instruments. During 9 August to 12 August 2012, the skies were clear with few to no clouds during the daytime; the 24 hour-mean temperature during this short period was 22 °C. The measured temperature, NO_x and O_3 time series during the FIOM period are shown in the following Figure 4.29,

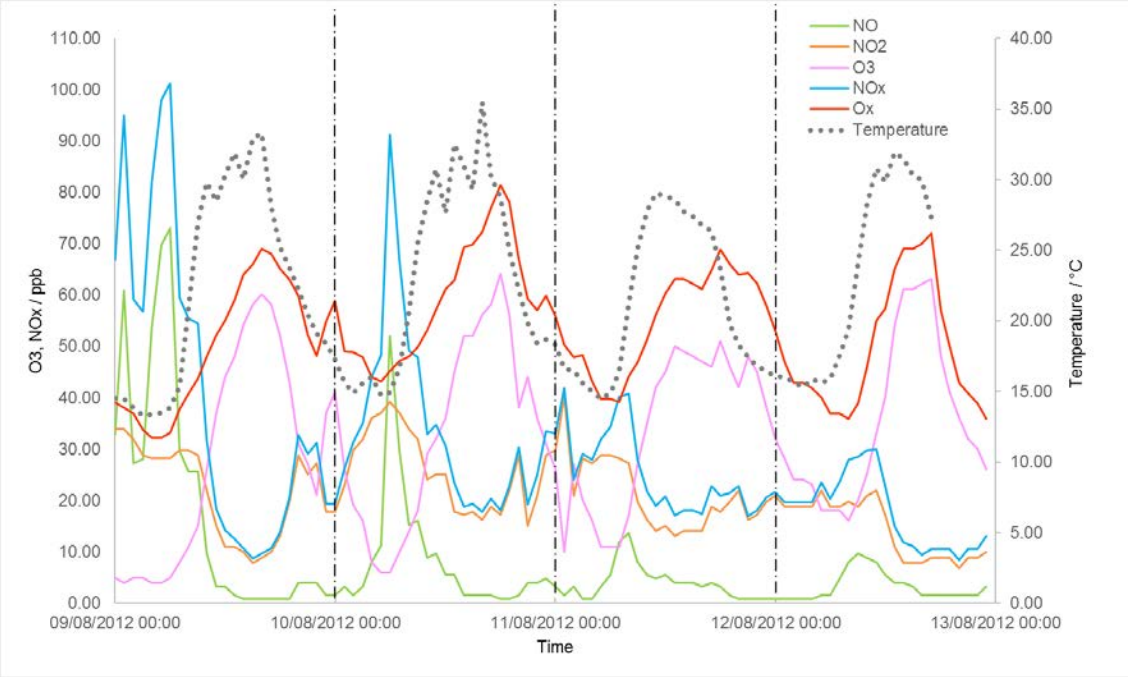

Figure 4.29. Temperature, NO_x and O_3 levels during the FIOM period. Data from the AURN NK site are used.

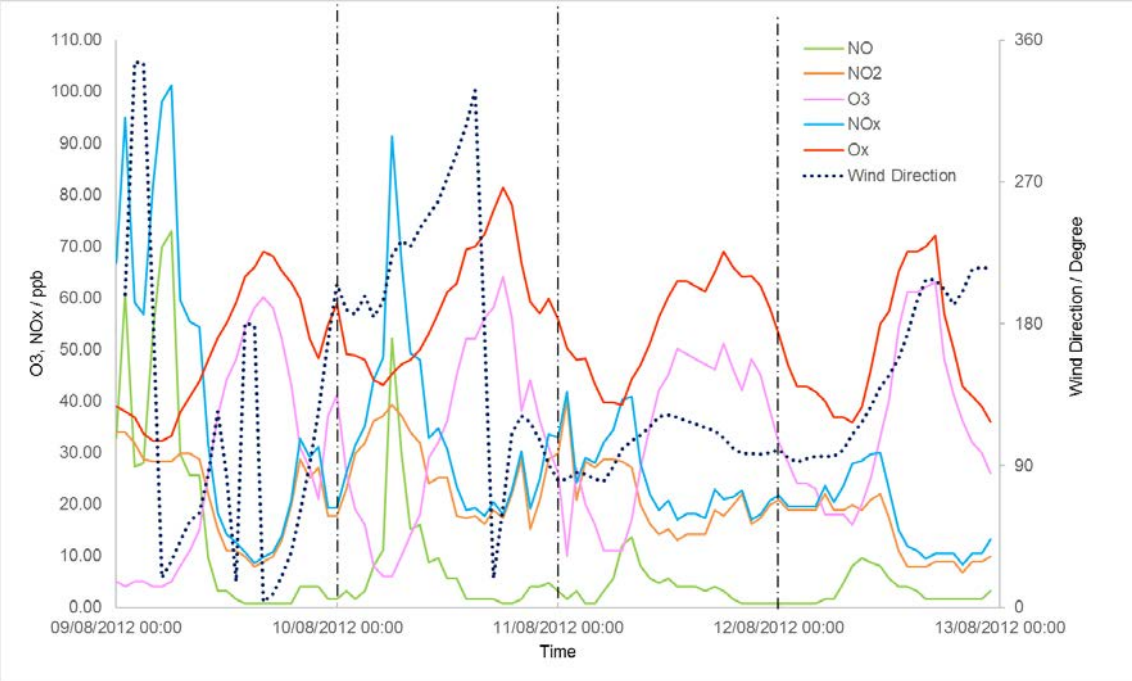

Figure 4.30. Wind direction, NO_x and O_3 levels during the FIOM period. Data from the AURN NK site are used.

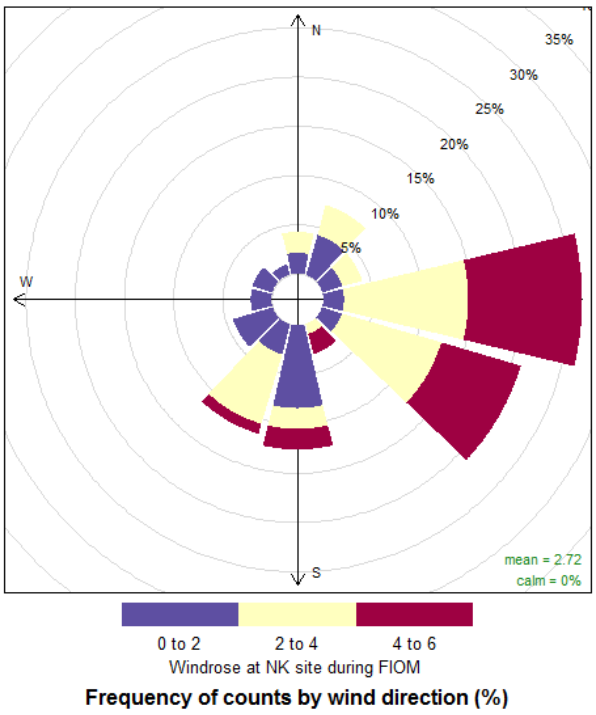

Figure 4.31. Wind rose at NK site during the FIOM period, prevalent wind direction was predominantly easterly. Data from AURN NK site

As Figure 4.31 shows, the wind direction on NK site was highly variable with many fluctuations on 9th and 10th August 2012, but it was relatively stable on 11th and 12th August 2012. This phenomenon suggests the air mass origin could be different between first two day period and second two day period. A Hybrid Single Particle Lagrangian Integrated Trajectory Model (HYSPLIT) model (Stein *et al*., 2015) was set to determine air mass origin of NK site during the FIOM.

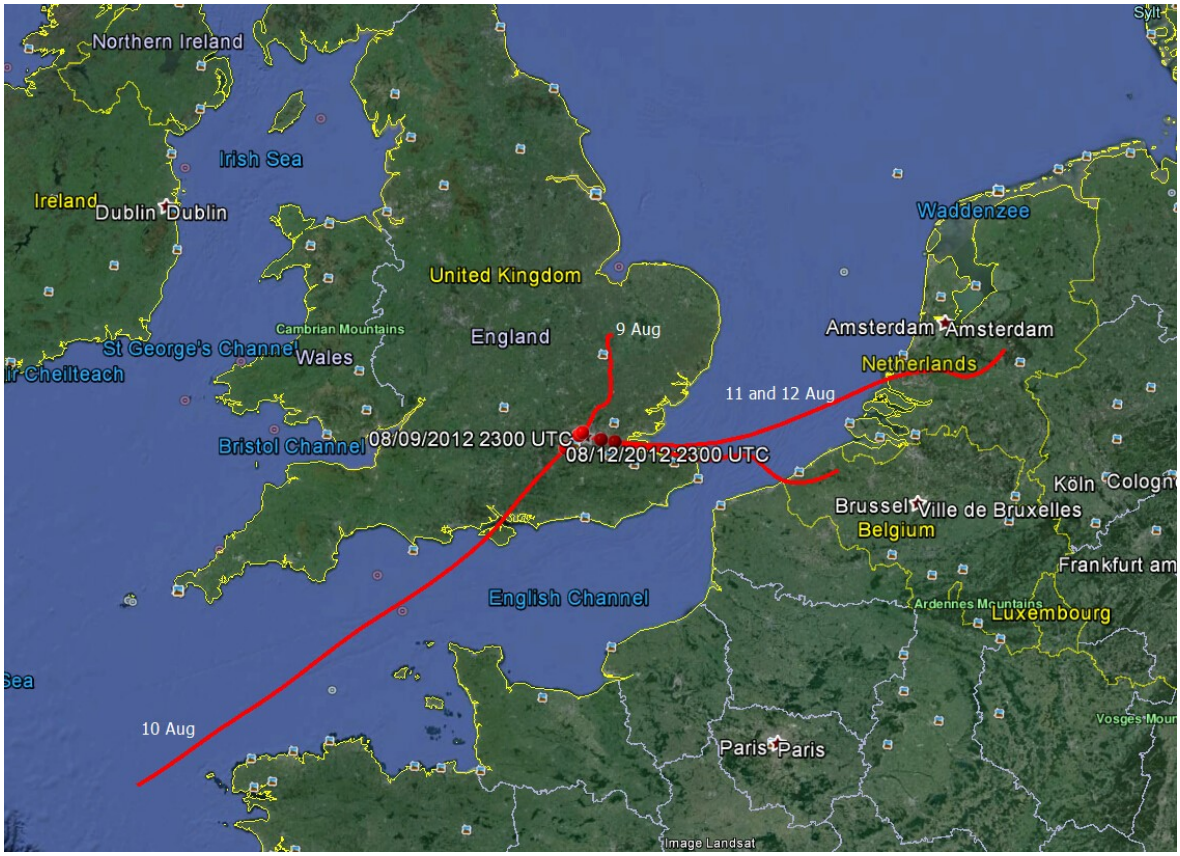

Figure 4.32. HYSPLIT back trajectory model results for air mass origin of NK site during FIOM period, red lines indicate air mass moving path prior to each measurement day-9th, 10th, 11th and 12th August 2012 (Stein *et al*., 2015).

According to the HYSPLIT results in Figure 4.32, it was clearly that the air mass origins of NK site on the second two day period (9th and 10th August 2012) were both from western Europe area, wind directions were mostly east. The air mass origins of NK site during the first two day period were completely different from each other and the second two day period.

This distinction is also apparent in the pollutant time series plots (Figures 4.29 and 4.30), and suggests it would be more logical to consider FIOM as two separate "two day periods" - 9th and 10th August as first two day period; 11th and 12th August as the second two day period in the following data analysis sections. Due to the similarity of air mass origins and stable wind directions on 11th and 12th August, the second two day period was considered optimal for both internal comparison between measurements on 11th and 12th August and external comparison with other indirect method of estimating oxidant production rates.

During the FIOM period, the daily ozone mixing ratio typically started increasing in the early morning as solar radiation initiated photochemical processes, and potentially as a consequence of mixing from aloft (from residual boundary layer air containing ozone, into the boundary layer itself which would have undergone ozone depletion overnight due to deposition). Ambient temperature rapidly rose to follow the solar radiation in the early morning. The NO_x level sharply rose at around 5:00 to 6:00 marking the onset of the "rush hour", then rapidly fell with the end of the peak traffic period. Ozone levels reached their peak around 13:00 to 14:00, and were maintained at around 60 ppb from 14:00 to 18:00 in the afternoon before beginning to fall in late afternoon. At the same time, NO_x levels rose again as the O_3 level decreased, this is the second peak that caused by "rush hour" traffic emission. Unlike the typical double peaks NO_x diurnal pattern during the summer IOP, this behaviour was only observable (but not apparent) on the first two day period, which were Thursday and Friday. During the second two day period, 11th and 12th August were weekend days, the second peak of NO_x in the afternoon was absent due to the lowered traffic.

The O_x (NO_2 + O_3) trend, combining the NO_2 plus ozone trends, followed similar diurnal cycles to the ozone trend; O_x levels increased in the morning then reached their diurnal peak

around 13:00 to 14:00, followed with a descending trend in the late afternoon. The measured OPR ΔO_3 signals (the measured differential O_3 value from the instrument, without the residence time correction applied, in contrast to $p(O_x)$) increased in the early morning and reached peak levels around 9:00 to 11:00, after the middle of the day it dropped, reaching a negative value which was maintained through the afternoon as net ozone destruction began. Diurnal OPR ΔO_3 signals are shown with ambient O_3 and O_x levels to present a clearer view in the following figure,

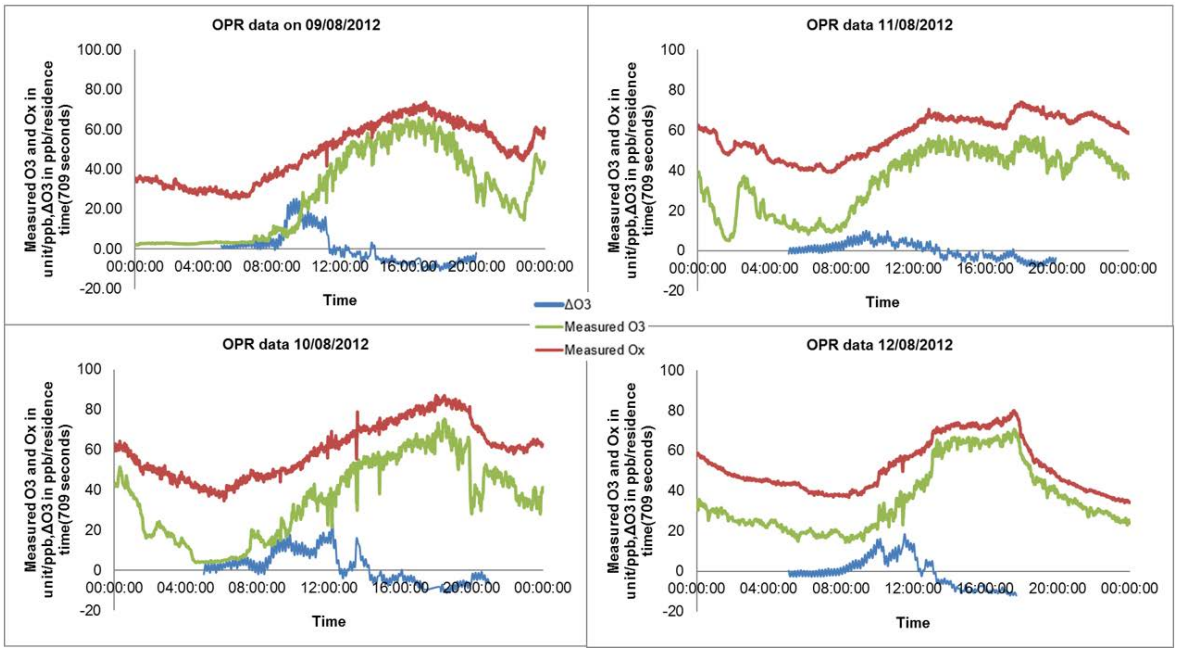

Figure 4.33. Diurnal measured ambient O_3, measured OPR instrument ΔO_3 signal and measured ambient O_x (O_3 + NO_2) during each day of the FIOM period.

During the FIOM period, the diurnal behaviour of the measured ambient O_3 mixing ratio was to increase in the morning then decrease in the late afternoon as expected. O_x levels steadily follows a positive trend to up to 80 ppb around 15:00 in the afternoon, then fall back in the afternoon. OPR ΔO_3 signals have the similar diurnal behaviour, but started rising up much earlier in the morning (8:00), then rapidly dropped to negative values. However, the

OPR ΔO_3 signals reached their diurnal peak levels on different time during the first two day period, but they reached diurnal peaks on similar time during the second two day period.

The nature of the O_3 and O_x trends during daytime may be influenced by three factors: The Photochemical Steady State (PSS), traffic emissions, and the chemical ozone production (and removal) processes. Each of these factors is considered in turn below.

4.4.1 Photochemical Steady State (PSS) Impacts

During a sunny day, in the absence of all other processes the PSS continuously changes the mixing ratio of NO_x and O_3 as sunlight levels vary with solar zenith angle, as defined by the equations presented below,

$$NO_2 + h\nu \rightarrow NO + O \quad (4.1)$$

$$O + O_2 + M \rightarrow O_3 + M \quad (4.2)$$

$$NO + O_3 \rightarrow NO_2 + O_2 \quad (4.3)$$

If the PSS was the only factor that was involved in ozone chemistry, in the absence of any other factors, as the sun rises, O_3 levels would be expected to increase as a consequence of the NO_2 photolysis reaction. At the same time, NO_2 levels would be expected to decrease, and NO levels to rise. The O_3 level would be expected to reach its diurnal peak around noon (at the maximum of solar radiation intensity / minimum solar zenith angle). As SZA (Solar Zenith Angle) increases again, O_3 levels would start to decrease as O_3 continuously shifts to NO_2 by reacting with NO. Consequently, during the day time, the NO trend would follow the same trend as O_3, while the trend for NO_2 would be the opposite shape. If only the PSS factor occurred, measured O_x levels would be constant / not vary during the daytime. However, the diurnal measured O_x trend during four days period showed a positive trend in

the morning then become negative trend in the afternoon, pointing to the presence of additional processes / factors.

4.4.2 Traffic Emissions

Traffic emissions are expected to be an important control that contributes to the changing O_x levels at the NK site (urban site in a major city). As discussed in chapter 1 section 1.4.1, during both morning and afternoon "rush hours", traffic emissions were thought to cause elevated NO_x levels (primarily in the form of NO; Figure 4.14c), leading to a typical double peak behaviour at NK site, which is shown in following figure,

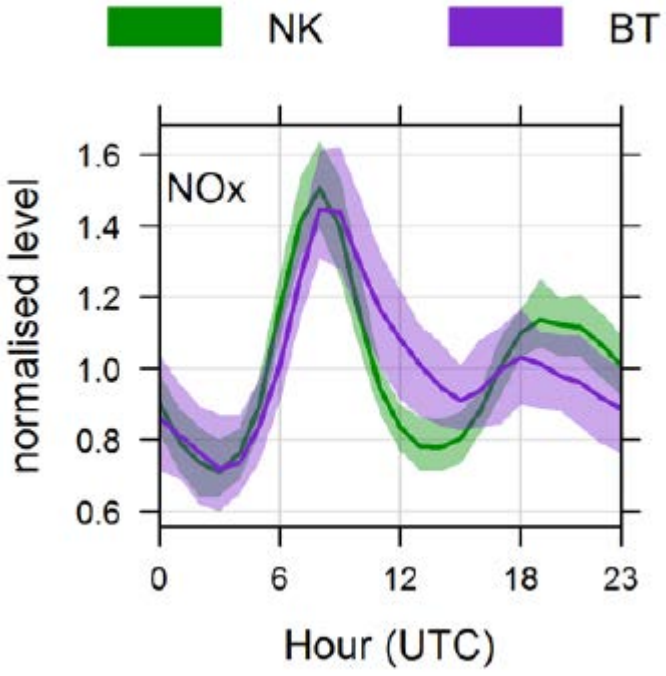

Figure 4.34. Mean diurnal variations of NO_x concentrations for the long-term measurement at NK site (from 24 January 2012 to 24 June 2013), normalised by the mean concentration at NK. Shaded areas represent 95% confidence intervals (Crilley *et al*., 2015)

As discussed in previous Figure 4.14, the characteristic NO_x double peak behaviour was only observable (but not predominant) on 9th and 10th August 2012 (Thursday and Friday). Due

to the lack of local traffic data, it was not certain if the somewhat obscure NO_x second peak in the afternoon was due to lower traffic than other days during summer IOP.

The following correlation plots compare the measured NO_x levels with measured CO and black carbon (both essentially conserved tracers of traffic emissions - particularly diesel emissions in the case of black carbon) and confirmed that the NO_x levels were highly correlated to both CO (within the limited precision of the observations at the low levels of CO observed) and to black carbon, as anticipated for a predominantly traffic source of NO_x during FIOM (Figure 4.35).

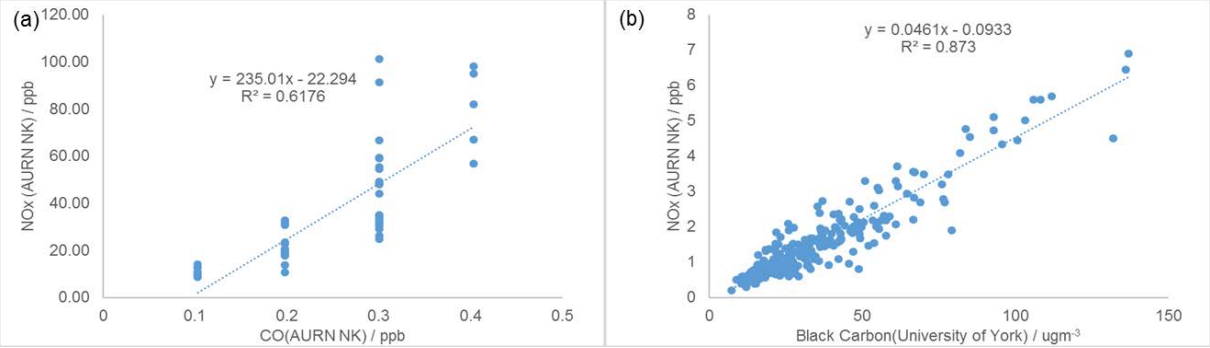

Figure 4.35. (a) Regression analysis between the CO and NO_x data at NK site; (b) Regression analysis between the Black Carbon and NO_x data at NK site. Both data from (a) and (b) were measured on 9 and 10 August 2012. CO and Black Carbon data from University of York.

4.4.3 Chemical Ozone Production Processes

NO_x actively participates in radical chemistry, during the day time through NO reactions with peroxy radicals to produce NO_2, the photolysis of which leads to net chemical ozone production. Net photochemical ozone production is thus linked to the production of OH (forming peroxy radicals through reaction with VOCs), the availability of NO, and of solar radiation to drive NO_2 photolysis. However, emission of substantial quantities of NO also leads, through the photochemical steady state, to the conversion of O_3 into NO_2; this effect

has a negative impact on ozone levels, particularly during peak traffic periods, and heightened in the early morning and late afternoon (as the NO_2 photolysis by solar radiation is reduced). It is known as the "urban decrement effect". However, the OPR measurements are blind to this factor as the instrument measures the chemical production / removal of O_x (O_3 + NO_2), rather than that of ozone. The third chemical factor of relevance is the destruction of O_x, for example through the formation of nitric acid (via OH + NO_2), alkyl nitrates (as a minor channel of peroxy radical + NO reactions), and chemical ozone destruction via HO_2 + O_3 and OH + O_3 reactions. The observed ozone / oxidant chemical production / removal rates from the OPR system during the FIOM period are discussed in the context of these mechanisms in the following sections.

The observed O_x levels during the FIOM period is shown in Figure 4.28 which compares $p(O_x)$ derived from the OPR instrument, and the observed $d(O_x)/dt$ from the *in situ* observations. Note that, in principle, these are different quantities as the change in the *in situ* mixing ratios ($d(O_x)/dt$) derives from a combination of transport, emission, deposition and mixing factors.

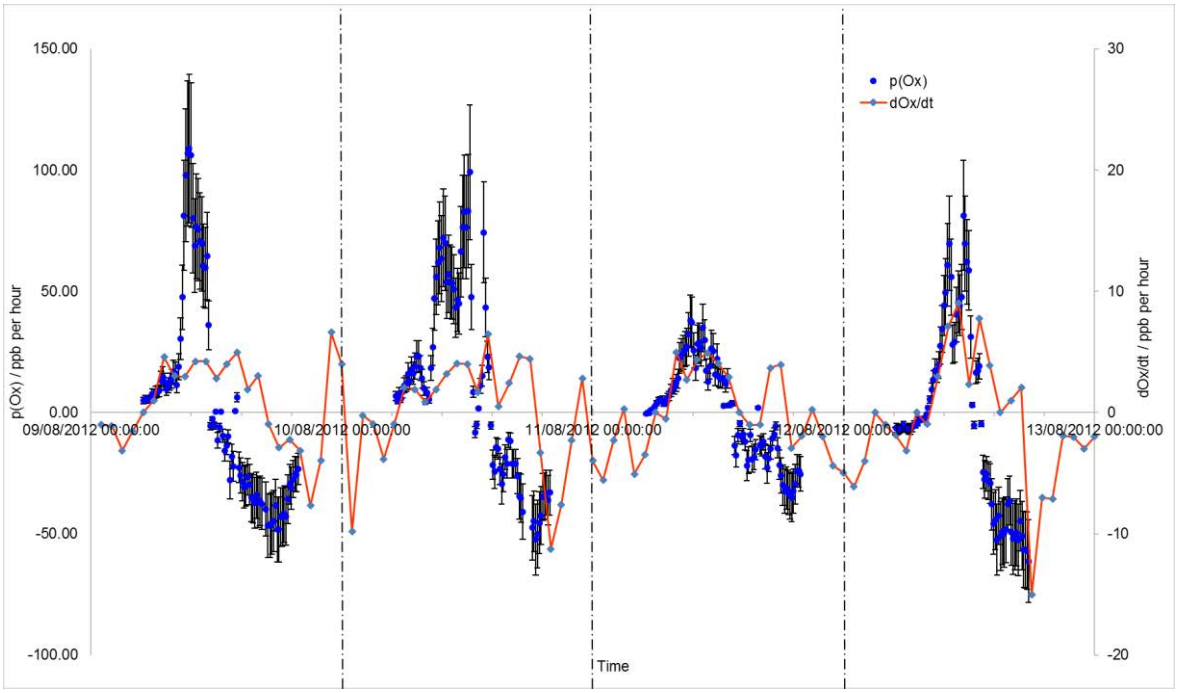

Figure 4.36. Comparison between $d(O_x)/dt$, derived from *in situ* observations, and $p(O_x)$, derived from the OPR measurements (estimated $p(O_x)$ systematic uncertainty is ± 28 %), during the FIOM period.

The estimated uncertainty in measured London $p(O_x)$ data set (U_{London}) was based upon four factors: ozone loss in the sampling reactors, NO_x loss in the sampling reactors, uncertainty in the ozone monitor measurement (differential mode, see Section 2.6) and uncertainty in the reactor residence time. Values for these factors were determined from previous tests. To recap, ozone loss in reactor inner surface was approximately 10 %, NO_x loss in reactor inner surface was neglected (see Section 3.4); the accuracy of the ozone monitor is stated as 1 ppb (although the differential measurement should be rather better than this statement), and the reactor residence time was 710 ± 133 seconds.

Consequently, uncertainty from the reactor wall losses was 10 % (derived from ozone and NO_x loss tests). Uncertainty from the error in ozone monitor was determined by comparing the stated accuracy (of the ozone monitor) to the mean ΔO_3 (measured by the OPR system)

during the FIOM period, *i.e.* as 1 ppb / 5.49 ppb or 18 %. The uncertainty from the reactor residence time was 133 seconds / 710 seconds or 19 %.

The estimated overall uncertainty, U_{London}, was evaluated by determining the square root of the sum of squares of the individual (fractional) uncertainties, given by:

$$U_{London} = \sqrt{(0.1^2 + 0.18^2 + 0.19^2)} = 28\ \%$$

The ambient air values for dO_x/dt were quite scattered in Figure 4.36, but had a broadly diurnal cycle during the FIOM. This diurnal pattern is particularly apparent during the second two day period, when the metrological conditions were stable. The dO_x/dt showed positive values, increasing from the early morning as sunrise started (and traffic activity rose), reaching a diurnal peak in the late morning. The dO_x/dt then decreased in the afternoon, becoming negative around 5:00 pm. This diurnal pattern, and its timing, was also reflected in the $p(O_x)$ data, but the magnitude of the two disagreed substantially during the first two day period, then the magnitude difference between the two data sets were less apparent during the second two day period. Due to different air mass origins and wind directions during the first and second two day periods, it was more suitable to divide this comparison into two, two day periods.

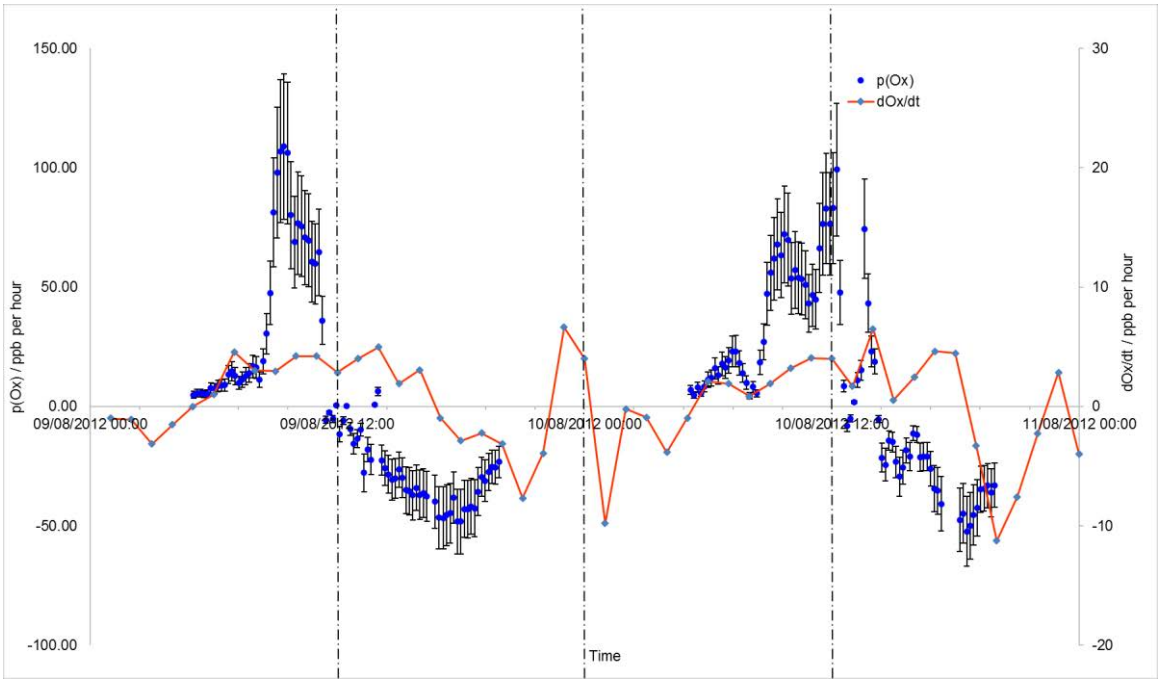

Figure 4.37. Comparison between d(O_x)/dt, derived from *in situ* observations, and $p(O_x)$, derived from the OPR measurements (estimated $p(O_x)$ systematic uncertainty is ± 28 %), during the first two day period of FIOM (9th and 10th August 2012).

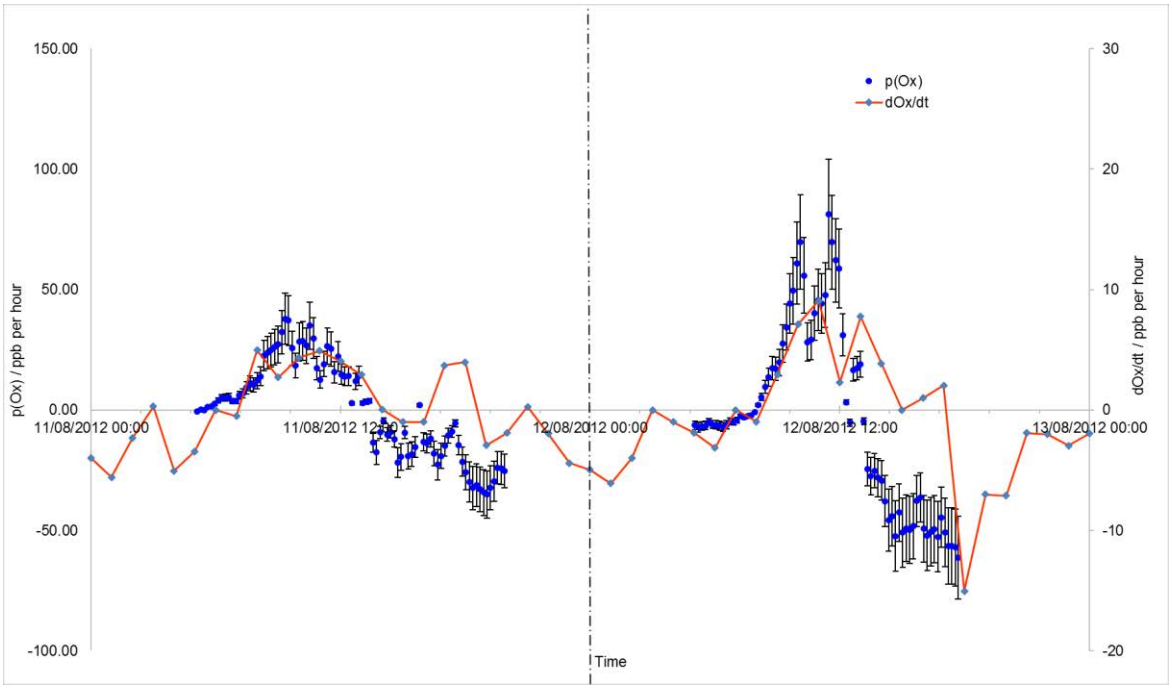

Figure 4.38. Comparison between d(O_x)/dt, derived from *in situ* observations, and $p(O_x)$, derived from the OPR measurements (estimated $p(O_x)$ systematic uncertainty is ± 28 %), during the second two day period of FIOM (11th and 12th August 2012).

In principle, a major reason for this different magnitude during FIOM may be the different definitions of two datasets. The $p(O_x)$ only represented the chemical oxidant (as ozone) production rate in ambient air; the dO_x/dt represented the rate of change of O_x levels, which was derived from oxidant advection, deposition and chemical production (and destruction) processes. It was apparent that dO_x/dt diurnal pattern were more similar to $p(O_x)$ during second two day period (Figure 4.38) than first two day period (Figure 4.37). A possible reason is the stable east wind direction - which related to the advection effects to cause this difference.

This possibility, and other factors relating to the chemical oxidant formation and destruction, are discussed in greater detail below, with a focus on the second two day period. Both deposition and advection processes (considered explicitly in Section 4.6) also affect the observed dO_x/dt.

Figure 4.39 then compares the measured $p(O_x)$ values with the time series of other relevant species (NO, NO_2, NO_x, O_3, O_x) during the FIOM period.

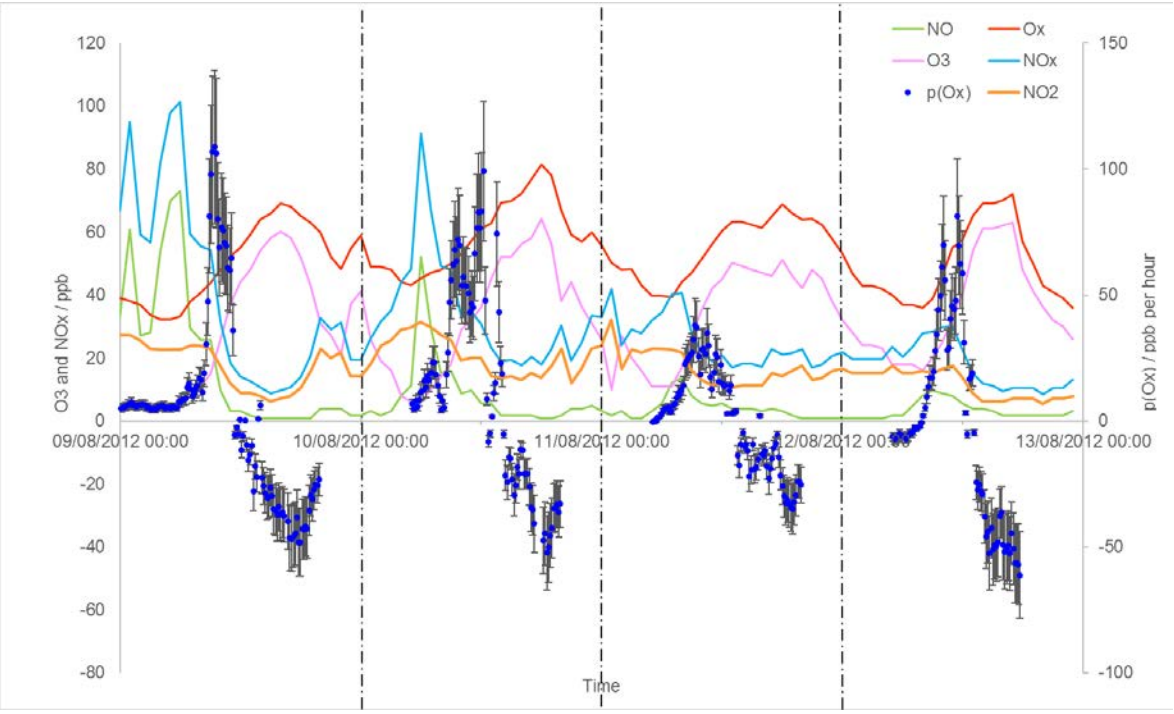

Figure 4.39. Time series of NO_x, O_x, O_3, NO, NO_2 and $p(O_x)$ during FIOM period (estimated $p(O_x)$ uncertainty is ± 28 %).

As the sun rose in the early morning, NO_x level started rapid rising then falling between 6:00 to 8:00, before and after the "rush hour". The NO_2 photolysis rate forming ozone would increase (but not in isolation leading to new O_x production) by the solar radiation; however, rising solar radiation would also initiate radical chemistry - OH and hence HO_2, RO_2 production - which then reacted with NO to form NO_2 - and consequently, to form ozone through NO_2 photolysis. $p(O_x)$ started to dramatically increase from around 6:00 to 8:00 am, rising to a diurnal peak between 9:00 and 10:00. On the same timescale, the ambient ozone level started ascending, reaching peak levels at around 16:00 to 18:00, and then falling once more as the sunset period began.

The measured oxidant production rate $p(O_x)$ fell to negative values in the afternoon, suggesting that net chemical oxidant destruction was occurring. In this sense, the measured $p(O_x)$ values agreed with the ambient ozone/oxidant trend in terms of diurnal shape. A particular example is on 11th August 2012, there was a small boost of measured $p(O_x)$ around 17:00, where ambient O_x and O_3 level corresponded to this change of values. However, the measured $p(O_x)$ values were far greater than the observed rate of increase of O_3 / O_x suggested. For example, on 12th August, $p(O_x)$ increased from 4 ppb per hour to a maximum of 80 ppb per hour in the morning, and correspondingly substantial increases in ambient ozone above 100 ppb would be expected. However, ambient ozone levels remained under 65 ppb throughout the day. Possible reasons for this discrepancy are discussed in Section 7.1.

The chemical production of ozone was driven by radical chemistry under solar radiation; the radical chemistry was initiated by photolysis of ozone to form the excited oxygen atom, O^1D (and by other primary OH initiation routes, *e.g.* HONO photolysis). The rate of ozone photolysis forming $O(^1D)$ is termed $j(O^1D)$, and is therefore related to the ozone production rate. Values of $j(O^1D)$ and measured $p(O_x)$ levels were compared:

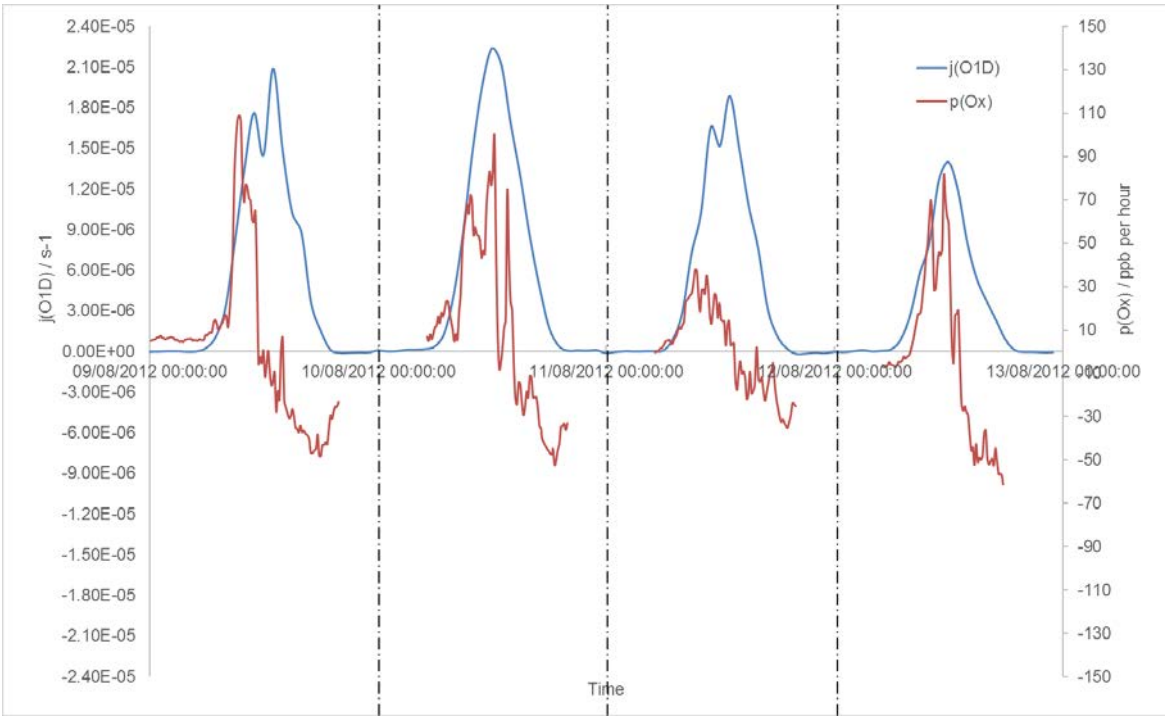

Figure 4.40. Comparison between $j(O^1D)$ and $p(O_x)$ during FIOM.

The overall rise in $j(O^1D)$ agreed well with that of $p(O_x)$ in timescale, suggesting that there could be a relationship between the two variables, however $p(O_x)$ fell to negative values much earlier than $j(O^1D)$ substantially declined. $j(O^1D)$ was somewhat variable on each of the measurement days (reflecting varying atmospheric transmission and cloud cover), however the relationship between $p(O_x)$ and $j(O^1D)$ was more variable; for example, during the first two days; peak $j(O^1D)$ was approximately 2.00×10^{-5} s^{-1}, and peak $p(O_x)$ was approximately 90 ppb per hour. On 11 August 2012, $j(O^1D)$ peaked at 1.89×10^{-5} s^{-1}, but peak $p(O_x)$ dropped to 37 ppb per hour. On 12 August 2012, peak $j(O^1D)$ was at 1.40×10^{-5} s^{-1}, the peak $p(O_x)$ increased to 81 ppb per hour. The variable relationship between the two variables is consistent with changes in local VOC and NO_x abundance also influencing the ozone production rate. To explore these co-dependencies in a more integrated way, the variation in the actual OH radical production rate was determined and compared with the $p(O_x)$ data.

4.5 Radical Production Rate: *p*(OH) and *p*(O_x)

OH and HO_2 radicals are key components of tropospheric oxidation processes, these species are directly related to photochemical O_3 production potential. OH initiates the oxidation process of many trace gases, included the commonly abundant species such as carbon monoxide (CO) and methane (CH_4) alongside most other VOCs, to produce H and CH_3. However, both CO and CH_4 have long chemical lifetime in the troposphere, CH_4 has a lifetime about 10 years (Seinfeld and Pandis, 2012); CO has a chemical lifetime of 30-90 days on the global scale of troposphere. (Seinfeld and Pandis, 2012) The other VOCs have much shorter chemical lifetime. *e.g.* Propene(C_3H_6) has an estimated lifetime of 7 hours in troposphere (Blake and Blake, 2002).

CO, CH_4 and other VOCs overwhelmingly react with the major gas O_2 to form peroxy radicals (HO_2 and RO_2). Peroxy radicals then react with the abundant NO in urban environments to form NO_2 – which photolysis by solar radiation to form ozone. Consequently, peroxy radicals are the key factor in chemical ozone production in the ambient air. The ozone production rate, *p*(O_x), is therefore closely related to chemical OH production rate, *p*(OH). A comparison between *p*(OH) and *p*(O_x) was performed to assess the contribution of variations in OH production rate to the observed variations in ozone production.

OH radicals in the urban boundary layer are expected to undergo primary formation (*i.e.* neglecting secondary OH formation through radical cycling, such as HO_2 + NO) through the following chemical processes,

i. $HONO + h\nu \rightarrow OH + NO$ (4.4)

ii. $O_3 + h\nu \rightarrow O^1D + O_2$, $O^1D + H_2O \rightarrow 2OH$ (4.5)

iii. $Alkene + O_3 \rightarrow OH + R'CHO + other\ species$ (4.6)

This analysis was conducted prior to release of the HO_2 data acquired by the University of Leeds; revised analysis using measured HO_2 levels is also presented in section 4.2. Following up analysis was performed to determine the contribution from reaction 4.6 to total chemical OH production rate *p*(OH), when alkene species data became available in early 2016. Four abundant alkene species were selected to in this analysis - Ethene(C_2H_4), Propene(C_3H_6), 1-Butene(C_4H_8) and Isoprene(C_5H_8), to represent all alkene species present.

The primary OH production rate was then defined as,

$$p(OH) = j_{HONO}[HONO] + 2\,j(O^1D)\,[O_3]\,f + j(C_2H_4)(O_3) + 2k[C_2H_4][O_3] + \text{total } Y_{alkene}\,k_{alkene}\,[O_3][Alkene] \quad (4.7)$$

Where j_{HONO} is the photolysis rate of HONO, measured by the spectral radiometer system operated by the University of Leicester, alongside $j(O^1D)$, the photolysis rate of O_3 to form O^1D atoms, and f is the fraction of O^1D atoms which react with water vapour to form OH, and may be derived from the relevant kinetic factors (see Section 4.5.1). Y_{alkene} is the yield of OH in alkene reaction with O_3 (see reaction 4.6), k_{alkene} is the rate constant the rate constants in reaction 4.6. Since there are a large range of alkene species in ambient air, Y_{alkene} and k_{alkene} values varies from different alkene species. In this analysis section, only four alkene species were used. Consequently, the reaction 4.7 is a lower limit to the total OH production rate.

4.5.1 Calculation of the OH yield from O^1D reaction, "f"

O^1D predominantly reacts with H_2O, N_2 and O_2 in ambient air, leading to either formation of OH radicals, or quenching of O^1D to the less reactive $O(^3P)$ (which will usually subsequently reform O_3 through reaction with O_2):

$$O^1D + H_2O \rightarrow 2\ OH \qquad k_{4.8} \qquad (4.8)$$

$$O^1D + O_2 \rightarrow O + N_2 \qquad k_{4.9} \qquad (4.9)$$

$$O^1D + N_2 \rightarrow O + O_2 \qquad k_{4.10} \qquad (4.10)$$

The fraction "f" value is the proportional of O^1D which reacts with H_2O (water vapour), and is given by:

$$f = \frac{k4.8[H2O]}{k4.8[H2O]+k4.9[N2]+k4.10[O2]} \qquad (4.11)$$

Where $k_{4.8}$, $k_{4.9}$ and $k_{4.10}$ are the rate constants for reactions 4.8 – 4.10, their values at 298 K (Sander *et al*., 2011) are:

$k_{4.8} = 2.00 \times 10^{-10}\ s^{-1}$

$k_{4.9} = 3.10 \times 10^{-11}\ s^{-1}$

$k_{4.10} = 3.95 \times 10^{-11}\ s^{-1}$

The H_2O concentration was determined from the measured RH using saturation vapour pressure as defined by the Antoine Equation.

When equation (4.8), (4.9), and (4.10) are combined, the fraction value "f" is known, which then represents the fraction of O^1D atoms which react with water vapour to form OH, such that the primary OH production rate from ozone photolysis is determined (see Section 4.5,

chemical process ii). The mean fraction value "f" is 0.08 during the FIOM. Since both j_{HONO} and HONO levels are known, the primary OH production rate from HONO photolysis is also determined. Therefore, the incomplete *p*(OH) in equation (4.7), is derived from combination of the two primary OH production processes and Alkene species reaction with O_3, in units of molecule cm^{-3} s^{-1}.

4.5.2 Contribution of OH production rate from alkene species reacting with O_3

Four relatively abundant alkene species were selected to represent the large range of alkene species, their reactions with O_3 to form OH are present as,

$$\text{Alkene species} + O_3 \rightarrow Y_{alkene}\ OH + R'CHO \qquad k_{alkene} \qquad (4.12)$$

Y_{alkene} is the yield of OH in the reactions of ozone with alkenes.

k_{alkene} is the rate constant the rate constants in the reactions of ozone with alkenes, its value varies from different alkene species.

The yield of OH and rate constant values in equation 4.12 are present in following table:

	Yield of OH	Rate constant (298K) / molecules cm^{-3} s^{-1}
Ethene	0.17	1.6×10^{18}
Propene	0.36	10.3×10^{18}
1-butene	0.56	9.6×10^{18}
Isoprene	0.45	13×10^{18}

Table 4.4. Selected alkene species yield of OH and rate constant in the reactions of ozone with alkenes (Atkinson *et al*., 2006; Alam *et al*., 2013)

According to equation 4.7, the result indicated alkene reactions contribute an average of 1.05% to the total incomplete OH production rate *p*(OH), with a peak value of 6.57% on 5:00 am

of 11th August 2012. The major source of the *p*(OH) were still from the two primary OH production processes (equation 4.4 and 4.5), alkene reactions' contribution was negligible in equation 4.7.

4.5.3 Comparison between evaluated *p*(OH) and measured $p(O_x)$

A comparison between the resulting Evaluated incomplete *p*(OH) values and the measured $p(O_x)$ during the FIOM period is shown in Figure 4.41,

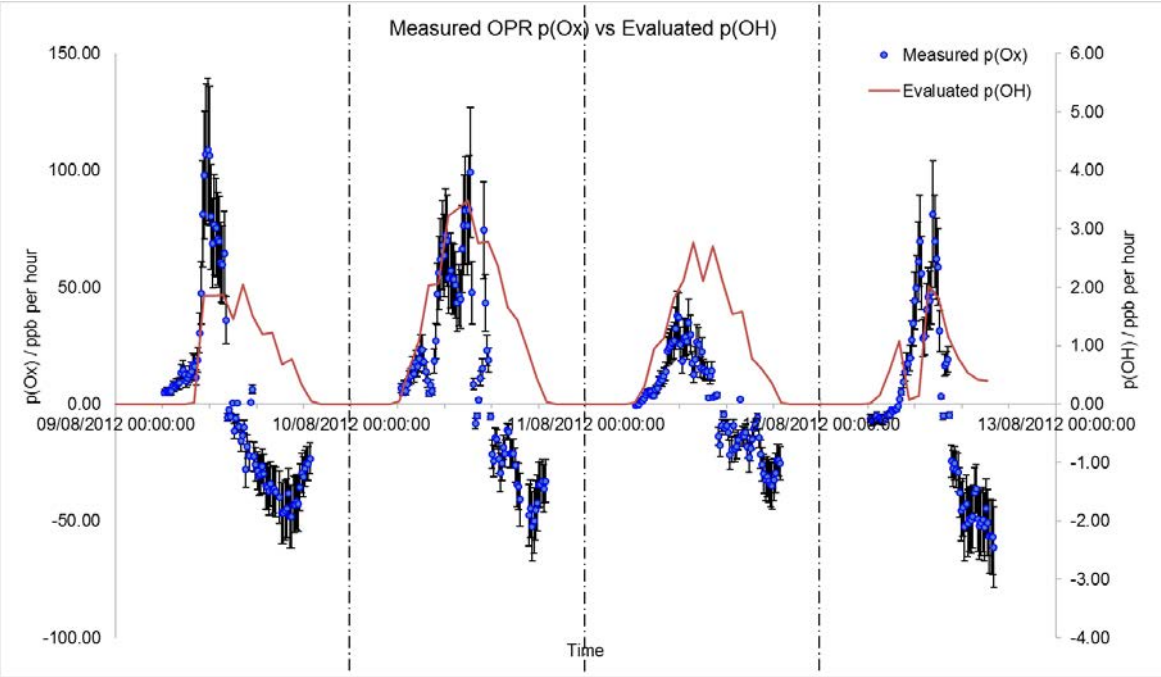

Figure 4.41. Comparison between evaluated *p*(OH) and measured $p(O_x)$ during FIOM; primary (left) axis is $p(O_x)$, secondary (right) axis is *p*(OH).

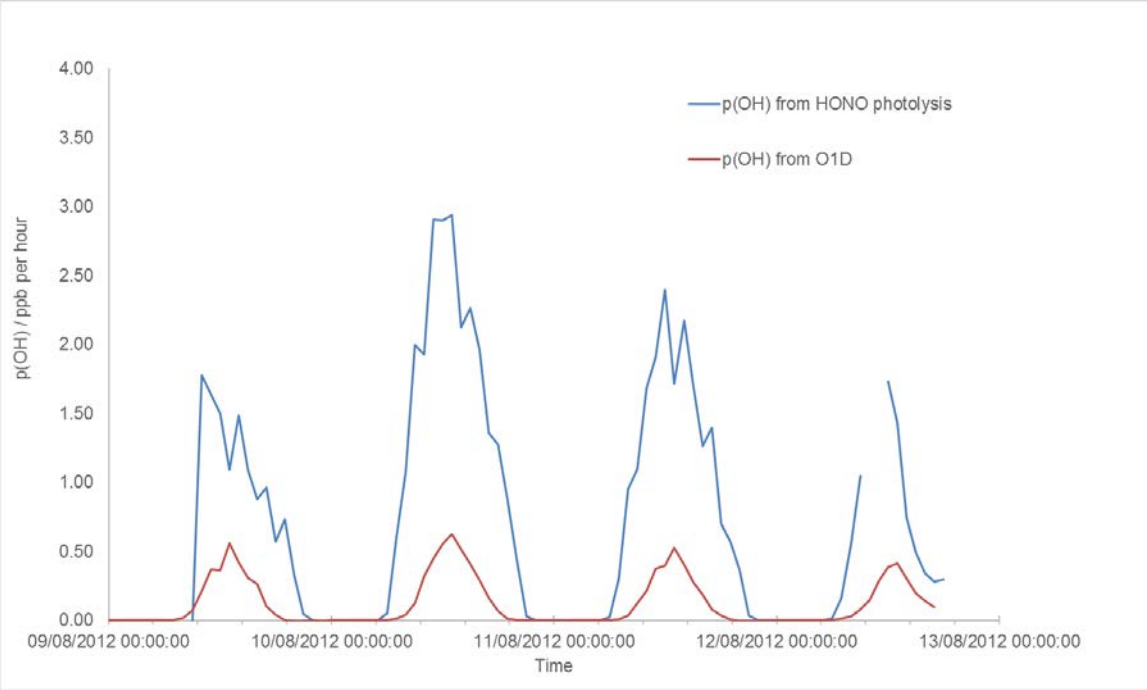

Figure 4.42. Evaluated *p*(OH) from HONO photolysis and *j*(O^1D) processes during FIOM.

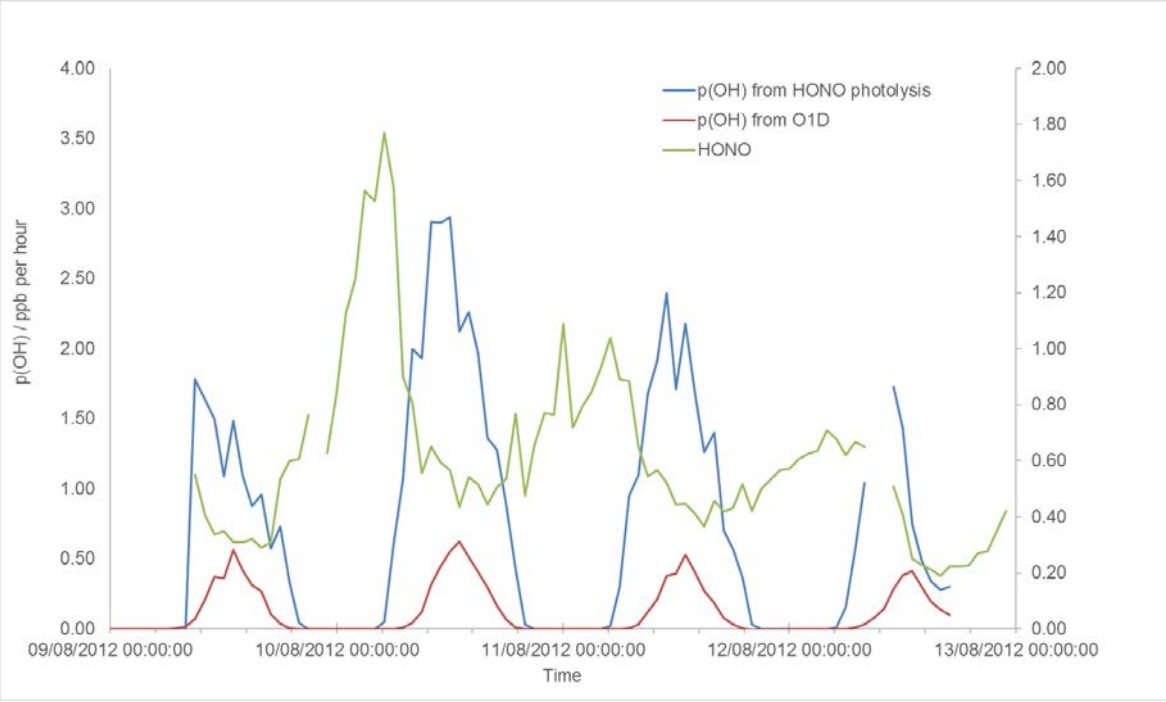

Figure 4.43. Evaluated *p*(OH) from HONO photolysis and *j*(O^1D) processes with time series of ambient HONO levels during FIOM. HONO data from University of York.

In Figure 4.41, the *p*(OH) temporal trend / shape can be seen to be similar to that of *p*(O_x) in part, during the daytime periods of the FIOM episode. A few fluctuations in the *p*(OH) were

due to the missing HONO values. *e.g.* The low values of p(OH) on 12 August between 9:00 and 10:00 was due to the missing measurement of HONO level.

In particular, the initial rise in p(OH) and $p(O_x)$ are very well correlated, even extending to the very rapid rise (following the sun clearing clouds) on the first morning, 9th August. Agreement between the magnitudes of p(OH) and $p(O_x)$ is not expected (as ozone formation arises from multiple steps following initial VOC break-down). The HONO photolysis process dominated the total p(OH), compared with $j(O^1D)$, during the day time, particularly in the early morning, but the contribution from $j(O^1D)$ became (relatively) more significant around the middle of the day, when shortwave UV would be expected to maximise (Figure 4.42). HONO photolysis contribute to an average of 85% total OH production rate during FIOM period, with a peak value of 98% contribution of the total OH production rate in early morning.

Such dominance of HONO photolysis in total OH production rate was also observed in other field studies performed in urban environments, *e.g.* HONO photolysis process contributed to 80.4% of the primary OH production at a suburban site in Colorado (Kim *et al*., 2014); it accounted 48 – 56% of the primary OH production in New York City (Ren *et al*., 2006). Figure 4.43 shows the diurnal ambient HONO levels corresponding to the change of p(OH) level from HONO photolysis, this trend further confirmed that the dominant source of p(OH) in London was from HONO photolysis during FIOM.

The p(OH) and $p(O_x)$ trends shown in Figure 4.41 were quite different on a full diurnal basis. On diurnal basis, both $p(O_x)$ and p(OH) trend had similar general characteristics; the two trends began to rise around 7:00 in the morning, then reached peak level around 11:00 to 12:00. After their peak levels, both trend started to decrease. In the free troposphere, the OH production rate is closely related to chemical O_3 production rate $p(O_x)$. However, p(OH)

and $p(O_x)$ are not the same. As introduced in chapter 1, OH reacts with VOCs to initiate peroxy radical reactions; peroxy radicals are an important factor to contribute to O_3 production. $p(O_x)$ accounted for the chemical O_3 production rate; while OH reacts with VOCs to form peroxy radicals, peroxy radicals potentially react with abundant NO to produce O_3 in urban environment. OH could also react with NO_2 and HO_2. Therefore, p(OH) was related to $p(O_x)$ but $p(O_x)$ was not fully dependent on p(OH); they are different indicators.

In Figure 4.41, contrasting characteristics between the two datasets can be noted. The afternoon $p(O_x)$ values started decreasing much faster than p(OH); $p(O_x)$ went to negative values around 14:00 to 15:00, while the p(OH) values decreased slowly to reach zero (which it necessarily cannot fall below) around 19:00 to 20:00. The fast $p(O_x)$ decrease was possibly caused by a combination of O_x removal process (OH + NO_2, amongst other processes). The slower p(OH) decrement was driven predominantly by the steadily decreasing solar radiation. On 11th August 2012, $p(O_x)$ values were much lower than the rest of days during FIOM. However, p(OH) values on 11th August 2012 remained at similar level to 10th August 2012. This may have been related to the lower ambient NO level on 11th August 2012 (Figure 4.29). The low ambient NO level limited the scope for radical chemistry to produce ozone.

4.5.4 Derived oxidant formation rates from HO_2 measurements

In tropospheric chemistry, HO_2 and RO_2 are tightly coupled to ozone production. Recapping from chapter 1, the chemical oxidant production process is shown in the following equations,

$$HO_2 + NO \rightarrow OH + NO_2 \qquad k_{4.13} \qquad (4.13)$$

$$RO_2 + NO \rightarrow RO + NO_2 \qquad k_{4.14} \qquad (4.14)$$

$NO_2 + h\nu \rightarrow NO + O$ (4.15)

$O + O_2 + M \rightarrow O_3 + M$ (4.16)

The estimated chemical ozone production rate can then be described as,

$p_c(O_x) = k_{4.12} [RO_2] [NO] + k_{4.13} [HO_2] [NO]$ (4.17)

If reactions between HO_2 and O_3 (or RO_2) are neglected; $RONO_2$ formation and OH removal (OH + NO_2) are also neglected, then ideally, rates of reactions (4.13) and (4.14) would expected to be equal under PSS conditions (see radical cycle, Figure 1.1, Chapter 1, Section 1.4.1), *i.e.* $k_{4.13} [HO_2] [NO] \cong k_{4.14} [RO_2] [NO]$. Although both the $k_{4.14}$ and $[RO_2]$ values were unknown, in this ideal estimation of chemical oxidant production rate, $k_{4.13} [HO_2]$ was assumed to be roughly equal to $k_{4.14} [RO_2]$.

Equation (4.17) can then be rewritten to give the (estimated) calculated chemical oxidant production rate, $p_c(O_x)$:

$p_c(O_x) = 2\, k_{4.13} [HO_2] [NO]$

Where $k_{4.13} = 8.0 \times 10^{-12}$ s^{-1} at 298 K (Sander *et al*., 2011)

Since both CO and CH_4 have long chemical lifetime in the air mass, as they are essential in OH oxidation to form peroxy radicals, it could be useful to focus on the second two days data, which has similar air mass origins, for estimation of oxidant production rate derived from the HO_2 measurement. The resulting calculated $p_c(O_x)$ values for the second two days of FIOM period are shown in Figure 4.44:

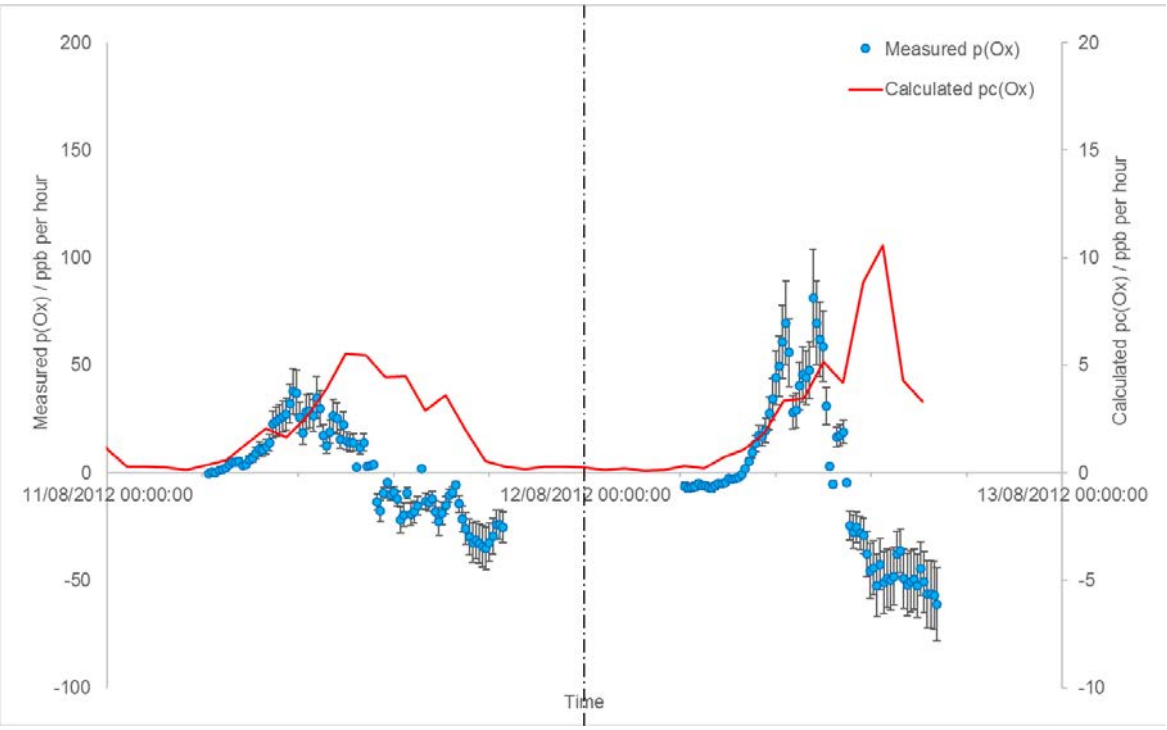

Figure 4.44. Comparison between calculated $p_c(O_x)$ (Right axis) derived from measured HO_2 concentrations, and measured $p(O_x)$ (left axis) from the OPR system during the second two day period.

Interestingly, the calculated $p_c(O_x)$ displays different time behaviour (and hence consistency with the $p(O_x)$ data) to the p(OH) values presented above (Figure 4.41) -presumably due to the influences of variations in NO_x and VOC levels. A diurnal trend of $p_c(O_x)$ is apparent for the second two days of the FIOM period, but with a later onset and extended persistence compared with the $p(O_x)$ data. As for the measured dO_x/dt levels, the calculated $p_c(O_x)$ values are substantially smaller than the $p(O_x)$ derived from the OPR measurements. One further limitation of the $p_c(O_x)$ approach is apparent from inspection of Figure 4.44: HO_2 levels do not fall to zero at night, while NO_2 photolysis (and hence ozone production) will cease - although in principle, peroxy radical driven NO-to-NO_2 titration (rather than cycling) could still occur, and would contribute to net O_x production.

The comparisons between the OPR-derived $p(O_x)$ and the observed $d(O_x)/dt$, calculated $p(OH)$ and calculate $p_c(O_x)$, $p(O_x)$ and $l(O_x)$ all neglect that fact that the quantities considered

are not directly comparable - self-evidently in the case of *p*(OH), but also in the case of $d(O_x)/dt$ (where advection and deposition effects are neglected) and $p_c(O_x)$ (where oxidant chemical removal effects are neglected). These two limitations (chemical oxidant removal, advection and deposition effects) are explicitly addressed in the following two sections, which consider advection and chemical destruction contributions to O_x abundance at the NK site during the FIOM period.

4.6 Advection effects on ozone mixing ratio changes during FIOM

Advection effects significantly contribute to changes in the local NO_x and O_3 levels as experienced at the NK site. Wind transfers NO_x and O_3 from the surrounding area to London and exports pollutants from London to the surrounding area (alongside vertical mixing and entrainment, which are not considered further here). A highly simplified, small-scale advection effect analysis was applied to the FIOM measurement period during the ClearfLo summer IOP at the North Kensington site, with a focus on the second two day period when wind direction was stable (east wind).

In the following subsections of 4.6, the terminology used in discussions is defined in the table below:

Terminology	Definition
NK $NO_x/O_3/O_x$	The ambient $NO_x/O_3/O_x$ by AURN monitoring station at NK site
Satellite time	The evaluated over pass time at satellite location which corresponds to NK time. Its calculation is presented in section 5.1.2.
Satellite location $NO_x/O_3/O_x$	The measured $NO_x/O_3/O_x$ levels from corresponding satellite locations AURN monitoring station at satellite time, which corresponds to the given NK site reference time.
dO_x/dt	dO_x is the differential values between ambient NK O_x mixing ratio and satellite locations O_x mixing ratio. dt is time which take the air mass travel from its original satellite location to NK site. It is also presented as t_{travel}. dO_x/dt was the idealized chemical O_x production (neglecting deposition and other processes).
dO_3/dt	dO_3 is the differential values between actual ambient NK O_3 mixing ratio and satellite locations O_3 mixing ratio. dt is time which take the air mass travel from its original satellite location to NK site. It is also presented as t_{travel}. dO_3/dt was the idealized chemical O_3 production (neglecting deposition and other processes).
dNO_x/dt	dNO_x is the differential values between actual measured NK NO_x mixing ratio and satellite locations NO_x mixing ratio. dt is time which take the air mass travel from its original satellite location to NK site. It is also presented as t_{travel}. dNO_x/dt was the idealized chemical NO_x production from advection effect alone (neglecting deposition and other processes).
$p(O_x)$	The measured Ox production rate from OPR system, it was derived by the measured ΔO3 divided by residence time.

Table 4.5. Definitions used in subsections of 4.6.

4.6.1 Advection Analysis: Methodology

The basic principle of this analysis was to consider wind direction as measured at the North Kensington (NK) site as an indicator of the air mass origin, to identify which of a number of satellite locations around the periphery of London the air mass encountered at the NK site at a given time had likely previously passed over. Four satellite locations were used; these are identified in table 4.4 and Figure 4.34, corresponding to north, south, west and east sectors. Wind speed data for each satellite location was obtained and used to determine the air mass transit time to the NK site and hence to identify the overpass time at each satellite location

corresponding to the air mass encountered at the NK site. With those time profiles, at a given time in the NK site, the air mass's original satellite locations' overpass time and hence its NO_x and O_3 levels were then determined. This simplified analysis enables comparison between NK NO_x/O_3 levels and satellite locations' NO_x/O_3 levels with local meteorological climatology; differences in pollutant levels between two locations (satellite and NK) are then caused by non-advection effects (discussed further below).

4.6.2 Advection analysis procedures

The simplified advection analysis was based on the assumptions of stable wind direction and wind speed, in addition to neglecting the role of other NO_y species, emissions, air mass mixing, NO_x/O_3 deposition and radical chemistry. This analysis consists of the following five stages:

1. Acquire the NO_x/O_3 ambient levels and wind speed/direction data at NK site.
2. Derive the original satellite location of the air mass from NK wind speed/directions data, estimate the satellite location overpass time then acquire the satellite location NO_x/O_3 levels at this time.
3. Compare the NK NO_x/O_3 levels with satellite location NO_x/O_3 levels, as an analysis of the advection effect.
4. Derive the differential value between NK $NO_x/O_3/O_x$ and satellite location overpass time $NO_x/O_3/O_x$, then divided by the air mass travelling time. The resulting value, dO_x/dt, is the idealized net O_x production rate (which is the sum of chemical production, emissions, mixing and deposition effects).
5. Compare the idealized chemical O_x production rate to measured $p(O_x)$ derived from the OPR system.

The details of the five stages are discussed in following subsections of 4.6.

4.6.3 Derivation of satellite location pollutant levels

NO_x/O_3 levels for the satellite locations were derived as follows: First of all, four satellite locations were selected from four directions for evaluation of air mass original composition. The satellite location details are shown in the following Figure 4.34:

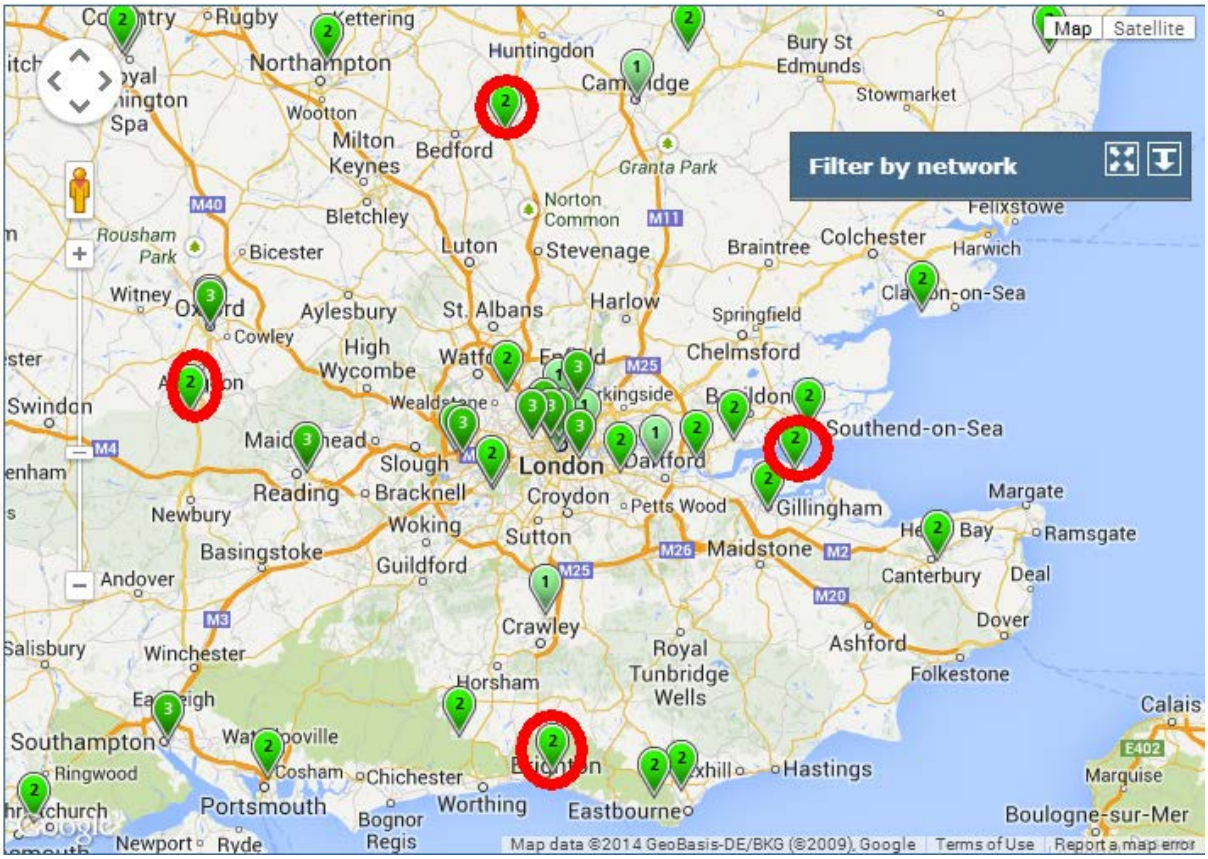

Figure 4.45. The selected four satellite locations on map (© Crown 2016 copyright Defra via uk-air.defra.gov.uk, licenced under the Open Government Licence (OGL)).

Site names	Distance to North Kensington	Cardinal Direction from NK	Wind direction in 90 degree sector(°C)
North site: Wicken Fen	102km	North	316-45
East site: Southend on sea	62km	East	46-135
South site: Brighton preston park	82km	South	136-225
West site: Harwell	83km	West	226-315

Table 4.6. The satellite location site information, for clearer view in some of the figures in the following sections, abbreviations were created for each site. these site names are: North site-Wicken Fen (WF), East site-Southend on sea (SS), South site-Brighton preston park(BPP), West site-Harwell (HW).

All four satellite locations (red circles) are at least 140 meters from nearest roads. The satellite locations' AURN monitoring stations had been continuously monitoring ambient NO_x, O_3 and wind speed/direction data during FIOM. Wind direction was classified for each station as shown in table 4.6. All data were averaged to 3-hourly resolution for analysis; note this is in contrast to the previous hourly based data presented in the proceeding FIOM section.

During procedure 2, the NK site time (T_{NK}) is used as reference time. At a given reference time, by applying the AURN NK monitoring site's wind direction data, the satellite location for the air mass at NK was determined. Once the air mass' original satellite location was determined, the satellite location time ($T_{satellite\ location}$) of the air mass was estimated by applying the NK site's wind speed data (S) to the distance (D) between satellite location and NK site. Therefore, at a given NK site reference time, the satellite location time is presented as,

$$T_{satellite\ location} = T_{NK} - (D/S)$$

$T_{satellite\ location} = T_{NK}$ is the NK site time, which is the reference time.

D is the distance from the NK site to satellite location in unit of kilometres.

S is the wind speed at NK site in unit of km/hour.

(D/S) is length of time which takes the air mass to travel from its original satellite location to NK site.

$T_{satelite\ location}$ is then the estimated overpass time at satellite location when that satellite location's O_3 and NO_x data were taken. This calculation enables comparison of the differential NO_x and O_3 levels at a given time point at NK, with those that would solely arise from air mass advection from the satellite locations.

4.6.4 Result of advection analysis

4.6.4.1 NO_x and O_3 levels from advection analysis during FIOM

The following figures showed NO_x and O_3 levels from advection analysis during FIOM.

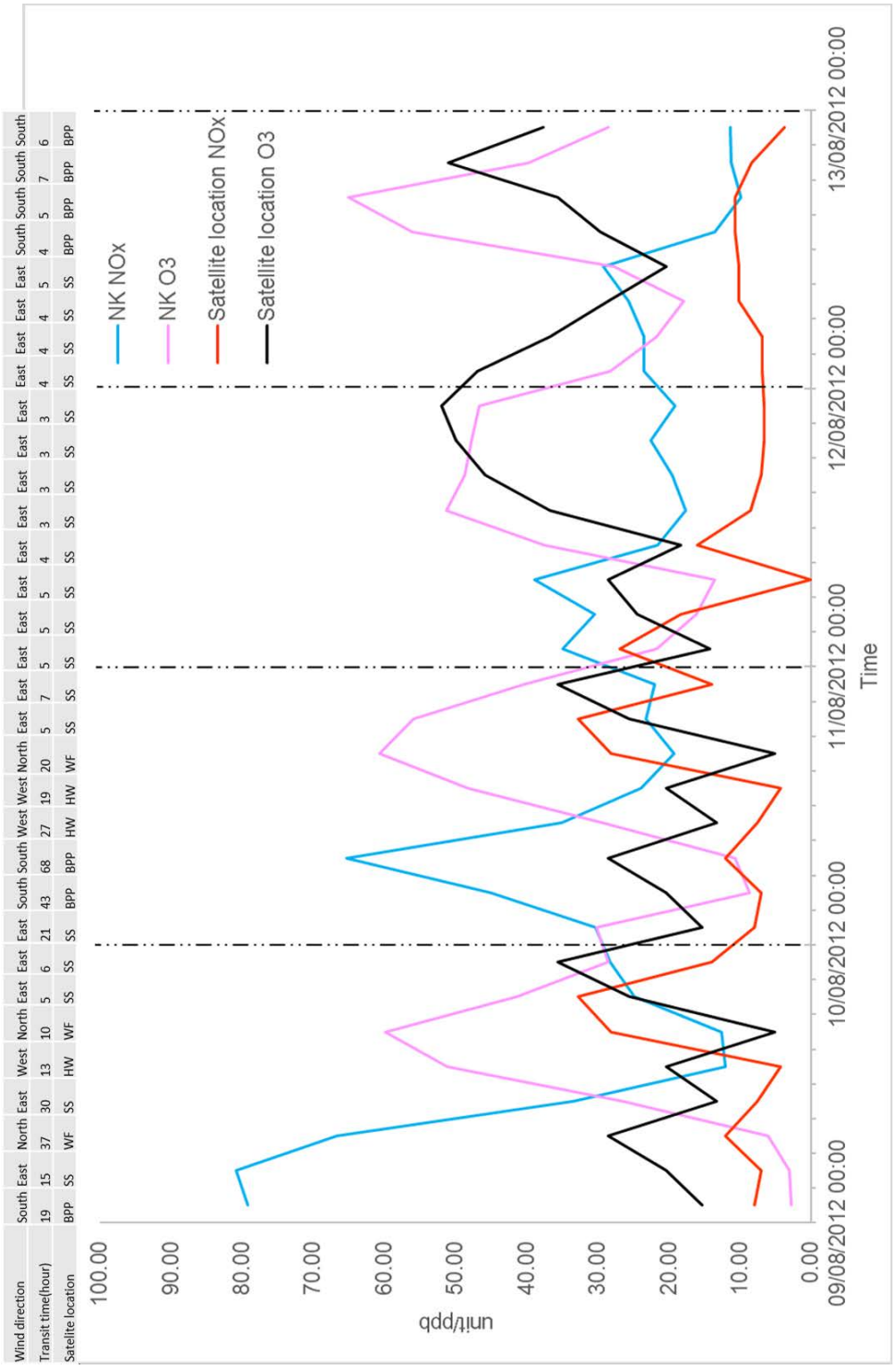

Figure 4.46a: Comparisons between NO_x and O_3 levels at NK, and at satellite locations at the corresponding overpass time during the FIOM period.

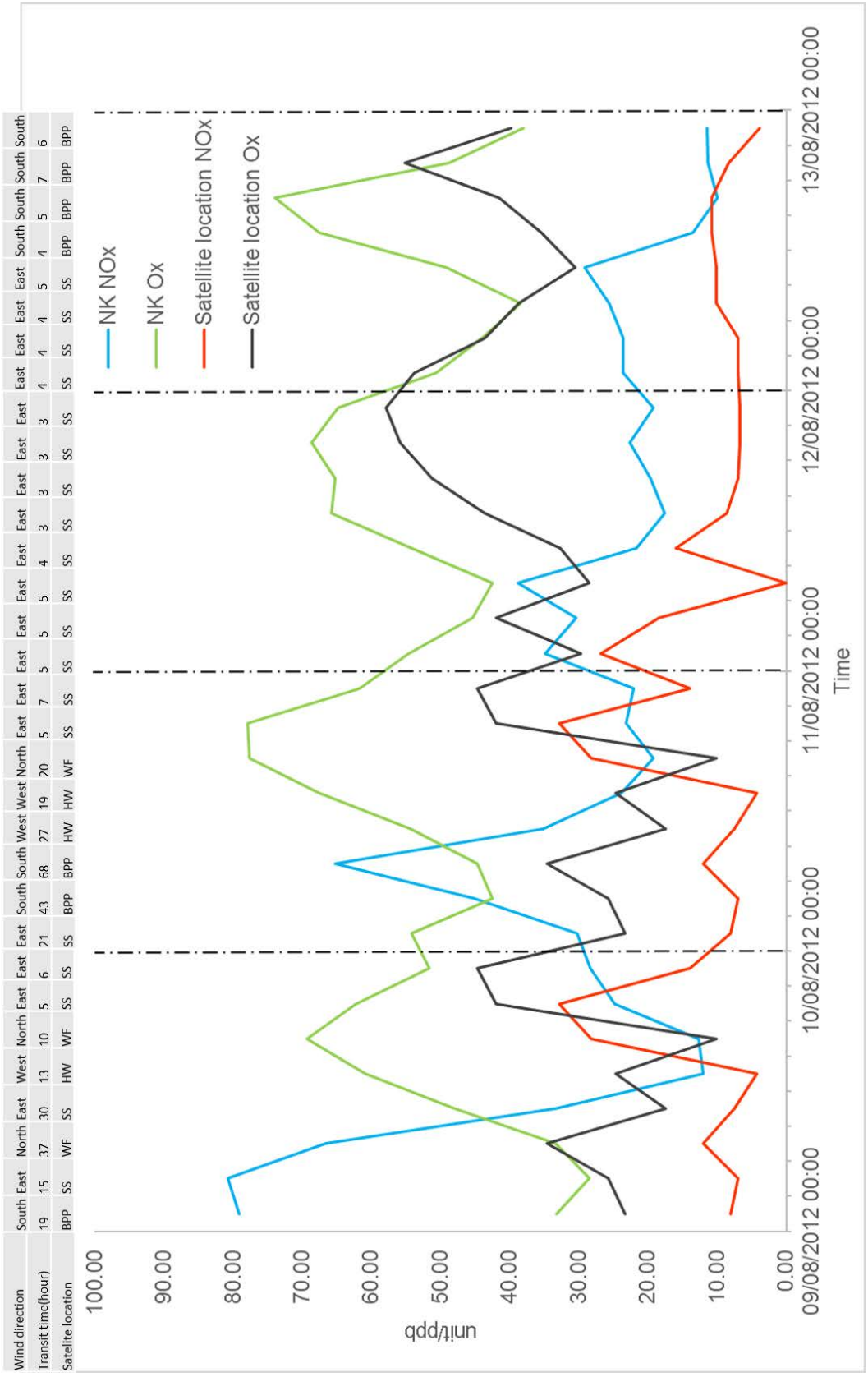

Figure 4.46b: Comparisons between NO_x and O_x levels at NK, and at satellite locations at the corresponding overpass time during the FIOM period.

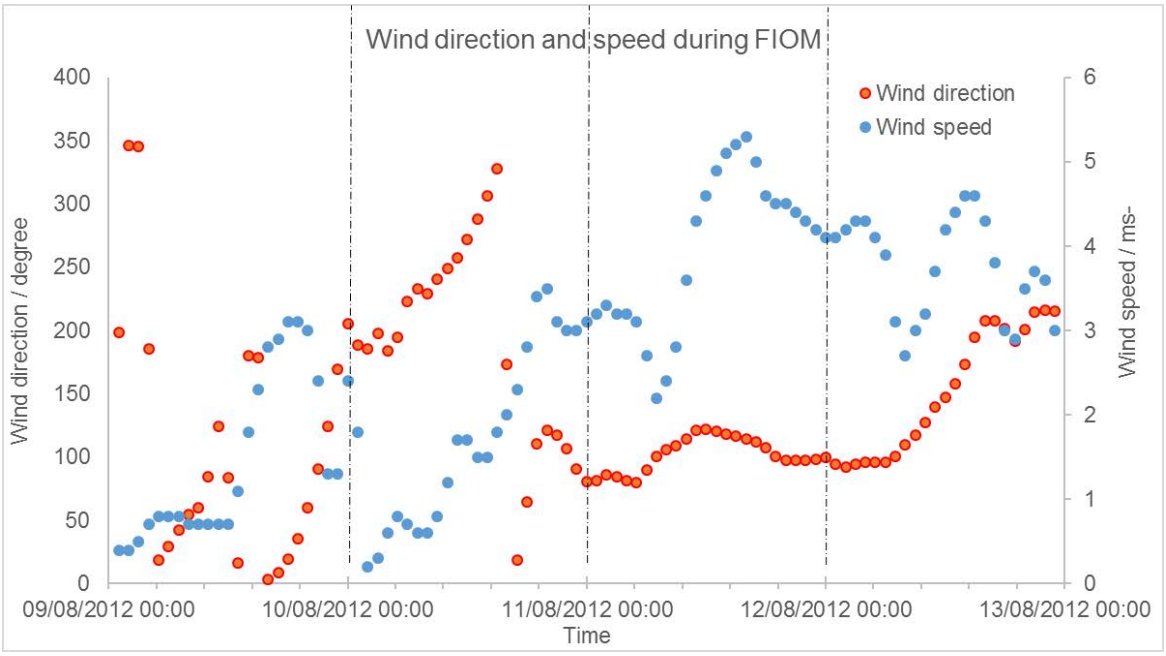

Figure 4.47: Time series of wind direction (left axis) and wind speed (Right axis) at NK site during FIOM.

In both Figure 4.46a and Figure 4.46b, overall NO_x levels are seen to be higher at NK than at the air mass' origin satellite location during the FIOM period. The increase in NO_x at the NK site was especially high in the early morning; the NK NO_x level reached its daily peak between 04:30 and 07:30 am on 9, 10 and 11 August 2012. The daily peak was slightly later (than previous 3 days) on 12th August 2012 at around 10:30 am. The elevated NK NO_x level compared with the satellite location NO_x level was anticipated; when air mass travels from its original satellite location to London, it will receive large NO_x emissions from anthropogenic sources (*i.e.* vehicle emissions). Such NO_x emissions contribute to a substantial increase in the NO_x level of the air mass, which is then detected at the NK AURN monitoring station. The elevated NO_x level was probably caused predominantly by the anthropogenic NO_x emissions from London traffic "rush hour" in the early mornings. NO_x level was particularly higher on the first and second day (Thursday and Friday) than the third and fourth day (Saturday and Sunday).

Ozone levels at the NK site were generally higher than those at the satellite locations during the FIOM period, potentially caused by overall emissions of ozone precursors in the region near London (given the ozone formation timescale, these could likely include VOC emissions from surrounding areas, and NOx emissions across the transit from satellite location to NK site). The shape of the O_3 profile between the NK site and satellite locations were variable each day. During the first two days of the FIOM period (9th and 10th August 2012) the NK O_3 trend was very different from (substantially elevated compared with) the satellite location's O_3 trend, but the two O_3 trends had very similar shapes and magnitudes during the second two days. Figure 4.46a shows that the NK O_3 level was always 20-30 ppb higher than the satellite location's O_3 level during the first two days, but were of similar magnitude for the second two day period. HYSPLIT back trajectory model results (Figure 4.32) confirmed the similar air mass origins during the second two day period caused such agreement.

Figure 4.47 suggests there was a variable distribution of wind directions and speeds at NK site during the first two days, with the (local NK site) wind lying predominantly from the North-East, and then the West, before adopting a steady south-easterly direction during the second two days. This wind pattern is reflected in changes in the synoptic air mass region, shown in Figure 4.17. During the first two days the sampled air mass at NK site combined local London (grey) and Midlands (Brown) origins, alongside SE (Light blue) areas. During the second two days, sampled air mass at NK site were mostly from Benelux/North Europe (Green), alongside smaller fractional contributions from the local London conurbation.

Both HYSPLIT back trajectory model and NAME model indicated that different air mass origins between first and second two days caused the contrasting NK vs satellite location shapes of the O_3 trends – for example, with lower ozone levels in the origin air for the first two days (which originated from the, primarily clean marine, south western sector) compared with higher ozone levels reflected aged polluted emissions from continental Europe during third and fourth day of the FIOM period, consistent with the variation in local wind direction.

The other distinctive phenomenon in Figure 4.46a is the time offset of ozone peaks, particularly apparent on the second two day period, with the NK peaks appearing to precede those from the satellite locations (as adjusted for overpass time). Variations in the wind direction / speed could account for the time offset of ozone peaks between the two profiles during the FIOM period; the transit time of the air masses is unlikely to have precisely, or accurately, corresponded to a single mean value for a three-hour period as implicitly assumed in this (primitive) analysis.

Due to the NO_2 and O_3 interconversion process during the daytime, with consideration that the OPR system measures the total oxidant production rate $p(O_x)$ under sunlight, it is more logical to perform the comparison between NK O_x and satellite location's O_x for advection effect analysis. If the NO + O_3 titration reaction is considered as the only existing reaction, performing an O_x based analysis removes the impact of traffic emissions of NO (but not NO_2) on the data – the resulting profiles are shown in Figure 4.46b. The time offset phenomenon of O_x peaks between the two O_x trends (NK vs satellite location) was also apparent, and similar to that for the O_3 trend, suggesting a common cause in both cases, which could be possible errors in the air mass transit time estimation.

Comparing the ozone trends in Figure 4.46a, the difference between first and second two days is slightly less distinctive, but still maintained, for the O_x trend shown in Figure 4.46b. The NK O_x level was 20 ppb to 40 ppb higher than the satellite location O_x level during the first two days, and 2 to 20 ppb higher than the satellite location O_x level during the second two days. The repeating pattern of daily elevated O_x level at the NK site (compared to the satellite location O_x) may therefore indicate chemical production of O_x during transport, rather than effects from vehicle NO emissions / NO + O_3 titration.

4.6.4.2 Evaluation of idealized ozone/O_x production rate

In order to evaluate the value of the measured $p(O_x)$ from OPR system, this advection analysis could be a useful tool to derive the estimated idealized O_x production rate. The approach neglects NO_x emissions (other than NO + O_3 titration through consideration of O_x), air mass mixing, NO_x/O_3 deposition and radical chemistry during transit time. It compares the differential $O_3/NO_x/O_x$ values between NK and the satellite locations, assuming differences in values were caused only by chemical production process during the air mass transportation. The differences in derived values were then divided by the air mass transit time to estimate an idealised hourly ozone/O_x production rate, shown in following figure:

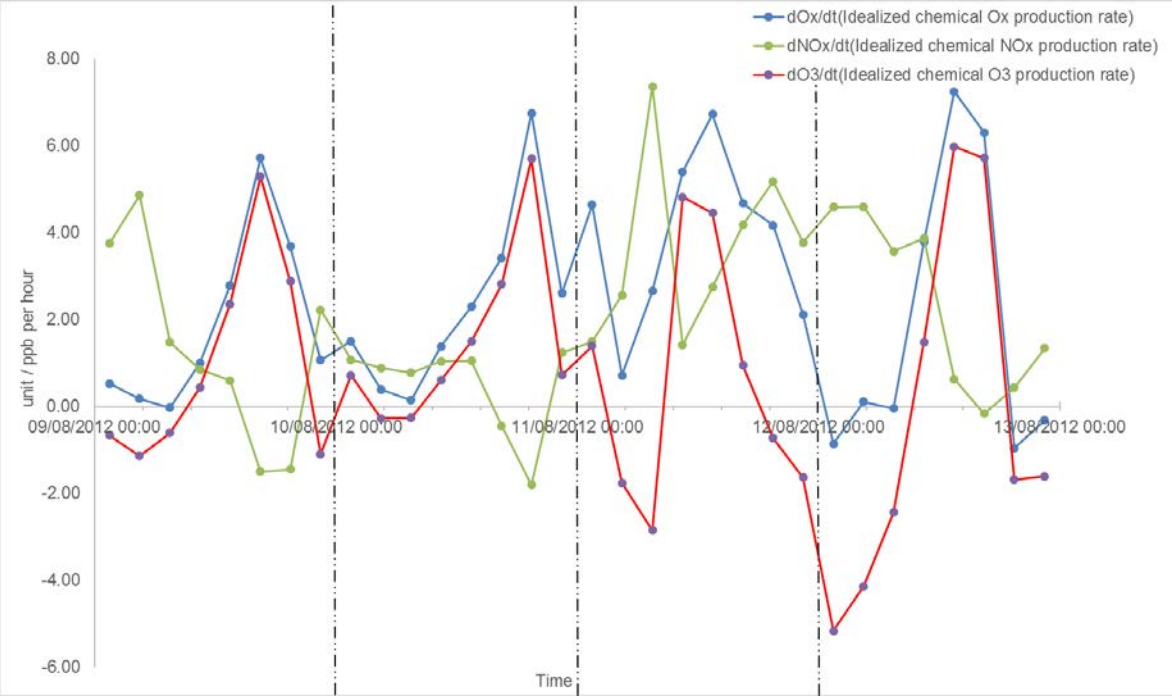

Figure 4.48. Time series of dO_x/dt, dNO_x/dt and dO_3/dt derived from non-advection effects (idealised chemical production only) during the FIOM period.

dNO_x/dt is the rate of change of NO_x mixing ratio with respect to time, when the air masses were transported to London (NK) from the satellite location. It maintained a generally positive value during the FIOM (especially during the second two day period, where air mass is from east of London), expected as air masses were entering an urban environment, with substantial NO_x sources, from surrounding rural environments, and was most likely caused by the net NO_x emissions during the air mass transit from satellite location.

dO_3/dt as shown in Figure 4.48 represents the idealised chemical ozone production rate as inferred from the advection analysis. There were broadly diurnal cycles in the dO_3/dt trend during FIOM. The dO_3/dt was generally positive across the middle of the day during the first two days, and exhibited substantial negative periods overnight during the second two days, which meant loss of ozone and/or NO_2 between the satellite locations and the NK site on 11th and 12th August 2012. In contrast, the dO_x/dt values were almost always positive during

this second two day period, and approximately zero overnight, while the dNO_x/dt values were variable but significantly positive overnight towards the end of the FIOM period. These observations are consistent with the "urban decrement effect" being the primary factor to cause negative values in the dO_3/dt trend. The positive dO_x/dt trend during FIOM also indicated that overall oxidant level were increasing as the air mass entering London. During the day, the dO_x/dt had its peak about 13:30, and chemical ozone production (by photochemical reactions) was likely responsible for the trend in dO_x/dt, rather than alternatives such as traffic NO_2 emissions during "rush hours" in early morning and late afternoon (the timings of which did not correspond with the peaks in dO_x/dt).

According to the air mass origin (Figure 4.17) and wind directions, there is a complex range of emission, mixing and deposition factors to influence air mass entering NK site (which lead to estimation of idealized chemical oxidant production rate dO_x/dt) during the first two days, but air mass entering NK site during the second two days were much simplified. Similar to previous comparison between indirect estimation of chemical oxidant production rate in section 4.5, it is more suitable to focus on dO_x/dt data during the second two days in contrast to the OPR measurement.

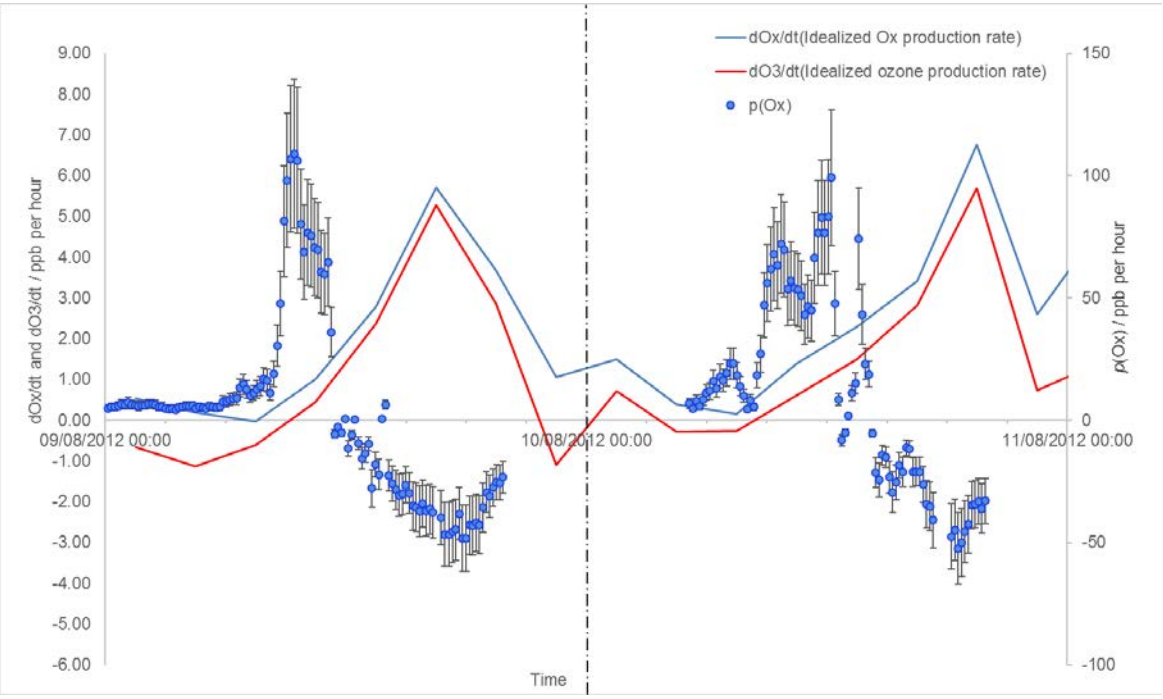

Figure 4.49. Measures of photochemical oxidant production: Comparison between advection analysis results (Left axis) and measured OPR data $p(O_x)$ (Right axis) (uncertainty of $p(O_x)$ is ± 28 %) during the first two days of FIOM period.

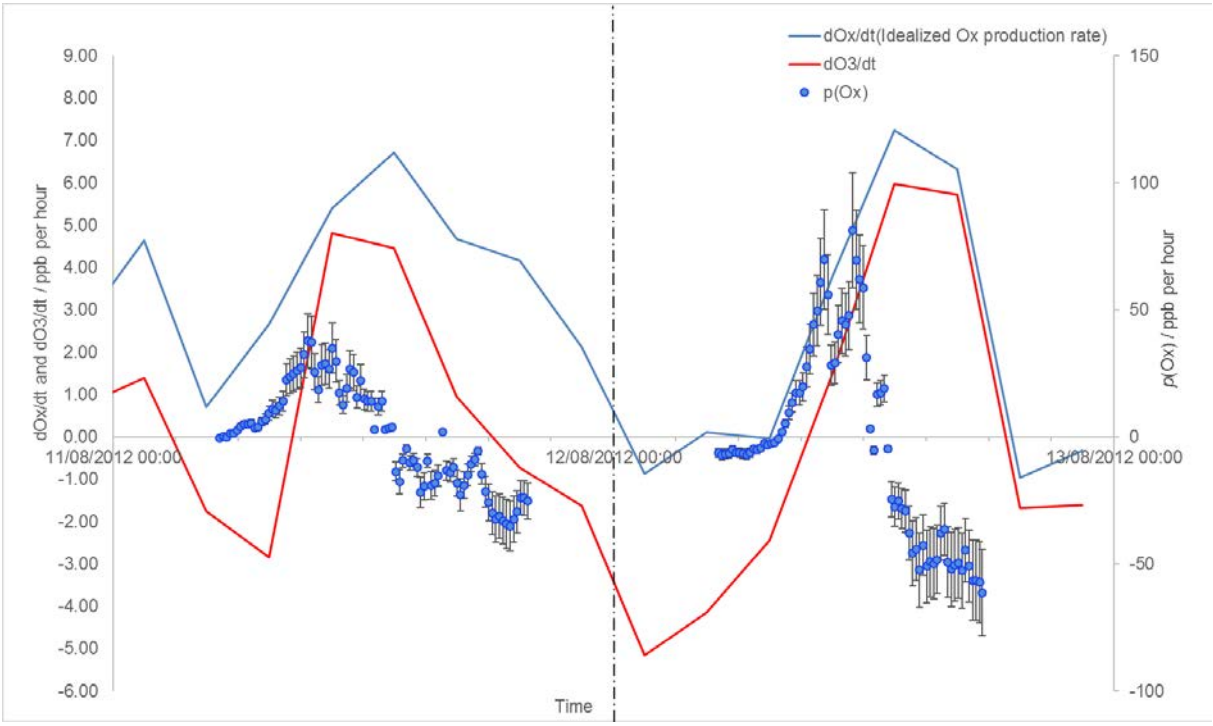

Figure 4.50. Measures of photochemical oxidant production: Comparison between advection analysis results (Left axis) and measured OPR data $p(O_x)$ (Right axis) (uncertainty of $p(O_x)$ is ± 28 %) during the second two days of FIOM period.

During the first two period (Figure 4.49), the idealized chemical O_x production rate (dO_x/dt) trend was different from the measured $p(O_x)$ trend during the FIOM period in both trend (diurnal profile) and absolute values. Although there is a similar diurnal trend, the time offset between two data sets were dramatic (up to 8 hours). The variation of air mass origins during the first two days caused this disagreement, it was not useful to compare the idealized chemical O_x production rate to $p(O_x)$ for the first two day period.

The idealized chemical O_x production rate (dO_x/dt) trend was much similar to the measured $p(O_x)$ trend during the second two day period (Figure 4.50). There was a similar diurnal pattern between dO_x/dt and $p(O_x)$, with a slight time offset (ca.3 hours). The measured $p(O_x)$ level peaked in the mid-morning, ca. 10:00 each day, while the dO_x/dt level peaked in the early afternoon, ca.13:00. However, the absolute values were still very different (peaked at 6 ppb comparing to peaked at 100 ppb) between two data sets. A possible reason for the time offsets is the inaccurate assessment of transit time; it is possible that the corresponding time between two data sets were unlikely to match. This possibility of inaccurate transit time is then assessed by the following wind speed comparison test.

As the NK site is located in a built-up residential area, it may exhibit relatively lower wind speeds than surrounding rural areas, and the actual wind transit speed between satellite location and NK site could be underestimated. A wind speed variation test was therefore performed, to investigate the potential inaccurate transit time issue (by wind) that caused the timing disagreement between two data sets. London Bexley and Rochester stoke AURN sites were used as indicators of wind speed outside the city centre. The comparisons between NK and the two indicator sites wind speed and directions during second two days of FIOM period is shown in following Figure 4.51:

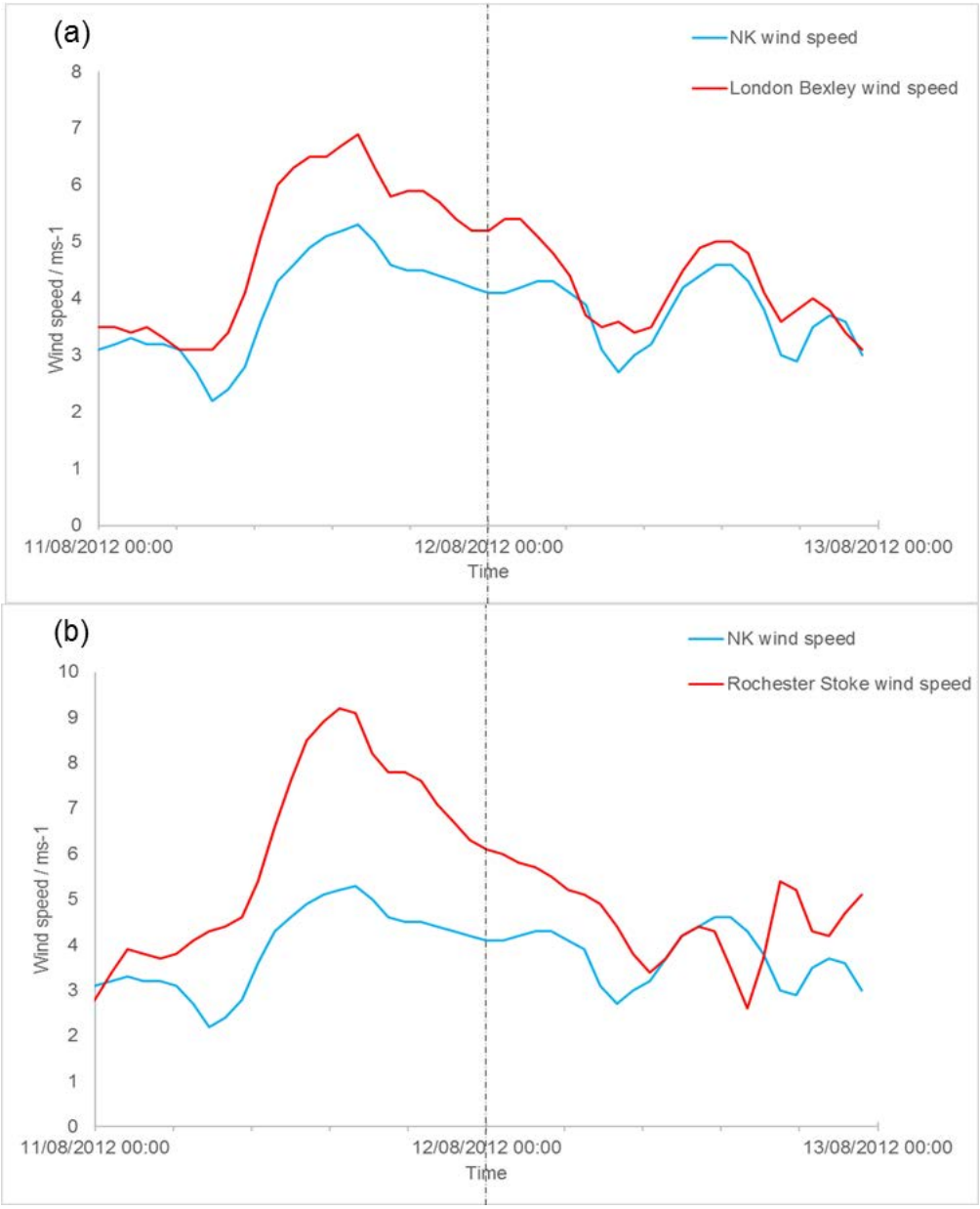

Figure 4.51. (a) Comparison between wind speed at NK and London Bexley (Suburban background) during second two days of FIOM period; (b) Comparison between wind speed at NK and Rochester Stoke (Rural background) during second two days of FIOM period.

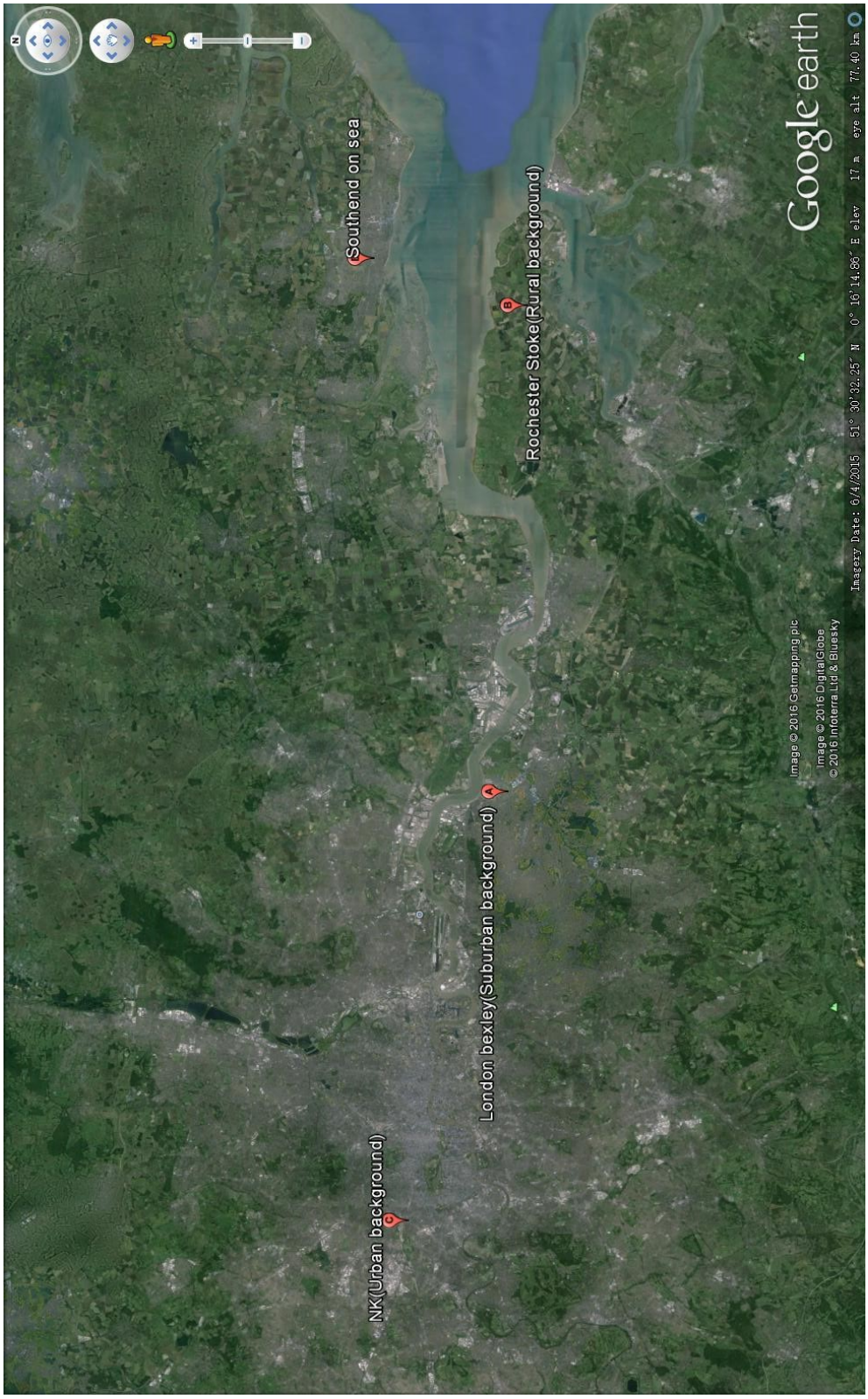

Figure 4.52. Locations of AURN monitoring sites: (A) London Bexley (Suburban background), (B) Rochester Stoke (Rural background), (C) North Kensington (Urban background), (D) Southend on sea (Urban background).

As Figure 4.52 shows, Rochester Stoke is a rural background site which is 11km south to Southend on sea, it is also 30km east of London Bexley site. During the second two day period, as the east wind approach central London, the wind air mass travel pass Rochester Stoke and London Bexley then arrive at NK site. The peak wind speeds were reduced from $9ms^{-1}$ on Rochester stoke to $5ms^{-1}$ on London Bexley when approaching NK site. It was clear that the wind speed used(wind data measured from NK site) for transit time estimation was underestimated during the second two days of FIOM period (Figure 4.50), where the wind directions were stable. The actual faster transit time lead to earlier peak time of diurnal dO_x/dt trend, which would reduce the time offset between two data sets. This is consistent with the rapid, early rise in O_x production observed at NK.

In Figure 4.50: One distinctive phenomenon of the dO_x/dt data was its sign; dO_x/dt was primarily positive during the second two days of FIOM period. Considering the diurnal cycles of the two trends, both dO_x/dt and $p(O_x)$ started increasing in the morning between 06:00 and 08:00, increased sharply to reach their daily peak level, then started decreasing. In the afternoon, as the solar radiation became less intense, NO_2 destruction and O_3 deposition process were expected to contribute to net O_x destruction. The $p(O_x)$ level decreased to negative values (O_x destruction); however, the idealized chemical O_x production rate remained predominantly positive every afternoon during these two days. This simplified analysis to derive dO_x/dt neglects NO_x emissions, air mass mixing, NO_x/O_3 deposition and radical chemistry. However, in the actual ambient air, those processes actively alter / contribute to the O_x production process. Such disagreements between two data sets indicated the advection-inferred dO_x/dt may not represent the actual O_x production rate, remaining something of an idealised concept. As the measured $p(O_x)$ only represented the chemical O_x production rate, the idealized O_x production rate dO_x/dt was not comparable

to measured $p(O_x)$. However, the shape of dO_x/dt morning trend indicated there was an evidence of rapid net O_x production every morning of the FIOM period. A further evaluation of chemical oxidant loss is performed to investigate its contribution to such negative values of the afternoon $p(O_x)$ in section 4.6.6.

4.6.5 Conclusion and Limitations of the Advection Analysis

The major limitation of this advection analysis is the simplistic estimation of wind speed and direction. In the actual environment, both wind speed and direction were not stable during the transport of air masses from various satellite locations to the NK site. The four direction assumption was also a very rough estimation of trajectory origin; selecting four satellite locations could not reproduce the actual air mass transition process from variable wind directions and hence variable overpass locations. The radical chemistry and in particular NO_x emission during transit time were an important component of chemical ozone abundance, which were neglected in this advection analysis. Although a regional model would be an ideal solution for more complex advection analyses to include more factors that are related to pollutant transport, the current simplistic analysis still showed general agreements between the temporal profiles of the idealized chemical ozone production rate and the measured $p(O_x)$ by OPR system.

4.6.6 Evaluation of the Chemical Oxidant Loss Rate during FIOM

Oxidant (O_x) loss processes in the troposphere predominantly occur through the following four reactions:

(i) $OH + NO_2 + M \rightarrow HNO_3 + M$ $k_{4.18}$ (4.18)

(ii) $HO_2 + O_3 \rightarrow OH + 2O_2$ $k_{4.19}$ (4.19)

(iii) $OH + O_3 \rightarrow HO_2 + O_2$ $k_{4.20}$ (4.20)

(iv) $RO_2 + NO_2 \rightarrow RO_2NO_2$ $k_{4.21}$ (4.21)

Rate constants for reactions (4.18) to (4.21) were readily obtained using literature data and measured temperature and pressure (Sander *et al*., 2011). As a large range of organic species ("R") is in principle present, no single value for $k_{4.14}$ may in principle be used. Here, the rate constant value for formation of $CH_3C(O)O_2$ was used to simulate the maximum oxidant loss rate in (4.20) (as a representative upper limit value). Estimated RO_2 levels were derived from the assumption of $k_{4.13}[HO_2][NO] \cong k_{4.14}[RO_2][NO]$ (see Section 4.5.3). The total oxidant loss rate, $l(O_x)$, is then presented as the sum of the rates of reactions 4.18 - 4.21:

$$l(O_x) = k_{4.18}[OH][NO_2] + k_{4.19}[HO_2][O_3] + k_{4.20}[OH][O_3] + k_{4.21}[RO_2][NO_2] \quad (4.22)$$

The estimated net chemical oxidant production rate $p_e(O_x)$ was then derived from calculated chemical oxidant production rate $p_c(O_x)$ (equation 4.17) and estimated chemical oxidant loss rate $l(O_x)$ (equation 4.22), presented as:

$$p_e(O_x) = p_c(O_x) + l(O_x) \quad (4.23)$$

The resulting evaluated net chemical oxidant production rate for the second two days of the FIOM period is shown in Figure 4.53:

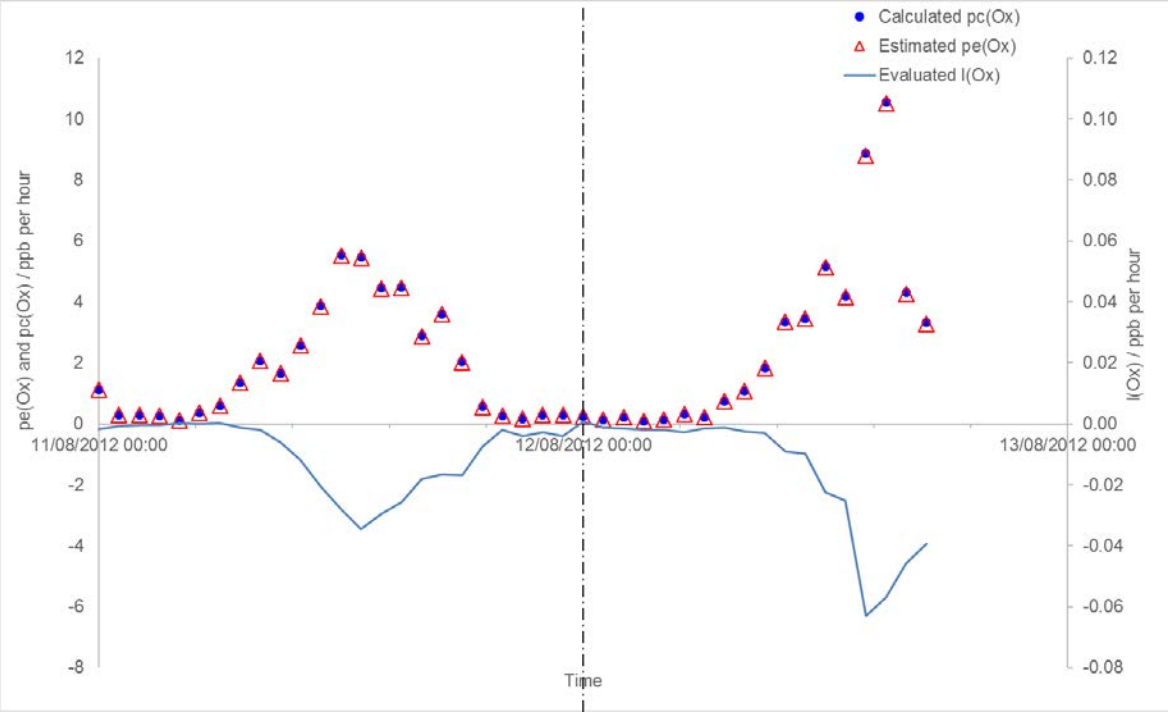

Figure 4.53. Comparison between evaluated $l(O_x)$ (blue line), estimated $p_e(O_x)$ (red triangle) and calculated (estimated) $p_c(O_x)$(dark blue dot) data sets on second two day period, where $p_e(O_x) = p_c(O_x) + l(O_x)$; $p_c(O_x)$ and $p_e(O_x)$ are on primary (left) axis, $l(O_x)$ is on secondary (right) axis.

The calculated chemical oxidant loss rate $l(O_x)$ displays a strong anti-correlation to $p_c(O_x)$, the two data sets correspond well to each other in terms of diurnal pattern on second two day period (Figure 4.53). However, the calculated chemical oxidant destruction rates were substantially smaller than the calculated chemical oxidant production rates. Consequently, the estimated $p_e(O_x)$ values were very similar overall to $p_c(O_x)$, it was not practically possible to separate the two data sets in Figure 4.53 due to the similarity between them. Consequently, blue dot stacked up top of red triangle stacked in Figure 4.53. The estimated net chemical oxidant production rate was then compared with measured net chemical oxidant production rate $p(O_x)$ and dO_x/dt (idealised oxidant production rate from advection analysis):

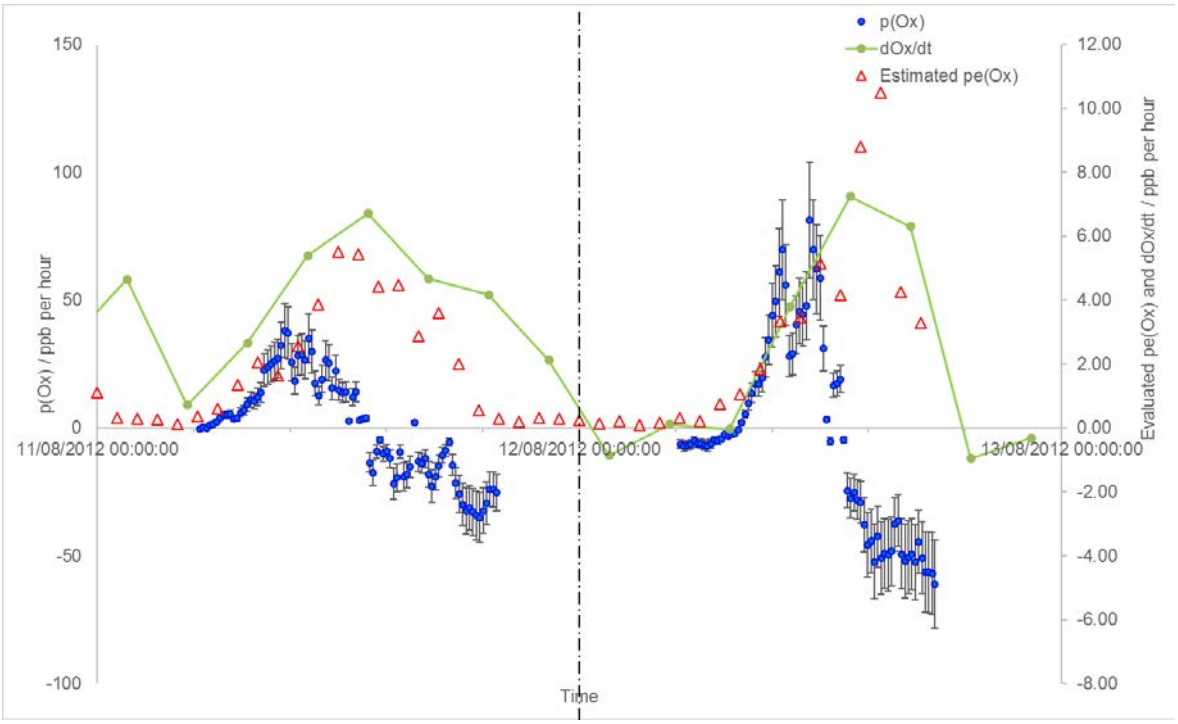

Figure 4.54: Comparison between $p(O_x)$, estimated $p_e(O_x)$ and dO_x/dt data sets during the second two days of FIOM period; $p(O_x)$ is on primary (left) axis (uncertainty is ± 28 %), estimated $p_e(O_x)$ and dO_x/dt are on secondary (right) axis.

Similar to $p_c(O_x)$ data in Figure 4.44, the diurnal pattern of $p_e(O_x)$ is apparent on 11th and 12th August, but with a later onset and extended persistence compared with the $p(O_x)$ data. Interestingly, the $p_e(O_x)$ displayed values close to dO_x/dt on 11th and 12th August. Particularly on the 11th August, the $p_e(O_x)$ showed very similar diurnal pattern to dO_x/dt, with slightly lower values (1 - 2 ppb per hour during the daytime). Although some limitations of this approach still remain (e.g. uncertainty regarding the complex range of peroxy radicals in the urban atmosphere), the comparison between the estimated $p_e(O_x)$ and dO_x/dt further supported the evidence of rapid rise of net oxidant production in the morning during the second two days of FIOM period, but also that $p(O_x)$ levels measured by the OPR were substantially higher than those indicated by other analyses.

4.7 Uncertainties in measured $p(O_x)$ values during FIOM

It was clear that net oxidant production rate rose sharply in the morning during the FIOM period (especially apparent on 11th and 12th August 2012), and dropped to zero / negative value in the afternoon, but the absolute values of $p(O_x)$ remain uncertain. Compared to measured $p(O_x)$ levels, the calculated oxidant production rates ($p_e(O_x)$ in Figure 4.44 and dO_x/dt in Figure 4.50) both showed substantially lower (smaller in magnitude) values of overall oxidant production rate. Figure 4.39 also indicated that the measured $p(O_x)$ did not agree with ambient ozone levels; adoption of the measured $p(O_x)$ would lead to estimated ozone levels substantially beyond the measured maximum ozone levels during FIOM. Although there were uncertainties in both the calculated oxidant production rate $p_e(O_x)$ and dO_x/dt (see Section 4.5.3, 4.6.5 and 4.6.6), the comparisons suggested the measured $p(O_x)$ overestimated the *in situ* chemical oxidant production rates. The measurement represents the diurnal pattern of chemical oxidant production during FIOM well, especially on the second two day period, where wind directions were stable, $p(O_x)$ agree with other estimation of oxidant production rate by indirect methods on diurnal pattern, particularly in the afternoon, measured $p(O_x)$ corresponded to boost of ambient oxidant level and $p_e(O_x)$ around 17:00. However, uncertainties remain in the absolute values of oxidant production rate measured by OPR system.

One possible reason for such uncertainty of $p(O_x)$ values is underestimation of the mean reactor residence time in the OPR system. Flow visualisation experiments showed turbulent flow patterns existed in the sampling reactors, after flow straighteners were installed (see Section 2.3.4). The turbulence could potentially increase the air mass mean residence time in reactors, resulting lower $p(O_x)$ values - but this should be captured in the residence time

measurements, unless leaks were present in both OPR reactors, introducing different (shorter) flow routes through the reactors, resulting lower mean residence time than laboratory test results. In preparation for future deployments, neoprene rubber gaskets were introduced after the ClearfLo experiments to ensure the reactor tubes were sealed to their end pieces.

Two main systematic uncertainties still remained in the analysis: systematic errors from the contrasting photochemical steady state (PSS) between the two reactors, and the resulting variable conversion efficiency in the conversion unit (introduced in more detail in the following chapter), were in effect included measured $p(O_x)$ values. Corrections for these effects were not implemented during the London OPR deployment.

4.8 Summary of OPR deployment in London

The London OPR deployment chapter started with description of details of OPR system deployment settings, location and its surrounding environment, then comparisons of the NO_x and O_3 levels between London NK (urban site) and Harwell (rural site) were performed to provide a view of air pollution climatology during the summer IOP in London, results suggested an observable urban decrement effect (NO titration) in London. According to the air pollution climatology, two heavy pollution events happened during the summer IOP, it was essential to focus on the second pollution period (FIOM)-which represented the typical summertime urban pollution episode. HYSPLIT back trajectory model was set to determine the NK air mass origin during FIOM. The results showed different diurnal pattern between the first two day period (9th and 10th August 2012) and second two day period (11th and 12th August 2012), air mass was from west-continental Europe on 11th and 12th August. It was then more logical to focus on measurement results during the second two day period.

OPR measurement results $p(O_x)$ during FIOM period were then compared to a range of correlative parameters. These parameters included the rate of change of ambient oxidant level dO_x/dt, evaluated ambient OH production rate $p(OH)$ and the estimated net oxidant production rate $p_e(O_x)$ from HO_2 measurement (indirect measurement method of oxidant production rate). In general, the OPR-measured $p(O_x)$ have similar diurnal pattern as these estimated values during the second two day period, but the absolute values of $p(O_x)$ were substantially higher than these estimation of ambient oxidant production rate.

The advection analysis section implemented a simplified four direction satellite location to simulate air mass transport to the NK site, based on measured wind direction and speed. The results agreed with HYSPLIT model, higher O_3 levels on 11th and 12th August 2012 were

likely to have been caused by aged pollutant emissions from west-continental Europe. A further estimation of chemical oxidant production rates was performed using the *in situ* data via the advection analysis, following on from the (hypothetical) assumption that differences between O_x at satellite locations and NK site were caused only by chemical production process during the air mass transport. Results showed similarity of two data sets in diurnal pattern, particularly on second two day period, but OPR-measured $p(O_x)$ were still substantially higher than the idealized ambient O_x production rate.

To summarize, the OPR deployment was reasonably successful performed in London summer 2012, it was certain that OPR system represents diurnal pattern of chemical oxidant production rate very well with stable wind direction / air mass origins. However, uncertainties remained in the measured $p(O_x)$ – unusually high values of oxidant production rates, possibly arising sue to systematic errors (for which corrections are presented in chapter 5), or possibly due to imperfect reactor sealing in the field, subsequently improved with additional seals in the follow up Indian OPR measurement campaign.

Chapter 5: System Accuracy and Correction Factors

This chapter describes some uncertainties and issues of instrument performance (systematic errors) within the OPR system. The variable conversion efficiency in the conversion unit and differences in photochemical steady state (PSS) between the two sampling reactors are the main issues. A correction procedure was developed to simulate those effects within the OPR system and correct the resulting measurements. Other possible uncertainties are also discussed in this chapter. These and other corrections were implemented for the measured $p(O_x)$ values presented in chapter 6 (Indian OPR deployment).

5.1 Origin of Chemical Errors in ΔO_3 from the OPR system

As discussed previously (section 5.3), when ambient NO_x and O_3 enter the conversion unit from the dual sampling reactors, NO reacts with O_3 to regenerate NO_2 both during and after the NO_2 to O_3 photolytic conversion process driven by the UV lamps, which influences (reduces) the conversion efficiency (differently - as NO_x and O_3 levels differ in each flow) in each of the converter cells. The existence of this reaction ($NO + O_3$) also indicates that the conversion efficiency cannot ever reach the theoretical maximum of 100 %.

To recap, section 2.2.3 indicated that the photostationary steady state (PSS) established in the sample and reference reactors are different. In the sample reactor, the PSS is same as in ambient air, while in the reference reactor, solar radiation is attenuated, and there is greater net reaction of NO with O_3 to form NO_2 (with reduced NO_2 photolysis). Consequently, the PSS in the reference reactor is different from the PSS in the ambient air. After exiting the reference reactor, the reference flow has a reduced O_3 level and elevated NO_2 level. In contrast, the sample flow retains the same NO, NO_2 and O_3 levels as in the ambient air (if

the non-PSS chemical changes are neglected, e.g. ozone formation). Neglecting the radical chemistry, the total O_x in each flow is still the same after the reactors. When both sample and reference flows enter the conversion unit, due to the incomplete NO_2 to O_3 conversion process, NO_2 levels are partly and to a different extent converted to O_3 in the two flows; the difference arises as the NO levels, and hence the NO + O_3 back-reaction, differ - which leads to slightly different converted O_3 levels between the two flows. Since the ozone monitor only measures the differential O_3 levels between two flows (as the ΔO_3), after the conversion unit, by assuming the conversion efficiency is the same in both converter cells, the incomplete and differing NO_2 conversion leads to a non-zero differential measured O_3 level (and hence inferred O_x) between the two flows, even in the absence of any (non-PSS) radical chemistry. As a result, there is always an artefact reading from the differential measured O_x levels (measured as O_3) between two flows. In conclusion, the different PSS between two reactors leads to a systematic artefact in the measured ΔO_3.

Furthermore, NO_2 conversion efficiency measurement from section 3.6 describes the relationship between NO_2-O_3 conversion efficiency and synthetic air containing NO_2. However, in reality, the NO_2-O_3 conversion efficiency in the conversion unit is immediately variable with the shifting ambient air composition, *i.e.* this factor varies with atmospheric conditions, which need to be taken into account. A correction procedure to account for these effects was developed.

5.2 A Modelling approach to parameterise the NO_2 conversion efficiency

One disadvantage of the differential conversion efficiency measurement outlined in chapter 3 was the lack of full simulation of the ambient air composition: The test was based on purely synthetic air + NO_2 input, in absence of addition of NO and O_3. During the OPR field deployment, various levels of NO and O_3 will flow through the conversion unit, depending upon the ambient atmospheric conditions, which will subsequently lead to different NO_2 conversion efficiency from that determined in the laboratory tests (as a consequence of differing rates of the NO + O_3 back reaction): The operational (actual) cell conversion efficiency will depend on the ambient NO_x and O_3 levels, an effect not considered in previous work (Cazorla and Brune, 2010).

A more accurate method to estimate the operational conversion efficiency, accounting for these effects, was developed, using a modelling approach to calculate the estimated output of NO_x and O_3 levels from the converter cells for a given NO_x and O_3 input.

5.2.1 Basis of the modelling method of conversion efficiency (CE) estimation

In the conversion unit, when the UV lamps are powered, the PSS in converter cell is presented as,

$$NO_2 + h\nu \rightarrow NO + O \qquad jNO_{2\,lamp} \qquad (5.1)$$

$$O + O_2 + M \rightarrow O_3 + M \qquad (5.2)$$

$$NO + O_3 \rightarrow NO_2 + O_2 \qquad k_{NO+O_3} \qquad (5.3)$$

Where k_{NO+O_3}= 1.9 × 10^{-14} $molecule^{-1}$ cm^3 s^{-1} at 298 K (Sander *et al*., 2011).

The NO_2 photolysis frequency in the converter cells, $jNO_{2\ lamp}$, was determined from the results of the previous conversion efficiency tests in chapter 3, under the conditions of absence of NO or O_3, with lowest synthetic NO_2 input (to minimise back reaction effects).

5.2.2 Calculation of $jNO_{2\ lamp}$ in converter cell

From R 5.1, disregarding the NO + O_3 back reaction, the rate of loss of NO_2 could be expressed as:

$$d[NO_2]/dt = - jNO_{2\ lamp} \times [NO_2] \quad (5.4)$$

$$d[NO_2]/[NO_2] = - jNO_{2\ lamp} \times dt \quad (5.5)$$

The integration of the equation 5.5 is presented as:

$$\int d[NO_2] \times 1/[NO_2] = \int - jNO_{2\ lamp} \times dt \quad (5.6)$$

As a result, $\ln[NO_2] = - jNO_{2\ lamp}\ t_{res\ cell} + \ln[NO_2]_{t=0}$ is established from equation (5.6), therefore, the photolysis rate in the converter cell is rewritten as:

$$jNO_{2\ lamp} = (\ln[NO_2]_{t=0} - \ln[NO_2]) / t_{res\ cell}$$

Where $t_{res\ cell}$ = 55 seconds (from section 3.3)

By applying the two sets of test results from previous conversion efficiency test of 12.29 ppb synthetic NO_2 input, a mean photolysis rate in the converter cells, $jNO_{2\ lamp}$= 0.04 ± 0.01 s^{-1} (1 standard deviation) was determined.

However, this result was established from measured NO_2 values after synthetic NO_2 flow pass the converter cell, which includes PSS / NO + O_3 → NO_2 backward conversion,

consequently the $j\mathrm{NO_2}_{\text{ lamp}}$ was underestimated, with the actual $j\mathrm{NO_2}_{\text{ lamp}}$ being higher. Consequently, the maximum ${}_j\mathrm{NO_2}_{\text{ lamp}}$ value was taken to determine an estimated operational ${}_j\mathrm{NO_2}_{\text{ lamp}}$ for the converter cells of 0.05 s^{-1}.

5.2.3 Principle of the modelling method

During OPR field deployments, the ambient NO, NO_2 and O_3 levels were measured with NO_x and O_3 monitors, while both $j\mathrm{NO_2}_{\text{ lamp}}$ (0.05 s^{-1}) and k_{NO+O3} values are now known, along with the converter cell residence time (55 seconds). With those parameters, neglecting other chemical reactions such as the formation and reactions of NO_3, it is possible to apply the known chemical reactions to model the evolving NO-NO_2-O_3 in the converter cells, and so to determine the operational conversion efficiency in converter cells. At any given time point (in this case, 55 seconds from time 0), when ambient NO_x and O_3 (as input) are known, it is then possible to estimate the output concentrations of NO_x and O_3 after air flows through the converter cells, and therefore, the operational conversion efficiency is determined.

This conversion cell chemistry model was constructed within excel, using a time step of 1 second and ${}_j\mathrm{NO_2}_{\text{ lamp}}$ value at 0.05 s^{-1}, calculating the change in NO, NO_2 and O_3 concentrations after each second, through to the total conversion cell residence time of 55 seconds taken as the output values. This model was used for NO_x inputs from 0.1 to 100 ppb, and O_3 inputs from 1 to 100 ppb, to gain a relatively complete simulation of the conversion efficiency as a function of anticipated ambient air composition. The initial ambient NO_2 and NO values were derived from the input NO_x and O_3 levels assuming PSS applied. After calculation of the simulated conversion efficiency values as a function of NO_x and O_3, a multi linear regression analysis was applied to enable prediction of the (model derived)

conversion efficiency of converter cell ($CE_{converter}$) as a function of ambient (incoming) NO_x and O_3 levels.

5.2.4 Conversion cell chemistry model: Calculation Procedure

Under normal power settings, the UV lamp outputs correspond to an NO_2 photolysis frequency, $jNO_{2\ lamp}$, of 0.05 s^{-1}, and k_{NO2+O3}= 1.9 × 10^{-14} $molecule^{-1}$ cm^3 s^{-1}. Input NO, NO_2 and O_3 levels are known at time 0, denoted as NO_{time0}, NO_{2time0} and O_{3time0}.

The change in NO value in every second is presented as $d[NO]/dt = + jNO_{2\ lamp} - k[NO][O_3]$

The change in NO_2 in every second is presented as $d[NO_2]/dt = - jNO_{2\ lamp} + k_{NO2+O3}\ [NO][O_3]$

The change in O_3 in every second is presented as $d[O_3]/dt = + jNO_{2\ lamp} - k_{NO2+O3}\ [NO][O_3]$

By applying those values, NO, NO_2 and O_3 values are calculated after 1 second (time 1), given by :

$NO_{time1} = NO_{time0} + d[NO_{time0}]/dt = NO_{time0} + j[NO_{2time0}] - k[NO_{time0}][O_{3time0}]$

$NO_{2time1} = NO_{2time0} + d[NO_{2time0}]/dt = NO_{2time0} - j[NO_{2time0}] + k[NO_{time0}][O_{3time0}]$

$O_{3time1} = O_{3time0} + d[O_{3time0}]/dt = O_{3time0} + j[NO_{2time0}] - k[NO_{time0}][O_{3time0}]$

This process may be repeated each second through to the full residence time of the converter cells. As the sequence continues until time 55 seconds, the output value of NO, NO_2 and O_3 are calculated. The converter cell's conversion efficiency is then determined as $CE = (NO_{2time0} - NO_{2time43})/ NO_{2time0}$, expressed as a percentage. The multi linear relation between ozone, NO_x and $CE_{converter}$ is shown in the following three dimensional Figure 5.1:

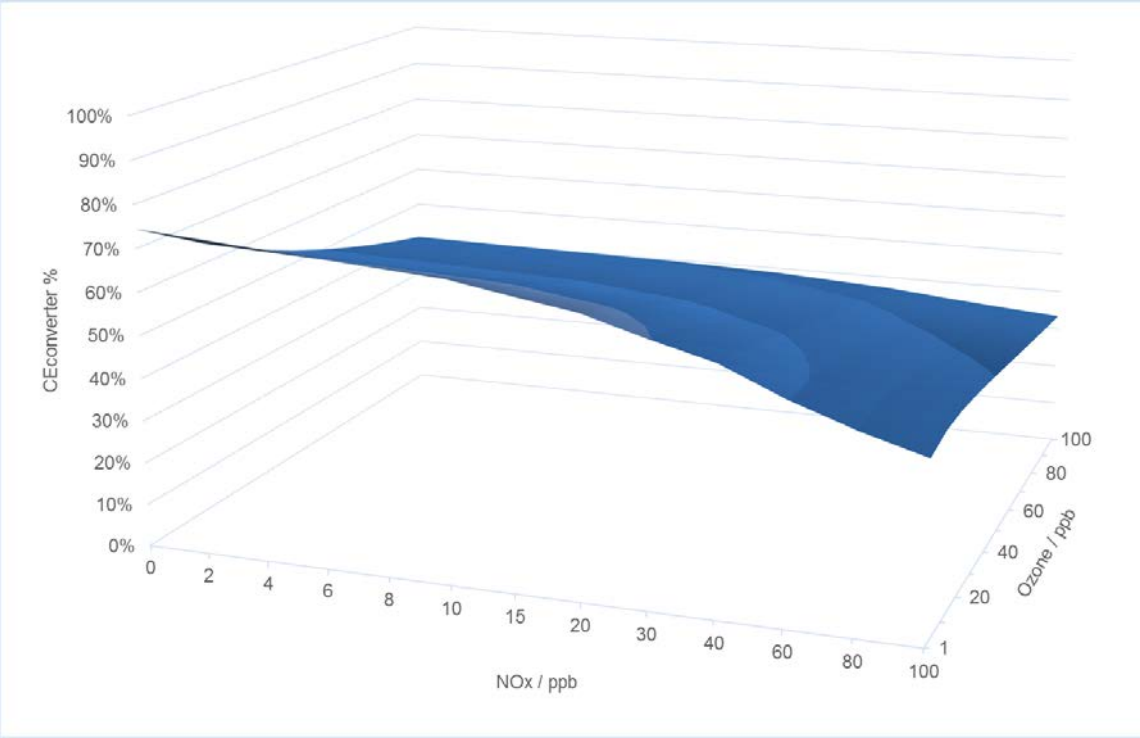

Figure 5.1. The multi linear relationship between NO_x (x axis), ozone (y axis) and $CE_{converter}$ (z axis).

Subsequently, a multi linear regression analysis was applied to the $CE/NO_x/O_3$ dataset to estimate the model derived conversion efficiency of converter cell from Figure 5.1. The result is then presented as:

$$CE_{converter} = 66.755 - (0.167 \times NO_x) - (0.250 \times O_3), \text{ unit in percentage \%.} \quad (5.7)$$

5.2.5 Conversion Cell Chemistry Model Validation

In reality, other NO_y species may in principle affect the conversion efficiency and NO_x-O_3 PSS. (e.g. NO_3, N_2O_5) To assess if they were significant, a FACSIMILE model using standard MCM 3.1(Saunders *et al*., 2003) inorganic (photo) chemistry was implemented to validate the results from the conversion cell chemistry model. The MCM's inorganic chemistry reactions are shown in the following table 5.1:

```
thermal gas-phase reactions ;
;
5.60D-34*O2*N2*((TEMP/300)@-2.6)  : O = O3
6.00D-34*O2*O2*((TEMP/300)@-2.6)  : O = O3
8.00D-12*EXP(-2060/TEMP)          : O + O3 =
KMT01                             : O + NO = NO2
5.50D-12*EXP(188/TEMP)            : O + NO2 = NO
KMT02                             : O + NO2 = NO3
3.20D-11*O2*EXP(67/TEMP)          : O1D = O
1.80D-11*N2*EXP(107/TEMP)         : O1D = O
1.40D-12*EXP(-1310/TEMP)          : NO + O3 = NO2
1.40D-13*EXP(-2470/TEMP)          : NO2 + O3 = NO3
3.30D-39*EXP(530/TEMP)*O2         : NO + NO = NO2 + NO2
1.80D-11*EXP(110/TEMP)            : NO + NO3 = NO2 + NO2
4.50D-14*EXP(-1260/TEMP)          : NO2 + NO3 = NO + NO2
KMT03 % KMT04                     : NO2 + NO3 = N2O5
2.20D-10*H2O                      : O1D = OH + OH
1.70D-12*EXP(-940/TEMP)           : OH + O3 = HO2
7.70D-12*EXP(-2100/TEMP)          : OH + H2 = HO2
1.30D-13*KMT05                    : OH + CO = HO2
2.90D-12*EXP(-160/TEMP)           : OH + H2O2 = HO2
2.03D-16*((TEMP/300)@4.57)*EXP(693/TEMP)  : HO2 + O3 = OH
4.80D-11*EXP(250/TEMP)            : OH + HO2 =
2.20D-13*KMT06*EXP(600/TEMP)      : HO2 + HO2 = H2O2
1.90D-33*M*KMT06*EXP(980/TEMP)    : HO2 + HO2 = H2O2
KMT07                             : OH + NO = HONO
KMT08                             : OH + NO2 = HNO3
2.00D-11                          : OH + NO3 = HO2 + NO2
3.60D-12*EXP(270/TEMP)            : HO2 + NO = OH + NO2
KMT09 % KMT10                     : HO2 + NO2 = HO2NO2
1.90D-12*EXP(270/TEMP)            : OH + HO2NO2 = NO2
4.00D-12                          : HO2 + NO3 = OH + NO2
2.50D-12*EXP(-260/TEMP)           : OH + HONO = NO2
KMT11                             : OH + HNO3 = NO3
4.00D-32*EXP(-1000/TEMP)*M        : O + SO2 = SO3
KMT12                             : OH + SO2 = HSO3
1.30D-12*EXP(-330/TEMP)*O2        : HSO3 = HO2 + SO3
;
photolysis reactions ;
;
J<1>                              : O3 = O1D
J<2>                              : O3 = O
J<3>                              : H2O2 = OH + OH
J<4>                              : NO2 = NO + O
J<5>                              : NO3 = NO
J<6>                              : NO3 = NO2 + O
J<7>                              : HONO = OH + NO
J<8>                              : HNO3 = OH + NO2
```

Table 5.1. Inorganic chemistry reactions in the MCM 3.1 (Saunders *et al*., 2003).

This validation process determines the difference between the modelled NO, NO_2 and O_3 concentrations using the (comprehensive) FACSIMILE / MCM model and those from the (simplified) excel conversion cell chemistry model, when all significant chemical reactions were considered in FACSIMILE model. Both methods were set to run from time 0 to 100 seconds to simulate the NO_x and O_3 levels entering the conversion unit (at time 0) and leaving the conversion unit (at time 55 seconds). The results from conversion cell chemistry model, and the detailed FACSIMILE model, are compared in following Figure 5.2:

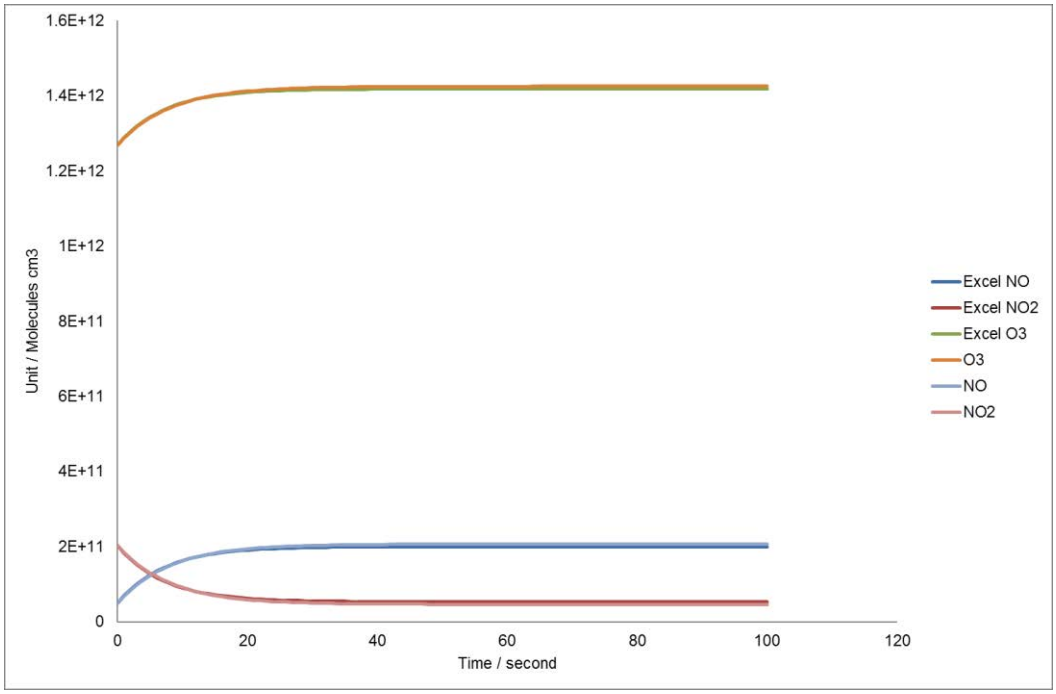

Figure 5.2. Comparison of simulated NO, NO_2 and O_3 levels in the conversion cells using a detailed numerical model (based on the MCM running within FACSIMILE) and the simplistic NO_x-O_3 PSS-only conversion cell chemistry model (constructed within excel).

The MCM model result showed similarity with the conversion cell chemistry model. This result shows that the assumption of only NO-NO_2-O_3 chemistry evolving in the converter cell is an appropriate approximation, at least over the short time periods (55 seconds, the mean residence time of converter cell) and in the presence of photolysis radiation, can be applied to actual OPR deployment data.

5.3 ΔO_3 correction analysis

As NO_x and O_3 differ in the sample and reference flows (section 2.2.2), the conversion efficiency will also differ according to this Equation 5.7, aggravating the differences between measured O_3 levels in the two flows after the conversion unit; this fact leads to a further artefact in the measured ΔO_3. A correction is required to solve this problem.

5.3.1 Different PSS in both reactors

The ΔO_3 correction analysis is based on the assumption that NO_x and O_3 are in PSS in both sample and reference reactors, in addition to neglecting (non-PSS) radical chemistry in both reactors. In the sample reactor, the photochemical reactions are the same as in the ambient air. The PSS in the sample reactor is presented as,

$$j\mathrm{NO_{2\ sample}} \times [\mathrm{NO_{2\ ambient}}] = k \times [\mathrm{NO_{ambient}}] \times [\mathrm{O_{3\ ambient}}] \quad (5.8)$$

In equation (5.8), $j\mathrm{NO_{2\ sample}}$ is the photolysis rate of NO_2 in sample reactor, the NO + O_3 rate constant k is known (e.g. 1.9×10^{-14} molecule^{-1} cm3 s^{-1} at 298 K. (Sander *et al*., 2011). Then the $j\mathrm{NO_{2\ sample}}$ value is presented as,

$$j\mathrm{NO_{2\ sample}} = (k \times [\mathrm{NO_{ambient}}] \times [\mathrm{O_{3\ ambient}}])/[\mathrm{NO_{2\ ambient}}] \quad (5.9)$$

Equation (5.9) therefore derives the $j\mathrm{NO_{2\ sample}}$ value from ambient NO_x and O_3 levels.

In the reference reactor, due to the UV filtering outer layer, the PSS is different from the sample reactor. The photolysis frequency of NO_2, $j\mathrm{NO_{2\ reference}}$, is reduced by the Ultem film. Previous reactor wall loss experiments under sunlight showed that the $j\mathrm{NO_{2\ reference}}$ is directly proportional to the sample reactor photolysis frequency $j\mathrm{NO_{2\ sample,}}$, with the proportionality constant derived from the reduction in NO_2 levels measured when NO_2 (only) was

introduced to each reactor (sample, ambient). Under the natural sunlight environment, the NO_2 wall loss effect experiment (see Section 3.4.2) indicated 19.31 % of synthetic NO_2 was lost after passing though the sample reactor; 2.76% of synthetic NO_2 was lost after passing though the reference reactor. By applying those two factors, the dependence between $j NO_{2\ reference}$ and $j NO_{2\ sample}$ may be presented as,

$$j NO_{2\ reference} = (0.0276/0.1931) \times j NO_{2\ sample}.$$

$$j NO_{2\ reference} = 0.14\ j NO_{2\ sample}.$$

The photolysis frequency of NO_2 in reference reactor $j NO_{2\ reference}$ is 0.14 $j NO_{2\ sample}$.

5.3.2 Change of NO_x/O_3 values in the reference reactor

The artefact correction procedure assumes that ambient NO_x and O_3 enter the reference reactor and reach PSS. The PSS in the reference reactor is then presented as,

$$j NO_{2\ reference} \times [NO_{2\ reference}] = k \times [NO_{reference}] \times [O_{3\ reference}] \quad (5.10)$$

$j NO_{2\ reference}$ is proportional to $j NO_{2\ sample}$ as discussed, k value is the same as that is in the sample reactor (with negligible temperature difference). When ambient NO, NO_2 and O_3 enter the reference reactor, they will take some period of time to reach PSS; the actual time required to reach PSS is dependent on ambient NO_x and O_3 level. An estimation based on $1/j NO_{2\ reference}$ suggested it will require from 1000 to 9000 seconds for levels to approach PSS in the reference reactor during FIOM, depending upon the ambient light level (time of day).

When $NO_{reference}$, $NO_{2\ reference}$ and $O_{3\ reference}$ reach PSS, their values differ from ambient NO, NO_2 and O_3 by a certain value (here introduced as an offset, X). By applying this difference X, an idealised representation of the reference reactor's PSS is shown below in Figure 5.3:

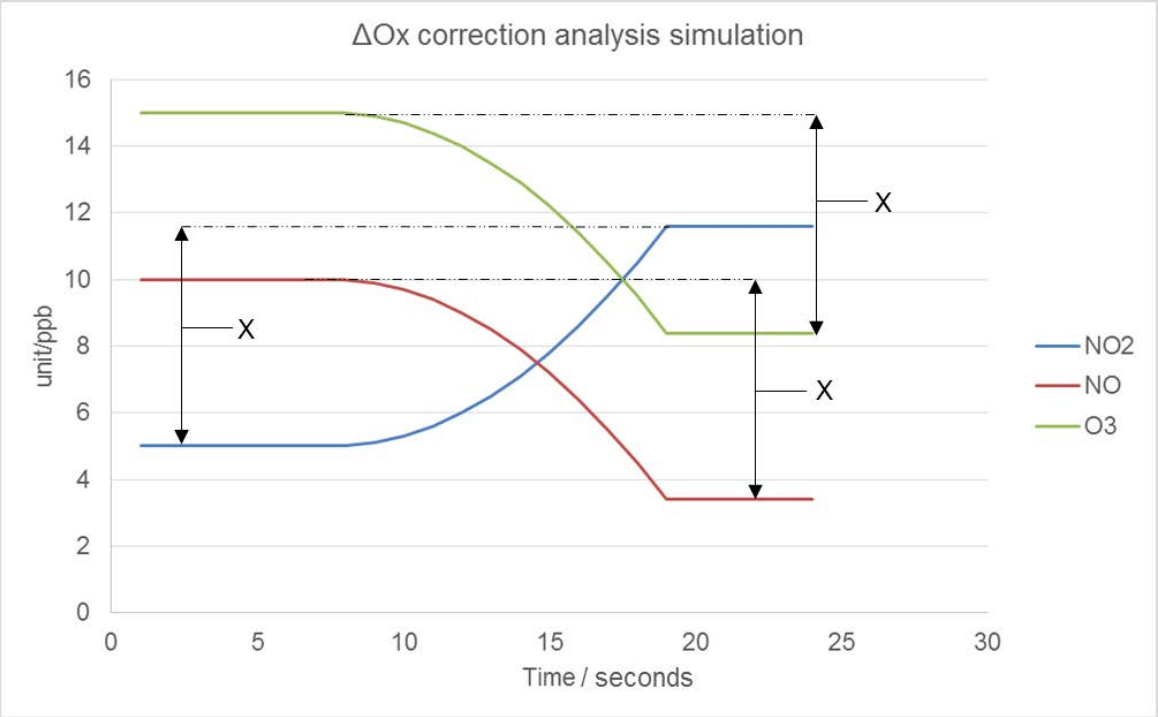

Figure 5.3. Idealised representation of chemical species evolution after ambient pollutants flow into reference reactor, X value represent the change in mixing ratio of NO, NO_2 and O_3 in the PSS. This figure is based on simulated data only for idealised representation, it does not include actual measurement data.

Figure 5.3 shows how the $NO_{reference}$, $NO_{2\ reference}$ and $O_{3\ reference}$ are related to $NO_{ambient}$, $NO_{2\ ambient}$ and $O_{3\ ambient}$ by a single offset factor X, which may be presented as,

$$NO_{2\ reference} = NO_{2\ ambient} + X \quad (5.11)$$

$$NO_{reference} = NO_{ambient} - X \quad (5.12)$$

$$O_{3\ reference} = O_{3\ ambient} - X \quad (5.13)$$

When equation 5.11, 5.12 and 5.13 are substituted into equation 5.10, it may be presented as,

$$j\mathrm{NO_{2\ reference}} \times [\mathrm{NO_{2\ ambient}} + \mathrm{X}] = k \times [\mathrm{NO_{ambient}} - \mathrm{X}] \times [\mathrm{O_{3\ ambient}} - \mathrm{X}] \quad (5.14)$$

Equation (5.14) can be rearranged as,

$$j\mathrm{NO_{2\ reference}}\ (\mathrm{NO_{2\ ambient}}) + j\mathrm{NO_{2\ reference}}\mathrm{X} = k\mathrm{X}^2 + k(\mathrm{NO_{ambient}})(\mathrm{O_{3\ ambient}}) - k(\mathrm{NO_{ambient}})\mathrm{X} - k(\mathrm{O_{3\ ambient}})\mathrm{X} \quad (5.15)$$

The two quadratic solutions for X are referred to as X_1 and X_2. X_1 is always higher than the ambient NO level in the actual data analysis, and so would lead to negative concentrations and may be discarded. Only X_2 is applied in data analysis, as the factor accounting for the differential NO_2 to O_3 ratios of total O_x level between two reactors. Compared to the sample flow, the reference flow has elevated NO_2 level, reduced O_3 levels and reduced NO levels.

After ambient air passes through the sample and reference reactors, the two flows enter the dual converter cells with built-in UV lamps to convert NO_2 to O_3. As discussed in chapter 2 (section 4.2), periodic valve switching system allows averaging out of any differences in UV radiation from the two sets of UV lamps; this approach leads to equal (averaged) UV radiation experienced by the flow through each of the converter cells.

As outlined above, before two flows enter the conversion unit, their O_x levels are the same, but their NO, NO_2 and O_3 levels are different, by the factor X. The reference reactor's flow always has higher NO_2 to O_3 ratio than sample reactor. Also as introduced above, $CE_{converter}$ is dependent on the NO_x and O_3 levels, and the conversion efficiency between two converter cells are subsequently different. The different conversion efficiency between two converter cells lead to differential measured O_3 levels as determined by the ozone monitor, even in the absence of (non-PSS) radical chemistry (*i.e.* even in the absence of ozone production). In addition, the $CE_{converter}$ is necessarily always lower than 100%. The incomplete NO_2

conversion causes reduced measured O_3 levels in both flows, to a greater extent in the reference than sample reactor.

5.3.3 The overall artefact correction procedure

The following procedures were introduced to represent and account for those processes in the OPR system.

i. In the sample reactor, ambient NO_x and O_3 levels were assumed to remain the same in the sample reactor as in the ambient air. Therefore, $j\mathrm{NO_2}_{\text{ sample}}$ is derived from the ambient NO_x and O_3 levels; the dependence between $j\mathrm{NO_2}_{\text{ reference}}$ and $j\mathrm{NO_2}_{\text{ sample}}$, derived from previous NO_2 comparison experiments, is used to determine $j\mathrm{NO_2}_{\text{ reference}}$ as $0.14\ j\mathrm{NO_2}_{\text{ sample}}$.

ii. At the point of entry to the conversion unit, sample reactor's NO, NO_2 and O_3 levels are assumed to remain the same as they are in the ambient air. By applying $j\mathrm{NO_2}_{\text{ reference}}$ and equations (5.10) from section 5.3.2, the change of NO_x and O_3 values (X) is determined, and the NO, NO_2 and O_3 levels in the reference flow are derived by applying the value X. (The reference flow has elevated NO_2 levels with reduced O_3 and NO levels compared with the sample flow).

iii. After both flows enter the conversion units, their NO_2 to O_3 conversion efficiencies are derived from the NO_x- and O_3-dependent expression for conversion efficiency, *i.e.* $CE_{converter} = 66.755 - (0.167 \times NO_x) - (0.250 \times O_3)$. By applying this equation to known NO_x and O_3 levels in both flows, the converted O_3 levels may be estimated in both flows.

iv. Adding this "converted O_3" to the O_3 entering each conversion cell in both sample and reference flows allows the artefact differential O_3 value to be determined. This differential value is the correction factor, here referred to $V_{correction}$.

v. The measured differential O_3 levels are lower than the actual (desired) differential O_3 levels due to the incomplete NO_2 conversion. Consequently, the measured ΔO_3 is underestimated compared with the true (reactor-only) ΔO_3, and is corrected by adding $V_{correction}$ to the measured ΔO_3.

The $V_{correction}$ is compounded by both the effect of different PSS in reactors and incomplete NO_2 conversion in converter cells. It is the result of this ΔO_3 correction analysis which needs to be added on to correct the measured ΔO_3. The mean value of $V_{correction}$ in TERI data set was 1.94 ± 1.18 ppb (Standard deviation). Compared to the measured ΔO_3 values from TERI OPR deployment, this was a correction of 16 % (mean) ± 597 % (maximum / minimum). This $V_{correction}$ is an important factor to add to measured ΔO_3, and one which has thus far been neglected by other groups pursuing similar methodology (*e.g.* Cazorla & Brune, 2010).

When generating $V_{correction}$, it is appropriate to apply the result from reactor wall loss tests to the ambient NO_x and O_3 levels in reactors (in section 5.3.3, procedure (i)). Therefore, 10% of the measured ambient ozone level is deducted (the NO_x loss is very low, and may be neglected).

5.4 Limitations of the correction approach

There are two main limitations in this correction approach. The main limitation is assuming PSS is established in the reference cell. In the previous characterisation chapter, the reactor's residence time test indicated the mean residence time of reference reactor is approximately 710 seconds. However, by applying $1/jNO_{2\ reference}$ from the FIOM hourly data, the estimated time required for air to reach PSS (1/e folding lifetimes) are between 1000 to 9000 seconds in the reference reactor, depending upon ambient light levels. This fact suggests that the reference flow's NO_2 levels are lower than expected in the reference PSS during the correction analysis, particularly at low light levels (twilight and dawn) which could potentially cause an artefact in the introduced X value. The true X value would be lower than that calculated / introduced here; this artefact potentially leads to increased actual $V_{correction}$ values, which lead to underestimated ΔO_3 values.

The second limitation is the $jNO_{2\ reference}$. The dependence between $jNO_{2\ reference}$ and $jNO_{2\ sample}$ was derived from previous NO_2 comparison experiments (section 3.4.2). The difference in dates between the ClearfLo summer IOP, and the times when the NO_2 comparison experiments were performed, leading to different actinic flux / sunlight wavelength distribution, which would cause different levels of reduction of UV by Ultem film. This variation potentially changes the dependence of $jNO_{2\ reference}$ to $jNO_{2\ sample}$, but is not considered to be a major factor in comparison with the uncertainty introduced by the need to assume PSS was fully established.

5.5 Conclusion of correction approach

This chapter addressed the issue of imbalances in chemical composition affecting the converter cells' NO_2 conversion efficiency to differing extents, and presents a simplified approach to apply a correction factor - $V_{correction}$. The correction methodology in this chapter 5 was implemented for the data presented in the following chapter 6. Indian OPR deployment.

Chapter 6: OPR measurements in New Delhi, India (with improvements)

India is a fast-developing country in southern Asia, with serious air pollution problems in many cities and rural regions. Major air pollutants in Indian cities include primary species (particulate matter, NO_x) and secondary components (aspects of particulate matter, ozone), while in rural regions ozone pollution is a major concern. Comprehensive research into sources of local and regional air pollutants are needed in order to understand - and most effectively address - the air pollution problem in India. During 2013, a collaboration between the University of Birmingham, TERI University (New Delhi) and IISER Mohali (Chandigarh) facilitated OPR measurements in Northern India as a proof-of-concept experiment to measure the local oxidant production rate. The OPR system could be a useful tool to inform local ozone pollution control and environment policy making in India, in particular as the necessary information for alternative approaches (*e.g.* emission inventories to drive numerical models) is not available. OPR measurements were performed during April and May 2013. Two measurement sites were involved: at TERI University in New Delhi from 23rd April to 7th May, and at IISER Mohali from 8th to 16th May. More importantly, the sealing disk of sampling reactor OPR system were redesigned to improve its sealing ability; the correction factor $V_{correction}$ (see chapter 5) were also implemented to the OPR results during India measurement. Both factors improved systematic accuracy in the OPR measurement.

6.1 Background: Indian Climatology & Air Pollution

6.1.1 Indian Climatology

India is a large country with multiple climatic regions. Its climate ranges from temperate and alpine in the northern areas to tropical in the southern areas. The two seasons of rains – summer (April to June) and monsoon (July to September) and seasonal reversal of prevailing wind direction (from January to July) are the predominant influences on Indian weather. Four distinct seasons are usually identified: winter, summer, summer monsoon and the post-monsoon season. During the Indian summer season, the ambient temperature starts to increase in March and April to reach a mean daily temperature of 30 to 35 °C; maximum temperatures during daytime can reach up to 40 °C in many cities. During May and July, the temperature may be as hot as 45 °C in the north and north-west region of India. The summer season is characterised by hot and dry winds blowing over the plains of north-west India. Rainfall is rare during the summer season, usually happening in the following monsoon season (Attri and Tyagi, 2010).

6.1.2 Indian Air Pollution problem

As a rapidly developing country, India has multiple air pollution problems in many cities, especially in megacities (*e.g.* Mumbai and New Delhi). The expansion of industry causes increases in emissions of ozone precursor species – NO_x and VOCs (Horowitz *et al.*, 2006).

National Indian ambient air quality standards specify that ozone levels are not to exceed a daily 8 hours mean of 100 µg m^{-3} (ca. 50 ppb) in industrial, residential, rural and ecologically sensitive areas, for 98 % of the days each year (with an allowance of a maximum of two

consecutive days of exceedance). The target value for NO_2 standard is set at annual maximum level of 40 μg m^{-3} (ca. 21 ppb), and 24 hours mean NO_2 concentrations are not to exceed 80 μg m^{-3} (ca. 42 ppb) in industrial, residential, rural and ecologically sensitive areas (CPCB, 2015). Ambient ozone levels have been increasing in recent years, particularly in the Indian capital, New Delhi, such that exceedances of air quality standards are frequent. The increasing pollution trends are shown in the following Figure 6.1:

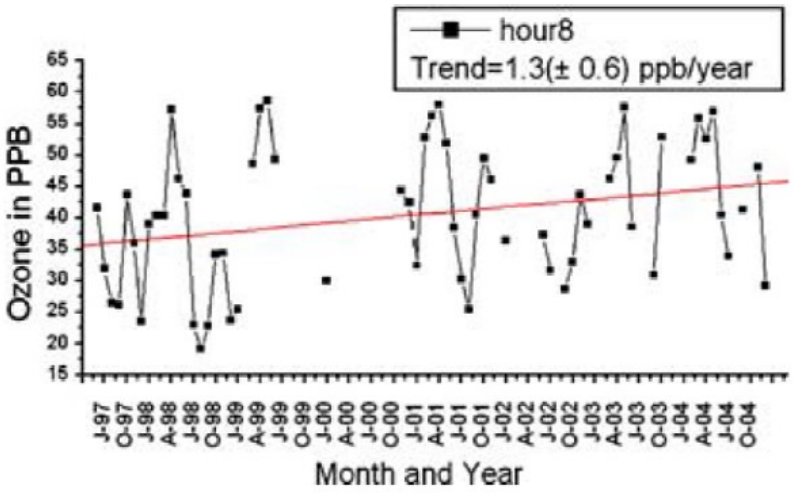

Figure 6.1. Temporal evolution of daily 8-hours mean ozone levels in New Delhi from 1997 to 2004 (Ghude *et al*., 2008).

Figure 6.1 describes the increasing ozone levels from 1997 to 2004; as industrial development continues, this positive trend of ambient ozone levels continued in New Delhi over the last decade (from 2004 to 2013) (Ghude *et al*., 2014). The exceedances of the daily 8 hours mean ozone target of 50 ppb are clear and frequent in Figure 6.1, indicating the serious situation of the ozone pollution problem in New Delhi. The consistently high level of ozone causes both chronic and short-term ozone exposure, leading to potential respiratory system problems among the local population.

Long-term exposure to high level of ambient ozone also causes substantial crop yield loss in Indian agriculture. Based upon 2005 data, a recent modelling study suggested there is 12%

(estimated) loss of the total cereal crops (rice, wheat and soybeans) per year from ozone exposure in India, which equates to a 61.2 Tg mass loss, that would be sufficient to feed 94 million people (Ghude *et al*., 2014).

In order to reduce the impact of ozone pollution on humans and crops, the OPR system could contribute to identification of local ozone production contributions, and hence support future ozone control strategy development in India.

6.2 Introduction to the Indian OPR deployment

The aim of the Indian deployment was to obtain proof-of-concept data for the application of the OPR approach to assess the contribution of local chemical factors to ozone formation, in a comparatively under-studied region known to suffer from substantial ozone pollution. In addition, Indian pollution and weather characteristics were significantly different from London, and so the deployment provided an important opportunity to test OPR system's performance under different environmental conditions. The deployment combined measurements in New Delhi, as a first test of operation of the OPR system in an easily accessible location where we had worked previously, but which lacked many supporting air pollution measurements, followed by measurements at an established air quality monitoring station in Mohali, from which greater insight into the OPR measurement (with addition of measurements of other gaseous species related to ozone chemistry) was anticipated.

OPR deployments were performed at two different sites: "TERI", located at TERI University, which is located in the southern sector of the Indian capital city New Delhi; and the "Mohali" site, at IISER Mohali which is located in Punjab region to the north-west of New Delhi. Both sites were in Northern area of India. Locations are shown in Figure 6.2. In both cases, OPR measurements were made on the University campuses.

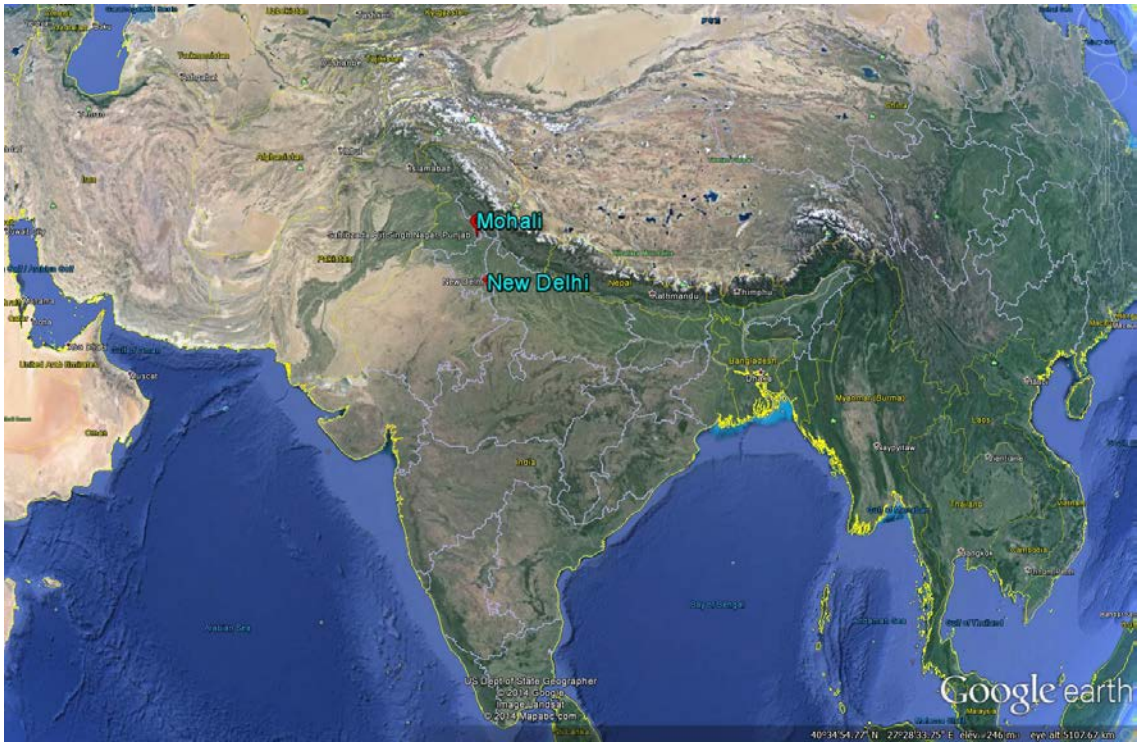

Figure 6.2. Indian OPR measurement locations: New Delhi and Mohali (Google Earth, 2015).

The TERI deployment was performed in New Delhi from 23rd April to 7th May 2013, and the Mohali deployment was performed in Mohali from 8th May to 16th May 2013. In both cases this corresponded to the summer season during the OPR deployments in India. The local weather was dry and hot, only two days of rainfall occurred during the Mohali measurement period. The average hourly temperature during the two deployments was 32°C, and a maximum temperature of 44°C was encountered in the afternoon on one measurement day. The prevailing wind direction was north-westerly.

During the TERI deployment, the OPR system was operated from 23rd April to 7th May 2013. There was no rainfall during this period. However, due to power failures, calibration experiments and other tests, the actual successful measurement days were 27, 28, 29, 30 April and 1, 2, 5 May 2013. This period is referred as "The Successful Measurement days at the TERI site (TSMT)" in following sections.

The Mohali deployment was generally not successful. The OPR system's quartz reference reactor was broken on 10 May 2013, which was the first day of the planned continuous measurement period. It could not be satisfactorily repaired in the field. As a result, the leaking reactor led to major errors in the OPR data, the estimated $p(O_x)$ values were not meaningful and no useful data were obtained from the Mohali deployment.

Therefore, the following India data analysis sections focused on TSMT in New Delhi.

6.3 Data source and availability

During the TERI deployment, the OPR system was deployed at TERI University to measure the oxidant production rate. Ideally, measurements of other species related to ozone chemistry would help interpret the data during the TERI deployment. However, due to the very limited instrumentation and monitoring in India, only ambient ozone, NO_x and meteorological data could be acquired (in addition to OPR measurements), and of these only ambient ozone was measured at the OPR location. The measured pollutant species available (which are related to ozone chemistry) are shown in table 6.1.

NO_x and meteorological data were measure by the Delhi Pollution Control Committee (DPCC) monitoring network. The DPCC Delhi airport monitoring station is located ca. 5 km west (280 degrees) from the TERI measurement site as Figure 6.4 shows, it is at east side of the airport, 200 m south from runaway. Measurements of important atmospheric chemical species such as HO_2 and HONO, which were related to ozone chemistry as discussed in section 4.3.2 (London OPR deployment), were not available at any location in India.

Data discussed	**Sources**
O_3	DPCC site by UV photometric based ozone analyser and TERI site by UoB 2B Ozone monitor
NO	DPCC site by Chemiluminescence NO_x analyser
NO_2	DPCC site by Chemiluminescence NO_x analyser
ΔO_3	TERI site by OPR system from UoB
Wind speed and direction	DPCC site
Ambient temperature, RH	DPCC site and TERI site: OPR system sensor
Solar radiation	DPCC site and TUV model

Table 6.1. Measured pollutant species potentially related to ozone chemistry available during the 2013 TERI deployment, New Delhi, India. Many of the pollutants (relating to ozone formation) are not measured due to limited instrumentation.

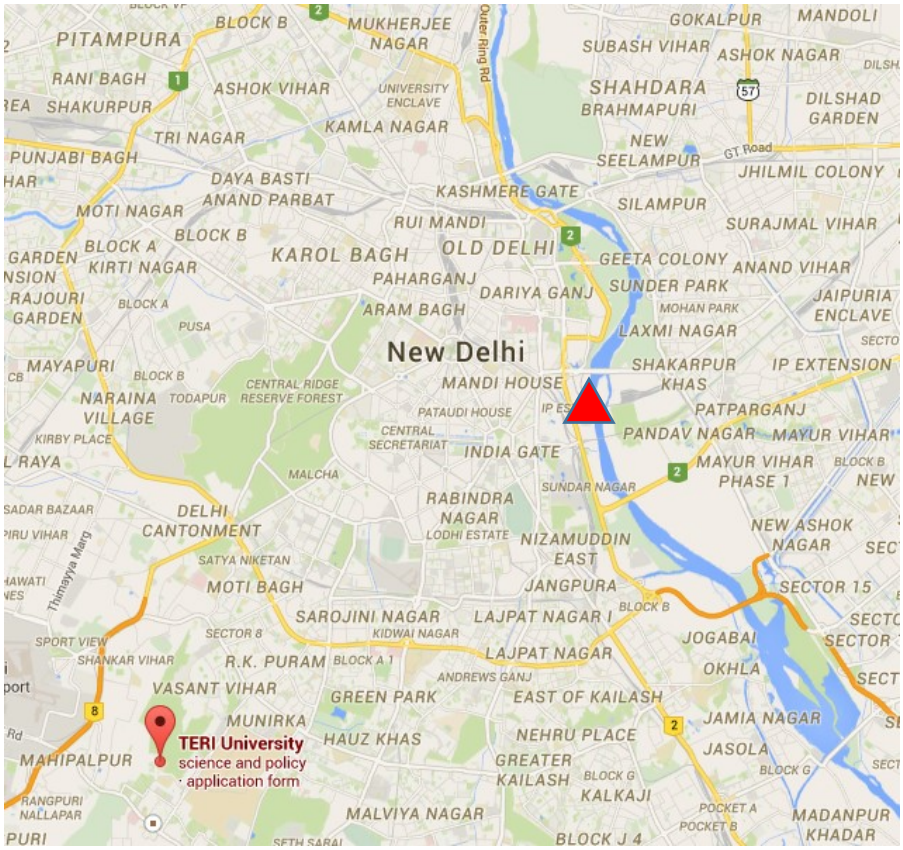

Figure 6.3. Location of TERI University in the southern area of New Delhi; the red triangle shows location of New Delhi city centre (Connaught Place) (Google, 2015).

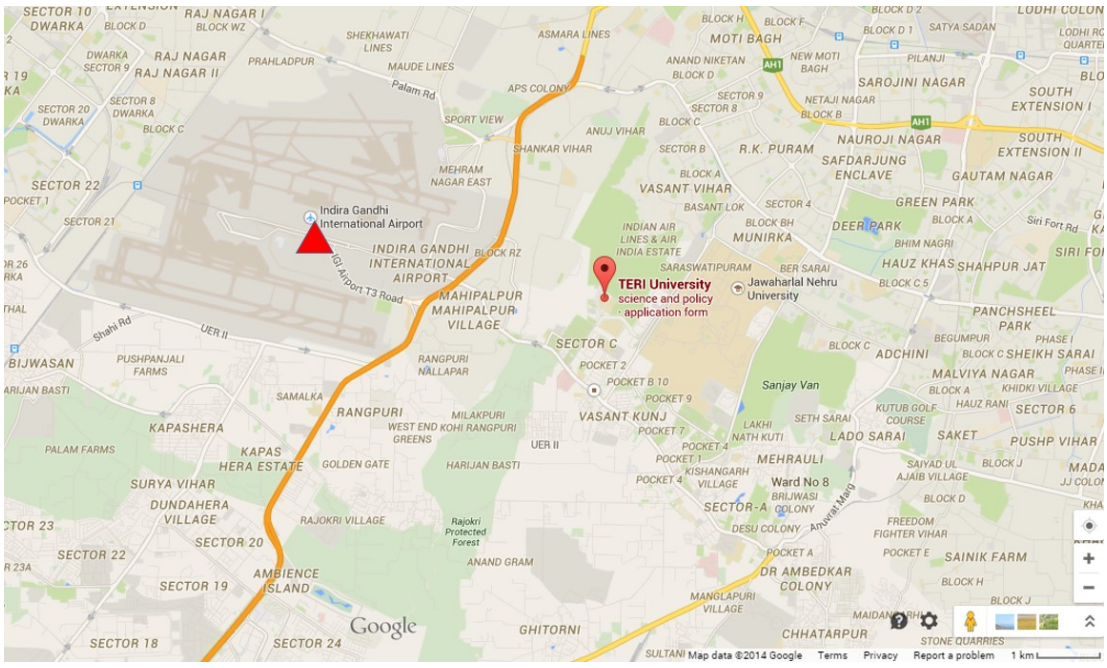

Figure 6.4. Local environment of the TERI University site. The Red Triangle is the DPCC airport monitoring station location, it is approximately 5 km west (280 degrees) from the TERI measurement site (Google, 2015).

Figure 6.5. Location of DPCC monitoring station inside the Delhi Gandhi International airport, it is located on the east side of the airport, toward to TERI University (Google, 2015).

6.4 Location information of OPR deployment site in TERI University, New Delhi

6.4.1 OPR system location

The OPR system was located inside the TERI University campus in the south-west area of the city of New Delhi. Figure 6.3 shows the relation of this suburban measurement site to New Delhi city centre (15 km), and Indira Gandhi International Airport (5 km) (Figure 6.4). Within the TERI University campus, the OPR system's dual sampling reactors were located on the roof of a 5 story administration building (Figure 6.7), positioned on a flat surface with open space, such that the reactors were directly exposed to incident solar radiation. The pillars positioned around the reactors were 25 cm in height, their shading did not interfere with the solar radiation experienced by either reactor.

The reactor inlets were positioned beside two small cement pillars. The pillars were 20 cm away from the inlets; the reactors inlets were exposed to circulating ambient air and were not considered to be obstructed by the pillars. A 2B-technologies model 202 UV absorption O_3 monitor was deployed with the OPR system to measure ambient ozone levels. The O_3 monitor inlet was positioned beside the dual sampling reactors of the OPR system, toward the edge of the roof. The ambient NO_x data and meteorological data were taken from DPCC Delhi airport monitoring station.

6.4.2 Local Climatology during the measurement

It was summer season during the TERI measurement; local weather was correspondingly hot and dry. Figure 6.9 shows the ambient temperature and RH time series as measured at the DPCC airport monitoring station; temperature ranges were between 23°C and 39.5°C,

with a maximum temperature (39.5°C) reached on both the 29th April and 2nd May; the mean temperature was 34°C during TSMT. Indian local time (IST = GMT + 5:30) is used in all figures and data analysis presented in this chapter.

During the TERI deployment the weather was continuously sunny with clear skies; no rainfall occurred during TSMT. RH was low, ranging between 7 % and 46 % (Figure 6.9). The diurnal solar radiation pattern was consistent throughout TSMT (Figure 6.10). The similarity of solar radiation between each measurement day during TSMT may suggest similarity in OH primary productivity, depending upon the RH and ozone abundance. Diurnal peak solar radiation levels were ca. 215 Wm^{-2} during the daytime; it decreased to ca. 75 Wm^{-2} at night. It was uncertain if such solar radiation readings during the night were realistic - or were (likely) caused by the inaccuracy of instrument at low levels of light radiation, although they may possibly also reflect contributions from background light sources near the DPCC monitoring station - which is located within east side of the Delhi international airport, 200 m south from runaway.

Wind data from the DPCC Delhi international airport monitoring station showed that the prevailing wind direction during TSMT in New Delhi was westerly (Figure 6.8). Consequently, the DPCC monitoring station (east side of airport, Figure 6.5) capture most of the local emissions from airport area. The TERI University measurement site was 5 km east from the airport, so airport pollutant emissions (from aircraft and ground operations) could potentially be readily transferred from Delhi airport to the TERI measurement site.

Figure 6.6. Immediate vicinity of the TERI University campus: mixed semi-residential/agricultural area, New Delhi, India 2013.

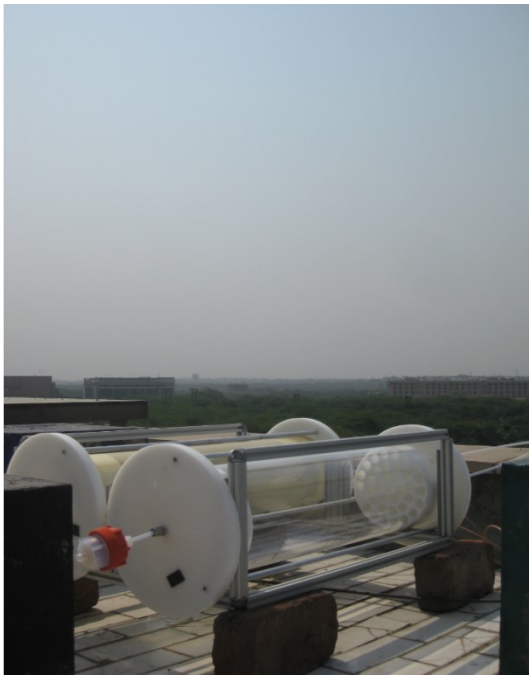

Figure 6.7. Location of the OPR system dual sampling reactors on the roof of the main administration building, TERI University site, New Delhi, India 2013.

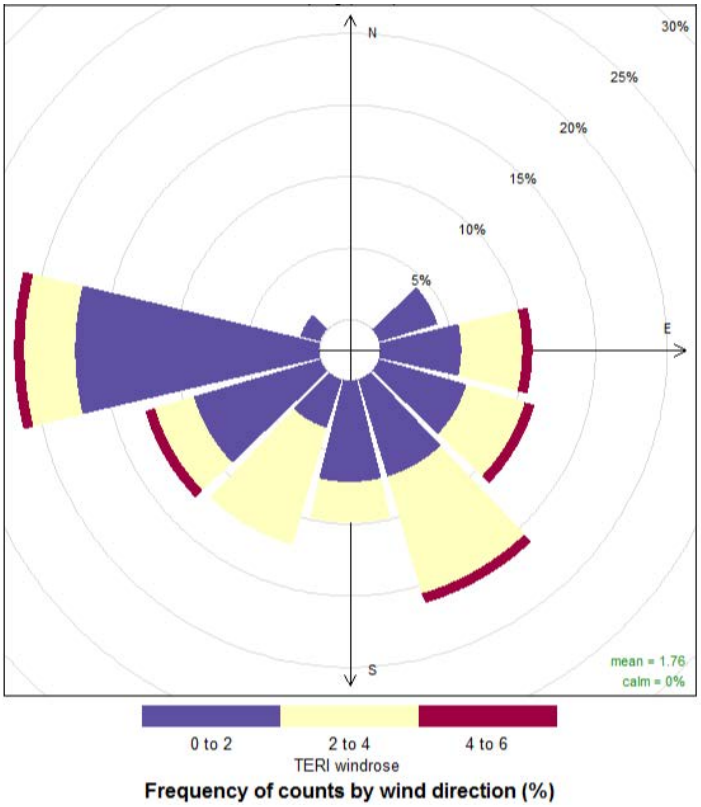

Figure 6.8. Windrose during TSMT, prevailing wind was westerly during this period. Wind speeds are given in units of m s^{-1}. Data from DPCC Delhi airport monitoring station.

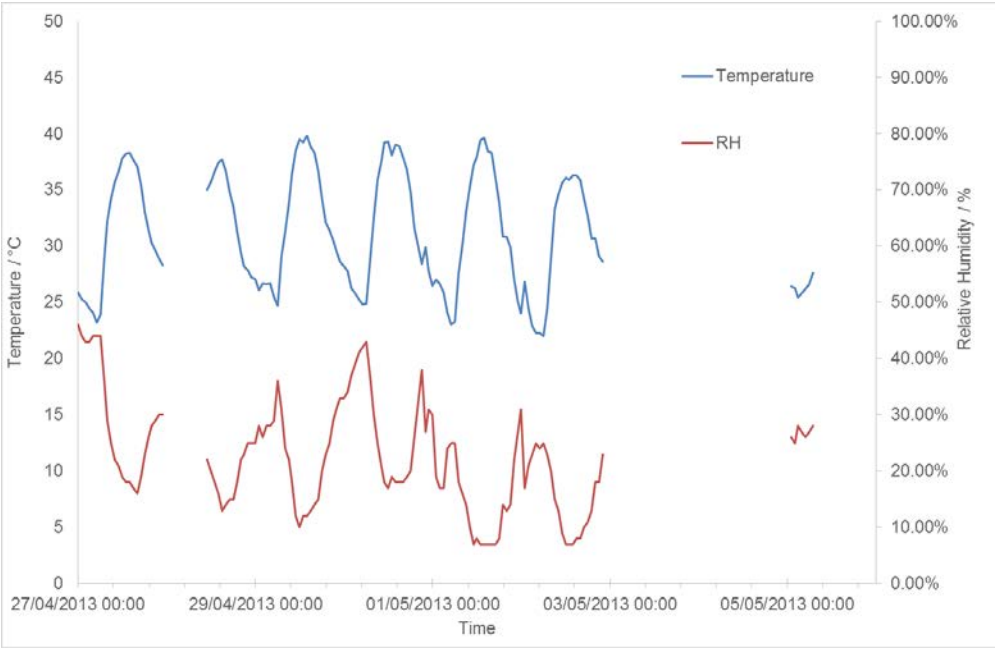

Figure 6.9. Time series of temperature (primary / left axis) and RH (secondary / right axis) during TSMT. Data from DPCC Delhi airport monitoring station.

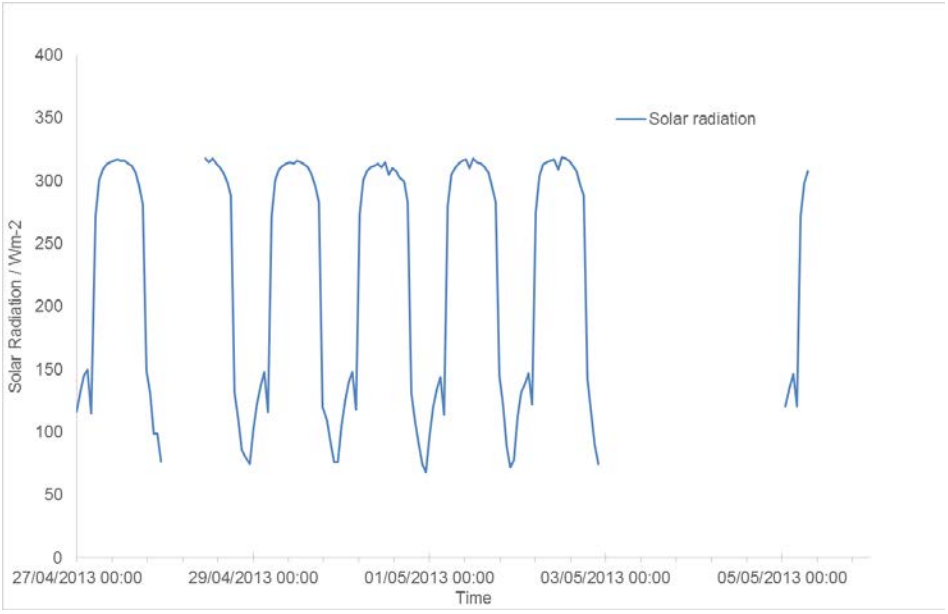

Figure 6.10. Time series of solar radiation level during TSMT. Data from DPCC Delhi airport monitoring station.

6.5 Comparison between measured O_3 at TERI University and DPCC site

During TSMT, two sets of ambient O_3 data were available from different locations: DPCC Delhi airport monitoring station (Thermo 49i ozone monitor) and TERI University site (2B ozone monitor, from the University of Birmingham). As Figure 6.3 describes, the Delhi airport monitoring station is 5 km west of TERI University, upwind during much of the TSMT. Due to the likely presence of (different) local emission sources between the two measurement locations, there may be substantial differences between measured ozone data sets. The two ozone data sets were compared to assess this issue, and hence investigate the confidence with which O_3 and NO_x data from the DPCC monitoring station might be applied to the TERI University site – the OPR measurement location. A time series of the two ozone measurements is shown in Figure 6.11:

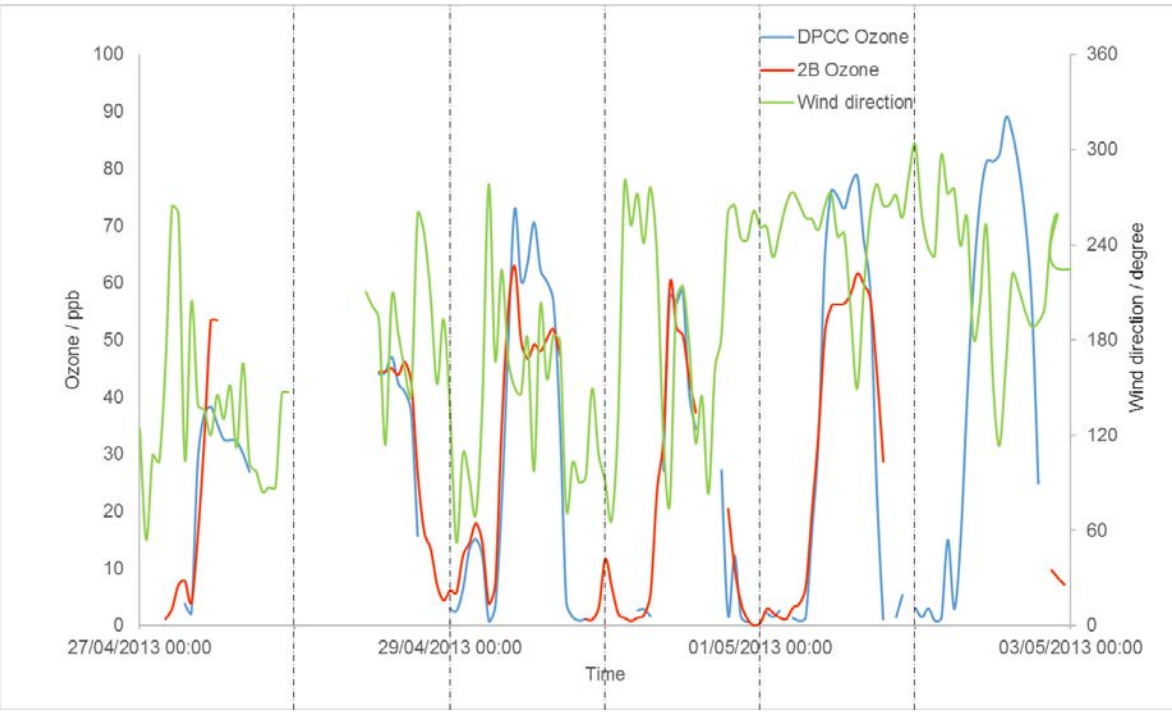

Figure 6.11. Comparison between ozone levels measured at the DPCC Delhi International Airport monitoring station, and those measured using the University of Birmingham 2B monitor at TERI University during TSMT period (left axis). The wind direction during this period is shown on the right axis.

Figure 6.11 indicates partial agreement between measured ozone data at the TERI site and at the DPCC site during TSMT, both in terms of the overall magnitude and particularly with regard to the diurnal pattern. However, there were also disagreements between the two data sets. The DPCC ozone data set showed higher values of peak ozone on 29th April and 1st May than the 2B ozone data. The peak ozone level at the DPCC site was 10 ppb (16 %) higher than that at the TERI site on the 29th April; the peak ozone level was 17 ppb (28 %) higher at the DPCC site than at the TERI site on the 1st May.

A possible reason to cause this variation is the different measurement location. The timing of the positive ozone trends were very similar for both data sets, pointing to regional-level behaviour captured at both sites, rather than localised emission influences. Differences

between the ozone records can be considered in the context of differencing local emission levels between the DPCC airport site and TERI University sites.

The TERI University campus is located in a suburban area surrounded by residential buildings at a low density. There was an agricultural area / fields located to the north of the campus. The roads surrounding TERI had low levels of traffic during TSMT, with only a few three-wheeled motorcycles ("autos") on the roads. Power was supplied through the grid, rather than (for example) on-site coal fired boilers. Consequently, the local NO_x emission sources were thought to be minor at and around the TERI University site. In contrast, Delhi International Airport is a large airport with a peak capacity of 85 flights per hour (Indian Times, 2012). VOC and NO_x emissions from aircraft, and (more significantly) the associated ground-based activities were anticipated to have been much greater than those around the TERI site. The DPCC monitoring site is at mostly downwind (east side) of the airport, which captured local airport emissions. Under the abundant solar radiation (peak level at 315 Wm^{-2}), the VOCs and NO_x emissions from the airport area potentially increased the local ozone production downwind. In addition, the $NO\text{-}O_3$ titration is likely to have reduced ozone levels immediately within and downwind of the airport (*i.e.* prior to their arrival at the TERI site), although not to affect total oxidant level. Both high ozone events coincided with the westerly wind directions in Figure 6.11, to further support this possibility. Consequently, the higher ozone peak values at DPCC airport site on 29th April and 1st May 2013 was possibly caused by the complex of elevated pollutants emission and transportation by westerly wind from Delhi airport leading to $NO\text{-}O_3$ titration during the air mass transit to the TERI University site.

The other potential factor to cause disagreement between the two locations would be a changing air mass, *i.e.* non-connected flow between TERI and the airport, represented most simply by the local wind direction. Delhi international airport is 5 km west (280 degrees) from TERI University, and as Figure 6.8 indicated the prevailing wind direction was westerly during TSMT. NO_x and VOCs were potentially transported directly from Delhi international airport to TERI University by west wind during TSMT. However, the wind direction did exhibit variability during TSMT (Figure 6.12). Different wind directions naturally led to sampled air belonging to different air mass between the measurement sites, hence contrasting ozone levels might be expected and the agreement between the sites in fact to be remarkably good.

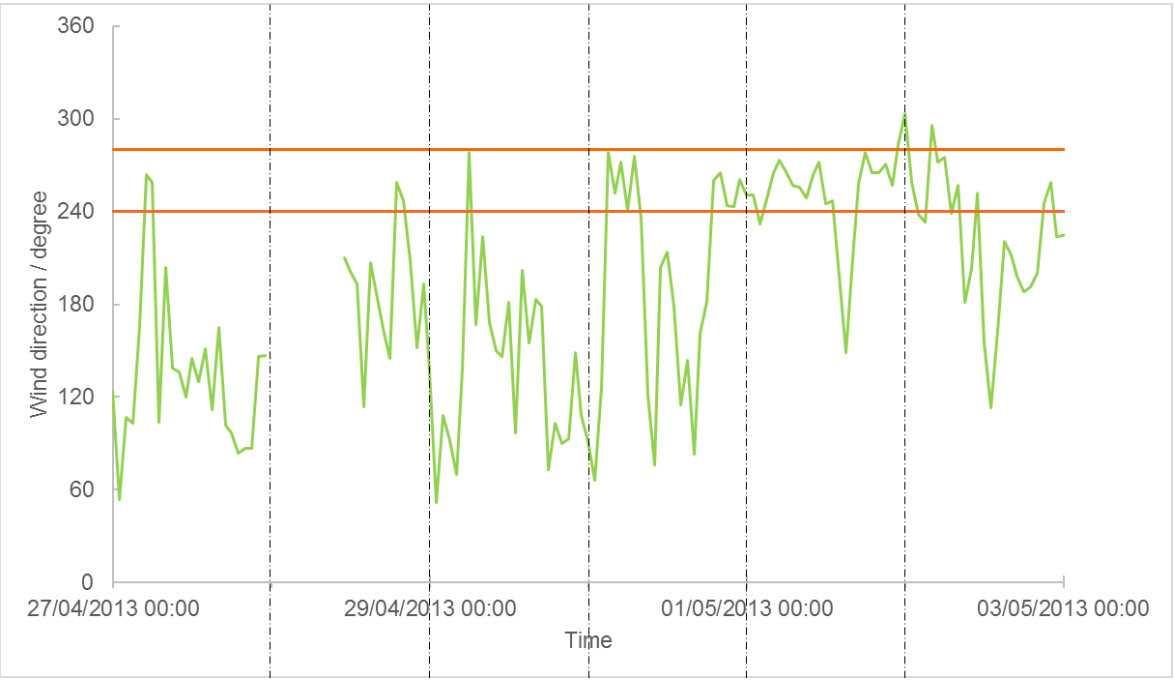

Figure 6.12. Time series of wind direction during TSMT; area between two horizontal orange lines describes the westerly wind regime (from 240 to 280 degrees), representing the extent of direct flow from the airport area to TERI. Data from DPCC Delhi airport monitoring station.

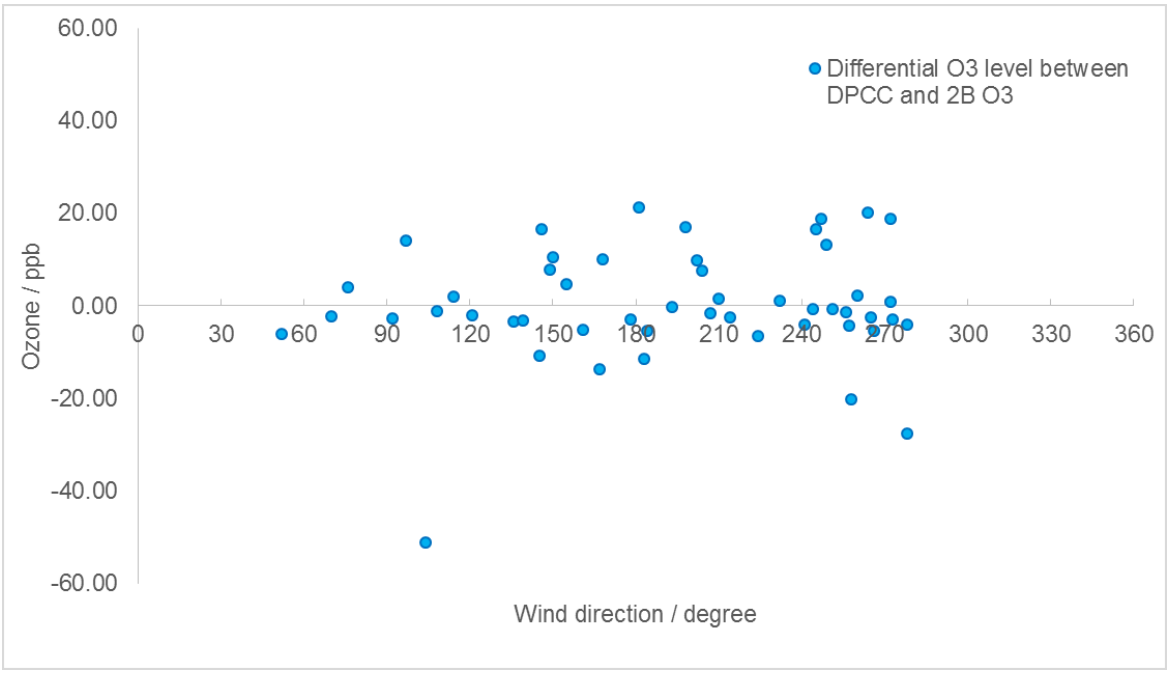

Figure 6.13. The difference in ozone levels between the two measurement sites (DPCC - TERI) as a function of wind direction during TSMT.

In Figure 6.13, the difference in ozone levels between the two locations is seen to be somewhat variable under different local wind directions. The mean differential ozone level is 8.34 ± 10.24 (S.D.) ppb, with a largest difference of 51 ppb. Noticeable from the correlation graph (and wind rose) is the lack of any northerly wind regime (no data for the sector from 290 to 50 degrees). Given that both ozone measurement sites were located in the southern area of the New Delhi conurbation, and well to the south of both New and Old Delhi city centres, this indicates that pollutant emissions from Delhi city centre were unlikely to affect the local pollutant levels at either measurement site. The westerly wind regime (from 240 to 280 degrees) showed higher frequency of positive values of differential ozone, suggesting higher DPCC ozone levels than TERI ozone levels, while for the easterly wind regime (from 60 to 120 degrees), negative values for the differential ozone level were more frequent, suggesting higher TERI ozone levels than DPCC ozone levels. As discussed in the previous paragraph, different wind directions likely led to sampled air belonging to different

air masses, which originated from different locations with contrasting emission sources (*e.g.* a busy railway station (Tuglakabad) is located ca. 20 km east of TERI University). Another possible contrasting emission source is Gurgaon's DLF city, which is an industrial park ca 8 km southwest of TERI University.

6.5.1 Correlation between Ozone Datasets

The correlation between the two measured ozone data sets is shown below:

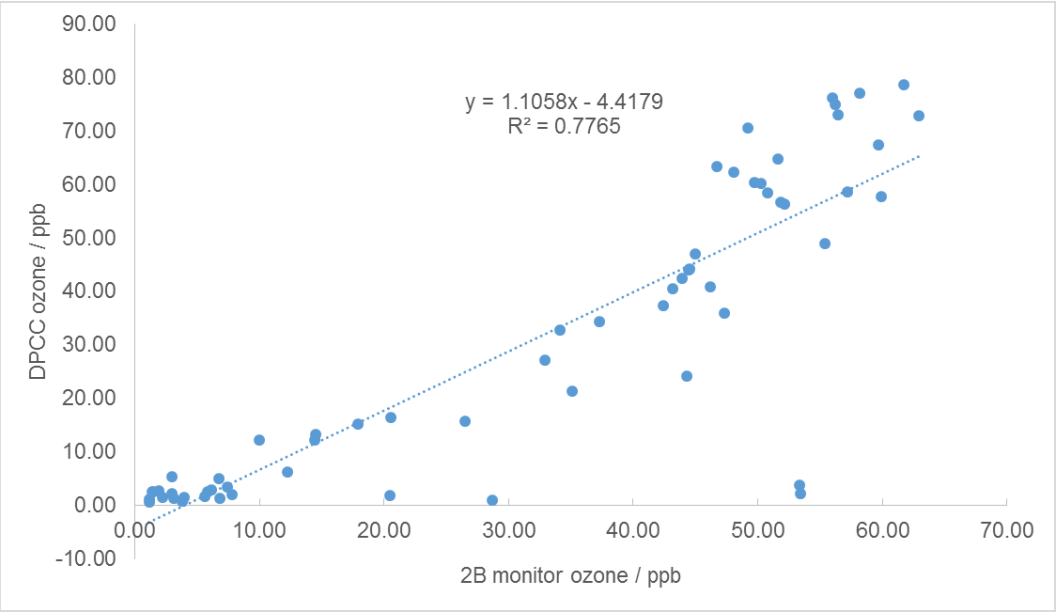

Figure 6.14. Correlation between ozone levels (at each point in time) measured at the DPCC and TERI sites during TSMT.

Regression analysis indicated the intercept is -4.42 ± 2.9 ppb and the gradient is 1.11 ± 0.08, with an R^2 value of 0.77. The result suggested that the two data sets were reasonably well correlated.

6.5.2 Mean diurnal ozone dataset comparison

During TSMT, due to the gaps and incomplete coverage in both the OPR measurement $p(O_x)$ and the two ozone data sets (shown in Figure 6.11), it was necessary to average the 7 days' data of TSMT into a single 24 hours mean diurnal dataset.

Measured hourly ozone data during TSMT (27, 28, 29, 30 April and 1, 2, 5 May) were averaged to produce a mean diurnal profile. (24 hours, at hourly resolution). The averaged

single diurnal profiles for ozone from TERI and DPCC are shown in the following figure 6.15:

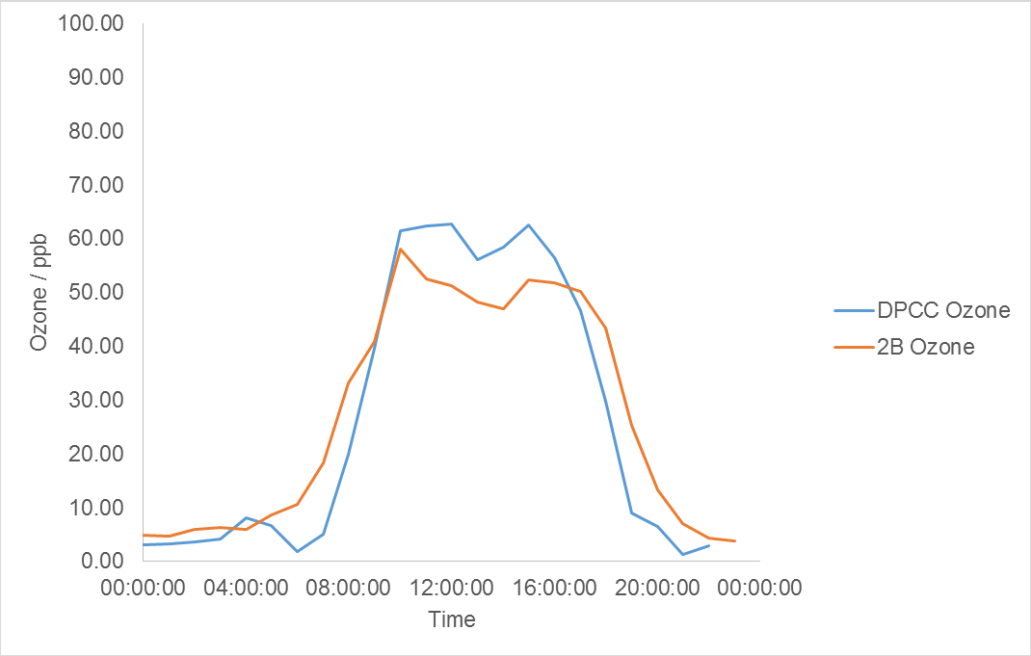

Figure 6.15. Comparison between hourly mean ozone levels (to a 24 hours coverage) at DPCC Delhi International Airport monitoring station's data and at TERI site by 2B monitor ozone during TSMT.

The hourly mean ozone levels shown in Figure 6.15 are in reasonably good agreement between two data sets, although the elevated ozone peak levels for DPCC are still apparent as shown in Figure 6.11. The elevated peak DPCC O_3 levels on 29th April and 1st May did not lead to an overall difference to hourly mean ozone levels (in 24 hours coverage) between two data sets. However, the DPCC ozone data showed a slightly slower rise and faster fall in levels than the TERI data.

In summary, the two data sets were quite similar in measured ambient ozone levels. There were a few differences, but the general diurnal profiles were very similar. The good correlation (R^2 = 0.77) also indicated that variability within the two data sets arose from a common cause. The differences in ozone levels between the two measurement sites was

probably caused by a combination of differing air mass / variable pollutants emission sources, and NO titration during transit between the sites; nonetheless the substantial similarity between the ozone data sets gives confidence that other pollutant (O_x, NO_x) levels were broadly similar at both the TERI and DPCC sites, reflecting regional abundances, and hence that data from the DPCC site could be used to interpret measurements made at TERI, albeit with some caveats. Due to the power failures, monitor warm-up processes (potential data error) and frequent data gaps in the 2B ozone data set, the following data analysis sections are based upon ambient pollutant data (NO_x and O_3) from the DPCC airport monitoring station. The uncertainty introduced by this approach is discussed in section 6.7.

6.6 Pollutant Characteristics at TERI during TSMT

During TSMT, it was important to analyse the distribution of the local NO_x and O_3 mixing ratios, in order to understand the characteristics of New Delhi's local pollution. A number of data gaps existed in the DPCC data (which were better than the TERI measurements in terms of coverage); consequently, the following discussion relates only to those hours within TSMT period where measurements of all three species (NO, NO_2 and O_3) were available. This represents 78 % (99 out of 129 hourly data points) of measured data during TSMT period.

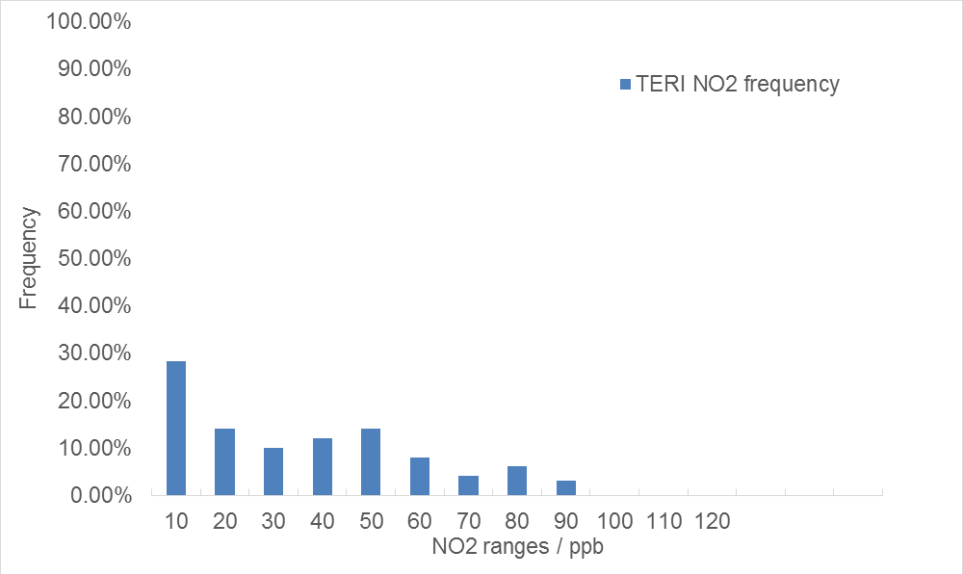

Figure 6.16. Frequency distribution of hourly NO_2 mixing ratio measured during TSMT period of TERI deployment, at the DPCC airport monitoring station.

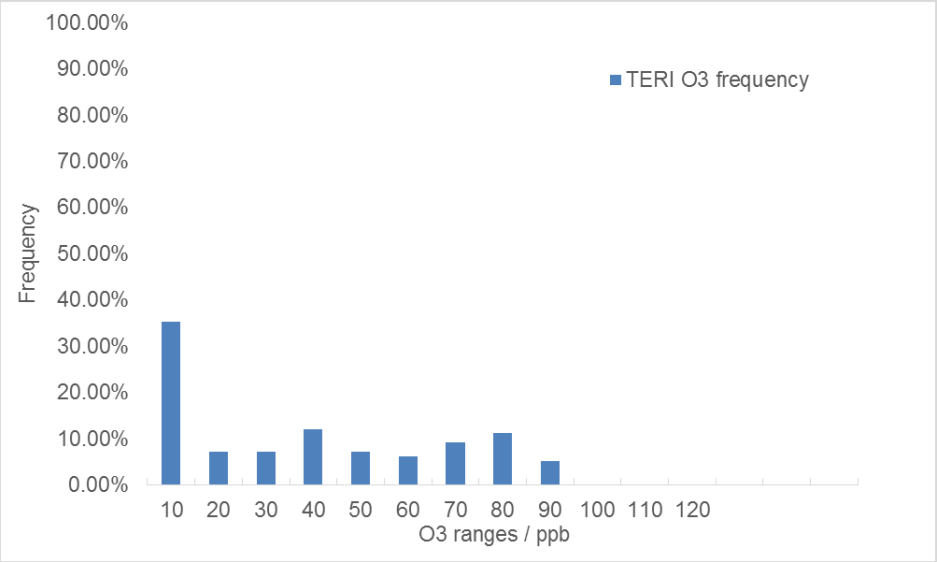

Figure 6.17. Frequency distribution of hourly O_3 mixing ratio measured during TSMT period of TERI deployment, at the DPCC airport monitoring station.

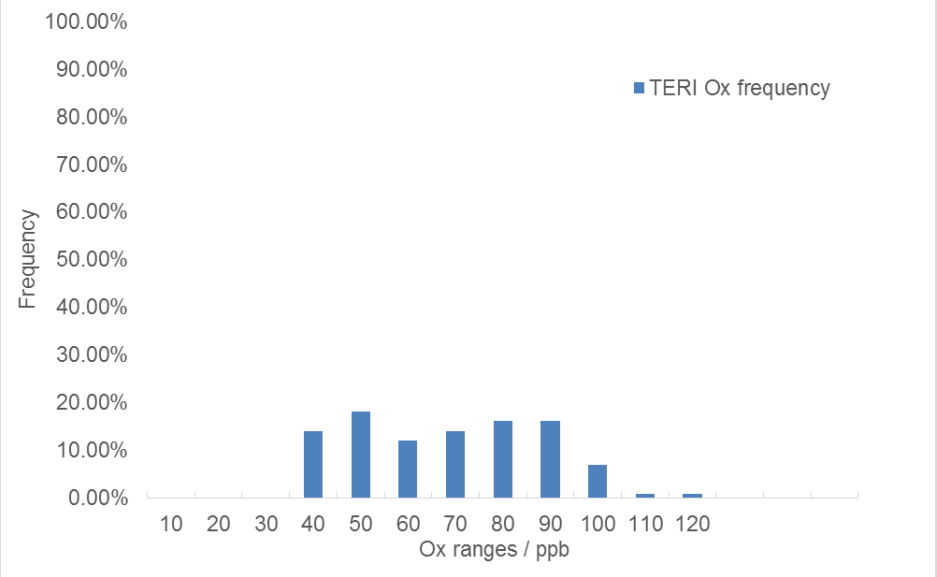

Figure 6.18. Frequency distribution of hourly O_x mixing ratio measured during TSMT period of TERI deployment, at the DPCC airport monitoring station.

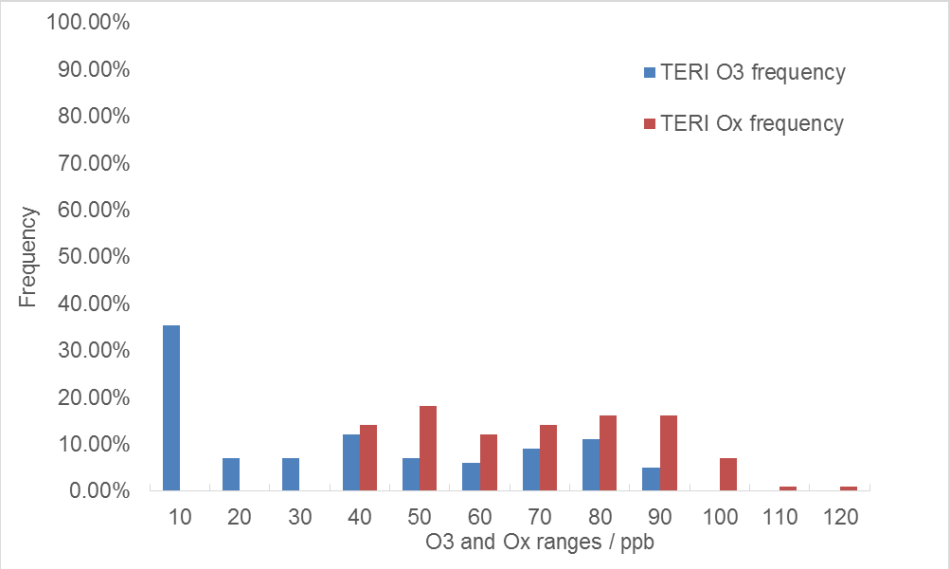

Figure 6.19. Comparison between frequency distribution of hourly O_3 mixing ratio and frequency distribution of hourly O_x mixing ratio measured during TSMT period of TERI deployment, at the DPCC airport monitoring station.

Figure 6.17 showed over 35 % of hourly ozone measurements during the TERI deployment were distributed below 10 ppb. There were ca. 15 % of hourly O_3 measurements distributed between 10 and 30 ppb range. About 20 % of hourly O_3 measurements were distributed between 30 and 60 ppb range, and the remaining O_3 measurements were distributed between 60 and 90 ppb range.

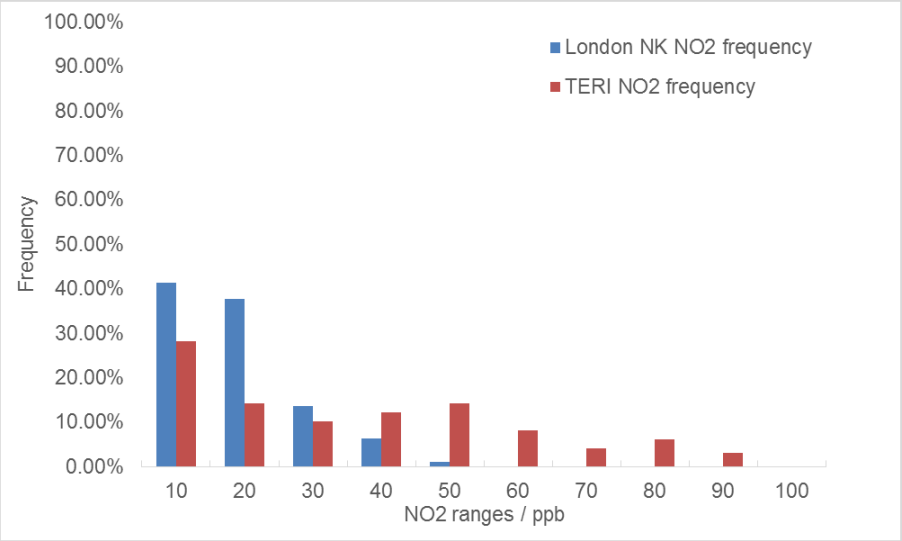

Figure 6.20. Comparison of frequency distributions of hourly NO_2 mixing ratios between the London summer IOP OPR deployment (including FIOM) and the TERI deployment.

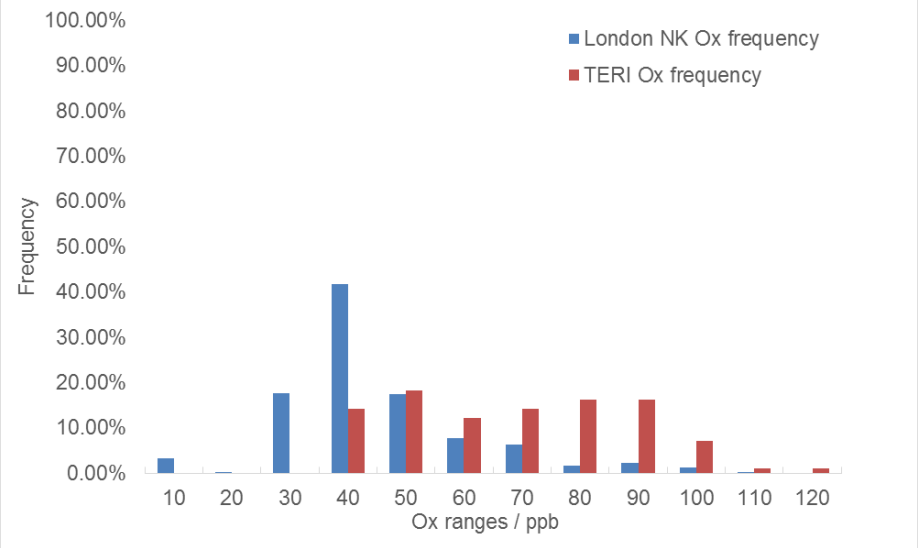

Figure 6.21. Comparison of frequency distributions of hourly O_x mixing ratios between the London summer IOP OPR deployment (including FIOM) and the TERI deployment.

In Figure 6.20, only 20 % of hourly NO_2 measurements were distributed under 10 ppb in TSMT; there were about 35 % of hourly NO_2 measurements distributed between 10 and 40 ppb range. More than 40 % of hourly NO_2 measurements distributed were distributed between the 40 ppb to 90 ppb range in Delhi. According to the NO_2 measurement location-

downwind (mostly) inside the busy Delhi International airport, such high levels of NO_2 is likely be caused by the local airport emissions.

In comparison, as Figure 6.20 showed, ca. 40 % of total hourly NO_2 measurements were distributed under 10 ppb during the London summer IOP at the NK measurement site; 38 % of hourly NO_2 measurements were distributed between 10 and 20 ppb, and more than 12 % of hourly NO_2 measurements were distributed between 20 and 40 ppb range. There were only 2 % of hourly NO_2 measurements above 40 ppb. Average hourly NO_2 levels in Delhi were much higher than those at NK. This phenomenon could be related to the substantially elevated NO_2 emission (Figure 6.23) during the early evening at ca. 20:00 (possibly from airport and local traffic emissions). More importantly, NO_x emission from the busy airport is expected to be much higher than urban background area. The high level of NO_2 could potentially contribute to higher ozone production, both directly (through NO_2 photolysis in the NO_x-O_3 PSS) and through peroxy-radical mediated ozone formation chemistry.

As Figure 6.21 shows, over 90 % of hourly O_x measurements were distributed between 30 and 110 ppb range during TSMT. In contrast, there were approximately 75 % of hourly NO_2 levels distributed between 10 and 40 ppb range (Figure 6.21) during the London summer IOP. Much higher levels of O_x were more frequently measured during the TERI deployment. This comparison shows that overall O_x levels were higher at TERI than at NK. The different overall O_x levels between the two measurement sites could be related to the different local oxidant production rate $p(O_x)$, but other factors (*e.g.* different annual background ozone levels, seasonal variation of NO_x / VOC emissions) could also influence local oxidant levels. The variation in local oxidant production rates between two locations is discussed further in section 6.9.

6.7 Pollutant levels during TSMT

As stated in section 6.5.2, the OPR deployment was only successfully performed during TSMT (27, 28, 29, 30 April and 1, 2, 5 May), for which the measured pollutant (NO, NO_2, O_3) data are shown in the following figure:

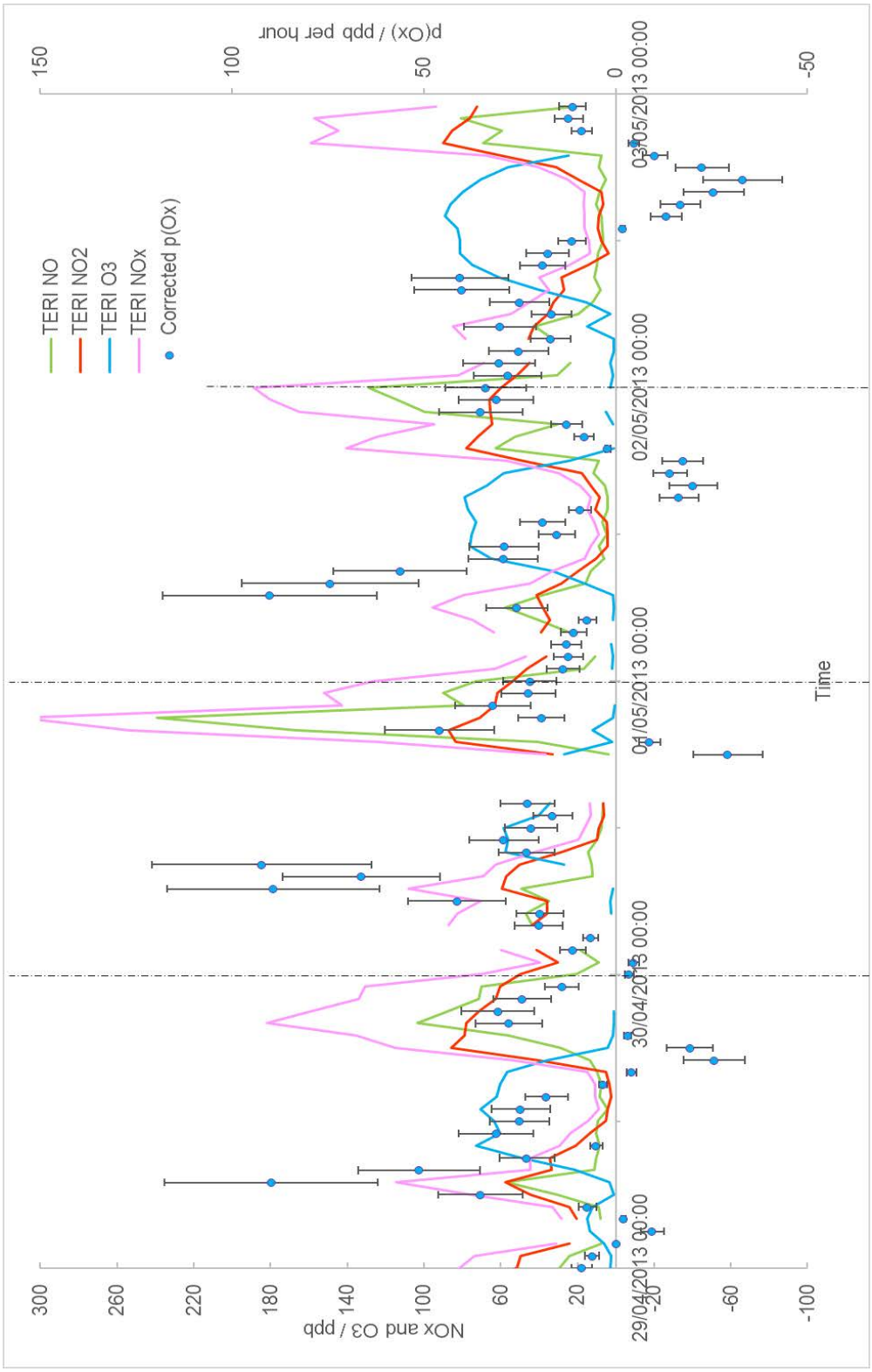

Figure 6.22. Time series of ambient NO, NO_2, O_3 levels, and OPR-derived $p(O_x)$ (after implementation of correction approaches) during TSMT* at TERI University site. Primary axis (left) refers to NO, NO_2 and O_3 data (Data from DPCC airport monitoring station), secondary axis (right) refers to the $p(O_x)$ data. Error bars represents estimated $p(O_x)$ uncertainty of ± 31 %.

(*Due to the incoherent data on 27th April, 28th April and 5th May 2013, these days are not shown on the Figure 6.22)

Figure 6.22 describes the measured $p(O_x)$ and ambient pollutant behaviour during TSMT. The correction factor $V_{correction}$ (derived following the approach described in chapter 5) was applied to obtain the $p(O_x)$ data shown in Figure 6.22. Therefore, the error propagation process (detail of procedures discussed in Section 4.4.3) was changed: the uncertainty from ozone loss to the sampling reactor walls (10 %) was deducted from overall uncertainty; this factor was already taken into consideration in the correction factor $V_{correction}$ incorporated in the resulting $p(O_x)$ value. Uncertainties from the ozone monitor, and estimation of reactor mean residence time, still remain in the overall uncertainty. Consequently, the uncertainty from the error in the ozone monitor measurement was 24.39 % (1 ppb / 4.1 ppb); and the uncertainty from the estimation of reactor mean residence time was 18.73 % (133 seconds / 710 seconds). The estimated overall uncertainty in measured TERI $p(O_x)$ data (U_{TERI}) was then presented as:

$$U_{TERI} = \sqrt{(0.24^2 + 0.19^2)} = 31\ \% \qquad (6.1)$$

There were substantial gaps in the measured data time series; consequently, measured TSMT hourly data were averaged to a single diurnal dataset (in 24 hours coverage), which is presented in Figure 6.23. In contrast to the pollutant frequency distribution analysis, which only used hourly data where values for all three species (NO, NO_2, O_3) were available at the same time, the following data analysis sections are based on averaging all hourly mean OPR data. The time series of hourly mean ambient pollutants and measured $p(O_x)$ are presented in the following Figure:

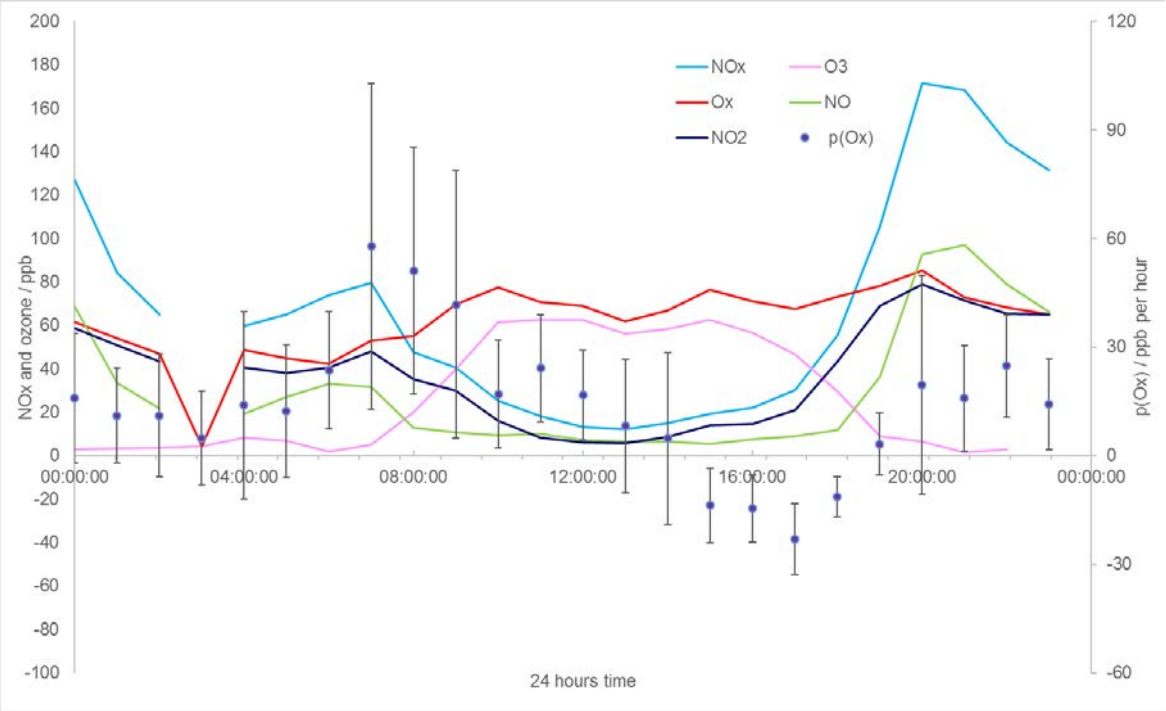

Figure 6.23. Diurnal hourly mean TERI pollutants time series; Pollutants (NO_x and ozone) are on primary axis (left), $p(O_x)$ is on secondary axis (right). Error bars represent individual uncertainty of hourly mean $p(O_x)$, in units of ppb hr^{-1}.

The uncertainties in the 24 hourly mean $p(O_x)$ values were calculated from the standard deviation of values within each hour though the 24 hours coverage, propagated with the systematic uncertainty factors, referred as "$U_{TERI\ hourly}$"

Similar to U_{TERI}, the uncertainty of hourly mean $p(O_x)$ ($U_{TERI\ hourly}$) was derived from three uncertainties: the standard deviation of hourly mean $p(O_x)$, the error in the ozone monitor reading, and the estimated reactor mean residence time. Uncertainty from the error in ozone monitor was 26.74 % (1 ppb / 3.74 ppb); uncertainty from the estimation of the reactor mean residence time was 18.73 % (133 seconds / 710 seconds).

The uncertainty for each hourly mean $p(O_x)$ was then presented as:

$$U_{TERI\ hourly} = \sqrt{((\text{fractional uncertainty from standard deviation of hourly mean } p(O_x))^2 + 0.27^2 + 0.19^2)} \quad (6.2)$$

These uncertainties are presented as the error bars in Figures 6.22 and 6.23.

In Figure 6.23, as the sun rose at 6:00, $p(O_x)$ increased and reached its peak level of around 50 ppb per hour relatively early in the morning, at 07:00 local time, before falling rapidly to near zero or negative values after 12:00. Local ozone levels started increasing from around 06:00 local time, and followed the $p(O_x)$ increase. The ambient ozone level reached its peak value of around 60 ppb at 10:00 and approximately maintained at this level until 15:00, then started to decrease. As ozone levels increased in the morning, NO_2 levels decreased at the same time. The NO_2 photolysis (by solar radiation) contributed to this effect, altering the NO : NO_2 ratio. The overall NO_x level started to decrease after 07:00, reaching a minimum at 13:00. A possible reason for this negative trend was the reduction of traffic emissions, after "rush hour" in the early morning, traffic activity and hence NO_x emissions from the surrounding area decreased. NO_x data were measured at DPCC airport site, this decrement was also possibly caused by the reduced aircraft and ground operation activities. In the afternoon, NO_x level started to increase from 13:00, before a rapid increase of NO_x reaching an extremely high level of 170 ppb at early evening (20:00), 212% higher than maximum NO_x level (80 ppb) in the morning. This phenomenon directly increased the $d(O_x)/dt$ values at the same time (Figure 6.24). It is certainly caused by excessive local NO_x emissions. In addition, NO_2 contributed to more than 40 % of the total NO_x level at this time.

These two distinctive characteristics of TERI diurnal NO_x pattern were in contrast to the behaviour of NO_x during FIOM in London (see Figure 4.29). During the FIOM, morning NO_x levels were much higher than NO_x level at early evening (reflecting a more intense morning vs afternoon rush hour, and lower boundary layer height in the morning compared to afternoon). These differences indicated there were very different NO_x emissions in both

levels and timing between TSMT and FIOM. Such different local pollution characteristics were suitable to explore the OPR system performance under contrasting environmental conditions.

6.8 Comparison of measured oxidant production with changes in ambient O_x levels during TSMT

The measured $p(O_x)$ values are local chemical oxidant production rates (as explained in chapter 2), and represent the net chemical production rates of O_x in ambient air. It is important to validate this value as far as possible, through comparison with other indicators. However, during the TERI deployment, the available pollutant measurements related to ozone chemistry were very limited; the only method is to compare the rate of change of O_x levels in ambient air to the measured oxidant production rate $p(O_x)$. This comparison is shown in Figure 6.24:

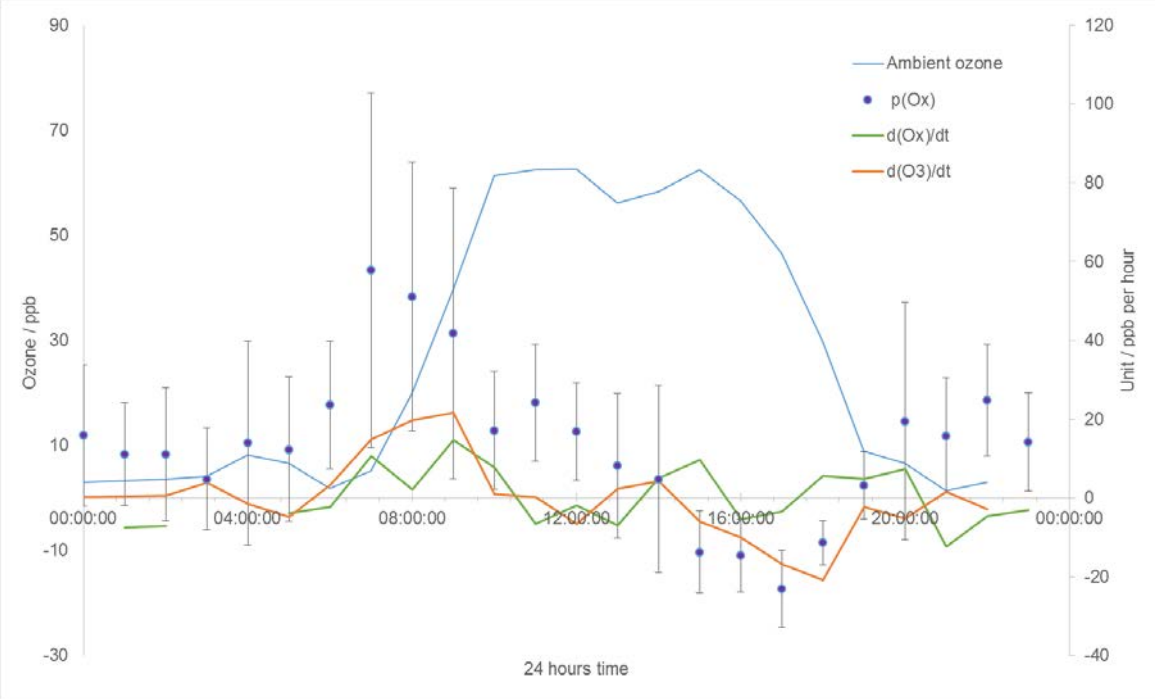

Figure 6.24. Measurements of photochemical oxidant production: Comparison between hourly mean ambient ozone levels in 24 hours coverage (left axis), and measured $p(O_x)$ (right axis. Rate of change of oxidant / ozone, $d(O_x)/dt$ and $d(O_3)/dt$, were derived from *in situ* observations results (right axis). Error bars represent individual uncertainty of hourly mean $p(O_x)$, in unit of ppb hr^{-1}.

To recap, $d(O_x)/dt$ represents the rate of change of the O_x levels in ambient air, the combination of deposition, advection and chemical production processes of O_x. There is similarity in the diurnal pattern of $d(O_x)/dt$ and the net oxidant production rate $p(O_x)$. As sunrise began, both quantities start increasing around 6:00 in the early morning, followed by a peak at ca. 8:00, then fall steadily to negative values in the afternoon. Both data sets retained positive values during most of the daytime. Numerical values of the two data sets are somewhat different, $p(O_x)$ was a factor of 1.5 – 2 higher than $d(O_x)/dt$ in the morning, but fell to comparable levels in the afternoon. The mean diurnal pattern of $d(O_x)/dt$ during TSMT in Delhi is similar to its equivalent during FIOM in London (see Chapter 4, Section 4.4.3, Figure 4.36).

Three principal factors could affect this comparison. First was the diurnal data itself, based on averaging 7 days hourly data, each day with differences in solar radiation, wind direction and pollutant levels; the averaging method itself may leads to inaccuracies. The second factor was the difference in definitions between $d(O_x)/dt$ and $p(O_x)$. The rate of change of O_x included measurement of both rate of change of NO_2 plus O_3; it consists of the combination of advection, deposition and chemical production processes for both NO_2 and O_3, while the OPR-derived $p(O_x)$ only represents chemical oxidant production. Local VOC and NO_x emissions could significantly affect $p(O_x)$, leading to a high level of chemical oxidant production under solar radiation, which (if localised to the TERI site) would not be reflected in $d(O_x)/dt$.

The third factor is that $p(O_x)$ and $d(O_x)/dt$ were measured at different locations. The measurement location for O_x (to derive $d(O_x)/dt$) was the DPCC airport monitoring site, which is 5 km west from the $p(O_x)$ measurement location – TERI University; as a result, the

measured $p(O_x)$ were downwind of the measured $d(O_x)/dt$. Emissions of ozone precursors - either at the airport location, or across the air mass transit from the airport to the TERI site - would lead to higher $p(O_x)$ values in comparison with the airport-derived $d(O_x)/dt$.

Figure 6.24 indicates there is significantly more similarity between $d(O_3)/dt$ and the OPR-derived $p(O_x)$, than was the case for $d(O_x)/dt$. The $d(O_3)/dt$ values increased in the morning and reaches its peak around 10 am, then fell steadily to -20 ppb hr^{-1} in the late afternoon, before returning to approximately zero overnight. The oxidant production rate $p(O_x)$ mirrors this trend in diurnal profile, but at somewhat higher oxidant production rates in the morning, suggesting that some of the chemical ozone formation is offset by mixing processes – *e.g.* with the night time residual layer as the boundary layer breaks down through the morning - or that the NO_x and VOCs driving the ozone formation have been added to the sampled air mass comparatively recently (*i.e.* near to the measurement point), such that the instantaneous ozone formation rate as derived from the OPR is greater than that observed in the ambient data - again, consistent with the contrast between $p(O_x)$ and $d(O_x)/dt$ noted above. This might particularly apply for emissions from the vicinity of the airport, which would not be reflected in the (airport site) $d(O_3)/dt$, but would impact upon the local atmospheric chemistry at the TERI University site. A second point is that NO_2 is a very substantial component of O_x in TERI (compared with London - see *e.g.* Figures 6.19 and 6.20). There is a better correlation between $p(O_x)$ and $d(O_3)/dt$, than compared with that between $p(O_x)$ and $d[O_x]/dt$, which may reflect the very substantial impact of local NO_x emissions upon O_3 (and O_x).

The discussions above suggest that local NO_x and VOC emissions significantly contributed to the chemical oxidant production rate at TERI site, and hence in this region of southern

New Delhi in general. The prevailing wind from the west transported abundant oxidant levels across the TERI site, resulting in significant chemical ozone and oxidant formation.

6.9 Comparison between OPR-measured Oxidant Production Rates $p(O_x)$ in London and New Delhi

The OPR system was deployed at the London NK site as part of the ClearfLo summer IOP 2012, followed by the Indian deployment in 2013. As a prototype system, it was important to compare its performance and continuity between the two deployments, particularly when a few development of the systematic performances were made after the London deployment in 2012. Two significant changes were made: redesign the sealing disk of dual sampling reactor to minimise air leak; the introduction of correction factor $V_{correction}$ was implemented in Indian measurement data. Both developments improved the system accuracy to the Indian deployment. In addition, wind direction, solar radiation level, regional pollutant level and local emission characteristics were significantly different between two measurement sites, it was a good opportunity to test and compare the OPR system performance under different environmental conditions.

To recap, FIOM was the four days intensive measurement period during London summer IOP, representing the heavy pollution period in London (only second two days period was used in following discussions). TSMT was the seven days successful measurement period during TERI OPR deployment, representing New Delhi's urban environment. Compared to the complete OPR deployments in London and India, both the FIOM and TSMT were relatively short periods, but the available data were intensively acquired and analysed.

Due to the data gaps existence in both FIOM and TSMT $p(O_x)$ data set, it was more sensible to compare mean $p(O_x)$ levels in 24 hours coverage for each measurement period. The measured $p(O_x)$ were then adjusted to each location's local (solar) time, *i.e.* $p(O_x)$ in Figures of section 6.9 were adjusted to Indian Standard Time IST (GMT + 5:30).

The resulting comparison between $p(O_x)$ is shown in Figure 6.25:

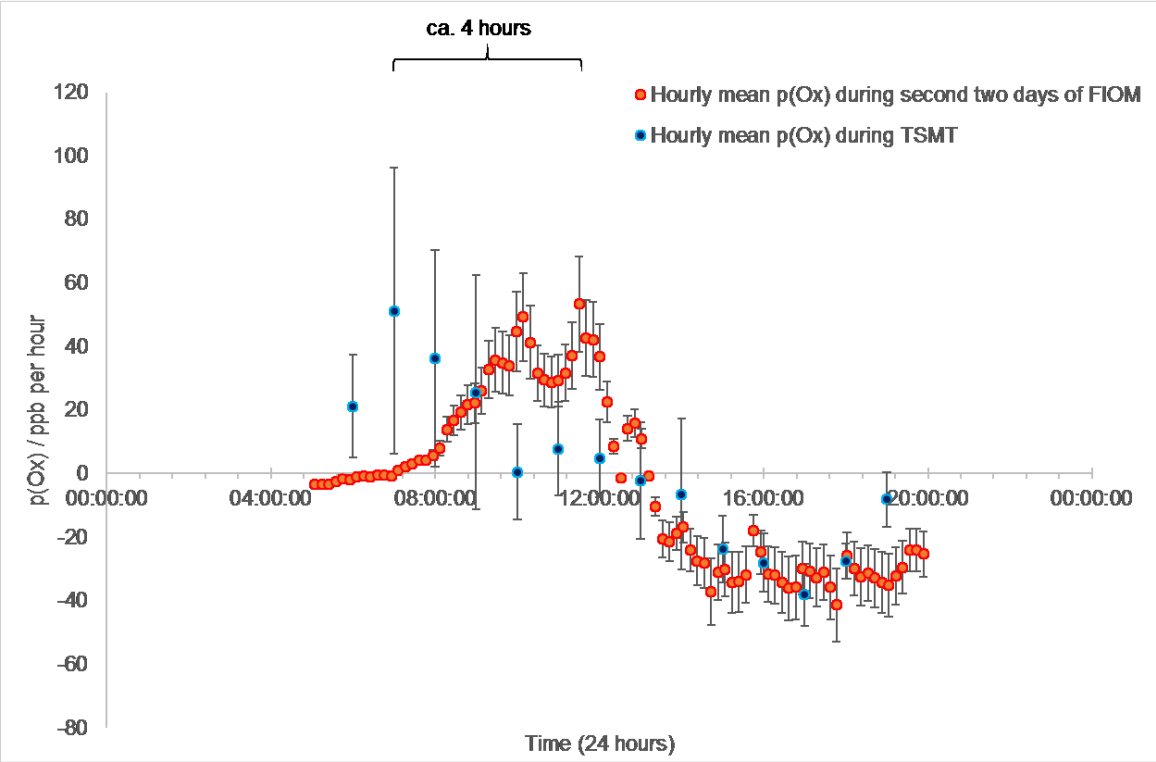

Figure 6.25. Comparison of mean $p(O_x)$ data (as a diurnal mean) between TERI (TSMT) and London (FIOM) measurement periods. TSMT $p(O_x)$ data were hourly mean values; London $p(O_x)$ data were 10-minute mean values. Error bars in London $p(O_x)$ data represent an estimated overall uncertainty of ± 28 %; error bars in TSMT $p(O_x)$ data represent variable uncertainties of hourly mean $p(O_x)$ value, derived from equation (6.2) as outlined above.

the London FIOM $p(O_x)$ data in Figure 6.25 was derived from averaged second two days data in Figure 4.50 (see Chapter 4, Section 4.6.4). The TSMT $p(O_x)$ data set showed reasonably similar diurnal pattern to the London FIOM $p(O_x)$ data set, particularly in the afternoon, when $p(O_x)$ from both data sets dropped to zero / negative values rapidly after

12:00. Similarity of negative values between two measurement site in the afternoon (ca. 15:00 – 18:00) suggests the net oxidant destruction process (NO_2 destruction and O_3 depositions) were apparent at both sites.

However, there were distinctive differences between the two data sets. The first of these is the diurnal $p(O_x)$ peak time, there is a four-hour time offset between diurnal peak $p(O_x)$ level in TSMT and FIOM data sets. Differences in the time variation of NO_x and VOC emissions between two measurement sites could account for this issue. The second difference between two datasets was the peak $p(O_x)$ values. The peak mean $p(O_x)$ value was 51 ppb hr^{-1} during TSMT; the mean peak mean $p(O_x)$ value was 61 ppb hr^{-1} during FIOM. The London peak $p(O_x)$ level was higher than that at the TERI site, but the London $p(O_x)$ values were thought to be uncertain - possibly substantially overestimated (discussed in section 7.1). However, the diurnal pattern of London $p(O_x)$ was validated by detailed chemical analyses in Section 4.4 and 4.6. Consequently, it normalised values are derived for both data sets to allow the diurnal trends to be more directly compared.

The normalization method adopted the peak value as the reference point for each dataset, with all measured $p(O_x)$ values normalized by dividing by the corresponding peak value. The normalized $p(O_x)$ comparison between FIOM and TSMT data sets is shown in following figure:

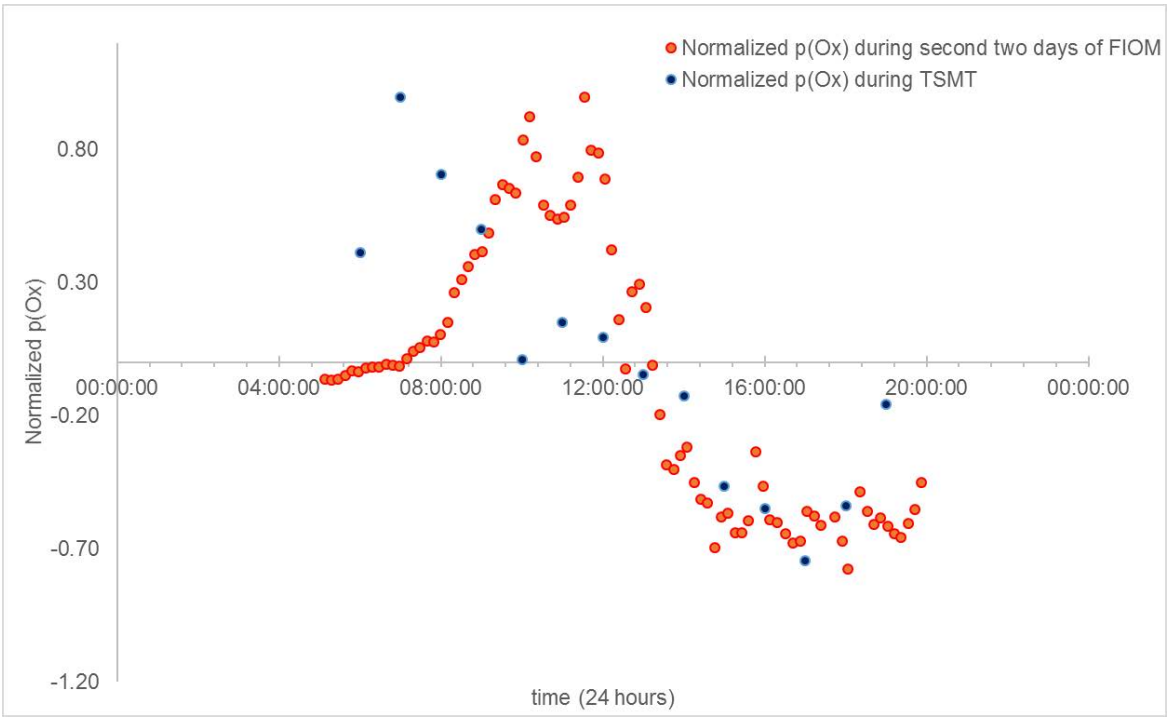

Figure 6.26. Comparison of normalized mean $p(O_x)$ trends in 24 hours coverage between TSMT and FIOM data. Error bars are omitted for clarity.

The normalized $p(O_x)$ comparison retains similarity in terms of the diurnal pattern of the two data sets, but the time offset in peak timing still remains. A potential factor causing this disagreement could be different diurnal solar radiation pattern at each location. The calculated clear-sky $j(O^1D)$ (ozone photolysis frequency) at the New Delhi TERI site during TSMT and at the London NK site during FIOM were calculated using the TUV model (TUV model, 2015), shown in the following figure:

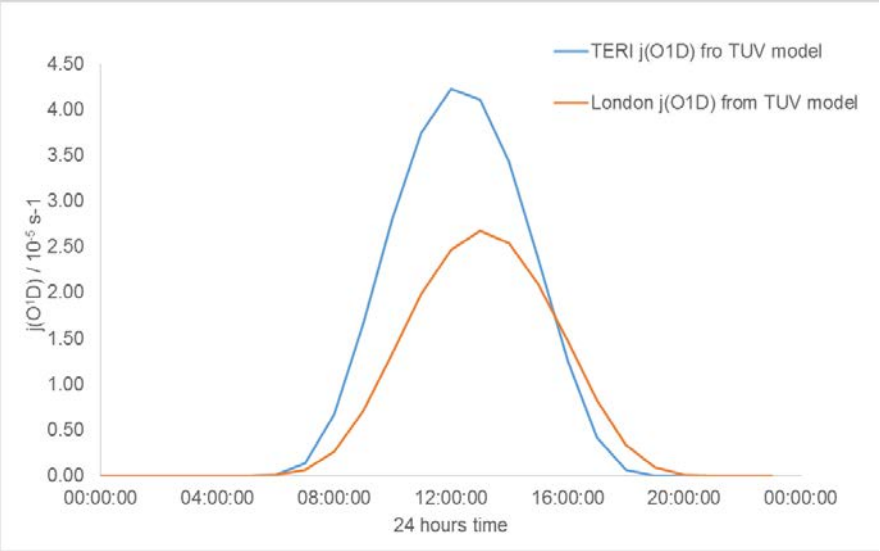

Figure 6.27. Comparison of estimated mean $j(O^1D)$ at New Delhi TERI site (blue) during TSMT and at London NK site (orange) during FIOM. Data were derived from TUV model.

The hourly mean $j(O^1D)$ of two locations have similar diurnal pattern, but there was a one-hour time offset of $j(O^1D)$ peak time-it was 12:00 at TERI site and 13:00 at NK site. Another apparent difference between two data sets was that overall $j(O^1D)$ levels were much higher at TERI site than NK site, suggesting higher OH production at TERI site, which could potentially relate to a higher chemical oxidant production rate (depending upon local VOC and NO_x levels). The mean $j(O^1D)$ comparison was then combined with the normalized $p(O_x)$ comparison between two locations, in the following figure:

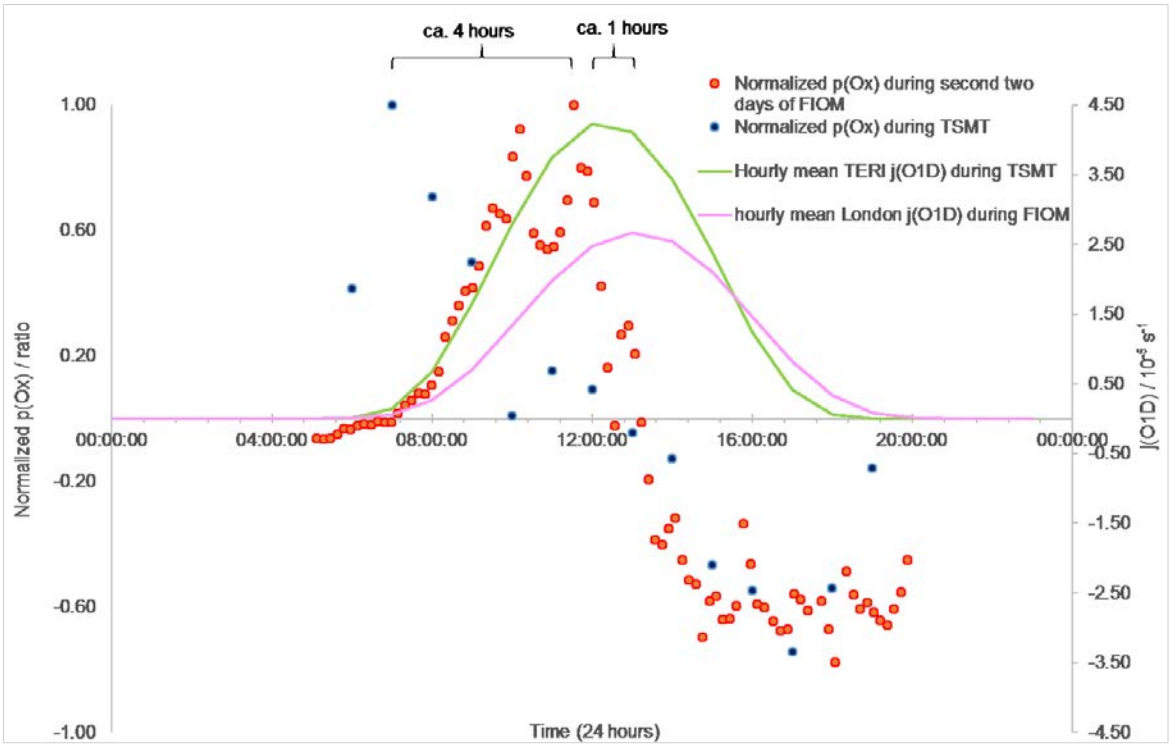

Figure 6.28. Comparison of normalized mean $p(O_x)$ trends in 24 hours coverage between TSMT and FIOM data sets, with additional data series of estimated mean $j(O^1D)$ values (derived from TUV model). Error bars are omitted for clarity.

The hourly mean $j(O^1D)$ from two locations described same pattern of solar radiation during the day time, similarity in solar radiation timing lead to similarity in $p(OH)$. As discussed previously, the $p(OH)$ and $p(O_x)$ were closely related in the urban area. There must be substantial differences in the time variation of NO_x and VOC emissions between London and New Delhi to account for the different timing of the $p(O_x)$ peaks. HONO, as an important source of OH production in urban area (Kim *et al.*, 2014), could also account for such difference. But due to the lack of HONO data at TERI site, it was not possible to evaluate this possibility. Apart from the timing issue (4 hours time offset), both OPR measured datasets $p(O_x)$ showed a similar diurnal pattern.

6.10 Mohali OPR Deployment

Following measurements at TERI University site, the OPR system was moved and set up on the campus of the Indian Institute of Science Education and Research (IISER) in Mohali, Punjab. The State of Punjab is predominantly (> 80 %) agricultural; the IISER is based on a spacious suburban campus located 10 km away from the Mohali city centre (30.667° N, -76.729° E). As Figure 6.29 showed, this campus was in an enclosed area with a few hundred residents (University staff and students). The prevailing wind direction was north-westerly during the measurement period, such that emissions from the IISER residences were to the downwind of the OPR measurement site, and residential emissions are thought to have had minor influences upon the site conditions.

Figure 6.29. Location of the city of Mohali in Northern India (Google, 2015).

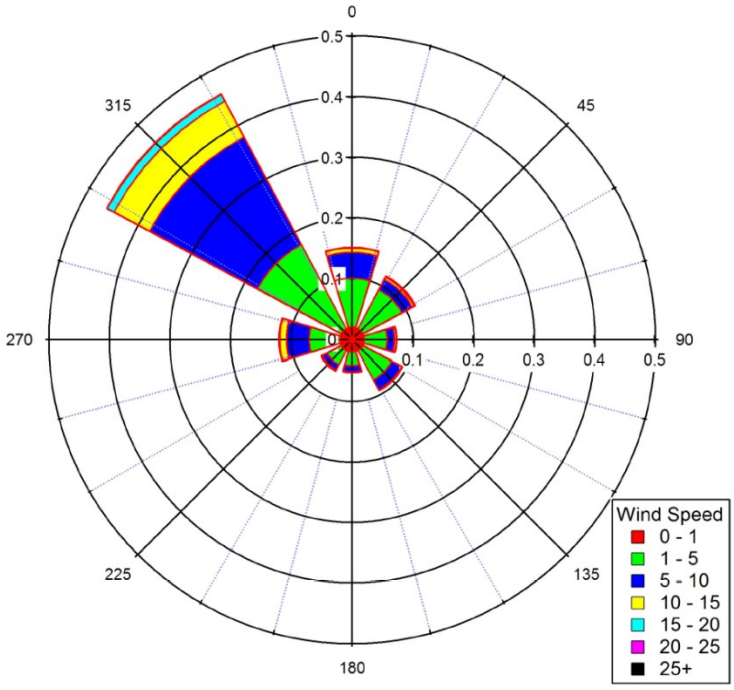

Figure 6.30. Wind rose plot derived from *in situ* one-minute time interval wind speed and direction data at IISER measurement site for May 2013. The prevailing wind was overwhelmingly from the north-west.

6.10.1 Mohali Measurement Challenges.

The OPR system was transported from the TERI measurement site to Mohali by road on 7th May 2013, and was set up for ambient measurements from ca. 20:00 on 9th May. However, during the afternoon of 10th May, the reference reactor suffered a large fracture, thought to be caused by stones kicked up from nearby construction activity, which caused large cracks that leaded to substantial air leaks. The cracked reactor could not be repaired to a satisfactory degree during the Mohali deployment (even very small leaks of ambient air substantially perturb the differential ozone measurement). As a consequence, no useful oxidant production rate data were obtained from Mohali.

6.11 Indian OPR Deployment: Concluding Remarks

The prototype OPR system was successfully deployed at the TERI site in New Delhi, after modifications as described in Chapter 4, and the implementation of the correction approaches described in chapter 5. The measured diurnal mean oxidant production rate, $p(O_x)$, agreed reasonably well with the local rate of change of the ambient O_x levels (dO_x/dt), and to changes in the ambient ozone level at TERI site, and pointed to substantial local ozone production driven by emissions local to the southern New Delhi area: local emissions were found to make a substantial contribution to ozone formation at this location.

Chapter 7: Conclusion

7.1 Summary of the OPR system development

Ambient ozone, as a secondary air pollutant in the troposphere, is a major threat to human health, plants and the environment. It is important to develop quantitative understanding of the chemical factors which drive ozone formation, and develop efficient control policy based upon real-world understanding. However, a number of limitations and uncertainties arise from current models and indirect measurement methods, currently employed to determine chemical ozone production rates. The direct measurement approach - "Ozone Production Rate (OPR) measurement system" was developed to complement these approaches and provide an alternative, direct assessment of the chemical ozone production rate in ambient air.

The OPR system consists of a pair of sampling reactors (sample and reference reactors), a NO_2 to O_3 photolytic conversion unit and a modified ozone analyser. The two reactors were identical, except for a UV blocking jacket which was installed on one (the reference) reactor. The other (sample) reactor simulates ambient air conditions, allowing chemical ozone formation arising from radical chemistry; in the reference most radical chemistry is eliminated. Measurement of the ozone difference between the flows – after NO_2-to-O3 conversion – enabled the chemical oxidant production rate to be determined.

Six principal characterisation tests were performed to measure key factors which influenced the ultimate oxidant production rate derived. Tests included assessment of the mean residence time of sampled air in the system, the NO_2 to O_3 photolytic conversion efficiency in the conversion unit, and calibration tests of system components. Uncertainties and issues

of instrument performance (systematic errors) arising from the test results have been extensively discussed, and corrections for these derived, and applied to the measured field data. Impacts from dark radical sources were evaluated, indicating that these factors would not substantially bias the OPR measurements during the daytime.

The OPR system was deployed in London 2012, as part of the ClearfLo summer IOP. The OPR measurement was performed from 21st July to 23rd August 2012, with a focus on a "Four days Intensive OPR Measurement (FIOM)" from 9th August to 12th August.

The air pollution climatology of NO_x and ozone during both the summer IOP and the FIOM were statistically analysed; the results showed contrasting characteristics in NO_x / O_3 levels between Harwell and London. The comparison suggested that the "urban decrement" effect contributes significantly to controlling NO_x and O_3 levels in London. The thesis then focused on the FIOM period, which represented a summertime (photochemical) pollution episode for London, to perform an intensive analysis and gain a greater understanding of the local pollution precursors, and the performance of the OPR system.

During the FIOM period, ambient NO_x and O_3 data were measured from both UoB and NK AURN instruments. Regression analysis indicated they were well correlated. Traffic emissions were the predominant source of NO_x, as shown by correlations with CO and black carbon data. The $p(O_x)$ measured by the OPR system was compared to ambient NO_x and O_3 levels, the results showed relatively good *qualitative* agreement in diurnal pattern with measured ambient O_x, but *absolute* $p(O_x)$ values were substantially higher than trends in the ambient ozone levels suggested.

Detailed chemical analyses were performed to compare the measured $p(O_x)$ to estimated OH production rates, $p(OH)$. HONO photolysis and ozone photolysis, as primary OH production

process, were evaluated to determine *p*(OH). The analysis showed a good agreement between two datasets in terms of diurnal timescale.

An estimation of net chemical oxidant production rate, $p_e(O_x)$, was performed to allow comparison with $p(O_x)$. This analysis quantified chemical oxidant formation reactions, $p_c(O_3)$, and chemical oxidant loss reactions, $l(O_3)$. The chemical oxidant production rate calculations were based upon the rates of conversion of NO to NO_2 via measured HO_2 and inferred RO_2 concentrations. Chemical oxidant loss processes considered were $OH + NO_2 + M$, $HO_2 + O_3$, $OH + O_3$ and $RO_2 + NO_2$ reactions. The comparison showed general agreement between the two data sets on the second, third and fourth days of the FIOM period in terms of trend and diurnal behaviour, but not for absolute magnitude.

An advection analysis was carried out to determine the contribution of transport effects to oxidant increases at the NK site. This analysis used monitoring sites around the four cardinal directions (North, South, West and East) as satellite locations, simulating air mass transport to the NK site, based on measured wind direction and speed. The results showed higher ozone levels on 11th and 12th August at NK site were likely to have been caused by aged polluted emissions from continental Europe. A further estimation of chemical oxidant production rates was performed using the *in situ* data via the advection analysis, following on from the (hypothetical) assumption that differences between O_x at satellite locations and NK site were caused only by chemical production process during the air mass transport. Result suggested both data sets had similar diurnal patterns, but the ambient-measurement-derived dO_x/dt values were substantially lower than their OPR-measured $p(O_x)$ equivalents. The unusually high values of oxidant production rates $p(O_x)$ may have arisen from systematic errors relating to reactor flow pathways, or possibly due to the imperfect reactor

sealing in the field. Both aspects were substantially modified for the subsequent OPR measurements in New Delhi.

Systematic errors in the OPR measurements consisted of two major factors: The variable NO_2 conversion efficiency in the conversion unit, and differences in photochemical steady state (PSS) between the two sampling reactors.

A simplified conversion cell chemistry model was implemented to address the actual NO_x chemical processes occurring in the converter cells. This was based upon the simulation of changes in NO, NO_2 and O_3 levels after the air flow entered the converter cell, assuming the presence of NO_x and O_3 only in the air flow. The NO_2 to O_3 conversion efficiency were derived from comparison between NO_2 input and simulated O_3 output from the converter cell. A multi linear regression analysis was applied to determine the dependence of the simulated NO_2 to O_3 conversion efficiency to NO_x and O_3 levels, allowing the model results to be operationally applied to the OPR measurements. The resulting estimated *in situ* conversion efficiency was referred as "$CE_{converter}$".

A further correction approach was developed to simulate the changes in NO, NO_2 and O_3 in both sample and reference reactors, based upon the NO_x and O_3 in the ambient air, and the changes in NO_2 photolysis frequency in the reference reactor. This model was integrated with $CE_{converter}$ to determine the systematic measurement artefact in measured $p(O_x)$ values from these effects, and the corrections implemented for measured values of $p(O_x)$ in New Delhi.

India, as a fast developing country, is facing serious ozone pollution problems in both urban and rural areas. Ambient ozone levels have continued to increase in India, and exceedance of ozone air quality standards are frequently observed in New Delhi, causing health impacts

on the local population. Ozone also causes substantial (ca. 12 % in rice, wheat and soybean) crop yield losses in Indian agriculture (Ghude *et al.*, 2014). There is a demand for comprehensive research into the sources of local and regional ozone pollution, in order to develop possible control strategies. The OPR system could be a useful tool for this requirement, in particular as the necessary information for alternative approaches (*e.g.* emission inventories to drive numerical models) is largely absent in India.

OPR measurements were performed during April and May 2013 at two measurement sites: at TERI University in New Delhi from 23rd April to 7th May, and at IISER Mohali from 8th to 16th May.

The main aim of OPR deployment in India was to obtain proof-of-concept data for the application of the OPR approach to assess the contribution of local chemical factors to ozone formation. The Indian measurements allowed a comparison with the London OPR deployment, to test the system performance with after developments to the instrument, and correction approaches under significantly different environmental conditions.

The New Delhi OPR measurement was successful from an OPR-operation perspective, but due to the modest supporting measurements available, wider chemical interpretation of the results obtained was limited: Only ambient O_3, NO_x and meteorological data could be acquired, with NO_x levels measured from the DPCC Delhi International Airport monitoring station (5 km west of TERI University).

Compared to the London observations, a statistical analysis of New Delhi's air pollution climatology showed significant differences in NO_x / ozone levels, in particular that the NO_2: NO ratio are substantially higher than in London.

Power failures during the measurement period caused a number of "data gaps"; with relatively complete measurement of $p(O_x)$ seen over seven days during the New Delhi OPR measurements. Consequently, the OPR-measured $p(O_x)$ and ambient NO_x and O_3 levels were averaged to produce a mean diurnal profile. The measured diurnal mean oxidant production rate agreed reasonably well with the local rate of change total oxidant (dO_x/dt), and the diurnal hourly mean time series of $p(O_x)$, NO_x and O_3 indicated that substantial local ozone production occurred, driven by emissions local to the southern New Delhi area. This fact, along with the inter comparison between first and second two day periods time series of OPR measured $p(O_x)$ from section 4.6.4, showed clear evidences of significant contribution from local chemical process to changes in ambient ozone levels by comparing to advection, mixing and deposition processes.

In addition, the OPR's concept was pioneered by Cazorla and Brune's MOPS system, both OPR and MOPS are based on the same principle. Although they were built in significantly different design / materials (different materials and design of sampling reactors, different conversion unit, different flow pattern), it is logical to compare the performance between OPR and MOPS. Particularly, the MOPS was recently developed to version 2 with two redesigned sampling reactor in 2013 (Baier *et al.*, 2015) (Figure 7.2). MOPS version 1 & version 2 (MOPS1 and MOPS2) was deployed in Houston in 2013 to measure ambient oxidant production rate. The measurement results of MOPS were manually adjusted to match the 24 hours coverage from results from OPR measurements (Figure 6.25), the comparison between two systems are presented in following figure:

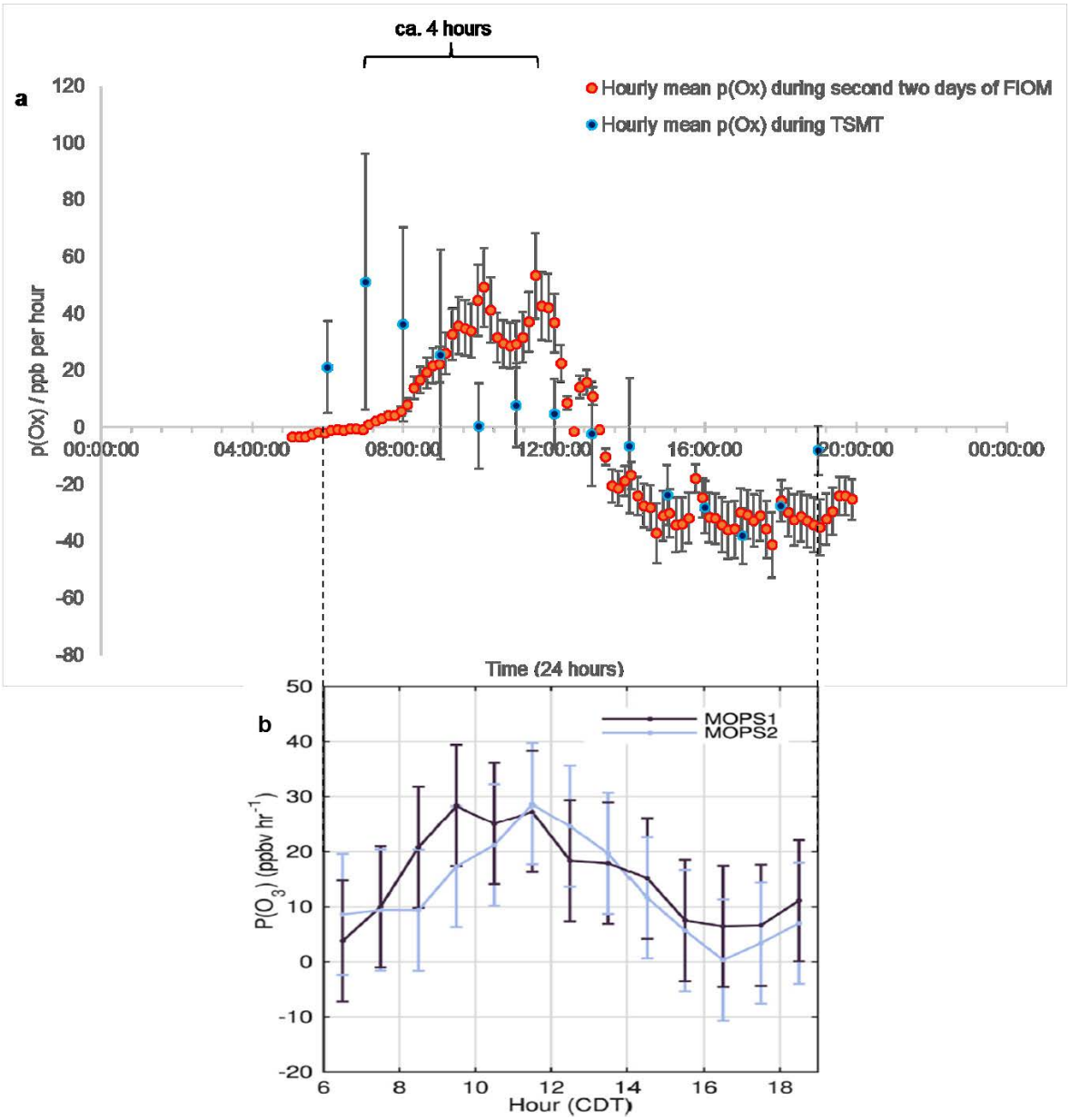

Figure 7.1. Comparison of averaged $p(O_x)$ data (as a diurnal mean) between OPR measured $p(O_x)$ (FIOM and TSMT) and MOPS measured $P(O_3)$. TSMT $p(O_x)$ data were hourly mean values; FIOM $p(O_x)$ data were 10-minute mean values; MOPS $P(O_3)$ data were hourly mean values. Error bars in London $p(O_x)$ data represent an estimated overall uncertainty of ± 28 %; Error bars in TSMT $p(O_x)$ data represent variable uncertainties of hourly mean $p(O_x)$ value, derived from equation (6.2) as outlined above; Error bars in both MOPS1 and MOPS2 data represent 1 σ level of standard deviation (Baier *et al*., 2015).

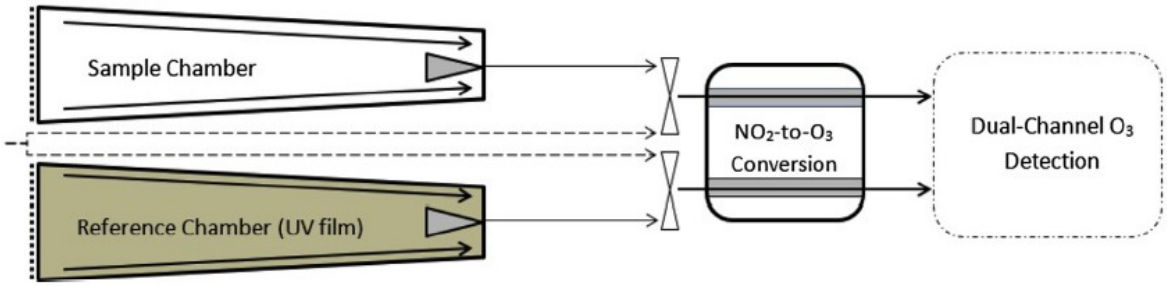

Figure 7.2. Schematic of MOPS version 2 (Baier *et al*., 2015).

The measured $P(O_3)$ by MOPS had the same definition as $p(O_x)$ by OPR, but in different abbreviation. Both measured oxidant production rate by different systems were similar in diurnal pattern, the sharp rise of the oxidant production rate in the morning were measured by both systems. But the afternoon negative values of $p(O_x)$ in OPR measurement were not apparent in the MOPS measured $P(O_3)$. As previously discussed in section 6.9, variations of local NO_x levels, background ozone levels and VOC emissions between three locations substantially contributed to the chemical oxidant production rate during the day. It was likely that local chemical process caused higher oxidant production rate in the afternoon in Houston. This comparison provided further validation to OPR measurement results, it was confirmed that OPR is capable of measuring ambient oxidant production rate.

The broad hypothesis (see section 1.9) that local chemical processes make a substantial contribution to the observed increase in ozone - or oxidant - levels may be accepted following these OPR measurements.

To conclude, a prototype chemical ozone production rate (OPR) instrument was constructed and evaluated in the laboratory, and its performance evaluated during two contrasting field deployments, in London and New Delhi, providing proof-of-concept evidence for the application of the OPR approach. The inter comparison between OPR and MOPS measurements further validated the OPR approach. This thesis reports substantial

developments to the MOPS concept pioneered by Cazorla & Brune (2010), in particular relating to materials choices (quartz vs Teflon), reactor design, NO_2 conversion efficiency, and the implementation of correction procedures for systematic uncertainties in the measurement.

7.2 Future work

The OPR system remains under development, and a number of improvements could be made to the instrument, and a range of further atmospheric experiments performed.

In the sample and reference reactors, flow visualisation (smoke) tests showed that "mini" turbulence patterns remained after the addition of the flow straighteners; there is scope to change the reactor design, allowing more time / distance for laminar flow to form. The NO_2 to O_3 conversion efficiency estimation model highlighted the greater correction needed with less complete NO_2 conversion (pointing to a need for brighter photolysis lamps). The error assessment did not consider the possibility for HONO formation to occur on the OPR reactor surfaces, which could affect the ozone production chemistry following photolysis. A recent report suggested $p(O_x)$ can exhibit up to a 10 ppb h^{-1} bias due to surface HONO production, but this estimation was based on a simple photo chemical box model to estimate HONO levels generated in the reactors, it was also not clear which surfaces were producing HONO (Baier *et al*., 2015). Further works are required to accurately measure the artefact from surface HONO formation.

Currently, the OPR system is predominantly manually controlled. Automation is essential for such a system to increase its practicability (and user friendliness). Possible automated functions may include periodic zeroing (*e.g.* by removing the Ultem jacket of the reference reactor), auto-data uploading to some form of cloud server, and auto-restart for the control programme after communication errors, alongside remote access (now implemented).

Further understanding of atmospheric chemical processing could result from extensions to the OPR capability. For example, addition of NO_x or VOCs to directly probe the ozone

production regime would provide greater insight for control policies. The addition of artificial light to selectively enhance specific radical formation routes (*e.g.* O_3 photolysis vs HONO photolysis vs HCHO photolysis, based upon their different wavelength sensitives) would provide unique insight into the atmospheric chemical processing.

During the field measurements, the OPR system could be a useful tool to validate HO_x measurements (*e.g.* OH and HO_2 measurement by LIF) by allowing comparison of the estimated oxidant production rate derived from HO_x measurement and the *in situ* OPR readings. As future developments reduce the remaining systematic uncertainties, and these are counter-validated by comparison with HO_x measurements, the OPR approach can then be implemented as a stand-alone instrument to provide ozone production rate measurements at much reduced cost and complexity compared with LIF or PERCA techniques, providing potential opportunity for more routine or even commercial versions of the OPR system.

If the OPR system reaches broad acceptance, networks of OPR instruments could be set up in urban and rural areas, to develop an ozone productivity "map". The measured $p(O_x)$, alongside ambient NO_x / VOC data, could be used to identify areas of predominantly chemical ozone formation, and determine the controlling ozone formation regime. Subsequently, emissions control strategies (NO_x vs VOCs) could be developed to target those emissions sources with the greatest contribution to ozone formation (or to which measured ozone levels would show the greatest sensitivity), reducing the impact from ozone exposure to humans, vegetation and crop yields. In polluted areas with a current lack of instrumentation, such as China and India, there is a clear demand for such direct measurement systems to identify local chemical factors driving boundary layer ozone formation.

References

Alam, M.S., Rickard, A.R., Camredon, M., Wyche, K.P., Carr, T., Hornsby, K.E., Monks, P.S. and Bloss, W.J. 2013. Radical Product Yields from the Ozonolysis of Short Chain Alkenes under Atmospheric Boundary Layer Conditions. *The Journal of Physical Chemistry A.* **117**(47), pp.12468-12483.

AQEG. 2007. *Trends in Primary Nitrogen Dioxide in the UK. Report of the UK Air Quality Expert Group, AQEG. Prepared for the Department for Environment, Food and Rural Affairs, the Scottish Executive, the Welsh Assembly Government and the Department of the Environment in Northern Ireland.*

AQEG. 2009. *Ozone in the United Kingdom. Report of the UK Air Quality Expert Group, AQEG. Prepared for the Department for Environment, Food and Rural Affairs, the Scottish Executive, the Welsh Assembly Government and the Department of the Environment in Northern Ireland.*

Atkinson, R., Baulch, D.L., Cox, R.A., Crowley, J.N., Hampson, R.F., Hynes, R.G., Jenkin, M.E., Rossi, M.J., Troe, J. and Subcommittee, I. 2006. Evaluated kinetic and photochemical data for atmospheric chemistry: Volume II: gas phase reactions of organic species. *Atmos. Chem. Phys.* **6**(11), pp.3625-4055.

Attri, S. and Tyagi, A. 2010. Climate profile of India. *Environment Monitoring and Research Centre, India Meteorology Department: New Delhi, India.*

Authority, G.L. 2008. *London atmospheric emissions inventory 2008.* Greater London Authority.

Avnery, S., Mauzerall, D.L., Liu, J. and Horowitz, L.W. 2011. Global crop yield reductions due to surface ozone exposure: 1. Year 2000 crop production losses and economic damage. *Atmospheric Environment.* **45**(13), pp.2284-2296.

Baier, B.C., Brune, W.H., Lefer, B.L., Miller, D.O. and Martins, D.K. 2015. Direct ozone production rate measurements and their use in assessing ozone source and receptor regions for Houston in 2013. *Atmospheric Environment.* **114**, pp.83-91.

Barker, T., Davidson, O., Davidson, W., Huq, S., Karoly, D., Kattsov, V., Liu, J., Lohmann, U., Manning, M. and Matsuno, T. 2007. Climate change 2007: Synthesis report. *Valencia; IPPC.*

Bauer, D., D'Ottone, L. and Hynes, A.J. 2000. O 1D quantum yields from O3 photolysis in the near UV region between 305 and 375 nm. *Physical Chemistry Chemical Physics.* **2**(7), pp.1421-1424.

Bigi, A. and Harrison, R.M. 2010. Analysis of the air pollution climate at a central urban background site. *Atmospheric Environment.* **44**(16), pp.2004-2012.

Blake, N. and Blake, D. 2002. *Tropospheric chemistry and composition*. Elsevier science.

Bloss, W.J. 2009. Atmospheric chemical processes of importance in cities. *Issues in Environmental Science and Technology.* **28**, p42.

Bloss, W.J., Evans, M.J., Lee, J.D., Sommariva, R., Heard, D.E. and Pilling, M.J. 2005. The oxidative capacity of the troposphere: Coupling of field measurements of OH and a global chemistry transport model. *Faraday Discussions.* **130**(0), pp.425-436.

Bohnenstengel, S.I., Belcher, S.E., Aiken, A., Allan, J.D., Allen, G., Bacak, A., Bannan, T.J., Barlow, J.F., Beddows, D.C.S., Bloss, W.J., Booth, A.M., Chemel, C., Coceal, O., Di Marco, C.F., Dubey, M.K., Faloon, K.H., Fleming, Z.L., Furger, M., Gietl, J.K., Graves, R.R., Green, D.C., Grimmond, C.S.B., Halios, C.H., Hamilton, J.F.,

Harrison, R.M., Heal, M.R., Heard, D.E., Helfter, C., Herndon, S.C., Holmes, R.E., Hopkins, J.R., Jones, A.M., Kelly, F.J., Kotthaus, S., Langford, B., Lee, J.D., Leigh, R.J., Lewis, A.C., Lidster, R.T., Lopez-Hilfiker, F.D., McQuaid, J.B., Mohr, C., Monks, P.S., Nemitz, E., Ng, N.L., Percival, C.J., Prévôt, A.S.H., Ricketts, H.M.A., Sokhi, R., Stone, D., Thornton, J.A., Tremper, A.H., Valach, A.C., Visser, S., Whalley, L.K., Williams, L.R., Xu, L., Young, D.E. and Zotter, P. 2015. Meteorology, Air Quality, and Health in London: The ClearfLo Project. *Bulletin of the American Meteorological Society*. **96**(5), pp.779-804.

Bowdalo, D.R., Evans, M.J. and Sofen, E.D. 2016. Spectral analysis of atmospheric composition: application to surface ozone model-measurement comparisons. *Atmos. Chem. Phys. Discuss.* **2016**, pp.1-24.

Carbajo, P.G., Smith, S.C., Holloway, A.-L., Smith, C.A., Pope, F.D., Shallcross, D.E. and Orr-Ewing, A.J. 2008. Ultraviolet Photolysis of HCHO: Absolute HCO Quantum Yields by Direct Detection of the HCO Radical Photoproduct. *The Journal of Physical Chemistry A.* **112**(48), pp.12437-12448.

Carslaw, D., Beevers, S., Westmoreland, E., Williams, M., Tate, J., Murrells, T., Stedman, J., Li, Y., Grice, S. and Kent, A. 2011. Trends in NOx and NO2 emissions and ambient measurements in the UK. *Defra, London.*

Castellanos, P., Boersma, K.F. and van der Werf, G.R. 2014. Satellite observations indicate substantial spatiotemporal variability in biomass burning NO_x emission factors for South America. *Atmos. Chem. Phys.* **14**(8), pp.3929-3943.

Cazorla, M. and Brune, W.H. 2010. Measurement of Ozone Production Sensor. *Atmos. Meas. Tech.* **3**(3), pp.545-555.

Chang, W., Liao, H. and Wang, H. 2009. Climate responses to direct radiative forcing of anthropogenic aerosols, tropospheric ozone, and long-lived greenhouse gases in eastern China over 1951–2000. *Advances in Atmospheric Sciences.* **26**(4), pp.748-762.

Cofala, J., Amann, M., Klimont, Z., Kupiainen, K. and Höglund-Isaksson, L. 2007. Scenarios of global anthropogenic emissions of air pollutants and methane until 2030. *Atmospheric Environment.* **41**(38), pp.8486-8499.

Collins, W.J., Derwent, R.G., Johnson, C.E. and Stevenson, D.S. 2000. The impact of human activities on the photochemical production and destruction of tropospheric ozone. *Quarterly Journal of the Royal Meteorological Society.* **126**(566), pp.1925-1951.

Cooper, O.R., Gao, R.-S., Tarasick, D., Leblanc, T. and Sweeney, C. 2012. Long-term ozone trends at rural ozone monitoring sites across the United States, 1990–2010. *Journal of Geophysical Research: Atmospheres.* **117**(D22).

Thermo Electron Corporation. 2004. *Model 49i UV photometric Ozone analyser.* [Online]. [Accessed 10 Oct]. Available from: http://www.thermoscientific.com/en/product/model-49-i-i-i-ozone-analyzer.html

Cox, R. 1999. Ozone and peroxy radical budgets in the marine boundary layer: Modelling the effect of NOx. *Journal of Geophysical Research: Atmospheres (1984–2012).* **104**(D7), pp.8047-8056.

CPCB (Central Pollution Control Board). 2015. *National ambient air quality standards in India.* [Online]. [Accessed 11 Jan]. Available from: http://cpcb.nic.in/National_Ambient_Air_Quality_Standards.php

Crilley, L.R., Bloss, W.J., Yin, J., Beddows, D.C.S., Harrison, R.M., Allan, J.D., Young, D.E., Flynn, M., Williams, P., Zotter, P., Prevot, A.S.H., Heal, M.R., Barlow, J.F., Halios, C.H., Lee, J.D., Szidat, S. and Mohr, C. 2015. Sources and contributions of wood smoke during winter in London: assessing local and regional influences. *Atmos. Chem. Phys.* **15**(6), pp.3149-3171.

Davenport, C. 2014. *Obama to Introduce Sweeping New Controls Aimed at Ozone.* [Online]. [Accessed 15 August]. Available from: http://www.nytimes.com/2014/11/26/us/politics/obama-to-introduce-sweeping-new-controls-on-ozone-emissions.html?_r=0

Davidson, E.A. and Kingerlee, W. 1997. A global inventory of nitric oxide emissions from soils. *Nutrient cycling in agroecosystems.* **48**(1), pp.37-50.

DEFRA (Department for Environment Food and Rural Affairs). 2014. *DEFRA monitoring networks.* [Online]. [Accessed 18 Nov]. Available from: http://uk-air.defra.gov.uk/networks/find-sites

Denman, K.L., Brasseur, G.P., Chidthaisong, A., Ciais, P., Cox, P.M., Dickinson, R.E., Hauglustaine, D.A., Heinze, C., Holland, E.A. and Jacob, D.J. 2007. Couplings between changes in the climate system and biogeochemistry. *Climate change 2007: The physical science basis.*

Derwent, D., Fraser, A., Abbott, J., Jenkin, M., Willis, P. and Murrells, T. 2010. Evaluating the performance of air quality models. *DEFRA Report.* (3), p7.

Di Carlo, P., Brune, W.H., Martinez, M., Harder, H., Lesher, R., Ren, X., Thornberry, T., Carroll, M.A., Young, V., Shepson, P.B., Riemer, D., Apel, E. and Campbell, C. 2004. Missing OH Reactivity in a Forest: Evidence for Unknown Reactive Biogenic VOCs. *Science.* **304**(5671), pp.722-725.

Doherty, R.M., Wild, O., Shindell, D.T., Zeng, G., MacKenzie, I.A., Collins, W.J., Fiore, A.M., Stevenson, D.S., Dentener, F.J., Schultz, M.G., Hess, P., Derwent, R.G. and Keating, T.J. 2013. Impacts of climate change on surface ozone and intercontinental ozone pollution: A multi-model study. *Journal of Geophysical Research: Atmospheres.* **118**(9), pp.3744-3763.

Donner, L.J., Wyman, B.L., Hemler, R.S., Horowitz, L.W., Ming, Y., Zhao, M., Golaz, J.-C., Ginoux, P., Lin, S.-J. and Schwarzkopf, M.D. 2011. The dynamical core, physical parameterizations, and basic simulation characteristics of the atmospheric component AM3 of the GFDL global coupled model CM3. *Journal of Climate.* **24**(13), pp.3484-3519.

Greater London Authority. 2008. *London atmospheric emissions inventory 2008.* Greater London Authority.

Edward, J.S. 2004. *Ozone damage to plants.* [Online]. [Accessed 25 July]. Available from: http://www.aces.edu/pubs/docs/A/ANR-0940/ANR-0940.pdf

Emery, C., Jung, J., Downey, N., Johnson, J., Jimenez, M., Yarwood, G. and Morris, R. 2012. Regional and global modelling estimates of policy relevant background ozone over the United States. *Atmospheric Environment.* **47**, pp.206-217.

Emmerson, K.M. and Evans, M.J. 2009. Comparison of tropospheric gas-phase chemistry schemes for use within global models. *Atmos. Chem. Phys.* **9**(5), pp.1831-1845.

EPA (United States Environmental Protection Agency). 2013. *Health Effects of Ozone in the General Population.* [Online]. [Accessed 15 Dec]. Available from: http://www.epa.gov/apti/ozonehealth/population.html

Eur-lex. 2004. *Directive 2004/42/CE of the European Parliament and of the Council of 21 April 2004 on the limitation of emissions of volatile organic compounds due to the*

use of organic solvents in certain paints and varnishes and vehicle refinishing products and amending Directive 1999/13/EC. [Online]. [Accessed 5 Feb]. Available from: http://eur-lex.europa.eu/legal-content/EN/TXT/?uri=OJ:L:2004:143:TOC

Filleul, L., Cassadou, S., Médina, S., Fabres, P., Lefranc, A., Eilstein, D., Le Tertre, A., Pascal, L., Chardon, B. and Blanchard, M. 2006. The relation between temperature, ozone, and mortality in nine French cities during the heat wave of 2003. *Environmental Health Perspectives.* pp.1344-1347.

Fried, A., McKeen, S., Sewell, S., Harder, J., Henry, B., Goldan, P., Kuster, W., Williams, E., Baumann, K. and Shetter, R. 1997. Photochemistry of formaldehyde during the 1993 Tropospheric OH Photochemistry Experiment. *Journal of Geophysical Research: Atmospheres.* **102**(D5), pp.6283-6296.

Ghude, S., Jain, S.L., Arya, B.C., Beig, G., Ahammed, Y.N., Kumar, A. and Tyagi, B. 2008. Ozone in ambient air at a tropical megacity, Delhi: characteristics, trends and cumulative ozone exposure indices. *Journal of Atmospheric Chemistry.* **60**(3), pp.237-252.

Ghude, S.D., Jena, C., Chate, D., Beig, G., Pfister, G., Kumar, R. and Ramanathan, V. 2014. Reductions in India's crop yield due to ozone. *Geophysical Research Letters.* **41**(15), pp.5685-5691.

Google. 2014. *Sion Manning School, 51.5205473,-0.2141255.* [Online]. [Accessed 9 Aug]. Available from: https://www.google.co.uk/maps/

Google. 2015. *Delhi International Airport, 28.555623, 77.117297.* [Online]. [Accessed 12 March]. Available from: https://www.google.co.uk/maps/

Gratien, A., Lefort, M., Picquet-Varrault, B., Orphal, J., Doussin, J.F. and Flaud, J.M. 2009. Experimental intercomparison of the absorption cross-sections of nitrous acid (HONO) in the ultraviolet and mid-infrared spectral regions. *Journal of Quantitative Spectroscopy and Radiative Transfer.* **110**(4–5), pp.256-263.

Green, T.J., Reeves, C.E., Fleming, Z.L., Brough, N., Rickard, A.R., Bandy, B.J., Monks, P.S. and Penkett, S.A. 2006. An improved dual channel PERCA instrument for atmospheric measurements of peroxy radicals. *Journal of Environmental Monitoring.* **8**(5), pp.530-536.

Gressent, A., Sauvage, B., Defer, E., Werner Pätz, H., Thomas, K., Holle, R., Cammas, J.-P., Nédélec, P., Boulanger, D., Thouret, V. and Volz-Thomas, A. 2014. Lightning NO x influence on large-scale NO y and O 3 plumes observed over the northern mid-latitudes. *2014.*

Gryparis, A., Forsberg, B., Katsouyanni, K., Analitis, A., Touloumi, G., Schwartz, J., Samoli, E., Medina, S., Anderson, H.R. and Niciu, E.M. 2004. Acute effects of ozone on mortality from the "air pollution and health: a European approach" project. *American journal of respiratory and critical care medicine.* **170**(10), pp.1080-1087.

Gurjar, B.R., Butler, T.M., Lawrence, M.G. and Lelieveld, J. 2008. Evaluation of emissions and air quality in megacities. *Atmospheric Environment.* **42**(7), pp.1593-1606.

Harrison, R.M., Peak, J.D. and Collins, G.M. 1996. Tropospheric cycle of nitrous acid. *Journal of Geophysical Research: Atmospheres.* **101**(D9), pp.14429-14439.

Heard D, W.L., Stone D, Clancy N, Lee J, KLeffman J, Laufs S, Bandy B,. 2013. Measurements of free radicals in a megacity during the Clean Air for London project. In: *EGU 2013, April 2013, Vienna, Austria*.

Hofzumahaus, A., Rohrer, F., Lu, K., Bohn, B., Brauers, T., Chang, C.-C., Fuchs, H., Holland, F., Kita, K., Kondo, Y., Li, X., Lou, S., Shao, M., Zeng, L., Wahner, A. and Zhang, Y. 2009. Amplified Trace Gas Removal in the Troposphere. *Science.* **324**(5935), pp.1702-1704.

Holloway, A.M. and Wayne, R.P. 2010. *Atmospheric chemistry.* Royal Society of Chemistry.

Horowitz, L.W. 2006. Past, present, and future concentrations of tropospheric ozone and aerosols: Methodology, ozone evaluation, and sensitivity to aerosol wet removal. *Journal of Geophysical Research: Atmospheres (1984–2012).* **111**(D22).

Hsu, J. and Prather, M.J. 2009. Stratospheric variability and tropospheric ozone. *Journal of Geophysical Research: Atmospheres.* **114**(D6).

Indian Times. 2012. *IGI Airport to use all runways together.* [Online]. [Accessed 11 Feb]. Available from: http://timesofindia.indiatimes.com/city/delhi/IGI-Airport-to-use-all-runways-together/articleshow/13829900.cms

Itoh, H., Isegame, S., Miura, H., Suzuki, S. and Rusinov, I.M. 2011. Surface Loss Rate of Ozone in a Cylindrical Tube. *Ozone: Science & Engineering.* **33**(2), pp.106-113.

Jaegle, L., Steinberger, L., Martin, R.V. and Chance, K. 2005. Global partitioning of NOx sources using satellite observations: Relative roles of fossil fuel combustion, biomass burning and soil emissions. *Faraday Discussions.* **130**(0), pp.407-423.

Jaffe, D. and Ray, J. 2007. Increase in surface ozone at rural sites in the western US. *Atmospheric Environment.* **41**(26), pp.5452-5463.

Jenkin, M.E. 2008. Trends in ozone concentration distributions in the UK since 1990: Local, regional and global influences. *Atmospheric Environment.* **42**(21), pp.5434-5445.

Jenkin, M.E., Saunders, S.M., Wagner, V. and Pilling, M.J. 2003. Protocol for the development of the Master Chemical Mechanism, MCM v3 (Part B): tropospheric degradation of aromatic volatile organic compounds. *Atmos. Chem. Phys.* **3**(1), pp.181-193.

Jenkin, M.E., Utembe, S.R. and Derwent, R.G. 2008. Modelling the impact of elevated primary NO2 and HONO emissions on regional scale oxidant formation in the UK. *Atmospheric Environment.* **42**(2), pp.323-336.

Kelly, F.J. 2003. Oxidative stress: its role in air pollution and adverse health effects. *Occupational and Environmental Medicine.* **60**(8), pp.612-616.

Kim, S., Guenther, A., Karl, T. and Greenberg, J. 2011. Contributions of primary and secondary biogenic VOC total OH reactivity during the CABINEX (Community Atmosphere-Biosphere Interactions Experiments)-09 field campaign. *Atmos. Chem. Phys.* **11**(16), pp.8613-8623.

Kim, S., VandenBoer, T.C., Young, C.J., Riedel, T.P., Thornton, J.A., Swarthout, B., Sive, B., Lerner, B., Gilman, J.B., Warneke, C., Roberts, J.M., Guenther, A., Wagner, N.L., Dubé, W.P., Williams, E. and Brown, S.S. 2014. The primary and recycling sources of OH during the NACHTT-2011 campaign: HONO as an important OH primary source in the wintertime. *Journal of Geophysical Research: Atmospheres.* **119**(11), pp.6886-6896.

Krupa, S.V. and Manning, W.J. 1988. Toxic Substance in the Environment Atmospheric ozone: Formation and effects on vegetation. *Environmental Pollution.* **50**(1), pp.101-137.

Kulkarni, P.S., Bortoli, D., Silva, A.M. and Reeves, C.E. 2015. Enhancements in nocturnal surface ozone at urban sites in the UK. *Environmental Science and Pollution Research.* **22**(24), pp.20295-20305.

Kumar, A., Wu, S., Weise, M., Honrath, R., Owen, R., Helmig, D., Kramer, L., Val Martin, M. and Li, Q. 2013. Free-troposphere ozone and carbon monoxide over the North Atlantic for 2001–2011. *Atmospheric Chemistry and Physics.* **13**(24), pp.12537-12547.

Lammel, G. and Perner, D. 1988. Sixteenth Annual Conference of the Gesellschaft fur Aerosolforschung: The atmospheric aerosol as a source of nitrous acid in the polluted atmosphere. *Journal of Aerosol Science.* **19**(7), pp.1199-1202.

Langford, B., Davison, B., Nemitz, E. and Hewitt, C.N. 2009. Mixing ratios and eddy covariance flux measurements of volatile organic compounds from an urban canopy (Manchester, UK). *Atmos. Chem. Phys.* **9**(6), pp.1971-1987.

Lee, J.D., Lewis, A.C., Monks, P.S., Jacob, M., Hamilton, J.F., Hopkins, J.R., Watson, N.M., Saxton, J.E., Ennis, C., Carpenter, L.J., Carslaw, N., Fleming, Z., Bandy, B.J., Oram, D.E., Penkett, S.A., Slemr, J., Norton, E., Rickard, A.R., K Whalley, L., Heard, D.E., Bloss, W.J., Gravestock, T., Smith, S.C., Stanton, J., Pilling, M.J. and Jenkin, M.E. 2006. Ozone photochemistry and elevated isoprene during the UK heatwave of august 2003. *Atmospheric Environment.* **40**(39), pp.7598-7613.

Lefohn, A.S., Shadwick, D.S. and Ziman, S.D. 1998. Peer Reviewed: The Difficult Challenge of Attaining EPA's New Ozone Standard. *Environmental Science & Technology.* **32**(11), pp.276A-282A.

Lefohn, A.S., Shadwick, D. and Oltmans, S.J. 2008. Characterizing long-term changes in surface ozone levels in the United States (1980–2005). *Atmospheric Environment.* **42**(35), pp.8252-8262.

Lelieveld, J., Butler, T.M., Crowley, J.N., Dillon, T.J., Fischer, H., Ganzeveld, L., Harder, H., Lawrence, M.G., Martinez, M., Taraborrelli, D. and Williams, J. 2008. Atmospheric oxidation capacity sustained by a tropical forest. *Nature.* **452**(7188), pp.737-740.

Lewis, A.C., Carslaw, N., Marriott, P.J., Kinghorn, R.M., Morrison, P., Lee, A.L., Bartle, K.D. and Pilling, M.J. 2000. A larger pool of ozone-forming carbon compounds in urban atmospheres. *Nature.* **405**(6788), pp.778-781.

Lobell, D.B., Schlenker, W. and Costa-Roberts, J. 2011. Climate Trends and Global Crop Production Since 1980. *Science.* **333**(6042), pp.616-620.

Matsumi, Y. and Kawasaki, M. 2003. Photolysis of Atmospheric Ozone in the Ultraviolet Region. *Chemical Reviews.* **103**(12), pp.4767-4782.

Meagher, N.E. and Anderson, W.R. 2000. Kinetics of the O(3P) + N2O Reaction. 2. Interpretation and Recommended Rate Coefficients. *The Journal of Physical Chemistry A.* **104**(25), pp.6013-6031.

Mills, G., Buse, A., Gimeno, B., Bermejo, V., Holland, M., Emberson, L. and Pleijel, H. 2007. A synthesis of AOT40-based response functions and critical levels of ozone for agricultural and horticultural crops. *Atmospheric Environment.* **41**(12), pp.2630-2643.

Mohanakumar, K. 2008. *Stratosphere troposphere interactions: an introduction.* Springer Science & Business Media.

Mudway, I.S. and Kelly, F.J. 2000. Ozone and the lung: a sensitive issue. *Molecular Aspects of Medicine.* **21**(1–2), pp.1-48.

Munir, S., Chen, H. and Ropkins, K. 2013. Quantifying temporal trends in ground level ozone concentration in the UK. *Science of The Total Environment.* **458–460**, pp.217-227.

Myhre, G., Shindell, D., Bréon, F., Collins, W., Fuglestvedt, J., Huang, J., Koch, D., Lamarque, J., Lee, D. and Mendoza, B. 2013. Climate change 2013: the physical science basis. Contribution of Working Group I to the Fifth Assessment Report of the Intergovernmental Panel on Climate Change. *K., Tignor, M., Allen, SK, Boschung, J., Nauels, A., Xia, Y., Bex, V., and Midgley, PM, Cambridge University Press Cambridge, United Kingdom and New York, NY, USA.*

NCR (National Research Council). 2008. *Estimating mortality risk reduction and economic benefits from controlling ozone air pollution*. National Research Council. The National Academies Press.

Parrish, D.D., Law, K.S., Staehelin, J., Derwent, R., Cooper, O.R., Tanimoto, H., Volz-Thomas, A., Gilge, S., Scheel, H.E., Steinbacher, M. and Chan, E. 2012. Long-term changes in lower tropospheric baseline ozone concentrations at northern mid-latitudes. *Atmos. Chem. Phys.* **12**(23), pp.11485-11504.

Parrish, D.D., Millet, D.B. and Goldstein, A.H. 2009. Increasing ozone in marine boundary layer inflow at the west coasts of North America and Europe. *Atmos. Chem. Phys.* **9**(4), pp.1303-1323.

Pidwirny, M. 2006. The Nitrogen Cycle. *Fundamentals of Physical Geography.* p4.

Prinn, R.G. 2003. THE CLEANSING CAPACITY OF THE ATMOSPHERE. *Annual Review of Environment and Resources.* **28**(1), pp.29-57.

Raes, F. and Hjorth, J. 2006. *Answers to the Urbino questions. ACCENT Secretariat, Universita di Urbino, Italy.* ISBN 92-79-02413-2.

Rebetez, M., Dupont, O. and Giroud, M. 2009. An analysis of the July 2006 heatwave extent in Europe compared to the record year of 2003. *Theoretical and Applied Climatology.* **95**(1), pp.1-7.

Reidmiller, D.R., Fiore, A.M., Jaffe, D.A., Bergmann, D., Cuvelier, C., Dentener, F.J., Duncan, B.N., Folberth, G., Gauss, M., Gong, S., Hess, P., Jonson, J.E., Keating, T., Lupu, A., Marmer, E., Park, R., Schultz, M.G., Shindell, D.T., Szopa, S., Vivanco, M.G., Wild, O. and Zuber, A. 2009. The influence of foreign vs. North American emissions on surface ozone in the US. *Atmos. Chem. Phys.* **9**(14), pp.5027-5042.

Ren, X., Brune, W.H., Mao, J., Mitchell, M.J., Lesher, R.L., Simpas, J.B., Metcalf, A.R., Schwab, J.J., Cai, C. and Li, Y. 2006. Behavior of OH and HO 2 in the winter atmosphere in New York City. *Atmospheric Environment.* **40**, pp.252-263.

Rickard, A.R., Johnson, D., McGill, C.D. and Marston, G. 1999. OH Yields in the Gas-Phase Reactions of Ozone with Alkenes. *The Journal of Physical Chemistry A.* **103**(38), pp.7656-7664.

RMI (Rocky Mountain Instrument). 2015. *Transmissions for UV-Grade Fused Silica (SiO2).* [Online]. [Accessed 15 May]. Available from: http://rmico.com/material-data#mgf2

Rooney, C., McMichael, A.J., Kovats, R.S. and Coleman, M.P. 1998. Excess mortality in England and Wales, and in Greater London, during the 1995 heatwave. *Journal of epidemiology and community health.* **52**(8), pp.482-486.

Royal Society. 2008. *Ground-level ozone in the 21st century: future trends, impacts and policy implications.* [Online]. [Accessed 2 Feb]. Available from: https://royalsociety.org/~/media/Royal_Society_Content/policy/publications/2008/7925.pdf

Sander, S., Friedl, R., Barker, J., Golden, D., Kurylo, M., Wine, P., Abbatt, J., Burkholder, J., Kolb, C. and Moortgat, G. 2011. *Chemical Kinetics and Photochemical Data for use in Atmospheric Studies–Evaluation Number 17, JPL Publication 10–6, June 10, 2011*.

Sarwar, G., Gantt, B., Schwede, D., Foley, K., Mathur, R. and Saiz-Lopez, A. 2015. Impact of Enhanced Ozone Deposition and Halogen Chemistry on Tropospheric Ozone over the Northern Hemisphere. *Environmental Science & Technology.* **49**(15), pp.9203-9211.

Saunders, S.M., Jenkin, M.E., Derwent, R.G. and Pilling, M.J. 2003. Protocol for the development of the Master Chemical Mechanism, MCM v3 (Part A): tropospheric degradation of non-aromatic volatile organic compounds. *Atmos. Chem. Phys.* **3**(1), pp.161-180.

Schumann, U. and Huntrieser, H. 2007. The global lightning-induced nitrogen oxides source. *Atmospheric Chemistry and Physics.* **7**(14), pp.3823-3907.

Seinfeld, J.H. and Pandis, S.N. 2012. *Atmospheric chemistry and physics: from air pollution to climate change.* John Wiley & Sons.

Sitch, S., Cox, P.M., Collins, W.J. and Huntingford, C. 2007. Indirect radiative forcing of climate change through ozone effects on the land-carbon sink. *Nature.* **448**(7155), pp.791-794.

Stedman, J.R. 2004. The predicted number of air pollution related deaths in the UK during the August 2003 heatwave. *Atmospheric Environment.* **38**(8), pp.1087-1090.

Stein, A.F., Draxler, R.R., Rolph, G.D., Stunder, B.J.B., Cohen, M.D. and Ngan, F. 2015. NOAA's HYSPLIT Atmospheric Transport and Dispersion Modeling System. *Bulletin of the American Meteorological Society.* **96**(12), pp.2059-2077.

Stevenson, D.S., Young, P.J., Naik, V., Lamarque, J.F., Shindell, D.T., Voulgarakis, A., Skeie, R.B., Dalsoren, S.B., Myhre, G., Berntsen, T.K., Folberth, G.A., Rumbold, S.T., Collins, W.J., MacKenzie, I.A., Doherty, R.M., Zeng, G., van Noije, T.P.C., Strunk, A., Bergmann, D., Cameron-Smith, P., Plummer, D.A., Strode, S.A., Horowitz, L., Lee, Y.H., Szopa, S., Sudo, K., Nagashima, T., Josse, B., Cionni, I., Righi, M., Eyring, V., Conley, A., Bowman, K.W., Wild, O. and Archibald, A. 2013. Tropospheric ozone changes, radiative forcing and attribution to emissions in the Atmospheric Chemistry and Climate Model Intercomparison Project (ACCMIP). *Atmos. Chem. Phys.* **13**(6), pp.3063-3085.

Stone, D., Whalley, L.K. and Heard, D.E. 2012. Tropospheric OH and HO2 radicals: field measurements and model comparisons. *Chemical Society Reviews.* **41**(19), pp.6348-6404.

Tang, Y., An, J., Wang, F., Li, Y., Qu, Y., Chen, Y. and Lin, J. 2015. Impacts of an unknown daytime HONO source on the mixing ratio and budget of HONO, and hydroxyl, hydroperoxyl, and organic peroxy radicals, in the coastal regions of China. *Atmos. Chem. Phys.* **15**(16), pp.9381-9398.

Theloke, J. and Friedrich, R. 2007. Compilation of a database on the composition of anthropogenic VOC emissions for atmospheric modeling in Europe. *Atmospheric Environment.* **41**(19), pp.4148-4160.

Topaloglou, C., Kazadzis, S., Bais, A.F., Blumthaler, M., Schallhart, B. and Balis, D. 2005. NO2 and HCHO photolysis frequencies from irradiance measurements in Thessaloniki, Greece. *Atmos. Chem. Phys.* **5**(6), pp.1645-1653.

Trebs, I., Bohn, B., Ammann, C., Rummel, U., Blumthaler, M., Königstedt, R., Meixner, F.X., Fan, S. and Andreae, M.O. 2009. Relationship between the NO2 photolysis frequency and the solar global irradiance. *Atmos. Meas. Tech.* **2**(2), pp.725-739.

TUV calculator. 2015. *TUV Calculator.* [Online]. [Accessed 15 May]. Available from: http://cprm.acom.ucar.edu/Models/TUV/Interactive_TUV/

Van Dingenen, R., Dentener, F.J., Raes, F., Krol, M.C., Emberson, L. and Cofala, J. 2009. The global impact of ozone on agricultural crop yields under current and future air quality legislation. *Atmospheric Environment.* **43**(3), pp.604-618.

Vestreng, V., Ntziachristos, L., Semb, A., Reis, S., Isaksen, I.S.A. and Tarrasón, L. 2009. Evolution of NO_x emissions in Europe with focus on road transport control measures. *Atmos. Chem. Phys.* **9**(4), pp.1503-1520.

Vieno, M., Dore, A.J., Stevenson, D.S., Doherty, R., Heal, M.R., Reis, S., Hallsworth, S., Tarrason, L., Wind, P., Fowler, D., Simpson, D. and Sutton, M.A. 2010. Modelling surface ozone during the 2003 heat-wave in the UK. *Atmos. Chem. Phys.* **10**(16), pp.7963-7978.

Vingarzan, R. 2004. A review of surface ozone background levels and trends. *Atmospheric Environment.* **38**(21), pp.3431-3442.

Vinken, G.C.M., Boersma, K.F., Maasakkers, J.D., Adon, M. and Martin, R.V. 2014. Worldwide biogenic soil NO_x emissions inferred from OMI NO_2 observations. *Atmos. Chem. Phys.* **14**(18), pp.10363-10381.

Visavale, G. 2015. *Introduction to Turbulence and Turbulence Modeling.* [Online]. [Accessed 12 May]. Available from: https://www.learncax.com/knowledge-base/introduction-to-turbulence-modelling

Walker, H.L., Derwent, R.G., Donovan, R. and Baker, J. 2009. Photochemical trajectory modelling of ozone during the summer PUMA campaign in the UK West Midlands. *Science of The Total Environment.* **407**(6), pp.2012-2023.

Wang, S. and Hao, J. 2012. Air quality management in China: Issues, challenges, and options. *Journal of Environmental Sciences.* **24**(1), pp.2-13.

Wargan, K., Pawson, S., Stajner, I. and Thouret, V. 2010. Spatial structure of assimilated ozone in the upper troposphere and lower stratosphere. *Journal of Geophysical Research: Atmospheres.* **115**(D24).

Wilcox, D.C. 1998. *Turbulence modeling for CFD.* DCW industries La Canada, CA.

Williams, M., Barrowcliffe, R., Laxen, D. and Monks, P. 2011. *Review of Air Quality modelling in Defra*. Defra.

WHO (World Health Organization). 2003. Health aspects of air pollution with particulate matter, ozone and nitrogen dioxide: report on a WHO working group, Bonn, Germany 13-15 January 2003.

WHO (World Health Organization). 2005. *WHO Air Quality Guidelines Global Update 2005: Report on a Working Group Meeting, Bonn, Germany, 18-20 October 2005.* WHO Regional Office for Europe.

Xie, Y., Elleman, R., Jobson, T. and Lamb, B. 2011. Evaluation of O3-NOx-VOC sensitivities predicted with the CMAQ photochemical model using Pacific Northwest 2001 field observations. *Journal of Geophysical Research: Atmospheres.* **116**(D20).

Young, P.J., Archibald, A.T., Bowman, K.W., Lamarque, J.F., Naik, V., Stevenson, D.S., Tilmes, S., Voulgarakis, A., Wild, O., Bergmann, D., Cameron-Smith, P., Cionni, I., Collins, W.J., Dalsøren, S.B., Doherty, R.M., Eyring, V., Faluvegi, G., Horowitz, L.W., Josse, B., Lee, Y.H., MacKenzie, I.A., Nagashima, T., Plummer, D.A., Righi, M., Rumbold, S.T., Skeie, R.B., Shindell, D.T., Strode, S.A., Sudo, K., Szopa, S. and Zeng, G. 2013. Pre-industrial to end 21st century projections of tropospheric ozone from the Atmospheric Chemistry and Climate Model Intercomparison Project (ACCMIP). *Atmos. Chem. Phys.* **13**(4), pp.2063-2090.

Zyrichidou, I., Koukouli, M.E., Balis, D., Markakis, K., Poupkou, A., Katragkou, E., Kioutsioukis, I., Melas, D., Boersma, K.F. and van Roozendael, M. 2015. Identification of surface NOx emission sources on a regional scale using OMI NO2. *Atmospheric Environment.* **101**, pp.82-93.